



THE UNIVERSITY OF QUEENSLAND
AUSTRALIA

**Design of a 3D Shape Transitioning Nozzle and Experimental
Thrust Measurements of an Airframe Integrated Scramjet**

Jens Kunze

Dipl.-Ing. Univ. Aerospace Engineering

A thesis submitted for the degree of Doctor of Philosophy at
The University of Queensland in 2020

School of Mechanical & Mining Engineering

Centre for Hypersonics

Abstract

The scramjet engine provides the means for airbreathing propulsion at flight speeds exceeding Mach 5. As part of a three-stage-to-orbit system it is envisioned to play a major role in sustainable access-to-space. When compared to a rocket engine, scramjets offer a higher specific impulse and increased mission flexibility through the manoeuverability of the vehicle.

At the scramjet's operating Mach number range, the aerodynamic drag forces acting on the vehicle require the engines to be highly efficient and to be integrated with the airframe to be able to produce net thrust. Scramjet engines with three dimensional shape transition inlets and nozzles allow for modularity of the propulsion system, engine-airframe integration and high efficiency of the individual engine components. The present study introduces a methodolgy to design three dimensional shape transition nozzles and experimentally investigates an airframe integrated Mach 12 scramjet fitted with a nozzle which was designed with the proposed methodology.

The nozzle design method is based on the rectangular-to-elliptical shape transition (REST) inlet design. A parent flowfield with the desired nozzle flow properties was designed first. In the present study the method of characteristics (MOC) was used to create an axisymmetric parent flowfield with a contoured centre body. The centre body creates a second set of expansion waves which ensure horizontal flow at a prescribed neutral streamline within the flowfield. This approach avoids the creation of forward facing surface area in the design; a common problem in similar design approaches. Rao's method of thrust optimisation was used to determine the length of the parent flowfield. In his approach, Rao defines a control surface over which the inviscid thrust of an axisymmetric nozzle is maximised. The maximum can be found by constraining the nozzle's length and the inflow and ambient conditions. Next, the desired combustor exit cross-section is discretised by a suitable number of points and each point is streamline traced through the parent flowfield. By combining the streamlines to a surface, a nozzle can be created that recreates a part of the parent flowfield and interfaces with the combustor of the scramjet powered vehicle. The streamline tracing is repeated for the desired cross-section at the nozzle exit. The last step consists of blending these two nozzles in such a way that a smooth surface is obtained. The final result is a quasi streamline traced nozzle that, in the present study, transitions in shape from an elliptical cross-section at the combustor exit to a rectangular cross-section at the nozzle exit. Cross-sections with different geometries can be used as required.

The proposed parent flowfield allows for high design flexibility through the use of the contoured centre body while at the same time avoiding the creation of drag surfaces which were observed in previous work.

A shape transition nozzle was designed for an airframe integrated Mach 12 REST scramjet model. Numerical simulations of the parent flowfield and the shape transition nozzle showed that the thrust performance of the shape transition nozzle is similar to that of the parent flowfield.

The experimental model was modified to accommodate an on-board fuel system and catch and release mechanisms suitable for free-flight experiments. Fishing line was used to suspend the model initially. Once the facility flow started the strands were pushed against razor blades installed on the model and it was released. An image tracking based force measurement technique was then used to track the motion of the model and from the determined trajectories derive the forces on the free-flying model.

The model was tested at a Mach 8 test condition with a dynamic pressure of approximately 80 kPa in the T4 shock tunnel at the University of Queensland. Fuelled experiments at various equivalence ratios with a combined injection scheme through two sets of fuel injectors were conducted; the first set located in the inlet and the second in the combustor. Approximately 40 % of fuel was injected into the inlet and 60 % into the combustor. It could be shown that the engine started successfully, robust combustion was achieved and the model was unrestrained during the test time. The results demonstrate that, despite vibrations of the experimental facility, the net forces in two dimensions were successfully measured. A distinct increase in thrust proportional to the equivalence ratio could be measured. Whether the engine produced positive net thrust during the experiments could not be determined due to the measurement uncertainty. However, a combination of results from cycle analysis and CFD at the Mach 8 condition suggests that the model does produce positive net thrust. Positive lift was observed at all fuelling conditions. Measurements of the pitching moment were found to be unreliable due to large measurement uncertainties.

The present study marked the first time that forces were measured on a free-flying experimental model in the T4 shock tunnel.

Declaration by author

This thesis is composed of my original work, and contains no material previously published or written by another person except where due reference has been made in the text. I have clearly stated the contribution by others to jointly-authored works that I have included in my thesis.

I have clearly stated the contribution of others to my thesis as a whole, including statistical assistance, survey design, data analysis, significant technical procedures, professional editorial advice, financial support and any other original research work used or reported in my thesis. The content of my thesis is the result of work I have carried out since the commencement of my higher degree by research candidature and does not include a substantial part of work that has been submitted to qualify for the award of any other degree or diploma in any university or other tertiary institution. I have clearly stated which parts of my thesis, if any, have been submitted to qualify for another award.

I acknowledge that an electronic copy of my thesis must be lodged with the University Library and, subject to the policy and procedures of The University of Queensland, the thesis be made available for research and study in accordance with the Copyright Act 1968 unless a period of embargo has been approved by the Dean of the Graduate School.

I acknowledge that copyright of all material contained in my thesis resides with the copyright holder(s) of that material. Where appropriate I have obtained copyright permission from the copyright holder to reproduce material in this thesis and have sought permission from co-authors for any jointly authored works included in the thesis.

Publications included in this thesis

No publications included

Submitted manuscripts included in this thesis

No manuscripts submitted for publication.

Other publications during candidature

Conference papers

J. Kunze, M. K. Smart, and R. J. Gollan (2018). “A Design Method for Shape Transition Nozzles for Hypersonic Vehicles”. In: *22nd AIAA International Space Planes and Hypersonics Systems and Technologies Conference*. Reston, Virginia: American Institute of Aeronautics and Astronautics. ISBN: 978-1-62410-577-7. DOI: 10.2514/6.2018-5318. URL: <https://arc.aiaa.org/doi/10.2514/6.2018-5318>

Contributions by others to the thesis

The present study was conceived by Prof Michael Smart. He conducted the computational simulation presented in Section 6.1.1. This includes the generation of the grid.

The pitot survey shots presented in Section 4.1.2 were conducted by Dr Tristan Vanyai.

Statement of parts of the thesis submitted to qualify for the award of another degree

No works submitted towards another degree have been included in this thesis.

[Research Involving Human or Animal Subjects]

No animal or human subjects were involved in this research.

Acknowledgements

And so it ends; with one of many cups of coffee on a Sunday afternoon, exactly 4 years in the making. The fact that I've made it to this point is testimony to the amazing support I have had over the course of my PhD. I'm grateful for everyone that has been a part of my life since I came to UQ; my life wouldn't be the same without you.

Michael, I want to thank you for being blunt. For telling me the things that I didn't want to hear when I needed to hear them. For always having an open door to talk and regularly checking in when I was buried in the T4 control room; for your guidance when I got lost in some detail and at the same time leaving me the freedom I had in how I did my work.

David, first of all thank you for insisting that I drop my model. I couldn't have gotten a decent measurement without it. Thank you for lots of conversations and advice on all things experimental and especially T4.

Stuart, thank you for your continued support and interest in my project despite the distance. Thank you for taking the time to look at my data and suggesting improvements and for answering all my questions on the image tracking technique.

Rowan, thank you for introducing me into the world of designing scramjet nozzles. For setting up simulations and showing me how to use the various codes that you've written that made my life a whole lot easier.

Keith, thank you for fixing everything that I broke. For making my vague idea of a mechanism to wind up fishing line a reality. For making my fuel system and helping me out with everything I needed to do during my three campaigns.

To everyone that operated for me, introduced me to T4 or otherwise contributed to my experiments: Sam, Kev, Zac, Augusto, Will, Ryan, Eric, Alex, Isaac and Wilson. Thank you guys for all your hard work, for coming in early and staying late and for making the time in the tunnel enjoyable in spite of the long hours and bad results.

PJ and Kyle, thank you for helping me get my simulation working, for tireless debugging and all your advice on all things computational.

To all the people that have kept me sane, read parts of my thesis, fed me and offered their support over the last four years and especially during the last six months. In no particular order: Jen, Ricardo, Julie, Bre, Jas, Lock and Casey. I couldn't have done it without you.

Thank you to everyone in the Gauls and the national team. The trainings, competitions, dinners, drinks and dancing with all of you made for some of my favourite memories of the last four years.

There are more people to thank. Ryan Flaherty for his idea of melting the fishing line with a resistor. Tim McIntyre for his help with the optics.

Finally, I want to thank everyone at the CfH. For lunches, coffees, Friday arvo beers, chicken, chats and the general great time I have had since I arrived here. I can't imagine a better place to do a

PhD.

These last four years have been challenging to say the least. It's on to new adventures now; but first I'm going to have a nap.

Financial support

This research was supported by the Northrup Grummon Corporation, a University of Queensland Research Training Tuition Fee Offset and a University of Queensland International Scholarship.

Keywords

scramjet, scramjet nozzle design, force measurements, hypersonics, airbreathing propulsion, access-to-space

Australian and New Zealand Standard Research Classification (ANZSRC)

ANZSRC code: 090107, Hypersonic Propulsion and Hypersonic Aerodynamics, 100%

Fields of Research (FoR) Classification

FoR code: 0901, Aerospace Engineering, 100%

CONTENTS

Contents	xiii
List of Figures	xvii
List of Tables	xxiii
Nomenclature	xxv
1 Introduction	1
1.1 Scramjets	1
1.2 Motivation	3
1.3 Objective and Methods	4
1.3.1 Methods: Design	4
1.3.2 Methods: Experimental Analysis	5
2 Literature Review	7
2.1 Scramjet Nozzle Design	7
2.1.1 General Analyses of Nozzle and Vehicle Performance	7
2.1.2 Design of the Nozzle Geometry	11
2.2 Thrust Measurements in Impulse Facilities and Free-Flying Experiments	20
2.2.1 Force Balances	21
2.2.2 Accelerometer Measurements	23
2.2.3 Optical Force Measurements	23
2.2.4 Free-Flying Experiments	25
2.3 Summary	27

CONTENTS

3 Nozzle Design Methodology	29
3.1 Rao's Method of Thrust Optimisation	30
3.1.1 Implementation	32
3.1.2 Validation	34
3.1.3 Comparison to Minimum Length Nozzles With Uniform Exit Flow	34
3.2 Dual Expansion Rao Nozzle	37
3.3 Streamline Tracing, Blending and the Combustor Interface	43
3.4 Mach 12 REST engine nozzle	45
3.4.1 Nozzle Flowpath	46
3.4.2 CFD Analysis of the Parent Flowfield Capture	49
4 Experimental Design	57
4.1 Experimental Facility	58
4.1.1 Facility Instrumentation	60
4.1.2 Test Condition	62
4.1.3 Determination of Test Time	69
4.2 Experimental Model	70
4.2.1 Nozzle	71
4.2.2 Catch and Release Mechanisms	72
4.2.3 Instrumentation	76
4.2.4 Fuel System	78
4.3 Motion Tracking Apparatus	81
5 Image Tracking Based Force Measurement Technique	87
5.1 Edge Detection with Sub-Pixel Accuracy	88
5.2 Calculation of the Model Trajectory	91
5.3 Calibration	94
5.4 Error Analysis Using Artificial Images	97
5.4.1 Artificial Images	98
5.4.2 Resolution, Frame Rate and Magnitude of Acceleration	99
5.4.3 Optical Distortion	102
6 Experimental Results	105
6.1 Pressure Data and CFD Results	107
6.1.1 Fuel-off CFD Simulation	107
6.1.2 Fuel-Off Shots	111
6.1.3 Fuel-On Shots	111
6.2 Image Tracking Data	112

6.2.1	Cycle Analysis	114
6.2.2	Facility Vibrations	119
6.2.3	Force Measurement Data	126
7	Conclusions	131
7.1	Findings of the Present Study	132
7.1.1	Nozzle Design	132
7.1.2	Image Tracking	133
7.1.3	Experimental	133
7.2	Recommendations	136
7.2.1	Nozzle Design	136
7.2.2	Image Tracking	137
7.2.3	Experimental	137
References		139
A	Supplemental Experimental Data	151
A.1	The 2 mm Test Condition	151
A.2	Supplemental Pressure Data	152
A.2.1	Unstart Behaviour	153
B	Vibration Data	159
C	Image Tracking Data	165
D	Shot Summary	175

LIST OF FIGURES

1.1	A schematic of a scramjet engine.	2
2.1	An airframe integrated scramjet.	8
2.2	A scramjet nozzle by Henry and Anderson.	9
2.3	A schematic of the scramjet engine module analysed by Weidner et al. (1977).	9
2.4	The experimental model of the nozzle investigated by Watanabe (1993).	12
2.5	A schematic showing Rao's design approach.	13
2.6	A schematic of a scarfed nozzle. Adapted from Shyne and Keith (1990).	13
2.7	A 2D nozzle design for non-uniform inflows according to Mo et al. (2015).	14
2.8	The thrust optimised nozzle design approach by Lv et al. (2017c).	15
2.9	A schematic of the nozzle proposed by Lv et al. (2017b).	15
2.10	Streamlines and cross-sections from Mo et al.'s nozzle.	16
2.11	Mach contours of Lv et al.'s nozzle.	17
2.12	The superposition-based nozzle design by Jegede and Crowther.	17
2.13	The nozzle used in Tanimizu et al.'s optimisation.	18
2.14	The contour of the axisymmetric scramjet nozzle optimised by Ogawa and Boyce (2012).	19
2.15	A streamline traced nozzle designed by Zhu et al. (2017).	20
3.1	A shape transition nozzle inside a parent flowfield.	31
3.2	A supersonic thrust nozzle designed with Rao's method.	31
3.3	A comparison of Rao's nozzle with one designed with IMOC.	35
3.4	A comparison of a Rao nozzle to two uniform flow nozzles.	36
3.5	A schematic of an axisymmetric nozzle with a constant radius centre body.	38
3.6	A streamline traced nozzle with a drag surface.	38

LIST OF FIGURES

3.7	A schematic of the dual expansion flow field.	39
3.8	An ellipse in an axisymmetric flowfield with a centre body in the r - ϕ -plane.	39
3.9	The combustor nozzle resulting from streamline tracing an ellipse through a dual expansion Rao nozzle without any drag surface.	40
3.10	Centre body radius/area ratio combinations for which the dual expansion flowfield could be created.	41
3.11	A shape transition nozzle with a small drag surface.	42
3.12	An illustration of merging a shape transition nozzle with a combustor extension. . . .	45
3.13	The pressure and Mach number distribution of the parent flowfield.	47
3.14	The elliptical combustor exit cross-section streamline traced through the parent flow-field.	47
3.15	A comparison of two shape transition nozzles with different exit shapes.	48
3.16	The unstructured computational mesh for the simulation of Nozzle 2.	50
3.17	The shape transition nozzle flowfield at the symmetry plane as calculated with eilmer4. .	51
3.18	A comparison of the Mach number distribution of the parent flowfield and the shape transition nozzle.	52
3.19	A comparison of the Mach number distribution of the parent flowfield and the shape transition nozzle.	53
3.20	The normalised thrust distribution for the shape transition nozzle and the parent flow-field.	54
4.1	The Mach 12 REST scramjet model inside the T4 test section. The direction of flow is from left to right.	58
4.2	A schematic of the T4 shock tunnel at the University of Queensland.	58
4.3	The wave processes in the compression and shock tube from the opening of the primary diaphragm assuming one dimensional flow.	60
4.4	The recoil signal for shot 12199.	61
4.5	The NENZFr response surface for the static pressure inside the T4 test section at the given test condition.	63
4.6	The repeatability of the Mach 8 test condition.	64
4.7	The T4 pitot rake inside the test section.	66
4.8	A comparison of two pitot survey shots at the Mach 8 condition with the nozzle exit flow.	67
4.9	A CAD representation of the Mach 12 REST model inside the T4 test section. . . .	68
4.10	Time histories of the nozzle supply pressure and four engine pressure transducer signals normalised by p_s from shot 12224.	70

4.11	The tracking object used to determine the model's motion with the image tracking technique introduced in Chapter 5.	72
4.12	Photographs of the 3D printed shape transition nozzle.	73
4.13	The middle part of the shape transition nozzle during the installation of the heat-set brass thread inserts.	73
4.14	Photographs of the Mach 12 REST model.	74
4.15	A partially exploded CAD representation of the Mach 12 REST model with focus on the catch and release mechanisms. The leading edge of the model is in the bottom left corner, the direction of flow is from bottom left to top right.	75
4.16	The rear support of the experimental model.	76
4.17	A cut through the symmetry plane of the Mach 12 REST engine.	77
4.18	A Schematic of the fuel system used in the experiments described in the present study.	79
4.19	A part of the Swagelok® 1/16" fuel supply line in the T4 test section.	80
4.20	Photographs of the Mach 12 REST on-board fuel system.	81
4.21	The sample cylinder, gas supply and instrumentation used to measure the fuel system volume.	82
4.22	A schematic of the optical setup used for tracking the motion of the Mach 12 REST engine.	83
4.23	Photographs of the source side components of the optical apparatus.	85
4.24	Photographs of the image side components of the optical apparatus.	86
5.1	The first image in the image series of shot 12235 with a close-up of the edge of the tracking object.	89
5.2	A schematic of edge motion without rotation.	92
5.3	The generalised edge tracking approach including rotation.	93
5.4	A schematic of the trigger mechanism used for the calibration.	94
5.5	Photographs of the experimental setup used for the calibration.	95
5.6	The trajectories of the Mach 12 REST model dropping in the T4 test section.	96
5.7	One of the artificial images created with the described method.	99
5.8	The error in the acceleration for each of the 100 image series with respect to the shift in starting position.	100
5.9	ΔI for diagonal edges	100
5.10	A performance curve of the Phantom® v611 showing the minimum attainable error for a given frame rate at the standard condition shown in Table 5.2.	101
5.11	The mean error in the acceleration in x for $0 \leq a_x \leq 20 \text{ ms}^{-2}$	102
5.12	A comparison of the edges detected by the sub-pixel edge detection routine with the undistorted contour of the tracking object.	102

LIST OF FIGURES

5.13 A comparison of the edges detected in a distorted artificial image with the edges detected during the calibration of the optical apparatus.	103
6.1 A schlieren image of the inlet.	106
6.2 The tracking object with a cut strand of fishing line.	107
6.3 The flowfield of the Mach 12 REST model without fuel.	109
6.4 Normalised pressure data from four fuel-off shots in comparison with that of the CFD solution.	112
6.5 Normalised pressure data from the low equivalence ratio shots ($\phi < 0.7$) in comparison with CFD.	113
6.6 Normalised pressure data from the high equivalence ratio shots ($\phi > 0.8$) in comparison with CFD.	114
6.7 The nozzle supply pressure trace, the combustor plenum pressure and the inlet plenum pressure from shot 12224.	115
6.8 The estimated streamwise force development for shot 12224. — designates the net thrust, - - - the gross thrust and - - - the drag.	117
6.9 The trajectory estimate together with the fitted quadratic polynomial for shot 12224.	118
6.10 Image tracking data from shot 12224 overlayed with the acceleration experienced by T4 during a shot.	120
6.11 The displacement in x and y and the pitch angle as measured with the image tracking technique for $t > 0$	121
6.12 An estimate of the measurement error introduced by a single harmonic vibration depending on its amplitude and frequency.	123
6.13 A quadratic trajectory superposed with a sinusoidal oscillation of $f = 400\text{Hz}$ and $A = 10\mu\text{m}$	124
6.14 Three different Fourier series fit to the displacement data in x of shot 12224.	125
6.15 The corrected signals in x , y and α from shot 12224.	127
6.16 The measured acceleration from all shots against the fuel equivalence ratio.	128
A.1 The repeatability of the 2 mm condition.	152
A.2 Normalised pressure data from the remaining fuel-off shots in comparison with that of the CFD solution.	154
A.3 Normalised pressure data from the remaining fuelled shots with $\phi < 1$ in comparison with that of the CFD solution.	155
A.4 Normalised pressure data from remaining fuelled shots with $\phi > 1$ in comparison with that of the CFD solution.	156
A.5 Normalised pressure data from all shots that unstalled during the third experimental campaign in comparison with that of the CFD solution.	157

C.1	The measured trajectories with their respective fit from shot 12 198.	167
C.2	The measured trajectories with their respective fit from shot 12 199.	168
C.3	The measured trajectories with their respective fit from shot 12 223.	168
C.4	The measured trajectories with their respective fit from shot 12 224.	169
C.5	The measured trajectories with their respective fit from shot 12 225.	169
C.6	The measured trajectories with their respective fit from shot 12 226.	170
C.7	The measured trajectories with their respective fit from shot 12 228.	170
C.8	The measured trajectories with their respective fit from shot 12 229.	171
C.9	The measured trajectories with their respective fit from shot 12 230.	171
C.10	The measured trajectories with their respective fit from shot 12 231.	172
C.11	The measured trajectories with their respective fit from shot 12 232.	172
C.12	The measured trajectories with their respective fit from shot 12 233.	173
C.13	The measured trajectories with their respective fit from shot 12 234.	173
C.14	The measured trajectories with their respective fit from shot 12 235.	174

LIST OF TABLES

3.1	The design constraints for the validation case of Rao's method in IMOC	34
3.2	Design conditions for the Rao nozzle used in the nozzle comparison.	35
3.3	A list of Rao nozzles with varying M_E compared to uniform flow nozzles respectively matching the area ratio and the inviscid thrust of the Rao nozzle.	37
3.4	The design conditions for which the limits of the proposed flowfield were explored. .	40
3.5	The free stream conditions for the shape transition nozzle design.	46
3.6	The design conditions for the parent flowfield.	46
3.7	A comparison of Nozzle's 1 and 2.	49
3.8	The inflow conditions and gas properties used in the inviscid simulation of the shape transition nozzle.	49
3.9	Relative differences in the Mach number and the pressure distribution of the parent flowfield and the shape transition nozzle.	54
3.10	A streamwise breakdown of the forces produced by the shape transition nozzle and the parent flowfield.	55
4.1	The facility configuration for the Mach 8 test condition used in the experiments described in the present study.	62
4.2	The average stagnation conditions and primary shock speed from all shots of the experimental campaign	64
4.3	The free stream conditions and test gas properties as calculated with NENZFr for the average shock speed and nozzle supply pressure and the nominal shock tube fill conditions.	65
4.4	The properties of the Mach 12 REST on-board fuel system.	80
4.5	List of the modes the LED driver can be run in.	84

LIST OF TABLES

5.1	The mean acceleration measured during the calibration experiments.	97
5.2	The default camera settings, engine forces and engine mass used for the artificial images.	97
6.1	The freestream conditions used for the fuel-off CFD simulation.	108
6.2	The total forces and pitching moment acting on the Mach 12 REST model according to fuel-off CFD.	110
6.3	The forces acting on the flowpath and the airframe.	111
6.4	The relative contribution of the side walls to the total drag force for multiple engine modules.	111
6.5	The estimated average acceleration and the acceleration from the curve fit for all shots from the experimental campaign.	118
6.6	The dominant components of the vibrations detected in the trajectories from shot 12224120	
6.7	The error caused by the vibration of the measurement hardware during shot 12224 calculated using Equations (6.20) and (6.19).	123
6.8	The quality of the curve fits for shot 12224.	127
6.9	The net and gross thrust and the thrust from fuel injection for all shots as well as the measured lift and the total produced lift.	130
A.1	The facility configuration for the 2 mm test condition used in the experiments described in the present study.	152
A.2	The average stagnation conditions and primary shock speed from all 2 mm shots.	152
A.3	The free stream conditions and test gas properties as calculated with NENZFr for the average shock speed and nozzle supply pressure and the nominal shock tube fill conditions.	153
B.1	The dominant components of the vibrations detected in the trajectories in x and y from all shots discussed in Chapter 6.	160
B.2	The dominant components of the vibrations detected in the pitch angle signals from all shots discussed in Chapter 6.	161
B.3	The estimated errors caused by the detected vibrations from all shots discussed in Chapter 6.	162
B.4	The Fourier series used to extrapolate the vibrations to the test time from all shots discussed in Chapter 6 and the resulting change in acceleration.	163
C.1	The quality of the curve fits for all shots.	165
D.1	The initial tunnel fill and nozzle supply conditions of all shots.	176
D.2	The freestream conditions, test gas properties and composition of all shots.	180

NOMENCLATURE

The nomenclature used in this thesis is outlined here. In some cases, the same variable has been used to indicate different quantities. In these instances, the section of the ‘special’ case has been included.

Acronyms and Initialisms

CFD	computational fluid dynamics
<i>NPR</i>	nozzle pressure ratio
RANS	reynolds averaged navier stokes
REST	rectangular-to-elliptical shape transition
T4	shock tunnel at the University of Queensland

Roman Symbols - Upper Case

<i>A</i>	amplitude, Section 6.2.2, m
<i>A</i>	area, m ²
<i>A_c</i>	engine capture area, m ²
<i>AR</i>	area ratio
<i>C</i>	polynomial coefficient
<i>C_D</i>	drag coefficient
<i>C_d</i>	discharge coefficient
<i>C_L</i>	lift coefficient

NOMENCLATURE

C_T	thrust coefficient
D	drag, N
\mathbf{G}_e	total intensity gradient matrix
G	total intensity gradient
H	nozzle height, Section 2.1.2, m
H	specific enthalpy, J kg^{-1}
H_{ij}	Gaussian filter kernel
\mathbf{I}	intensity matrix
\mathbf{I}_s	smoothed intensity matrix
I	electric current, Section 4.3, A
I	intensity
I_z	mass moment of inertia about the z -axis, m^4
L	lift, N
L	nozzle length, Section 2.1.2, m
M	Mach number
M	molar mass, Section 6.2.1, kg mol^{-1}
M_z	pitching moment, Nm
N_{cb}	combustor nozzle
N_{U1}	uniform flow nozzle 1
N_{U2}	uniform flow nozzle 2
N_v	vehicle nozzle
ΔQ	heat added by combustion, J
R	specific gas constant
R_A	radius of curvature at the throat of Rao's nozzle (Rao, 1958), m

Re_u	unit Reynolds number
S_a	error in acceleration
S_i	scale of the image with respect to the experimental model
$S_{x,n}$	Fourier series with n terms
T	period, Section 6.2.2, s
T	static temperature, K
T	thrust, N
T_F	sample period for a Fourier series fit, s
T_t	total temperature, K
U	voltage, V
V_{FS}	fuel system volume, m ³
V_{ss}	shock speed, km s ⁻¹
X_{O2}	mass fraction of available oxygen in the freestream
Y	species mass fraction

Roman Symbols - Lower Case

a	acceleration, m s ⁻²
a	major half axis of an ellipse, Section 3.2, m
a	speed of sound, m s ⁻¹ , Section 3.1
a_i, b_i	Fourier series coefficients
b	minor half axis of an ellipse, m
c'	factor in the determination of the rotation of an edge
d_D	diaphragm thickness, mm
d_s	distance of the true edge from the centre of a pixel, px
f	correction factor for diagonal edges, Section 5.1

NOMENCLATURE

f	frequency
fc	combustor fuel injector
fi	inlet fuel injector
g	gravitational acceleration, m s^{-2}
i	horizontal image coordinate
j	vertical image coordinate
l	length, m
\dot{m}	mass flow rate, kg s^{-1}
m	mass, kg
n	number
p	static pressure, Pa
p_t	total pressure, Pa
q	dynamic pressure, kPa
r_C^*	adjusted radius of the neutral streamline, m
r_d	distorted radial distance from the optical axis, m
r_u	undistorted radial distance from the optical axis, m
s	coordinate along a streamline, Chapter 3
s	coordinate normal to a detected edge within a pixel, Section 5.1
s	position uncertainty of the image tracking technique
t	time, s
$t_{f,s}$	start time of Fourier series data fits, s
\vec{u}	velocity vector, m s^{-1}
u	streamwise velocity, m s^{-1}
w	width, m

\vec{x}_s	streamline, m
x, φ, r	cylindrical coordinates
x, y, z	cartesian coordinates
x'_e, y'_e	edge point coordinates in the displaced image
x_e, y_e	edge point coordinates in the reference image

Greek Symbols

α	angle of attack, Chapter 2
α	blending parameter, introduction to Chapter 3
α	local Mach angle relative to the x -axis, Section 3.1
α	pitch angle
γ	ratio of specific heats
ε	error in mass flow rate comparison
ζ	adjustment factor for the neutral streamline
η_m	mass capture performance
Θ	edge angle matrix
θ	local flow angle relative to the x -axis
λ_2, λ_3	lagrangian multiplier constants
ρ	density, kg m^{-3}
σ	standard deviation
σ_G	standard deviation of a Gaussian blur filter
Φ	massflow rate per unit length, $\text{kg s}^{-1} \text{m}^{-1}$
ϕ	fuel equivalence ratio
φ	local edge angle in the reference image, Section 5.2
φ	phase angle

NOMENCLATURE

ξ distortion factor

Subscripts

0-9 engine stations

$A-E$ points in the parent flowfield

c cycle analysis

cov covered by the tracking object

CP combustor plenum

CT T4 compression tube

el center of an ellipse

exp exposed to the light beam

fit trajectory fitted to tracking data

fs flow establishment

g gross

i numerical index

IP inlet plenum

max maximum

N facility nozzle

n normalised

nom nominal

PF parent flowfield

px pixel

R T4 reservoir

s nozzle supply condition

s streamline, Section 3.2

<i>ST</i>	T4 shock tube
<i>ST</i>	shape transition nozzle, Chapter 3
<i>SW</i>	side wall of the Mach 12 REST model
<i>TO</i>	tracking object
<i>TS</i>	T4 shock timing station
<i>TS</i>	top surface of the Mach 12 REST model, Section 6.1.1

CHAPTER 1

INTRODUCTION

This introduction aims to establish the context for the research project presented in the document at hand. A brief general discussion of the scramjet engine and its role in hypersonic propulsion is followed by the motivation for this project, a definition of the project's objective and the methods used to achieve that objective.

1.1 Scramjets

Motivated by the prospect of an air breathing hypersonic engine, the supersonic combustion ramjet engine (scramjet) has been the subject of ongoing research since the late 1950s (Curran, 2001). By using ambient air as the main propulsive medium and the oxygen within for combustion, much higher specific impulses are attainable up to freestream Mach numbers of around $M_0 = 15$ when compared with a rocket engine, see for instance the work of Anderson et al. (2001). Air breathing engines using subsonic combustion, such as the turbojet and the ramjet, become ineffective at $M_0 \approx 3$ and $M_0 \approx 6$, respectively, due to high performance losses and structural and thermal loads associated with the deceleration of air to subsonic speeds. By mixing fuel and air and combusting while retaining supersonic speeds throughout the engine, acceleration past $M_0 = 6$ becomes viable. Within the range of $M_0 \approx 6$ to $M_0 \approx 15$ the scramjet engine is, at least in theory, the most efficient. To this date, however, experimental verification of positive net thrust at $M_0 \geq 10$ does not exist in the public literature. Above Mach 10 aerodynamic drag forces on the engine make it unlikely to achieve acceptable engine performance or positive net thrust at all. Based on these limits, Smart and Tetlow have designed a trajectory for a three-stage-to-orbit system, with a reusable scramjet powered vehicle as a second stage (Smart and Tetlow, 2009). Their research shows the viability of scramjet application in these types of systems, especially for small payloads, provided that further development in the field makes

scramjets more reliable and efficient in their assumed range of operation $M_0 = 6$ to $M_0 = 12$. While it is acknowledged that other applications for scramjets, such as single-stage-to-orbit configurations, are being or have been investigated, their feasibility has not been demonstrated, yet. A three-stage-to-orbit system is thus the most promising civil application for scramjet propulsion.

A scramjet engine is essentially a carefully designed duct. The internal flowpath is designed such that it achieves compression of the freestream, mixing of fuel and air, combustion and expansion of the exhaust gases without the need for rotating machinery. Figure 1.1 shows a schematic of a scramjet engine together with a Mollier diagram of the governing thermodynamic cycle, the Brayton cycle. The ideal Brayton cycle is characterised by adiabatic compression followed by isobaric heat

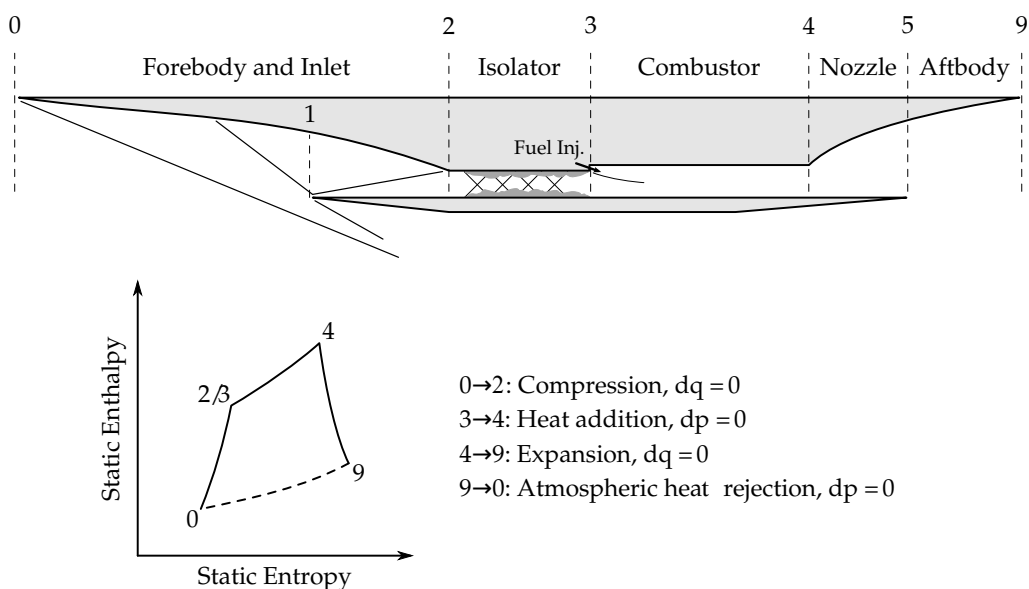


Figure 1.1: A schematic of a scramjet engine with a description of the Brayton cycle. Image by Doherty (2014).

addition, adiabatic expansion and isobaric heat rejection. Note that the scramjet engine cycle is open. The isobaric heat rejection, indicated by ---- in Figure 1.1, occurs in the atmosphere.

The station reference numbers follow the convention from Heiser and Pratt (1994). Station 0 denotes the undisturbed freestream. Between stations 0 and 2 the flow is compressed by the shock and compression waves generated by the forebody of the vehicle and the inlet. The compression process can be split into two regions: external and internal compression. Station 1 marks the cowl closure, where the air flow is fully enclosed by the engine walls, and thus the start of the internal compression region. Following the inlet, from station 2 to 3, is the isolator. The isolator does not serve a purpose in a thermodynamic sense. However, the pressure rise in a practical scramjet can adversely affect the inlet flow and lead to an unstart (Le et al., 2008). It is therefore a crucial part of a scramjet engine. Station 3 denotes the start of the combustor, where fuel and air are mixed and ignited by the pressure and heat resulting from the compression in the inlet. In Figure 1.1 a step fuel injector

is located at station 3. It should be noted that fuel injection does not always occur at only one location but can be staged throughout the inlet and combustor. Inlet injection has been found to be particularly beneficial, since it can feed a flow of pre-mixed fuel and air into the combustor and thereby reduce the required combustor length (Turner and Smart, 2010). The thrust nozzle, which expands the hot combustor exhaust gases to increase its momentum, forms the tail end of the engine (stations 4 to 9). Corresponding to station 1 in the inlet, station 5 marks the end of the internal expansion and the start of the external expansion. Stations 6 to 8 are omitted to make the notation consistent with that of the jet engine.

1.2 Motivation

Within scramjet research, the emphasis has been on inlets and combustors (Curran, 2001), while the nozzle was of relatively little or no interest at all. The complexity of creating a reliably working and efficient inlet/combustor pair, combined with the difficulties of experimentally testing a hypersonic engine, surmounts the effort it takes to design a working nozzle. However, in particular at the upper end of the range of scramjet operation, it becomes vital to capitalise on the full thrust potential of the exhaust gases leaving the combustor. The penalties of neglecting to optimise nozzle design include lower payloads, higher fuel consumption and a reduced range of operation. Individually, the forces that are relevant for thrust production on a scramjet powered vehicle, i.e. gross engine thrust, aerodynamic drag of the external vehicle surfaces and trim drag, are large compared to their sum, i.e. net thrust. Small gains in engine and vehicle performance can therefore result in large gains in net thrust. Hence, the motivation for nozzle design is to produce optimum thrust per nozzle weight at a given flight condition. As with the other engine components, accounting for varying flight conditions through adaptable nozzle geometries has the potential to increase engine performance, while at the same time increasing the complexity and the overall weight. In this project, only fixed geometry nozzles are designed and investigated. Stalker (1991) has shown, that for this type of engine it is most beneficial to design the nozzle for the higher end within the desired Mach number range, since drag penalties at off-design conditions increase significantly with Mach number. It should be emphasised, that the goal of optimum thrust is not achieved by designing the nozzle that produces the most overall thrust. It is achieved by maximising the thrust per weight ratio of the nozzle while at the same time providing a thrust vector that allows for stable flight of the vehicle, with minimal trim drag. Early work, like NASA's hypersonic research engine project (Andrews and Mackley, 1994), has demonstrated that in order to reduce drag and be able to achieve net thrust, airframe integration is vital for a scramjet engine. At the same time elliptical supersonic combustors have been proven to perform well at the University of Queensland (Suraweera and Smart, 2009). Rectangular combustors are beneficial for fuel injection from the walls given the short relative distance of two of the walls to the centre of the flow. However, corner vortices, high structural weights and high heat loads at the

corners are disadvantageous. Circular combustors mitigate the structural and heating problems and do not contain corner vortices. The large distance from the wall to the core of the combustor flow is, however, detrimental for the mixing of fuel and air when the fuel is injected from the combustor wall. Elliptical combustors combine the advantages of rectangular and elliptical combustors while exhibiting none of the listed disadvantages. The use of elliptical combustors and the requirement for vehicle integration demand for a shape transition of both the inlet and the nozzle, as common vehicle configurations either have a flat or a conical fuselage.

High ambient Mach numbers and efficient use of the available engine thrust require scramjet engines to be slender, as postulated by Stalker (1991). Furthermore, considering the increased redundancy of multiple engines, a modular engine design is considered superior to a single engine vehicle. Straight side walls are necessary to efficiently mount multiple engines side-by-side, thus further affirming the need for a shape transition of the inlet and the nozzle.

1.3 Objective and Methods

It is the objective of this study to create a design methodology for three dimensional elliptical to rectangular shape transition scramjet nozzles based on an axisymmetric parent flowfield and to analyse a nozzle designed with this methodology through optical thrust measurements on an unrestricted free-flying model engine in the T4 shock tunnel (Stalker et al., 2005) .

1.3.1 Methods: Design

Smart has created a design methodology for rectangular-to-elliptical shape transition (REST) inlets (Smart, 1999). Starting with an axisymmetric parent flowfield, which possesses the inlet's flow characteristics, the desired cross sectional geometries for the start and the exit of the inlet are streamline traced through the flowfield. They are then merged to obtain a smooth quasi streamline traced shape transition inlet. The same method is applied in the present study to design a shape transition thrust nozzle. The three following steps are performed in the design:

1. choice and design of an axisymmetric thrust optimised parent flowfield using Rao's method of thrust optimisation (Rao, 1958).
2. Streamline tracing of combustor and nozzle exit cross-sections through the parent flowfield.
3. Blending the two streamline traced nozzles into one quasi streamline traced shape transition nozzle with the method developed by Barger (1981).

1.3.2 Methods: Experimental Analysis

To analyse the performance of this methodology, a new thrust nozzle is designed for the airframe integrated Mach 12 REST engine tested by Doherty et al. (2015). Free-flying experiments are conducted in the T4 shock tunnel at the University of Queensland in order to measure the net thrust of the unrestricted engine. The analysis of the experiments employs Laurence and Karl's force-measurement technique, which is based on visual tracking of the engine movement and especially tailored to impulse facilities (Laurence and Karl, 2010).

CHAPTER 2

LITERATURE REVIEW

This chapter aims to create a summary of the literature relevant to the present study. First, hypersonic vehicle and scramjet nozzle performance analysis will be investigated to identify the requirements specific to nozzle design. Second, a summary of nozzle design techniques, that are currently available in the public literature, is given. The last part is focused on thrust measurement techniques in impulse facilities and hypersonic wind tunnel experiments with a free-flying model.

2.1 Scramjet Nozzle Design

In traditional aircraft, engine and airframe design were separated. The nozzle was exclusively part of the engine and therefore not considered in the design of the airframe (Mattingly et al., 2002). The engine designer was responsible for creating an interface to suit the airframe. However, early studies in hypersonic propulsion showed, that airframe integration of the engine is crucial for scramjets (Ferri, 1968). Airframe integration means that the underside of the vehicle serves as part of the engine and that pressure as well as viscous drag are reduced by minimizing the projected frontal and wetted surface area of the vehicle. The forebody of the vehicle thus compresses the freestream air before it enters the engine and the vehicle aft serves as an expansion surface, i.e. an extension to the thrust nozzle. It is therefore necessary to combine engine and vehicle design to account for the effects of the vehicle aerodynamics on the propulsion system and vice versa. Figure 2.1 shows a schematic of a number of scramjet engine modules that are integrated with the airframe of a hypersonic vehicle.

2.1.1 General Analyses of Nozzle and Vehicle Performance

In early work on scramjet engines particular emphasis was placed into analytically researching the effects of engine airframe integration. These studies formed the basis of understanding nozzle per-

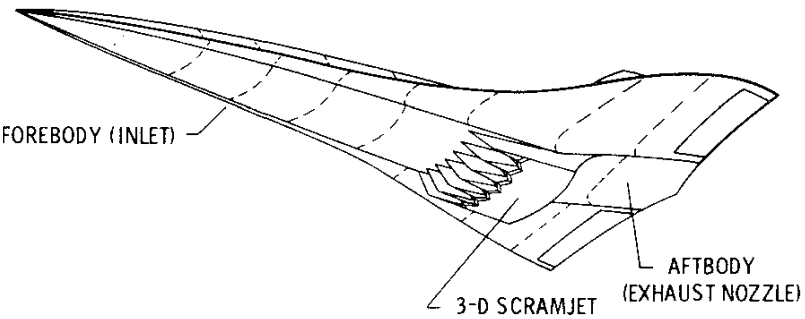


Figure 2.1: An airframe integrated scramjet. Graphic adapted from Weidner et al. (1977).

formance and provided insight into the requirements for scramjet nozzle design. More contemporary studies experimentally investigated nozzle performance with respect to specific phenomena, such as non-uniform inflow profiles or interactions of the nozzle exhaust plume with the external flow.

Ferri (1968) underlines the importance of an efficient nozzle and identifies three main areas of interest related to nozzle performance: the effects of flow non-uniformity caused by combustion, viscous effects and under expansion of the nozzle and the effect of non-equilibrium flow under various flight conditions and fuel-air ratios.

Kushida et al. (1964) have analysed the entire scramjet flowpath theoretically. They identify flow divergence at the nozzle exit, skin friction, incomplete combustion and a non-uniform inflow profile as the major sources for performance losses in the nozzle at 8.5 %, 1.5 %, 0.7 % and 1.6 % of thrust coefficient respectively. They determined that for an accurate quantification of the overall performance loss the different effects have to be analysed simultaneously because they are interdependant. However, a 1D analysis of the individual loss mechanisms can still provide a conservative estimate of performance losses. They concluded that minor gains in exit stream thrust can be significant for a scramjet, since the expected net thrust of the vehicle is very small compared to the gross thrust of the nozzle. Furthermore, they note that an asymmetric nozzle can contribute significant lift with negligible thrust losses and that non-uniform nozzle inflows can produce lateral forces, which can be as large as five times the net thrust.

Henry and Anderson (1973) have investigated an airframe integrated scramjet with the nozzle shown in Figure 2.2. They identify nozzle thrust over the whole range of operation, cooling requirements and the integration into the aerodynamic behaviour of the whole vehicle, i.e. effects on lift, trim and drag, as major considerations for nozzle design. They cite the advantages of engine airframe integration as the ability to use the vehicle aft as additional expansion surface, which allows for much higher effective engine exhaust velocities, and reduced external drag from a smaller frontal area and an asymmetric nozzle design. The authors emphasise that design and analysis methods need to be able to account for complex 3D flows, boundary layer separation at off-design conditions and large trim penalties induced by thrust vector misalignment.

Weidner et al. (1977) have analysed the performance of an airframe integrated scramjet powered

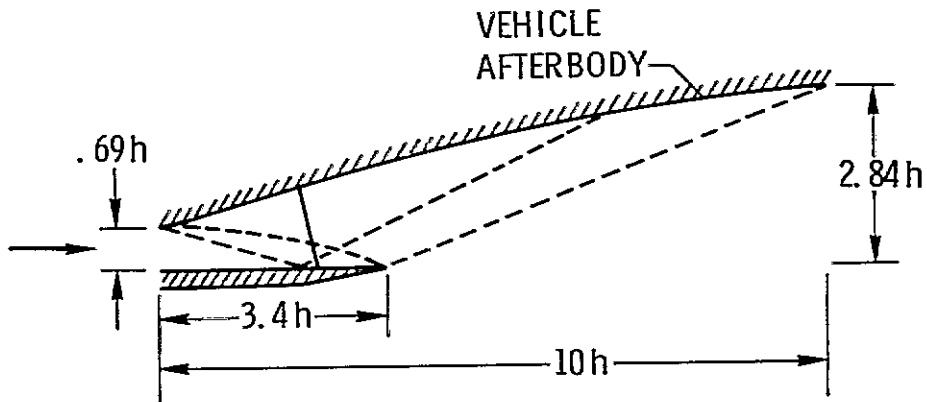


Figure 2.2: The nozzle designed for the airframe integrated hypersonic vehicle analysed by Henry and Anderson (1973), where h denotes the projected frontal height of the engine.

vehicle for cruise at $M_0 = 6$. The nozzle consisted of a planar upper expansion surface and an inclined planar cowl that served as a second expansion surface, see Figure 2.3. Their findings show that, for the nozzle considered, an expansion angle of 20° and a cowl expansion angle of 0° achieve optimum performance in terms of thrust to drag ratio and trim penalties. When the nozzle upper wall is changed to a parabolic contour the optimum angle increases to 24° , which results in a 3 % increase in thrust. The authors concluded that the reduced divergence in the exhaust flow is responsible for the increase in thrust. Furthermore, they found that close attention should be paid to the nozzle and vehicle geometries to maximize thrust and minimize drag.

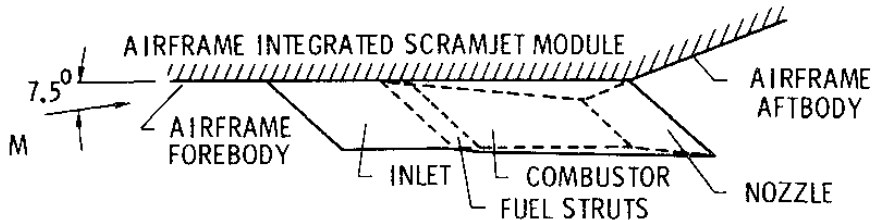


Figure 2.3: A schematic of the scramjet engine module analysed by Weidner et al. (1977).

Small et al. (1976) conducted a parametric study, investigating the effects of engine location, nozzle expansion angle and nozzle cowl geometry on thrust production, trim drag and vehicle stability. They found that, while there is an optimum for each individual property, an ideal nozzle, i.e. one that allows for longitudinal stability while efficiently producing positive net thrust, requires compromise in between the individual optima.

Johnston et al. (1971) and Perrier et al. (1996) emphasise the importance of factoring in trim penalties when evaluating nozzle performance. It is estimated that losses from trim can reduce the engine performance by as much as 10 %.

Haney and Bradley (1995) confirm that trim has to be factored in when designing the nozzle and emphasise the importance of engine airframe integration. Furthermore, they determined that the cowl

of a single expansion ramp nozzle (SERN) should only be long enough to reflect the last expansion wave that impinges on the upper expansion surface to save weight and avoid interactions with the external flow. Finally, it is remarked that over expansion of the nozzle flow should be avoided as it can result in losses of thrust and lift.

Hiraiwa et al. (1995) investigated the effects of ambient pressure on the flow inside a planar SERN. The expansion angle at the start of the nozzle was chosen as 15° . The cowl was parallel to the inflow and side fences were lining the expansion ramp for its entire length. In various cold flow experiments with different gas compositions and varying ambient pressure they determined that the nozzle thrust coefficient can be calculated accurately with the method of characteristics (MOC) for underexpanded conditions. In contrast, the shock induced three dimensionality of an overexpanded nozzle flow requires a more sophisticated analysis than the MOC to predict nozzle performance.

In a 1D analysis Schindel (1999) determined that the unrecoverable thrust loss due to a non-uniform nozzle inflow is unlikely to exceed 1 % of gross thrust unless there are large differences in velocity in the flow profile. He notes however that for a smaller engines than the one investigated the thrust loss could be more significant. Additionally, the non-uniformities were accounted for in the nozzle design and will result in larger losses in cases where they are not. The author further states that larger losses may be inevitable in a flight environment where nozzle inflow conditions vary.

Hirschen and Gültan (2009) conducted experiments with a three dimensional SERN at $M_0 = 7$ in the German Aerospace Center's H2K facility. They varied the Reynolds number, the nozzle pressure ratio (NPR), i.e. $p_{4,t}/p_0$, and the ratio of specific heats γ of the exhaust gas. They report lower wall pressures with increasing γ but also decreasing base drag due to weaker shocks from the interaction with the external flow. The total temperature of the exhaust gas was found to have a smaller influence on nozzle performance than γ . Increasing the NPR was found to increase thrust but also the base drag. A variation in Reynolds number of a factor of 2 had a negligible effect on thrust production.

Stalker et al. (2004) investigated the effects of chemical freezing of the exhaust gas and a continuation of combustion in the nozzle, a process they term kinetic afterburning, on nozzle performance. Numerical as well as experimental analyses were conducted on a 2D model with a small thrust nozzle with an area ratio of 3.8. Both methods confirm that the freezing of the exhaust gases has negligible effects on nozzle performance. Kinetic afterburning, however, can reduce gross thrust by up to 17 % according to the numerical results, which was expected due to the combustion occurring at lower temperatures. However, the experimental results show little variation in thrust from kinetic afterburning. The authors concluded that kinetic afterburning could provide a means to extend the range of a fixed geometry scramjet because unstarts at off-design Mach numbers can be avoided if the pressure rise from combustion occurs in the nozzle and not in the combustor.

2.1.2 Design of the Nozzle Geometry

The intense efforts in the 1950s to improve rocket propulsion led to several ways to design supersonic thrust nozzles. Uncontoured nozzles are widely used because of their simplicity both in design and analysis. For instance, Guderley and Hantsch (1955) and Rao (1958) invented design methods that create axisymmetric nozzle geometries for optimum thrust under the assumption of inviscid flow. Both methods work on the premise that nozzle length directly affects nozzle mass and that there exists an optimum where a nozzle for a given area ratio produces maximum thrust. Evvard and Maslen (1952) proposed the creation of three-dimensional nozzles by streamline tracing. This technique can be used in conjunction with two-dimensional flowfields in order to capture the properties of a two-dimensional nozzle in a different geometrical shape. In recent years and with progress in computational hardware and software numerical optimisation schemes became viable tools for nozzle design.

Uncontoured Nozzles

Watanabe (1993) designed a planar SERN for a combustor exit Mach number of $M_4 = 2.5$. The effects of the interaction of the nozzle flow with an external flow at $M_1 = 7.1$ were investigated experimentally. The test condition was designed to simulate flight at $M_0 = 10$ at an angle of attack of $\alpha = 3.4^\circ$. At this condition the nozzle was operating underexpanded. Figure 2.4 shows the experimental model used in Watanabe's study. Two different configurations were tested. One with side fences to isolate the flow on the nozzle ramp from the surrounding flow and one without fences. It was found that the configuration without side fences was affected by the external flow. Expansion waves from the trailing edge of the side walls of the internal part of the nozzle significantly reduced the pressure on the ramp. The barrel shock that forms because of the interaction with the freestream causes flow separations at either side of the nozzle ramp. Installing the side fences effectively turned the flow two-dimensional. It removed all effects from interactions with the external flow that were present without the fences and allowed for an accurate prediction of the wall pressure distribution using the method of characteristics. The pressure distribution along the centre line of the ramp was not affected by varying the freestream Mach number to $M_0 = 8.5$. For overexpanded nozzle flow it was found that two oblique shocks form at the side fences and detach the flow.

Two-Dimensional and Quasi Two-Dimensional Contoured MOC Nozzles

Rao's method is based on maximising the thrust over a control surface under the constraint of a given ambient pressure and constant length. He employs the langrangian multiplier method to obtain the equations that describe the control surface and the flow properties along it. As part of his optimisation Rao determined that the control surface coincides with a left running characteristic. It is thus possible to calculate the nozzle contour that produces the optimal flow properties across the control surface

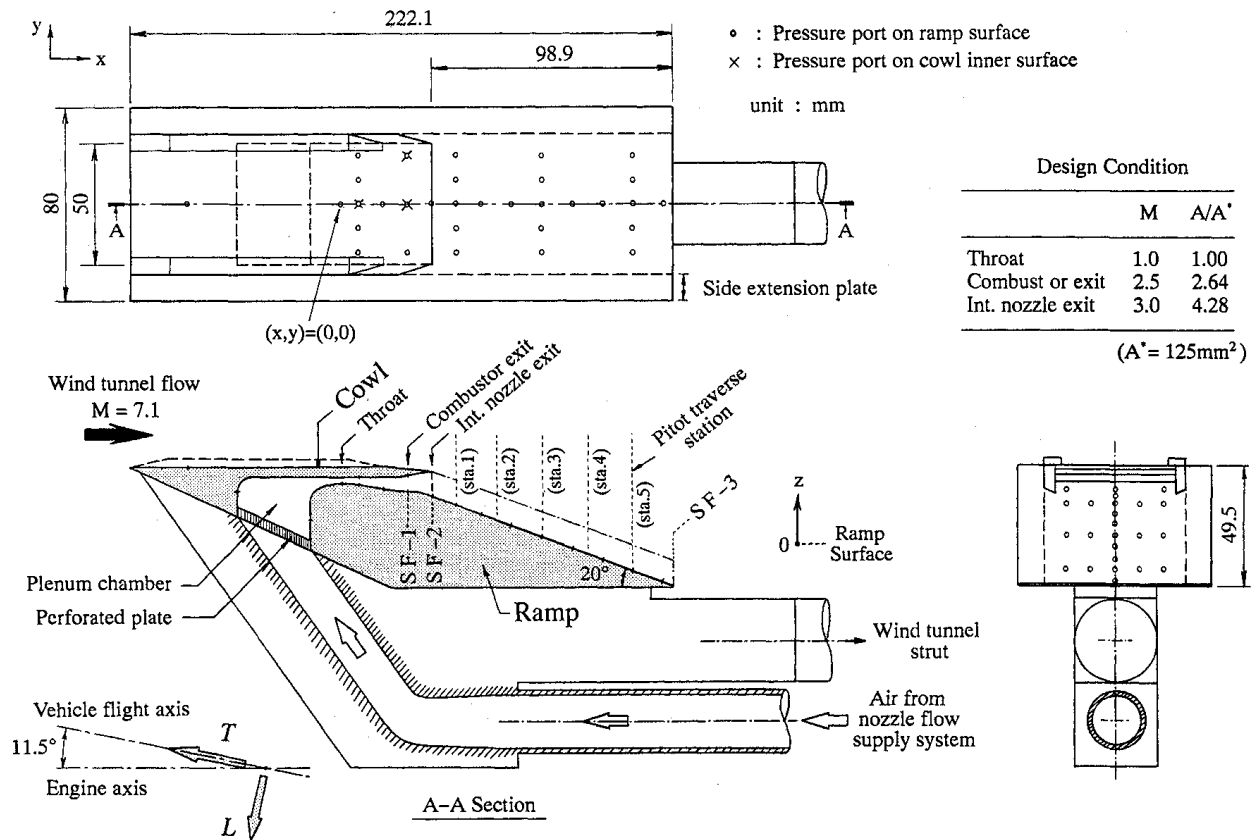


Figure 2.4: The experimental model of the nozzle investigated by Watanabe (1993).

with the MOC if one assumes inviscid and isentropic flow. Figure 2.5 displays the concept of Rao's design method for a convergent-divergent nozzle. The control surface is indicated by the dashed line from point C to point E. The optimised nozzle contour is shown as the line B'E. The throat portion of the contour AB is chosen to minimise flow separation at the throat and is not affected by the optimisation. The lines between the x-axis and the nozzle contour represent the characteristics mesh used in the design process.

Hoffman et al. (1972) built on Rao's method to include boundary layer effects in the optimisation. They make use of the calculus of variations and a numerical relaxation scheme to achieve their optimised nozzle contour. The authors note, however, that their design yielded insignificant gains in thrust when compared to Rao's approach and therefore conclude that the added complexity of their method is not warranted.

Nickerson et al. (1988) and Shyne and Keith (1990) modified Rao's method to create a scarfed nozzle, i.e. a 2D asymmetric nozzle with a contoured upper wall and a cowl that is parallel to the combustor axis. The design is shown in Figure 2.6. Nickerson et al. investigated families of nozzles for two different inflow Mach numbers $M_{4,1} = 2$ and $M_{4,2} = 6$ with two ratios of nozzle length to nozzle height $L/H = 3$ and $L/H = 4$ and varying total nozzle length L . They find that the optimal cowl length for this type of nozzle is such that the last expansion wave that is reflected on the cowl

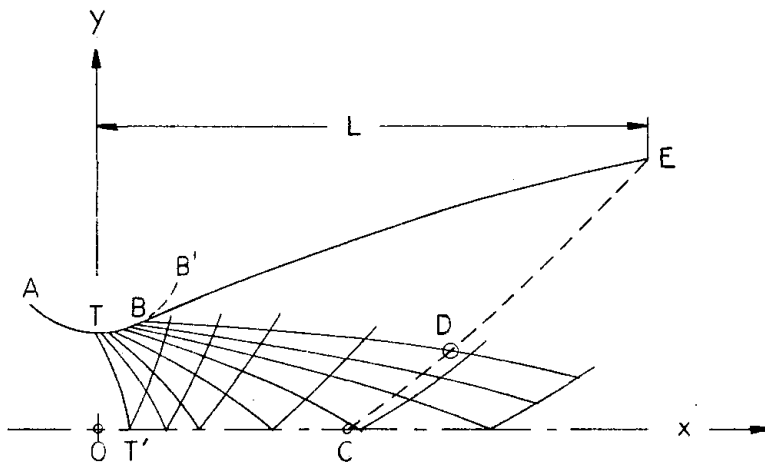


Figure 2.5: A schematic showing Rao's design approach. Adapted from Rao (1958).

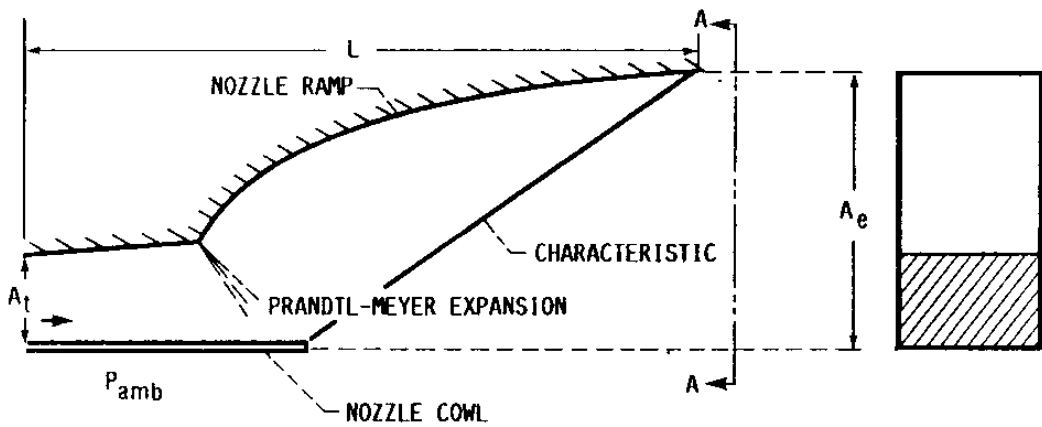


Figure 2.6: A schematic of a scuffed nozzle. Adapted from Shyne and Keith (1990).

just impacts on the trailing edge of the upper wall. A shorter cowl reduces the nozzle wall pressure because the expansion fan originating from the cowl's trailing edge interferes with the internal nozzle flow. A longer cowl doesn't affect the internal nozzle flow but generates a nose up pitching moment due to a change in orientation of the thrust vector. The nozzle wall contours designed for $M_{4,1}$ have much stronger curvature than those of the nozzles designed for $M_{4,2}$. They find that the centre of force moves downstream with increasing Mach number. Additionally, they note that the thrust vector angle varies greatly with inflow Mach number. In Shyne and Keith's study the effects of cowl length discovered by Nickerson et al. are confirmed. Furthermore, they add that a cowl that is truncated beyond the optimal point causes the external flow to affect the internal nozzle flow. They conclude that whether the cowl can be truncated beyond the optimal point should be determined by a trade-off between weight saved and thrust lost. Finally, Shyne and Keith remark that their design method can be modified to consider an internal oblique shock wave in the design. Simple chemical kinetics could also be incorporated.

Mo et al. (2015) employed the MOC to create a two-dimensional nozzle that consists of a con-

toured upper wall and a contoured cowl for non-uniform inflow profiles. The nozzle is first designed to produce a uniform exit flow and then truncated by 60 % of its original length to improve the thrust to length ratio at $NPR = 35$. Experimental comparison of the nozzle design with a nozzle that is designed for uniform inflow yielded an increase of the thrust coefficient of 1.8 % at the design point. Analysis with CFD resulted in a thrust coefficient increase of 1.5 % at the design point. The coefficients for lift and pitching moment were found to improve more significantly, by 6.5 % and 6.4 % respectively according to the experimental results and by 5.9 % and 5.4 % respectively according to the CFD. Generally, they find that the improvements over the nozzle designed for uniform inflow increases with decreasing NPR . Mo et al.'s design can be seen in Figure 2.7.

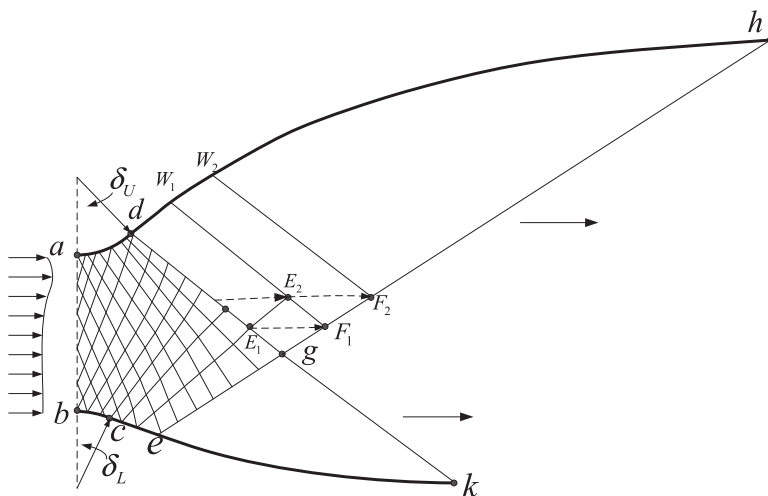


Figure 2.7: A 2D nozzle design for non-uniform inflows according to Mo et al. (2015).

Lv et al. (2017c) created a method to design a 2D nozzle with a contoured upper wall and cowl that is thrust optimised with an adaptation of Rao's method, see Figure 2.8. They report an increase in thrust by 5.5 % when compared with a nozzle designed with the method by Mo et al. (2015). Increases of 1100 % and 20 % were determined for lift and pitching moment respectively. Improved performance was also reported at off-design conditions.

In a different study Lv et al. (2017b) reformulated the 2D MOC equations to obtain a solution for quasi 2D flow with lateral expansions. The resulting nozzle is a modified version of the design proposed in Lv et al. (2017c). A schematic is shown in Figure 2.9. In comparison with a streamline traced shape transitioning nozzle similar to that presented in Mo et al. (2014) a thrust gain of 6.9 % and increases of 200 % and 640 % in lift and pitching moment respectively are reported. 22 % of the thrust force is attributable to the side walls and the lateral expansion.

3D Contoured MOC Nozzles

Cain (2010) describes scramjet nozzle design as a multi-step process. First, one defines the optimum propulsive mass flow and thrust vector angle through a control volume analysis. Secondly, Rao's

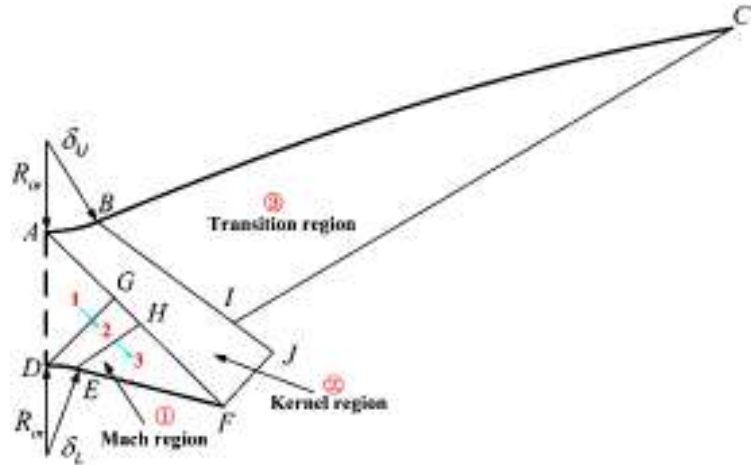


Figure 2.8: The thrust optimised nozzle design approach by Lv et al. (2017c).

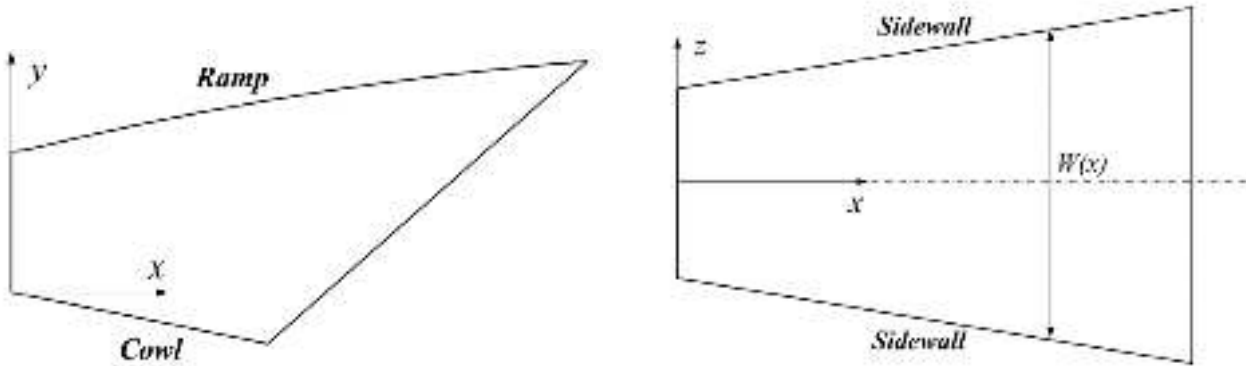


Figure 2.9: A schematic of the quasi 2D nozzle with lateral expansion proposed by Lv et al. (2017b).

method of thrust optimisation can be employed to create an optimum nozzle. For non-annular vehicles streamline tracing techniques are available to obtain a suitable nozzle. Cain notes, however, that using streamline tracing on a Rao flowfield does not necessarily constitute an optimum anymore since Rao uses the full 360° of the annulus to derive his equations. However, an analytical solution for arbitrary geometries has not yet been found. Cain emphasises that the last step, obtaining a nozzle contour, is not accomplished through Rao's technique, which merely results in a distribution of flow properties on a control surface. He proposes a way of extending the MOC to non-equilibrium flows to account for a reacting flow in the nozzle and use this to obtain a nozzle contour rather than assuming a chemically frozen exhaust gas mixture.

At the German Aerospace Centre (DLR) Riehmer and Gühan developed a method to predict the thrust of streamline traced nozzles without having to resolve the inlet and combustor flow to a high degree (Riehmer and Gühan, 2011). The parent flowfield was axisymmetric and calculated with the method of characteristics. Varying expansion angles and cut-off lengths on the parent flowfield and streamline tracing their combustor shape through it, led to a database of nozzle geometries from which to choose. Using the reference temperature method by Meador and Smart (2005), they calculated the

skin friction along the nozzle wall, to then attain a good estimate of the thrust. Considering the height constraint, imposed by their vehicle, they were able to choose the nozzle geometry that produced maximum thrust for their application. A comparison with 3D simulations showed good agreement with the predicted magnitude of thrust. However, the thrust vector angle varied by 10° between the prediction and the CFD analysis. This study confirms Ferri's statement that viscous effects can have a considerable influence on nozzle performance.

At Nanjing University Mo et al. (2014) created a quasi streamline traced scramjet nozzle with circular to rectangular shape transition. Based on Smart's approach for REST inlet design, they use a Rao optimised design flowfield with a conical centre body to then streamline trace their respective nozzle entry and exit shapes through. In a final step, the streamline traced geometries are merged to achieve shape transition. However, they create a fully enclosed nozzle, which extends past the control surface defined by Rao's method. In comparison with a nozzle designed by a method developed by Taylor and Wie (2008), they report significant increases in lift and thrust forces. Mo et al.'s nozzle can be seen in Figure 2.10.

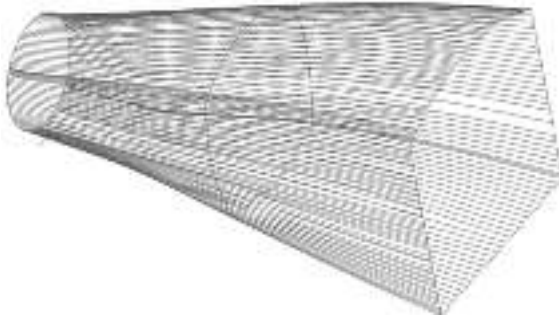


Figure 2.10: Streamlines and selected cross-sections of Mo et al.'s quasi streamline traced shape transitioning nozzle. The image is from Mo et al. (2014).

A variation of Mo et al.'s shape transitioning nozzle design is proposed by Lv et al. (2017a). They suggest a truncation of the nozzle at the control surface of Rao's optimised axisymmetric flowfield to save weight and increase lift and pitching moment. Furthermore, Lv removes the centre body from the design flowfield. The reference temperature method is used to correct the nozzle geometry for viscous effects. Figure 2.11 shows Mach contours on three planes perpendicular to the flow and on the control surface of the resulting nozzle. They report increases in lift and pitching moment of 430 % and 11 % respectively. The nozzle mass is reduced by 38 % while the thrust force only decreases by 0.76 %. In further analysis it was found that the thrust can be increased by increasing the aspect ratio of the combustor exit cross-section to an ellipse, which has its major axis aligned with the z -axis in Figure 2.9. Furthermore, they determined that an elliptical combustor can reduce overall engine weight by 5.7 % and friction losses by 10 %.

Jegede and Crowther (2016) propose to design a 3D nozzle by superposition of two 2D flowfields; each one designed with the two-dimensional method of characteristics. The desired nozzle flowfield is

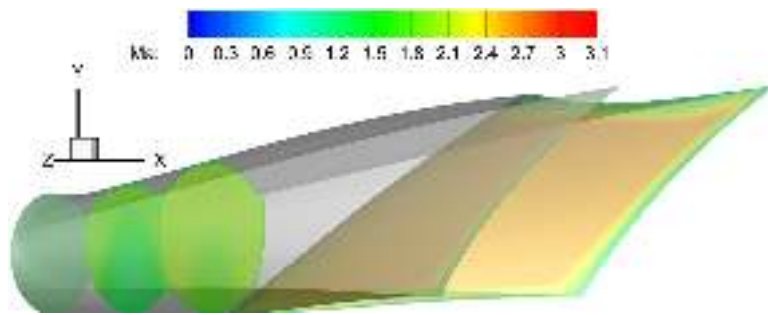


Figure 2.11: Mach contours inside the truncated shape transitioning nozzle designed by Lv et al. (2017a).

achieved iteratively with the aid of CFD. As a starting point two 2D velocity profiles in perpendicular planes are prescribed. The nozzles to produce each velocity profile are then created with the 2D MOC. CFD and experimental investigation are used to confirm the viability of the approach and assert robust off-design behaviour. The authors note, however, that their approach becomes less reliable with increasing nozzle area ratio. Figure 2.12 shows the targeted velocity profiles and shape of the nozzle.

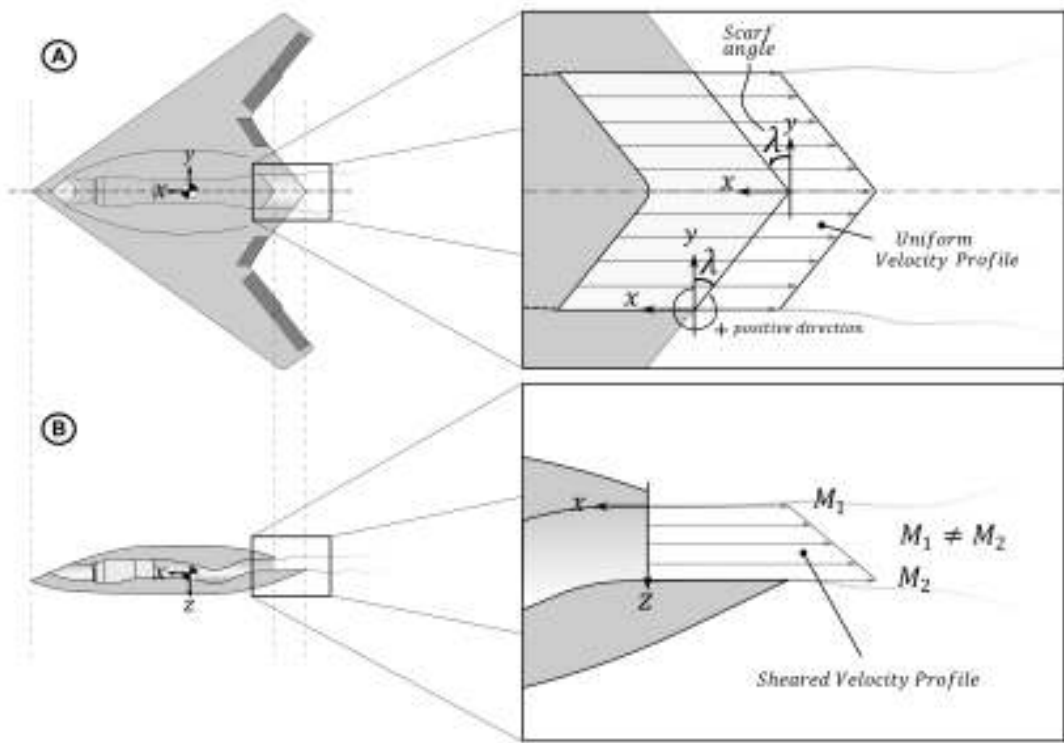


Figure 2.12: A 3D nozzle with target velocity profiles created by superposition of two 2D nozzles. The image was adapted from Jegede and Crowther (2016).

Nozzle Design by Numerical Optimization

Herring (1992) conducted a parametric study to optimise a two-dimensional nozzle with a parabolic wall contour for a hypersonic trajectory with freestream Mach numbers ranging from $M_0 = 7.5$ to $M_0 = 20$. Nozzles with varying nozzle attachment angle were designed for each of six points along the trajectory and analysed using a CFD program and cycle analysis. The optimum nozzles of each of the trajectory points were then analysed for off-design performance losses. It was found that an attachment angle of 21° results in minimal off-design performance losses and was thus chosen as the optimum. Having found the optimal ramp angle, the same procedure was used to determine the optimal cowl angle. Cowl angles larger than zero were found for each of the six trajectory points indicating that using the cowl for thrust production improves the performance of the entire nozzle. The optimisation determined that a cowl angle of 4° yielded the best performance and approaches that of a variable geometry cowl.

Another parametric nozzle design study was conducted by Tanimizu et al. (2011). The overall length and the external deflection angle of the cowl of the nozzle shown in Figure 2.13 were varied to minimise the drag force at a $M_0 = 8$ condition. The authors argue that given that the thrust coefficient can be calculated by

$$C_T = \frac{2\Delta Q}{u_0^2} \left(1 - \frac{0.5\Delta Q}{u_0^2} \right) - C_D, \quad (2.1)$$

where ΔQ is the heat added by combustion, u_0 denotes the flight velocity and C_D is the drag coefficient, it is reasonable to minimise the drag of the unfuelled engine in order to maximise engine performance. The experimental analysis yielded an optimal nozzle at 65 mm length and an external cowl deflection

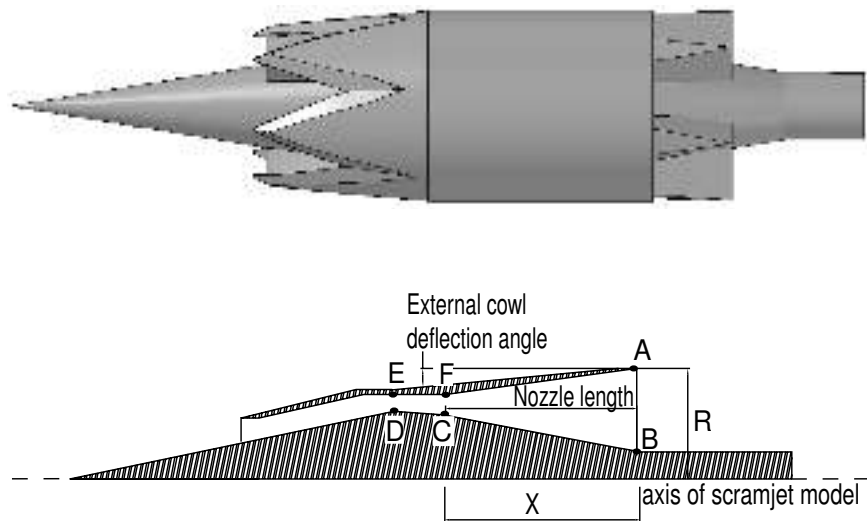


Figure 2.13: The axisymmetric scramjet model used in the parametric optimisation study. The image was adapted from Tanimizu et al. (2011).

angle of 1° . The multivariable optimisation based on inviscid CFD combined with simple viscous

theory found similar values to constitute the optimum. The improvements from the optimisation were found not to be significant, since any increase in thrust, through a larger cowl deflection angle or a longer nozzle, is offset by an associated increase in drag. It was noted by the authors that for higher Mach numbers a longer nozzle would produce optimum performance. In a second optimisation step the nozzle wall was contoured by use of Bezier points, which yielded an additional 3 % increase in thrust coefficient.

Ogawa and Boyce (2012) used surrogate assisted evolutionary algorithms to optimise the performance of an axisymmetric cruise nozzle for flight at $M_0 = 8$ at two different altitudes for fuelled and unfuelled operation. The nozzle contour was defined by an initial arc followed by a smoothly attached cubic Bezier curve defined by three parameters. It is displayed in Figure 2.14. The suit-

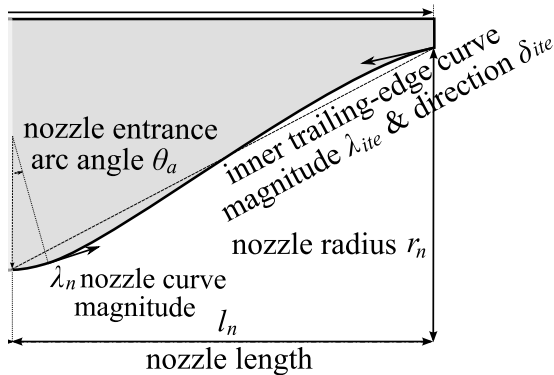


Figure 2.14: The contour of the axisymmetric scramjet nozzle optimised by Ogawa and Boyce (2012).

ability of the chosen contour is shown by optimising an axisymmetric nozzle for inviscid flow and comparing the result to that of Rao's method for the same condition. The optimum contours were bell shaped for fuelled and near conical for unfuelled operation. A comparison with an optimised conical nozzle showed a performance gain over the conical nozzle of 2 % for the fuelled case and 0.2 % for the unfuelled case. Similar performance was achieved for both altitudes.

Huang et al. (2013) used numerical simulations of a planar SERN to create a Kriging surrogate model to identify a nozzle optimised for thrust and lift. It was found that discrepancies between the performance predicted by the surrogate model and CFD were as low as 0.05 %.

Zhu et al. (2017) applied a non-linear compression to and then traced streamlines through an axisymmetric MOC flowfield. The non-linear compression is done such that upstream portions of the design flowfield wall are preserved since their contribution to the thrust force is the largest. The streamline traced nozzle is truncated at the characteristic behind which the flow is uniform. A boundary layer correction is then applied to account for viscous effects. The resulting geometry can be seen in Figure 2.15. A three variable surrogate based optimisation is finally used to optimise the nozzle for thrust and lift. The three variables are the pressure ratio of nozzle exhaust pressure to ambient pressure, i.e. p_{10}/p_0 , the level of flowfield compression and level of the conservation of the initial wall

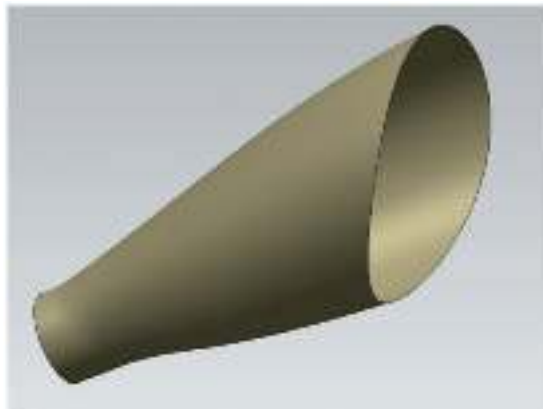


Figure 2.15: A streamline traced nozzle designed by Zhu et al. (2017).

contour following compression. The validity of the surrogate model is confirmed with CFD. It was found in the analysis that the pressure ratio has the largest impact on nozzle performance.

In Govinda et al. (2017) Reynolds averaged navier stokes (RANS) CFD solutions are used to create a meta model with the neural network radial basis function. The optimum 2D nozzle contour for flight at $M_0 = 6$ at 30 km altitude is then determined by the meta model. Following Ogawa and Boyce, the nozzle contour is defined with an initial arc that is smoothly joined with a cubic Bezier curve. The authors report an increase in thrust of 17 % over the baseline nozzle largely due to a higher exit velocity and nozzle wall pressure.

2.2 Thrust Measurements in Impulse Facilities and Free-Flying Experiments

Impulse facilities are characterised by very short test times on the order of milliseconds. At the same time they are the only facilities that can reproduce flight conditions at high Mach numbers. Due to the short test times, it is difficult to measure the forces on an experimental model; small forces or low accelerations in particular. Three basic techniques are commonly used:

1. force balances,
2. accelerometers and
3. optical force measurements.

Three types of force balances have been used in the impulse facilities: the strain gauge balance, the stress wave force balance and the accelerometer based balance. These systems are characterised by a supporting structure, the force balance, which is designed to have minimal interference with the quantity to be measured. Different designs allow for the measurement of up to six force components.

Accelerometers have been used on weakly restrained or free flying models to directly measure the acting aerodynamic accelerations. They don't require a mounting structure and can therefore be counted as a non-invasive technique. Careful design and analysis is required to be able to extract the aerodynamic forces from the obtained signals.

Optical force measurements are non-invasive techniques, where a free-flying or weakly constrained object is located in a series of photographs to determine its motion. Modern implementations employ digital high-speed photography and tracking routines to accurately determine the object's position. This way the model trajectory can be recorded, from which forces and moments can be derived. The two methods commonly used can be distinguished by the manner in which the motion of the model is tracked. The image tracking technique detects the complete or partial outline of the experimental model in each image and thus infers its trajectory whereas the so called free flight force measurement technique tracks the position of markers installed on the model.

The obvious advantage of non-invasive techniques is that they don't inhibit the flow and therefore allow for a study of wind tunnel models in what best resembles true flight conditions. In the following a brief review of each technique is given. Subsequently, an overview of free-flight experiments in various impulse facilities will be given.

2.2.1 Force Balances

The Strain Gauge Force Balance

The strain gauge force balance system was conceptualised by Jessen and Grönig (1989). The balance is designed as a cross of two beams with a square cross section. Two semiconductor strain gauges were fastened on each of the four sides of each of the four arms of the cross; giving it a total of 32 transducers. Due to the deformation of the beams, the strain gauges produce a signal proportional to each of the force components. Jessen and Grönig state that their balance is designed for a load of 1000 N. They claim, however, that with appropriate strain gauges loads of around 1 N should be observable.

Störkmann et al. (1998) have used the strain gauge force balance to measure the forces on a pointed cone, an Apollo CM capsule and a delta wing configuration in the TH2 shock tunnel (Olivier, 2016) at RWTH Aachen. They report good agreement of the force data with a reference data set for the pointed cone and note that forces can be measured without additional measures provided the test time is longer than the period of the lowest natural frequency of the force balance. For test times on the order of 1-2 ms, acceleration gauges on the balance sting were necessary to compensate for inertial forces of the force balance. The compensation allowed for accurate measurements of the forces on the capsule model. For the delta wing configuration, the lowest natural frequency prevented the use of acceleration gauges to compensate for inertial forces of the balance system. Hence, forces could only be obtained for longer duration tests of approximately 7 ms.

The Stress Wave Force Balance

The stress wave force balance was designed to overcome the limitations of force measurement techniques which require a state of stress equilibrium for an accurate measurement. It was introduced by Sanderson and Simmons (1991) at the University of Queensland for use at the T4 shock tunnel. Sanderson and Simmons measured the time history of the drag force on a pointed cone to within 10 % accuracy. The cone was mounted on a hollow sting made of brass, which was suspended in the T4 test section on strings in order to not inhibit its axial motion. Strain gauges were installed on the sting to measure the stress waves caused by the aerodynamic loads on the model. They note that a finite element model of the experimental model and sting are necessary to accurately determine its impulse response function. The impulse response can then be used to deconvolute the time history of the strain gauge signals and extract the drag force.

Initially, only single component balances for axisymmetric models were designed. However, the stress wave force balance was later extended to measure three components of force on full asymmetric scramjet models by Robinson et al. (2006). Lift, drag and pitching moment were successfully measured on a 0.567 m long model with a mass of 6 kg. The measured forces agreed well with analytical predictions but the measured pitching moment was substantially larger than estimated.

The most recent application of the three component stress wave force balance was performed by Doherty et al. (2015). Drag and lift force and pitching moment were successfully measured on a fully airframe integrated Mach 12 REST engine model at a Mach 10 condition in T4.

The Accelerometer Based Force Balance

The accelerometer based force balance, proposed by Vidal (1956), was first used in India in the HST2 facility (Sahoo et al., 2003). An experimental model is mounted on a sting and accelerometers are installed on the model. Rubber brushes are used to remove the effects of the sting on the motion of the model. Extensive FEM analysis is required to determine the appropriate dimensions and material of the brushes. As with the stress wave force balance, the dynamics of the behaviour of the model and balance need to be known in order to extract the force data from the measured signals. Sahoo et al. used the balance to measure three force components on a 60° blunted cone model. The authors report good agreement with force coefficients calculated via modified Newtonian theory.

The method has been used to successfully measure the forces on multiple small axisymmetric models (Sahoo et al., 2007; Saravanan et al., 2009). A variation of the accelerometer based force balance uses minimal friction ball bearings instead of rubber brushes to allow for motion in the axial direction (Joarder and Jagadeesh, 2004). However, only single component force measurements are achievable.

2.2.2 Accelerometer Measurements

Naumann et al. (1993) were the first to use accelerometers on an unrestrained free flying model in the shock tunnel B (STB) of the French-German Research Institute Saint-Louis (ISL Sauerwein et al., 2015). They operated a pyrotechnically operated spring-loaded catch-and-release mechanism to ensure unrestrained motion of the experimental model. The ballistic experimental model was fitted with a sting in the back which sat inside a chuck. Igniting the explosive charge inside the mounting structure released the chuck and the model was unrestrained during the test time. A spring closed the chuck again after the test flow had finished. The accelerometers used had a recording frequency of 25 kHz and were able to measure accelerations of up to $10\,000\text{ m s}^{-2}$. A low pass filter with a cut-off frequency of 2 kHz was sufficient to extract the aerodynamic forces from the signal. Accelerations of around 400 m s^{-2} were readily measured.

Takahashi et al. (1999) used accelerometers to measure drag on a 2.1 m long scramjet model in the high enthalpy shock tunnel (HIEST Itoh et al., 2002) at the National Aerospace Laboratory in Kakuda. The model was weakly restrained by shielded strings which allowed for motion in the axial direction. To be able to measure the expected acceleration of 10 m s^{-2} the model mass was limited to a maximum of 150 kg. The final mass of the experimental model was 139 kg. Time histories of axial acceleration were recorded during the test time of approximately 1 ms. The signals were then filtered using a moving average and a roughly estimated frequency response function of the experimental model.

The accelerometer technique was further refined by Tanno et al. (2004). Experiments on a weakly restrained sphere were performed in the vertical shock tunnel at the Shock Wave Research Center at Tohoku University. The 698 g sphere was held by a thin steel wire. Intensive analysis of the frequency response of the system allowed for the measured signal to be deconvoluted such that a resolution in time of $8\mu\text{s}$ of the unsteady signal was achieved. The measurements agreed very well with CFD.

2.2.3 Optical Force Measurements

The first mention of optical force measurements in the public literature can be found in Warren et al. (1961). Images were taken at 26000 frames per second and overlayed with a stationary grid in order to determine the model trajectory. The authors then calculated trajectories in two directions under the assumption of constant C_L and C_D respectively. The analytical trajectories that best matched the experimentally determined ones were chosen to estimate C_L and C_D respectively. Igra and Takayama (1991) used double exposure holography to track the motion of a number of small spheres. The spheres were initially positioned on the test section floor of the shock tunnel at the Shock Wave Reserach Center of the Institute of Fluid Science at Tohoku University. The acceleration imposed on them by the starting shock of the facility was enough the lift the spheres off the floor at which point their motion could be tracked. The authors derived the drag coefficient of a sphere in nonstationary

flow at Reynolds numbers ranging from 6000 to 101 000 from the results.

Image Tracking

Laurence and Hornung (2009) used a Sobel filter (Kanopoulos et al., 1988) to find the edge of the orion capsule in series of images taken at 12 000, 25 000 and 38 000 frames per second respectively. The authors estimated that the model position could be resolved to less than $15 \mu\text{m}$ and the pitching angle to 0.02° . Assuming constant forces during the test time, quadratic polynomials were fitted to the measured trajectories. The forces were found from the second derivatives of the fitted polynomials. Standard errors of 9 % and 15 % were reported for the drag and the lift force respectively. The authors conclude that the image tracking technique can be a valuable supplement to accelerometer based force measurements.

Laurence and Karl (2010) presented an improved image tracking algorithm to increase the accuracy of the edge detection in Laurence and Hornung's method. They use a Canny edge detection routine (Canny, 1986) for an initial estimate of the edges' locations. In a second step a subpixel detection routine is used to further refine the position. Following the implementation of Jain et al. (1995), the edge direction is determined as one of the eight main cardinal directions by comparing the edge pixel's intensity to that of adjacent pixels. A quadratic fitting routine is then employed to find the pixel intensity gradient's maximum normal to the defined edge direction. By using artificially constructed and experimental images the precision of the method was found to be on the order of $1 \mu\text{m}$ and 0.001° under ideal visualisation conditions. This precision should lead to an overall error in the acceleration of less than 1 % for the model considered in the analysis. In addition to the quality of the optical components and their alignment, they report facility vibrations as a likely source of error, which should be considered when using the technique.

Free Flight Force Measurement Technique

Several experiments analysing the behaviour of ballistic models using the free flight force measurement technique have been performed at ISL. Wey et al. (2012) used two cameras to track three corner points of a small model. It was initially supported by paper frames and piano wire which were removed by the starting flow of STB. A corner detection method based on local image contrast was used to locate the three corner points. Analysis of the derived trajectories yielded three components of force: drag, lift and pitch. Tests of 15 ms duration at Mach 3 and 4.5 were performed and yielded discrepancies between 1 % and 25 % in comparison with reference data.

At the same facility using a different ballistic model, Martinez et al. (2014) installed markers on a free flying model and tracked the motion of those during the test time. Two experimental setups were used, both employing a single camera. In the first, a single optical path provided one point of view on the model. The authors note that knowledge of the precise location of the markers was imperative

for accurate measurements. The second method used two sets of mirrors to create two separate light paths which were reflected onto a single camera sensor. The precision of the location of the markers was not as important as before. However, the spatial resolution was cut in half. The aerodynamic coefficients for six components of forces were determined successfully. Although a test time of 12 ms to 15 ms was required for accurate results.

A similar technique was used by Martinez et al. (2018) to determine the three rotational forces on a ballistic model mounted on a sting with two cameras. The sting was designed such that it allowed for rotation about all three axes albeit limited in the extent of the rotation. White dots were painted on the black model to act as the markers. Two of the dots were manually located in the first step of image analysis. A computer algorithm then superimposed a mesh of the ballistic model over the remaining points to determine model position and orientation. The authors state that both position and orientation of the model were located accurately. They conclude that the technique can be used on a free flying model to determine six components of force.

2.2.4 Free-Flying Experiments

Bernstein (1975, Chapter 4) provides a review of free-flight techniques until 1975. Detailed descriptions of design techniques, catch and release mechanisms and available measurement techniques are given.

General Electric Co.

Warren et al. (1961) measured drag and lift forces on a hypersonic vehicle shape over the range of $M_0 = 12$ to $M_0 = 15$, using the technique described in Section 2.2.3, in the General Electric MSVD shock tunnel (Warren, 1959). They used a light-weight model, weighing from 1 g to 5 g, made from cast Isofoam. The model was suspended by thin nylon strands, between 0.5 mm and 1.5 mm diameter, which were broken by the wind tunnel flow at the beginning of each experiment. The authors report that the models were generally destroyed in a single experiment and that satisfactory results could be obtained. A note refers to free-flying experiments at the Naval Ordnance Laboratory (NOL) (Seigel, 1959) being the first of their kind. However, details of the cited work could not be obtained.

California Institute of Technology (CALTEC)

Free-flying experiments at hypersonic speeds using image tracking based force measurements in combination with digital image processing were first made by Laurence et al. (2007). The authors were able to measure the drag coefficient on a sphere in the T5 facility (Hornung et al., 1991) to within 7 % accuracy at a $M_0 = 4.5$ and $H_0 = 9.4 \text{ MJ kg}^{-1}$ condition. The results were found to be consistent with the forces measured by accelerometers and to agree well with numerical simulations of the experiment.

German Aerospace Center (DLR)

In Germany, the researchers at DLR employed free-flight testing in the high enthalpy shock tunnel Göttingen (HEG Beck et al., 1991) to determine the forces on a scramjet model flying at 28 km altitude at $M_0 = 7.4$ as part of the LAPCAT II project (Hannemann et al., 2014; Steelant et al., 2015). Their model was suspended by Kevlar threads, which were torn downstream by the starting flow and subsequently cut by razorblades sitting inside the model. They achieved free-flight before the onset of steady test time in most of their experiments. To avoid damage to the model it is caught on a number of supports mounted on the test section rails after the flow has passed. Using the method by Laurence and Karl, they were able to track the motion of the model and, in conjunction with CFD results, successfully determined that the investigated model produced net thrust. In a consecutive study (Hannemann et al., 2017), the authors were able to refine the technique and confirmed the results from the first study. Effects of the varying density of the starting flow of the shock tunnel were found to affect the displacement curve of the model but had no effect on its curvature and hence the thrust measurement.

Japan Aerospace Exploration Agency (JAXA)

At JAXA, Tanno et al. (2014) preformed free-flight experiments with a blunted cone in Hiest. In their approach two electromagnets were used to suspend the model above the facility nozzle before the start of the experiment. Using a specially designed release controller, the deactivation of the magnets was timed such that the model was fully immersed into the core flow during the test time. The angle of the magnets could be adjusted to create different angles of attack. Tests were conducted with a high enthalpy $H = 14 \text{ MJ kg}^{-1}$ and a low enthalpy $H = 4 \text{ MJ kg}^{-1}$ condition. In addition to visual measurements, following the technique of Laurence and Karl, the cone carried 6 accelerometers and a data acquisition system to measure forces and moments on the cone. A comparison of the data from the low enthalpy condition experiment with that obtained in a blow-down wind tunnel yielded that the results are within the measurement uncertainties and are not adversely affected by the free-flight technique.

Tanno et al. (2015) used the same technique without the image tracking to determine the forces on an 880 mm long elliptic cone. The study served as a proof-of-concept for a model of that size. The authors note that in future projects their intention is to perform similar tests on a fuelled scramjet model.

University of Southern Queensland (USQ)

In the hypersonic facility of the University of Southern Queensland (TUSQ Buttsworth, 2010) a free-flying cylinder with a hemispherical nose was tested (Mudford et al., 2014). It was initially suspended

by a silk sling, which was cut by a solenoid-actuated blade at the onset of the test flow. The test conditions were: Mach number $M_0 = 5.8$, total pressure $p_t = 950\text{ kPa}$ and total temperature $T_t = 550\text{ K}$. The cylinder was equipped with a gyroscope and an accelerometer to measure forces and pitch and roll rate. For comparison, a simplified version of Laurence and Karl's image tracking algorithm was employed. The comparison of both methods yielded good agreement of the obtained measurements, confirming the validity of both and indicating that the application of both simultaneously provided the most reliable results.

2.3 Summary

A literature review has been performed listing the contemporary methods of designing scramjet models and measuring forces in impulse facilities. It is concluded that streamline tracing techniques based on flowfields created with the method of characteristics are promising. However, no practical approach of designing a three dimensional nozzle transitioning in shape from an elliptic combustor to an arbitrary vehicle shape exists in the presented literature. The review of the experimental force measurements in impulse facilities shows that the majority of experiments were performed on small scale light models. These models experience very high accelerations, which are easier to measure. The force balance techniques require a mounting structure which puts requirements on the model design and extensive analysis. Accelerometers have not yet been used to measured the forces on a fuelled scramjet. An extension of the technique to cover fuelled experiments is not within the scope of this project. It is one of the objectives to analyse the performance of a full airframe integrated scramjet model at a range of fuelling conditions. The image tracking technique is chosen for this purpose as it is simple, is suitable for measuring small accelerations and is non-invasive.

CHAPTER 3

NOZZLE DESIGN METHODOLOGY

The current section explains the shape transition nozzle design methodology proposed in the present study. As introduced in Section 1.3, and following the inlet design methodology by Smart (1999), the design process is split into three distinct steps:

1. design of an axisymmetric parent flowfield using Rao's method of thrust optimisation (Rao, 1958).
2. Streamline tracing of combustor and nozzle exit cross-sections through the parent flowfield.
3. Blending the two streamline traced nozzles into one quasi streamline traced shape-transitioning nozzle with the method developed by Barger (1981).

Step number one defines the nozzle's flow properties. It is here that the designer has the highest degree of control over the final result. Great care should therefore be taken to choose a suitable flowfield. The aim of steps two and three is to capture the properties of the parent flowfield to the highest extent possible while meeting the geometric constraints set by the vehicle and the combustor.

A suitable analogy for the process of streamline tracing is that of a cookie cutter. The combustor exit cross-section is first discretised by an appropriate number of points at the upstream end of the parent flowfield. A streamline $\vec{x}_{s,i}(s)$, i.e. the path a massless particle would follow if it were inserted into the flowfield at the given point, is then started from each point i . The complete set of n streamlines can be combined into a surface, where the gaps in between individual streamlines are closed by interpolation. Given the same inflow conditions, the thus created surface, hereinafter referred to as the combustor nozzle N_{cb} , reproduces a part of the parent flowfield. In other words it cuts a section out of the parent flowfield.

To meet the geometric constraints set by the shape of the vehicle, the streamline tracing process is repeated for the nozzle exit cross-section in the upstream direction using the same number of

streamlines. Hence, two separate streamline traced surfaces are created; N_{cb} and the vehicle nozzle N_v . The designer should ensure that they are as geometrically similar to one another as possible and that the distribution of streamlines over the surfaces is approximately the same.

Barger's blending algorithm

$$r_i(x) = (r_{i,cb}(x))^{1 - \left(\frac{x}{x_E}\right)^\alpha} \cdot (r_{i,v}(x))^{\left(\frac{x}{x_E}\right)^\alpha}, \quad (3.1)$$

where $r_{i,cb}$ denotes the radius of streamline i of nozzle N_{cb} and $r_{i,v}$ the radius of streamline i of nozzle N_v , x_E is the streamwise location of the downstream end of the parent flowfield and α is the blending parameter, is then used to blend pairs of corresponding streamlines. The blending parameter can be understood as a weight, which defines the rate of change from one streamline to the other. If α is small the streamline $r_{i,v}$ is dominant and most of the transition occurs near the combustor exit. Therefore, when α is large the transition happens gradually at first and most of the change occurs towards x_E . The blended streamlines can then be combined into a third surface, which constitutes the shape transition nozzle. α should be chosen to achieve a smooth transition between the two streamline traced nozzles and to minimise the effects of the shape transition on the properties of the nozzle flowfield. Reasonable transitions from N_{cb} to N_v can be achieved for $1 \leq \alpha \leq 4$. Figure 3.1 shows an elliptical to rectangular shape transition nozzle (blue) inside the parent flowfield. The outer wall and centre body of the parent flowfield are displayed in dark grey. The red surface constitutes the control surface as defined by Rao's method.

In the following, the design of a three dimensional shape transition nozzle for the scramjet model designed by Doherty et al. (2015) is discussed in detail. The first part covers Rao's method of thrust optimisation. In Section 3.2 the inherent advantages and disadvantages of using axisymmetric flowfields with a centre body as parent flowfields are discussed and a parent flowfield with a contoured centre body is introduced. The third section discusses the streamline tracing and the blending process as well as the integration of the nozzle with the combustor. In the last section the design choices and constraints of the shape transition nozzle alongside inviscid CFD results of the internal flow are examined.

3.1 Rao's Method of Thrust Optimisation

Rao's method of optimising the thrust for supersonic nozzles was established in 1958. It defines a control surface over which the analytical thrust of an axisymmetric inviscid nozzle is maximised using the lagrangian multiplier method. In his optimisation, Rao found that the control surface coincides with the last left characteristic of the nozzle. The method of characteristics, therefore, lends itself to calculate the position of the control surface and the nozzle wall contour.

Figure 3.2 shows a nozzle contour optimised by Rao's method for a combustor exit Mach number

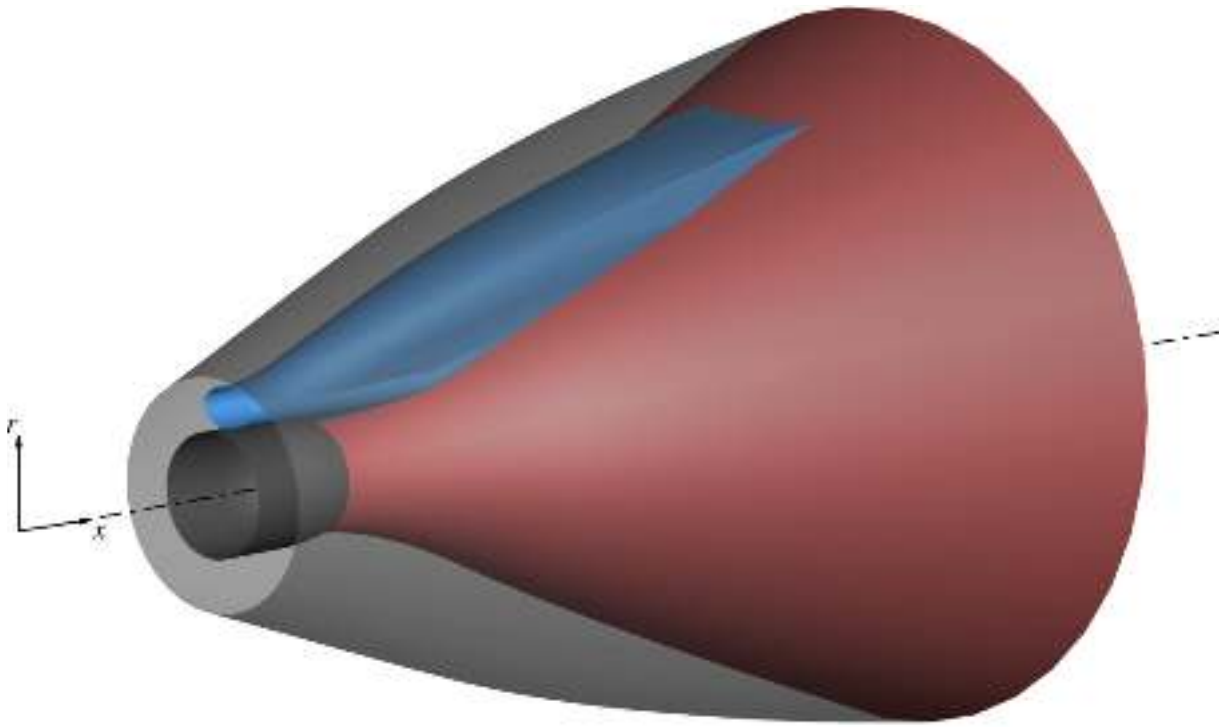


Figure 3.1: A shape transition nozzle (blue) inside a parent flowfield with a contoured centre body. The outer wall of the parent flowfield is shown in grey and the contoured centre body in black. The control surface as defined by Rao's method (red) terminates the flowfield on the downstream end. - - - indicates the axis of symmetry.

of $M_A = 2.52$, an ambient pressure of $p_0 = 638 \text{ Pa}$ and an exit Mach number of $M_E = 4.8$ along with the control surface and the first and last wave of the expansion fan originating from point A. The

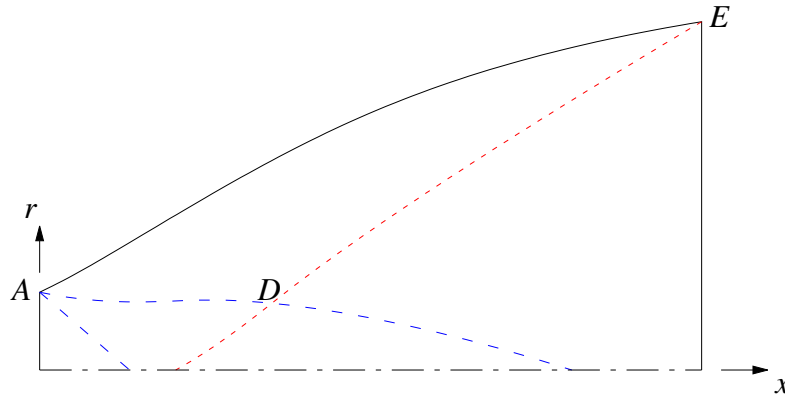


Figure 3.2: A supersonic thrust nozzle designed with Rao's method. The nozzle wall is designated by —; - - - indicates the first and last characteristic of the initial expansion fan, - - - the control surface and - - - the axis of symmetry.

control surface is defined by setting the Mach number at the downstream edge of the nozzle contour, i.e. point E, and the ambient pressure. These two parameters correspond to a nozzle of a distinct length. It can therefore be stated that, using Rao's method, one designs the nozzle that produces

the most thrust for a given set of flow conditions and a given length. Using the obtained lagrangian multiplier constants

$$\lambda_2 = - \left(\frac{1}{\gamma - 1 + \frac{2}{M^2}} \right)^{\frac{1}{2}} \cdot \frac{\cos(\theta - \alpha)}{\cos(\alpha)} = const., \quad (3.2)$$

$$\lambda_3 = rM^2 \left(1 + \frac{\gamma - 1}{2} M^2 \right)^{-\frac{\gamma}{\gamma - 1}} \sin^2(\theta) \tan(\alpha) = const. \quad (3.3)$$

and the condition at point E

$$\sin(2\theta_E) = \frac{2}{\gamma M_E^2} \left(1 - \frac{p_0}{p_E} \right) \cot(\alpha_E), \quad (3.4)$$

where θ and α are the local flow angle with respect to the x -axis and the local Mach angle respectively, value pairs of the Mach number and the flow angle can be calculated along the control surface, i.e. line DE . The position of each value pair can be expressed as the ratio of its radial position and the nozzle radius at point E . To completely define the control surface one has to find its starting point, i.e. point D , within the nozzle flowfield. Point D is defined as the intersection of the last characteristic of the initial expansion fan with the control surface. In essence, the angle of the nozzle wall at point A , i.e. θ_A , and therefore the initial expansion fan is defined by finding the point that satisfies the lagrangian multiplier constants and conserves the mass flow rate across the two line segments AD and DE , i.e. $\dot{m}_{AD} = \dot{m}_{DE}$. The resulting nozzle is significantly shorter than one of the same inflow conditions and initial deflection angle that expands the nozzle flow to uniform conditions; as can be seen from the distance in between the intersections of the control surface and the last characteristic with the axis of symmetry.

3.1.1 Implementation

IMOC is an interactive method of characteristics computational tool, developed by Jacobs and Gourlay (1991) at the University of Queensland. A number of routines, controlling the unit processes of the method of characteristics (Anderson, 2003, Section 11.5), can be called from a script in the TCL programming language, therefore allowing for very elaborate flowfield calculations to the full extent of the capabilities of TCL.

In IMOC the initial expansion fan is calculated starting from a user-defined characteristic, where the flow is assumed to be constant and parallel to the x -axis. The following characteristics are defined by incrementally changing the value of the Prandtl-Meyer function at point A and using the Interior Node routine to compute the properties and locations of the points on the new characteristics. Value triplets for the ratio of the radial coordinate r to the radius at point E r_E , the corresponding values for the Mach number and the flow angle are calculated in advance and stored as a look-up table. For each

characteristic in the centred expansion, the Mach number on the x -axis is compared to the minimum Mach number in the look-up table. Once that Mach number is exceeded, the routine starts looking for points that match the conditions for point D . From that point onwards, the value of λ_2 is calculated for each node on a new characteristic, moving upstream from the x -axis. The search stops if a node with the correct value of λ_2 is found. If $\lambda_{2,1} < \lambda_2 < \lambda_{2,2}$ or $\lambda_{2,1} > \lambda_2 > \lambda_{2,2}$ for two adjacent nodes 1 and 2, a new node is interpolated iteratively in between node 1 and 2 until it matches the desired λ_2 within a user defined tolerance. When a node satisfies the conditions for point D , the mass flow rates across AD and DE are calculated and compared. The mass flow rate across AD is computed using all nodes connecting points A and D , i.e.

$$\dot{m}_{AD} = 2\pi \sum_{i=1}^{n_{AD}-1} 0.5 (x_{i+1} - x_i) \cdot (\Phi_{AD,i} + \Phi_{AD,i+1}), \quad (3.5)$$

where

$$\Phi_{AD,i} = a_i \rho_i M_i \cdot \frac{\sin(\alpha_i)}{\cos(\theta_i - \alpha_i)} \cdot r_i. \quad (3.6)$$

Here, Φ designates the mass flow rate per length across a line segment, a denotes the local speed of sound and ρ the local density. For the mass flow rate across DE , the characteristic is split evenly into a number of segments. For each point thus created, the values of Mach number and flow angle are interpolated from the look-up table. The x -coordinate is approximated in a three step calculation, given by

$$\Delta x_{i+1,1} = (r_{i+1} - r_i) \cdot \tan(\theta_i + \alpha_i), \quad (3.7)$$

$$\Delta x_{i+1,2} = (r_{i+1} - r_i) \cdot \tan(\theta_{i+1} + \alpha_{i+1}) \text{ and} \quad (3.8)$$

$$x_{i+1} = x_i + 0.5 (\Delta x_{i+1,1} + \Delta x_{i+1,2}). \quad (3.9)$$

Nodes are then created at each of these points and connected to adjacent nodes in the characteristics mesh. Alongside the creation of the nodes along DE , the mass flow across the control surface is computed by

$$\dot{m}_{DE} = 2\pi \sum_{i=1}^{n_{DE}-1} 0.5 (r_{i+1} - r_i) \cdot (\Phi_{DE,i} + \Phi_{DE,i+1}), \quad (3.10)$$

where

$$\Phi_{DE,i} = a_i \rho_i M_i \cdot \frac{\sin(\alpha_i)}{\sin(\theta_i + \alpha_i)} \cdot r_i. \quad (3.11)$$

If the two mass flow rates are not equal the computation moves on to the next characteristic and repeats the above procedure.

To find the correct point, the error in the mass flow rate comparison is calculated by

$$\varepsilon_m = \frac{\dot{m}_{AD} - \dot{m}_{DE}}{0.5(\dot{m}_{AD} - \dot{m}_{DE})}. \quad (3.12)$$

As soon as ε_m changes its sign from one characteristic to the next, i.e. point D lies in between the two characteristics, a new increment of the Prandtl-Meyer function is calculated according to Newton's method and the computation is reset to the point where the Mach number on the x-axis exceeds the minimal Mach number in the look-up table for the first time. Once all conditions for point D are satisfied, the remainder of the flowfield is calculated using the nodes along the control surface DE as reference points. A streamline is started at point A and extended to each new C- characteristic until the streamline crosses DE . To ensure that the two lines are crossing, DE is extended linearly beyond point E .

3.1.2 Validation

In order to validate the implementation of Rao's method in IMOC, nozzle A described in Rao (1958) was designed. The nozzle is of the convergent-divergent type. As such, the nozzle contour starts with a pre-defined radius R_A and the initial characteristic of constant Mach number is a curved line. It should be noted that an exact description of that line is missing in Rao's publication. It is therefore approximated by a straight line. The design constraints are listed in Table 3.1.

Table 3.1: The design constraints for the validation case of Rao's method in IMOC.

M_A	M_E	γ	p_0, Pa	R_A/r_A
1.103	3.5	1.23	0	0.45

Figure 3.3a shows a comparison of the nozzle contour calculated with IMOC to the point data cited by Rao (Rao, 1958, p. 381). It should be noted that one of the contour points, at $x/r_A = 5.43$, from Rao's publication has been omitted, since it appears that it is not part of the nozzle contour (compare Rao, 1958, Figure 5 and Table 1). Figure 3.3b shows the Mach number along the nozzle contour and the associated wall angle. It is evident that the implementation in IMOC accurately reproduces Rao's original nozzle design. It appears that the assumption of a straight initial characteristic does not affect the result significantly.

3.1.3 Comparison to Minimum Length Nozzles With Uniform Exit Flow

To demonstrate the effect of Rao's method, two minimum length nozzles, that produce uniform nozzle exit conditions, have been computed and are compared to a Rao nozzle with the same inflow conditions in the following. The first uniform flow nozzle, designated N_{U1} , has the same area ratio as

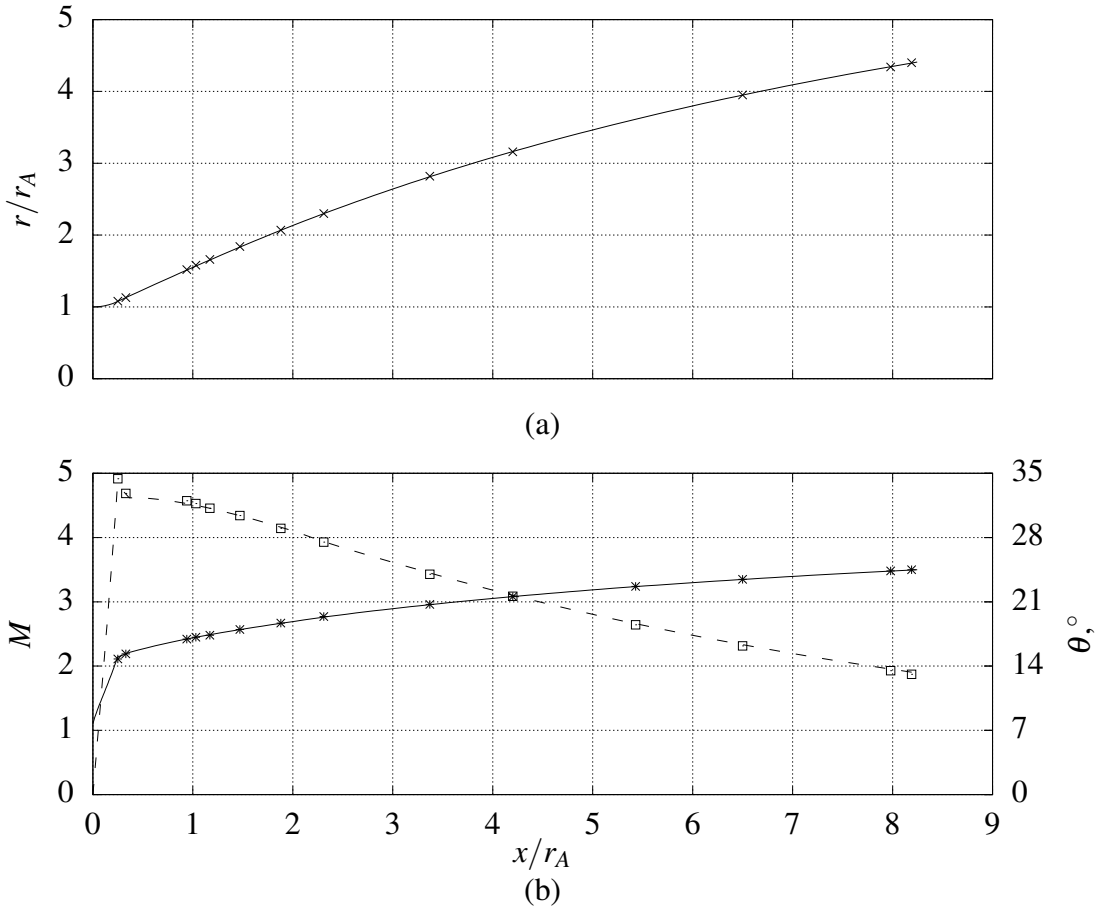


Figure 3.3: A comparison of the nozzle designed by Rao (Rao, 1958, p. 381) with a nozzle designed with IMOC under the same conditions. Plot (a) shows the nozzle contour designed with IMOC (—) and the contour points cited by Rao (×). Plot (b) shows the Mach number at the nozzle wall and the wall angle over the length of the nozzle as calculated by IMOC (— and - - - respectively) and the corresponding points given by Rao (* and □ respectively).

the Rao nozzle. The second uniform flow nozzle, designated nozzle N_{U2} , produces the same amount of inviscid thrust as the Rao nozzle. The conditions for the calculation of the Rao nozzle contour are given in Table 3.2. These result in a nozzle with a normalised length of $l/r_A = 17.2$, an area ratio of

Table 3.2: Design conditions for the Rao nozzle used in the nozzle comparison.

M_A	M_E	γ	$p_0, \text{ Pa}$	R_A/r_A
2.52	4.8	1.28	638	0

$AR = 20.5$ and normalised thrust of $T_n = 0.091$. The inviscid thrust is calculated by first computing the stagnation pressure of the flow using

$$p_{t,A} = p_A \left(1 + \frac{\gamma-1}{2} M_A^2 \right)^{\frac{\gamma}{\gamma-1}}. \quad (3.13)$$

Thus the wall pressure at each node along the wall contour can be calculated from the Mach number at each node. This leads to the following equation:

$$T = \sum_{i=2}^{n_{AE}} 0.5 \left(\frac{p_{t,A}}{\left(1 + \frac{\gamma-1}{2} M_{i-1}^2\right)^{\frac{\gamma}{\gamma-1}}} + \frac{p_{t,A}}{\left(1 + \frac{\gamma-1}{2} M_i^2\right)^{\frac{\gamma}{\gamma-1}}} \right) \cdot (r_{i-1}^2 - r_i^2) \pi, \quad (3.14)$$

where n_{AE} indicates the number of nodes along the nozzle wall. The normalised thrust is then calculated as

$$T_n = \frac{T}{p_{t,A} \cdot A_A}. \quad (3.15)$$

Figure 3.4 shows a comparison of the Rao nozzle with the two uniform flow nozzles. As evident,

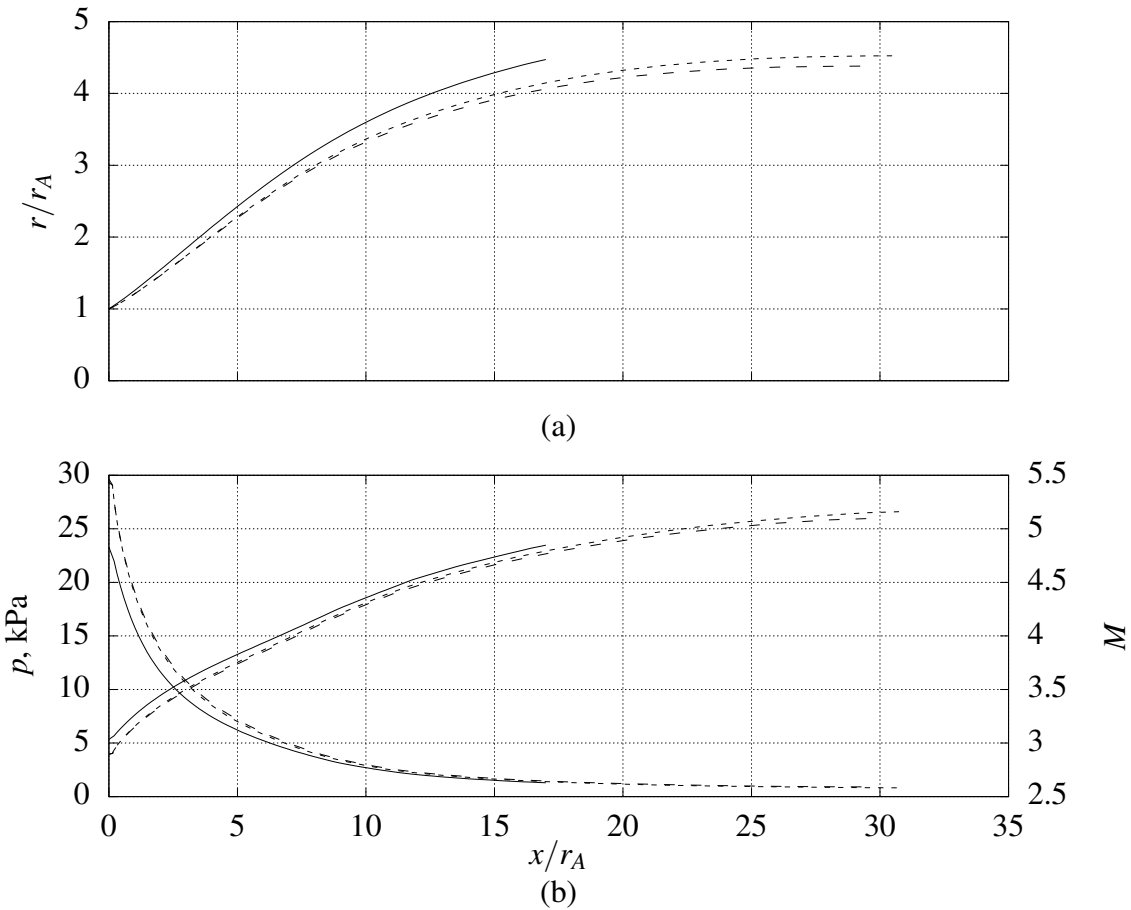


Figure 3.4: Plot (a) shows a comparison of the wall contours of a Rao nozzle (—), designed for $M_E = 4.8$ and $p_0 = 638$ Pa, with two uniform flow nozzles, N_{U1} (---) and N_{U2} (- - -). Plot (b) displays the static pressure at the nozzle wall and the Mach number over the nozzle length for the Rao nozzle (—), N_{U1} (---) and N_{U2} (- - -). N_{U1} has the same area ratio as the Rao nozzle and N_{U2} produces the same inviscid thrust force as the Rao nozzle.

the Rao nozzle is a lot shorter than both N_{U1} and N_{U2} . One should note, however, that the thrust force

produced by N_{U1} is about 1 % higher than that of the Rao nozzle. This effect can be attributed to the deflection angle at point A. As a consequence the wall pressure for N_{U1} is significantly higher than it is for the Rao nozzle, as can be seen in Figure 3.4b. The area ratio of N_{U2} is about 6 % less than the Rao nozzle's area ratio. Increasing the Mach number M_E for the Rao nozzle reduces the relative difference in length of the nozzles, while a lower M_E results in a larger relative Δl . Table 3.3 lists a comparison of a number of Rao nozzles with different M_E with their uniform flow counterparts. The

Table 3.3: A list of Rao nozzles with varying M_E compared to uniform flow nozzles respectively matching the area ratio and the inviscid thrust of the Rao nozzle.

M_E	N_{U1}		N_{U2}	
	$\Delta l, \%$	$\Delta T_n, \%$	$\Delta l, \%$	$\Delta AR, \%$
3.5	163	28	102	-33
4.0	124	7	92	-22
4.5	108	3	91	-14
4.8	81	1	74	-6

other design conditions are the same as the ones listed in Table 3.2.

3.2 Dual Expansion Rao Nozzle

In previous work (Kunze, 2014), it was determined that adding a centre body to an axisymmetric flowfield greatly affects the shape of N_{cb} and N_v . It was thus concluded that the radius of the centre body can be used as a design parameter in tailoring the shape of the nozzle to the geometric constraints of the vehicle. However, this type of parent flowfield inherently produces large drag surfaces in streamline traced nozzles as is explained in the following.

In an axisymmetric flowfield all streamlines are straight lines when viewed in the $r\text{-}\phi$ -Plane, i.e. $\partial\phi/\partial x = \partial\phi/\partial r = 0$. Figure 3.5 shows such a flowfield. An expansion fan is created at point A and reflected at the centre body. In crossing the first expansion wave, the flow is turned away from the centre body; and for any streamline $r_s(x_E) \geq r_s(x_A)$, as can be seen for the one depicted. When the ellipse in Figure 3.5 is discretised by a number of points and each of these points is streamline traced through the shown flowfield, a surface like the one in Figure 3.6 results. The hatched surface is forward facing, i.e. its normal vector points upstream, and therefore creates drag.

For the case investigated in Kunze (2014), the drag surfaces reduced the magnitude of the inviscid thrust of the shape transition nozzle by as much as 12 %. As stated in Chapter 1, an efficient engine is imperative for scramjet propulsion. Losses of this magnitude are therefore prohibitively large. In order to remove the drag surfaces from the shape transition nozzle, a neutral streamsurface, where the flow is parallel to the axis of symmetry, is introduced into the parent flowfield. The neutral

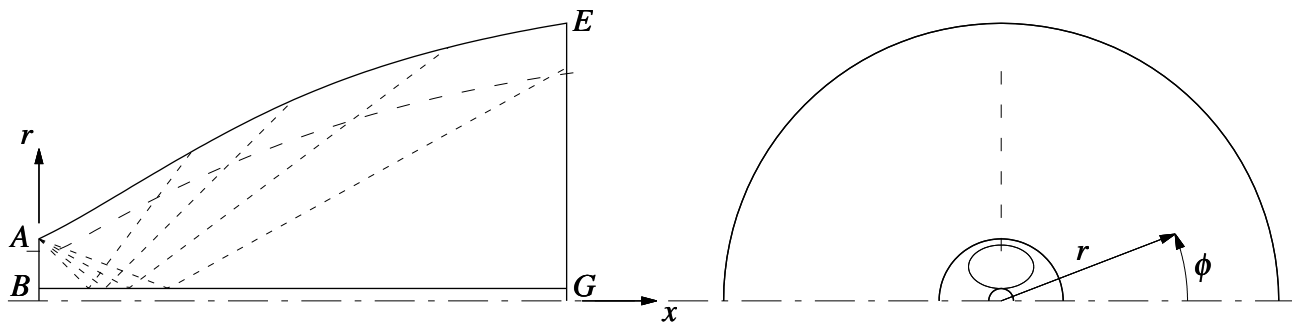


Figure 3.5: A schematic of an axisymmetric nozzle with a constant radius centre body. — designates the nozzle and centre body walls, - - - the axis of symmetry, - - - the expansion waves forming at point A, - - - a streamline through the nozzle and — the combustor exit cross-section.

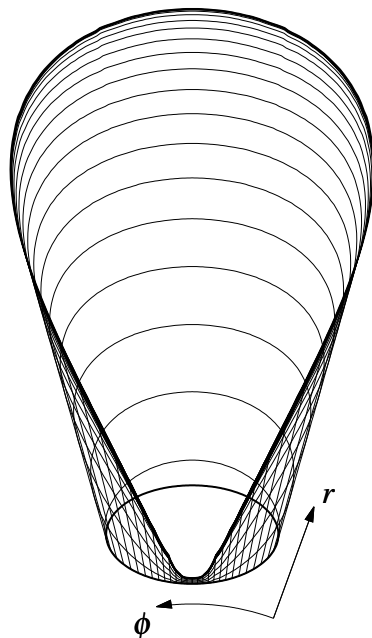


Figure 3.6: Cross-sections of a streamline traced ellipse through an axisymmetric flowfield with a constant radius centre body in the $r\phi$ -plane. The hatched area constitutes the drag surface. The design properties of the parent flowfield were $AR = 10$, $M_A = 2$ and $r_A/r_B = 0.65$.

streamsurface is attained by contouring the centre body, such that the expansion waves created by the centre body counteract the rotation of the flow, induced by the expansion fan from point A, at the neutral streamsurface. Figure 3.7 shows a schematic of the proposed flowfield.

The portion of the flowfield bounded by points A, C, F, D and E can be calculated using Rao's method with a centre body of constant radius that coincides with the neutral streamsurface. The flow properties along the neutral streamsurface can then be used to calculate the wall contour of the centre body that is required to achieve flow that is parallel to the axis of symmetry at r_C . Whether a forward facing surface is created depends on r_C . Thus, it needs to be chosen such that no forward facing surface is created in the streamline tracing process.

Examining the flowfield once more in the $r\phi$ -plane, see Figure 3.8, it becomes clear that, in

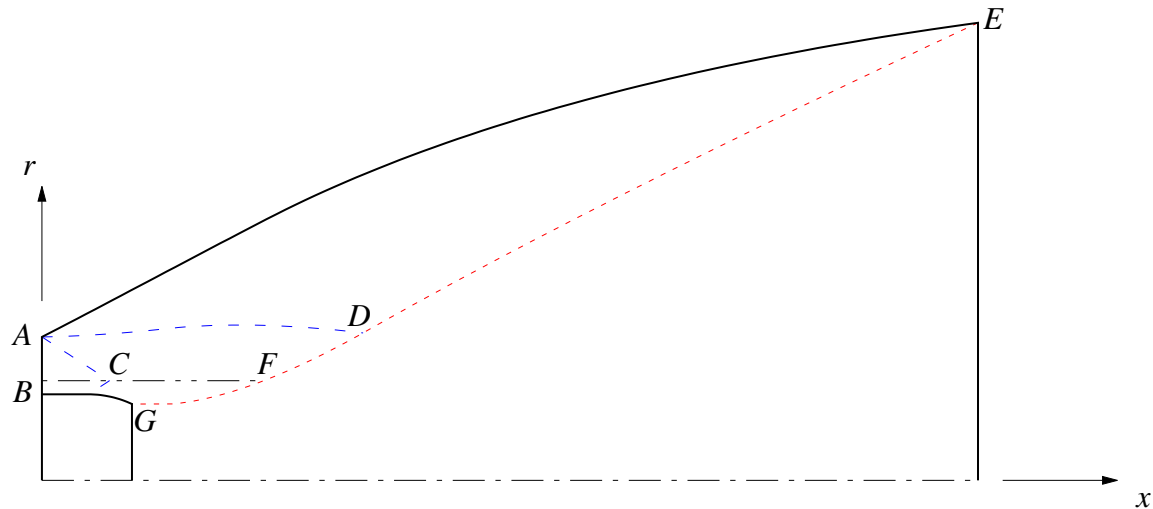


Figure 3.7: A schematic of the proposed dual expansion parent flowfield. — designates the parent flowfield walls, - - - the neutral streamsurface, - - - characteristics emanating from point A and the centre body, - - - the control surface as defined by Rao's method and - - - the axis of symmetry.

an axisymmetric flowfield with a cylindrical centre body, whether or not a streamline creates a drag surface is dependant on the radial value of its starting point, i.e. $r_s(x_A)$. The radial lines, indicated by

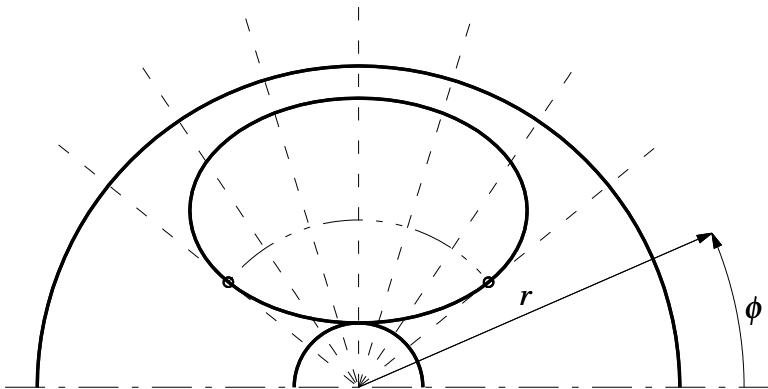


Figure 3.8: An ellipse in an axisymmetric flowfield with a centre body in the $r\phi$ -plane. The neutral streamsurface for the dual expansion nozzle without a drag surface is indicated by - - -. Radial lines designated by - - - indicate the paths which streamlines run along.

—, show sample paths that streamlines can follow. Consider, for instance, the path of a streamline that starts at a point on the ellipse where $r_s(x_A) > r_C$; r_C is indicated by - - -. Recalling that $r_s(x_E) \geq r_s(x_A)$ for every streamline in a parent flowfield with a cylindrical centre body, no forward facing surface is created. If, however, $r_s(x_A) < r_C$ the expansion waves force the streamline to cross through the ellipse, which thus contributes to the drag surface. In order for streamlines to follow the indicated paths, as is the case for any axisymmetric flowfield, and at the same time not to cross the ellipse, the centre body has to be contoured such that the neutral streamsurface is located where the streamline paths are tangent to the ellipse, indicated by \circ in Figure 3.8. The expansion waves where $r < r_C$ now turn the flow, and therefore the streamlines, towards the axis of symmetry, whereas the expansion

waves where $r > r_C$ still turn the flow away from the axis of symmetry. It follows that streamlines which start where $r_s(x_A) < r_C$ still follow the indicated paths but are now turning towards the centre body and away from the ellipse. Hence, choosing r_C as

$$r_C = \sqrt{\left(r_{el} - \frac{b^2}{r_{el}}\right)^2 + \left(1 - \left(\frac{b}{r_{el}}\right)^2\right)a^2}, \quad (3.16)$$

where a and b respectively designate the major and minor half axis and r_{el} is the radial coordinate of the centre of the ellipse, eliminates the drag surfaces from the resulting streamline traced nozzles. For the nozzles covered here $r_{el} = r_B + b$.

As Figure 3.9 demonstrates, an ellipse streamline traced through the proposed flowfield creates a combustor nozzle that does not contain any forward facing surface area and still allows for the flexibility of an adjustable centre body to tailor the nozzle to the vehicle. It has to be acknowledged,

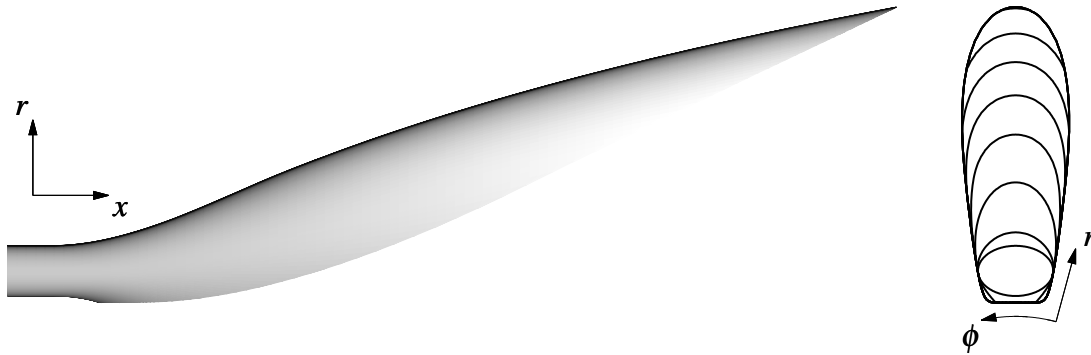


Figure 3.9: The combustor nozzle resulting from streamline tracing an ellipse through a dual expansion Rao nozzle without any drag surface. Centre body radius $\frac{r_B}{r_A} = 0.7$, area ratio of the Rao nozzle $\frac{A_E}{A_A} = 12$, combustor exit Mach number $M_A = 2.2$.

however, that this type of flowfield only exists for very large centre bodies, $r_B = 0.7r_A$ in the given example. Further investigation of the method is necessary to define the complete set of boundaries for its application. Figure 3.10 shows the minimal normalised centre body radius (+) for which the described flowfield could be successfully calculated at the given area ratio and the flow conditions given in Table 3.4. The hatched area designates the centre body radius/area ratio combinations, that allow

Table 3.4: The design conditions for which the limits of the proposed flowfield were explored.

M_A	γ	p_0, Pa
2.52	1.28	638

for the dual expansion flowfield to be created. To understand why this restriction exists, consider again that the contoured centre body's purpose is to create the neutral streamline at r_C . The expansion

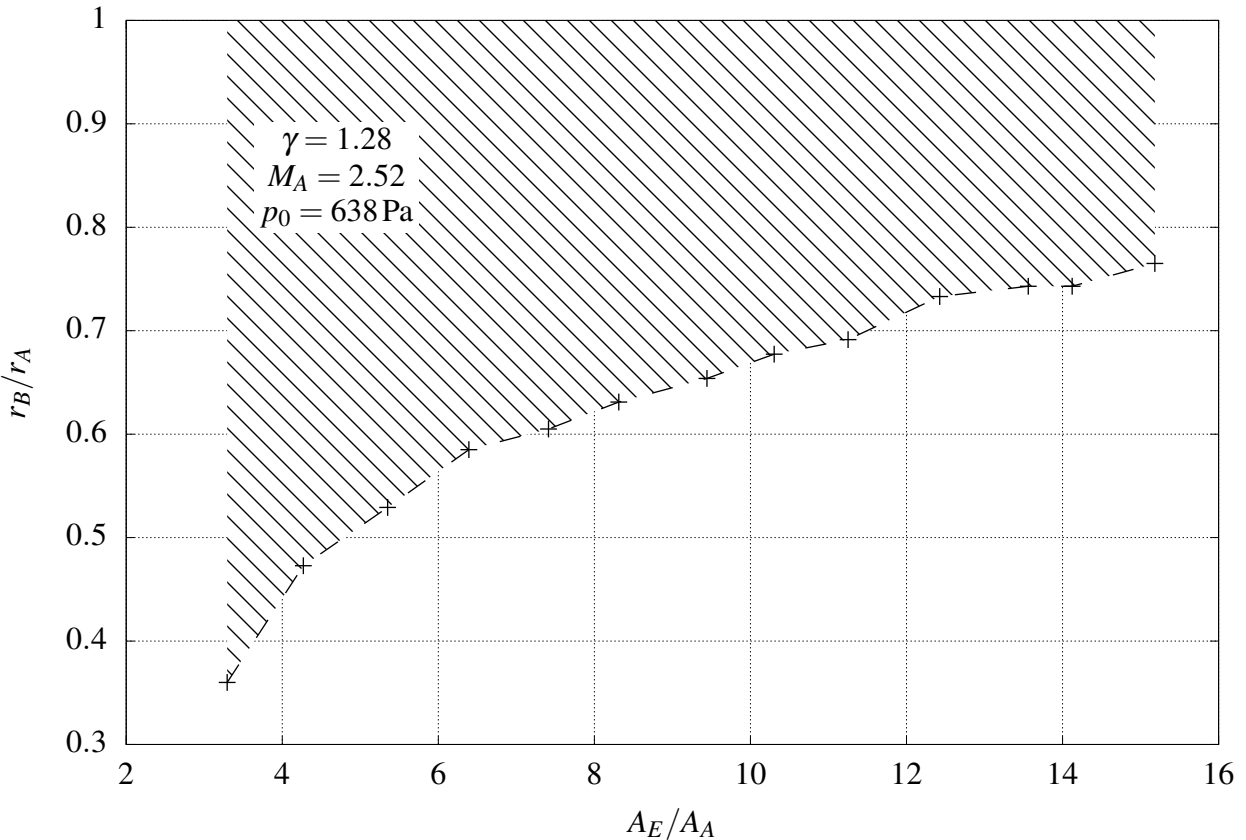


Figure 3.10: Centre body radius/area ratio combinations for which the dual expansion flowfield could be created.

waves which emanate from the centre body counteract the rotation of the flow imposed on it by the centred expansion fan originating at point A. In order to construct the required centre body, first, the flow conditions along the neutral streamline are calculated using the method of characteristics. Then, the characteristics below the neutral streamline are constructed starting on the neutral streamline and moving upstream and towards the centre body, keeping in mind that in an expanding flow the characteristics correspond to expansion waves. Moving upstream the characteristics converge, however, not to a single point. In fact, the characteristics the furthest downstream are much closer together than those further upstream. Reducing the centre body size past the boundaries shown in Figure 3.10 causes the characteristic lines the furthest downstream to cross. Physically this represents a shock wave, which means that the flow conditions on the neutral streamline can not be achieved with the given centre body. An increase in area ratio always entails an increase in the exit flow Mach number given the same inflow. A higher Mach number in turn reduces the Mach angle. However, the higher the Mach number the smaller the change in Mach angle for an incremental Mach number increase. The angle between two adjacent characteristics is the sum of the differences in local flow angle $d\theta$ and local Mach angle $d\alpha$ of the two characteristics. Now consider again the centred expansion fan at point A. With increasing Mach number the angle between adjacent characteristics reduces. It follows that on the neutral streamline the characteristics the furthest downstream are the closest together and

the higher the area ratio of the nozzle the closer they are. Since the characteristics running towards the centre body converge it follows that a larger area ratio nozzle causes the characteristics to cross at larger radii. Thus, larger centre body radii are required to create the proposed flowfield.

It is, however, possible to compromise by offsetting r_C to create a dual expansion flowfield with a smaller centre body radius and drag surfaces of acceptable size:

$$r_C^* = r_C - (r_C - r_B) \cdot \zeta. \quad (3.17)$$

Here, $0 \leq \zeta \leq 1$. $\zeta > 0$ commonly results in drag surfaces, which can be minimalised by carefully choosing ζ . $\zeta = 1$ places the neutral streamline at r_B and creates a flowfield with a non-contoured centre body. Figure 3.11 shows a complete shape transition nozzle, where a negligible part of the surface is forward facing and therefore creates drag. In the given example the drag surface is so

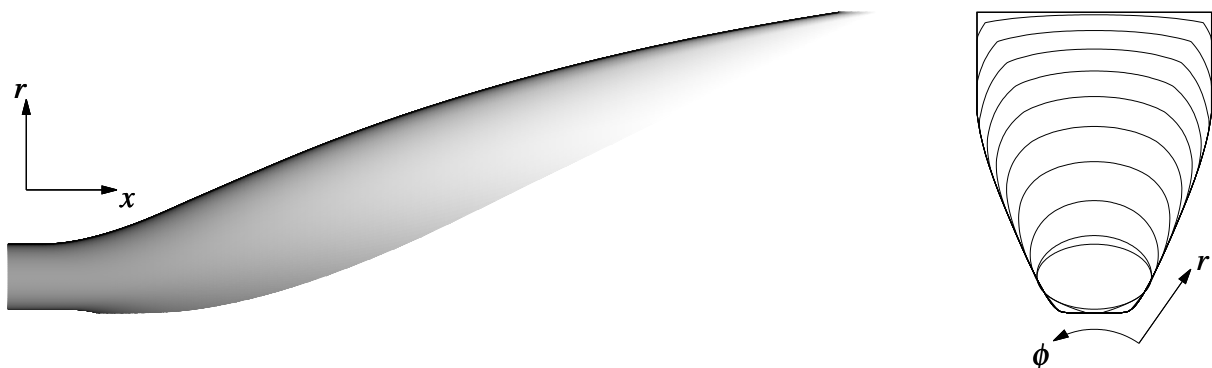


Figure 3.11: A shape transition nozzle with a small drag surface. Centre body radius $\frac{r_B}{r_A} = 0.54$, area ratio of the Rao nozzle $\frac{A_E}{A_A} = 10$, combustor exit Mach number $M_A = 2.2$.

small that it is hardly noticeable. A feature of this size can easily be removed in the blending process without having a large effect on the nozzle flow. Introducing r_C^* therefore increases the flexibility of the dual expansion flowfield. Note that the lateral expansion is much more prominent than it is in Figure 3.9. This is due to the smaller centre body and displays the effect of varying the centre body radius on the streamline traced geometry. Examining both Figures 3.9 and 3.11, the kinds of nozzle shapes that are attainable with the proposed method become apparent. The axisymmetric nature of the parent flowfield results in a nozzle exit cross-section that gets wider with increasing r . The rate of change of the width with respect to the radius, i.e. $\partial w / \partial r$, and the maximum and minimum width can be controlled with the radius of the centre body (compare Kunze, 2014, p. 33). It is, however, impossible to create a nozzle shape with lateral expansion where $r \leq r_C^*$. Any such nozzle can only be achieved in the blending process. As stated in the introduction to this chapter, the larger the difference in between N_{cb} and N_v , the larger the deviation from the parent flowfields properties in the shape transition nozzle and the smaller the control of the designer over the final result. If the difference between N_{cb} and N_v is too large, it becomes impossible to attain a smooth shape transition

nozzle altogether.

3.3 Streamline Tracing, Blending and the Combustor Interface

So far, this chapter has concerned itself with the design of the parent flowfield, arguably the most important step in the nozzle design process. In the following, the streamline tracing and the blending process are examined more closely.

A streamline may be expressed as

$$\frac{d\vec{x}_s}{ds} \times \vec{u}(\vec{x}_s) = 0. \quad (3.18)$$

Here, \vec{u} designates the velocity vector and s represents a coordinate along the streamline. Equation (3.18) demonstrates, that streamlines are, by definition, parallel to the velocity vector. In order to calculate the streamlines, the parent flowfield is first calculated using the finite difference solver Seagull (Salas, 1976).

Heun's method, a predictor corrector type integration, where an initial estimate of the next integration step is refined with the trapezoidal rule, is used to calculate streamlines from the flow solution, i.e.

$$\vec{x}_{s,E}(s + ds) = \vec{x}_s(s) + ds \cdot \vec{u}(\vec{x}_s(s)) \quad (3.19)$$

$$\vec{x}_s(s + ds) = \vec{x}_s(s) + \frac{ds}{2} \cdot [\vec{u}(\vec{x}_s(s)) + \vec{u}(\vec{x}_{s,E}(s + ds))]. \quad (3.20)$$

Here, $\vec{x}_{s,E}(s + ds)$ denotes the initial estimate calculated with Euler's method and $\vec{x}_s(s + ds)$ the corrected integration step.

In order to attain a smooth surface for the combustor and vehicle nozzle, an appropriate number of streamlines should be evenly spaced around the perimeter of N_{cb} and N_v . The ellipse is discretised at equal sweeps of angle around its centre. Since the velocity vector is unique for every streamline, the distribution of streamlines is different at the downstream end of the combustor nozzle. Considering that Rao's method optimises the thrust at the specified control surface, the streamline tracing process is started at x_A and terminated at the control surface of the parent flowfield. Thus follows, that the distance in between adjacent streamlines at the downstream end of the combustor nozzle is determined by the radial distance of their starting points $\Delta r_s(x_A)$, the axial distance of the points where each streamline respectively intersects the control surface, i.e. $\Delta x_{s,DE}$, and the number of points that are used to discretise the ellipse. The discretisation of the vehicle nozzle should be performed with the blending process in mind. Pairs of corresponding streamlines are blended to achieve the shape transition. That is, streamline i of the combustor nozzle is blended with streamline i of the vehicle nozzle for all streamlines. As stated in the introduction to this chapter, it follows that the two streamline

traced nozzles should be as similar to one another as possible under the given constraints. Not only does this mean that the surfaces need to be similar in shape, but that the distribution of streamlines of the combustor nozzle should be matched by the vehicle nozzle. The discretisation of the nozzle exit cross-section is therefore based on the intersections of the streamlines constituting the combustor nozzle with the control surface. The distances between the intersections of the streamlines are calculated and scaled by the length of the perimeter of the nozzle exit cross-section relative to the sum of the distances to determine the required point distribution. Once the nozzle exit cross-section is defined, each point is streamline traced upstream from the control surface to x_A .

As described in Kunze (2014), the defining features of the flow properties of the parent flowfield are the expansion waves. To capture the properties of the parent flowfield as much as possible in the shape transition nozzle it must reproduce the expansion waves to a high degree. The parts of the nozzle wall that create or absorb expansion waves can easily be identified; the slope of the wall is not constant there. Referring to Figure 3.5, the corner at point A creates the initial expansion fan and the waves are absorbed where the wall contour is curved. The linear part of the wall contour neither creates nor absorbs expansion waves. To recreate the expansion fan from point A in the shape transition nozzle, the onset of the shape transition is delayed such that it starts behind the expansion waves, i.e. where the wall contour's slope is constant, in the top half of the shape transition nozzle. Ideally, the same procedure is applied to the bottom half of the shape transition nozzle to capture the expansion waves created on the centre body. This, however, depends on the desired nozzle exit cross-section. For the nozzle presented in Section 3.4, for instance, the combustor and vehicle nozzle were very different from one another in that region. It was, thus, first ensured that no forward facing surface is created in the blending process and the exact capture of the expansion waves was secondary.

A caveat of the proposed parent flowfield, and any axisymmetric flowfield, is that it cannot be used to design nozzles with a laterally diverging inflow, i.e. $u_\phi = 0$. However, scramjet combustors in general and the model used here in particular use combustors that consist of a constant area and a diverging section. The divergence angle commonly is constant around the circumference of the combustor, i.e. $u_\phi \neq 0$. Attaching a shape transition nozzle that was designed with an axisymmetric flowfield, where $u_\phi = 0$, to a divergent combustor exit, where $u_\phi \neq 0$, forces the flow to change direction towards the centre of the ellipse on entering the nozzle and thus invariably leads to the creation of shock waves. In order to avoid this, the diverging section of the combustor is extended to the control surface and merged with the nozzle such that the nozzle diverges throughout. That is, the combustor extension replaces the areas of the nozzle surface where the local wall angle with respect to the combustor axis is smaller than the combustor's divergence angle. While this affects the flow inside the shape transition nozzle to deviate from the parent flowfield's, shock waves generated at the start of the nozzle are considered to be more detrimental since they reduce the total pressure of the flow and therefore the exhaust gases' potential to produce thrust. Figure 3.12 shows a shape transition nozzle, the combustor extension and the resulting nozzle after merging the two.

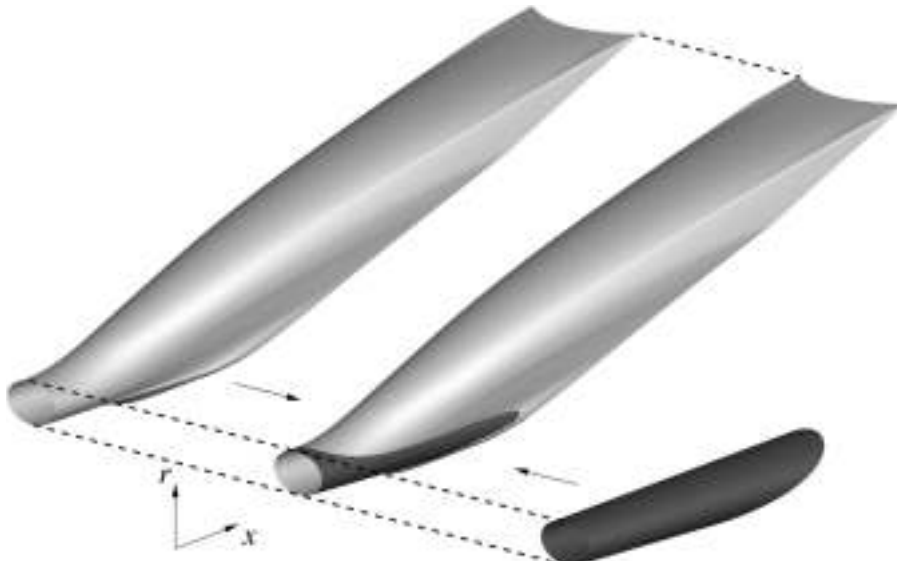


Figure 3.12: A shape transition nozzle (left), the combustor extension (right) and the resulting nozzle after merging the two such that the nozzle is divergent throughout (centre). The features that remain from the combustor extension are coloured in black. The grey surface is copied from the shape transition nozzle. - - - indicate lines of constant x for clarity.

A second option to avoid the generation of shock waves at the start of the nozzle is to shift its starting point upstream, to the end of the constant area section of the combustor, replacing the combustor's diverging section. In this case the flow entering the nozzle is not diverging and merging the start of the nozzle with a diverging combustor segment is not necessary. However, other complications arise. Significant combustion still occurs in the diverging combustor segment. Assuming a non-reacting flow at the start of the nozzle is therefore impossible. Furthermore, it must be ensured that the flow is not expanded too rapidly because this can result in cooling the flow to the point where the combustion reaction is terminated. Given these considerations, it was decided that it is preferable to design a nozzle starting from the end of the divergent section of the combustor.

3.4 Mach 12 REST engine nozzle

In the following, a nozzle designed with the method introduced in the previous section is presented. It is designed to fit the airframe integrated Mach 12 REST scramjet model designed by Doherty et al. (2015), see Section 4.2.

The nozzle is designed for a Mach 10 condition of T4, reproducing flight conditions at an altitude of 33.7 km. It should be noted that the condition is approaching the operational limit of T4. It was thus impossible to match the free stream temperature at the given altitude (Doherty, 2014, Section 3.3.2). The free stream conditions are listed in Table 3.5. The flow conditions at the combustor exit were determined using a 1D cycle analysis, following that detailed in Smart (2007). The exit Mach number M_E is calculated iteratively from the target area ratio assuming one dimensional isentropic

Table 3.5: The free stream conditions for the shape transition nozzle design.

M_0	$p_0, \text{ Pa}$	$u_0, \text{ m s}^{-1}$	$T_0, \text{ K}$
10.38	638	3036.8	213

flow:

$$AR = \frac{M_A}{M_E} \cdot \left(\frac{1 + \frac{\gamma-1}{2} M_E^2}{1 + \frac{\gamma-1}{2} M_A^2} \right)^{\frac{\gamma+1}{2(\gamma-1)}} = 13.8. \quad (3.21)$$

It should be noted that the choice of target area ratio does not equal the area ratio of the parent flowfield. Rao's optimisation truncates the nozzle contour such that the flow is non-uniform at the nozzle exit. Thus the one dimensional approximation is inaccurate and the true area ratio of the flowfield is significantly different. However, equation (3.21) provides a simple means to determine a starting point for the design that can later be adjusted to suit the requirements of the nozzle. For the design stage all dimensions are normalised by r_A . Table 3.6 sums up the conditions that are required to design the parent flowfield.

Table 3.6: The design conditions for the parent flowfield.

M_A	$p_A, \text{ kPa}$	γ	M_E	$p_0, \text{ Pa}$	r_C^*/r_A	r_B/r_A
2.52	56.185	1.2764	4.77	638	0.6945	0.6

3.4.1 Nozzle Flowpath

Figure 3.13 shows Mach number contours of the parent flowfield, as calculated with Seagull. It should be noted that the region downstream of the control surface is only calculated because Seagull requires both the centre body and outer wall contour to have the same length. Since the streamline tracing process is terminated at the control surface, that part of the flowfield has no effect on the shape transition nozzle. The extended centre body wall, downstream of point G in Figure 3.7, is designed such that the shock wave that forms in the concave corner at $x/r_A \approx 2$ does not interfere with the flowfield upstream of the control surface.

Streamline tracing the elliptical combustor exit cross-section through this flowfield results in the surface shown in Figure 3.14. As evident, the adjustment of r_C using equation (3.17) with $\zeta > 0$ results in drag surfaces. However, they are minimal compared to the ones in Figure 3.6 and can be eliminated in the blending process. In reference Kunze (2014), it was stated that preserving the cowl-side features of the streamline traced ellipse in the shape transition nozzle is desirable to capture the parent flowfield's properties. However, the external airframe of the given scramjet model has a vastly different shape than the cowl-side portion of the streamline traced ellipse. The shape transition nozzle would thus not make use of the entire base area of the scramjet. In order to determine whether it

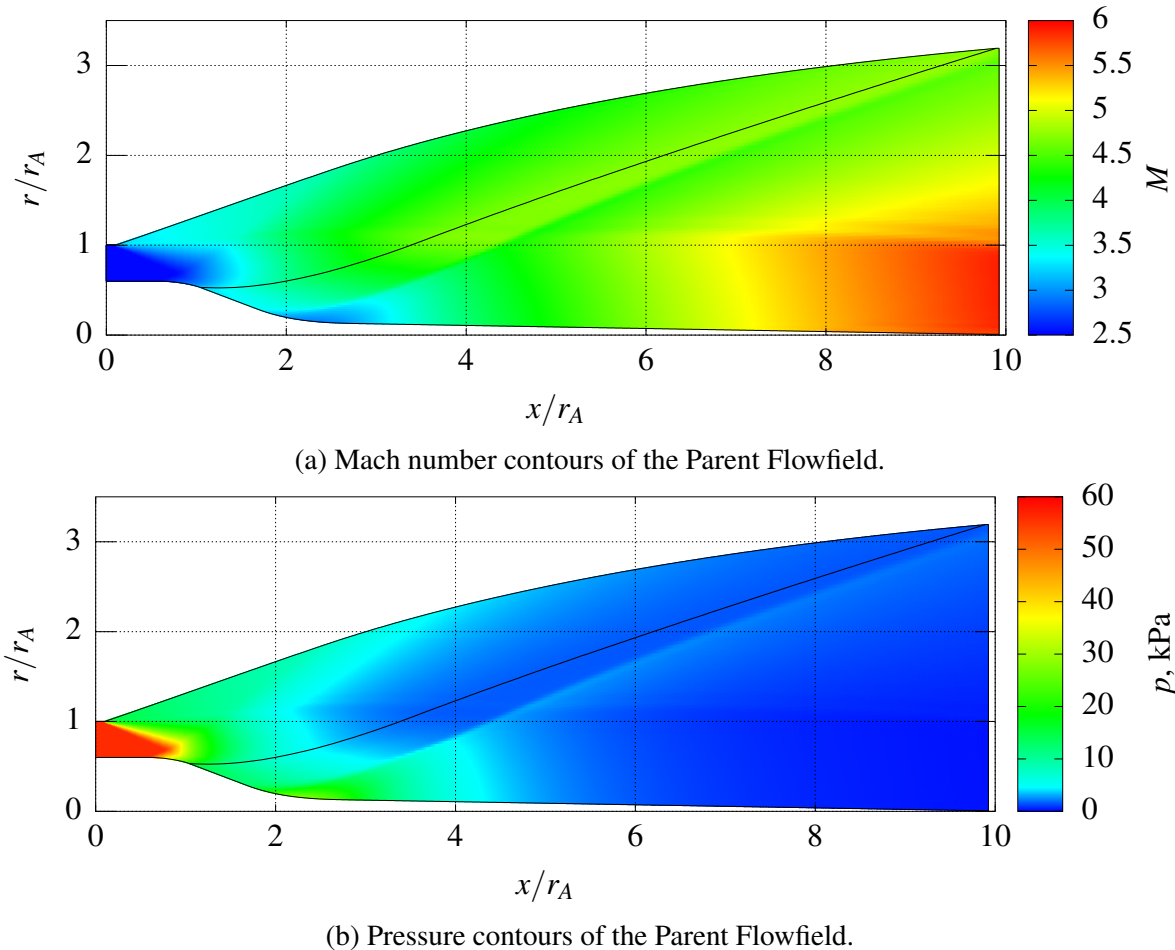


Figure 3.13: The parent flowfield as calculated with Seagull. — designates the control surface and the boundaries of the computational domain.

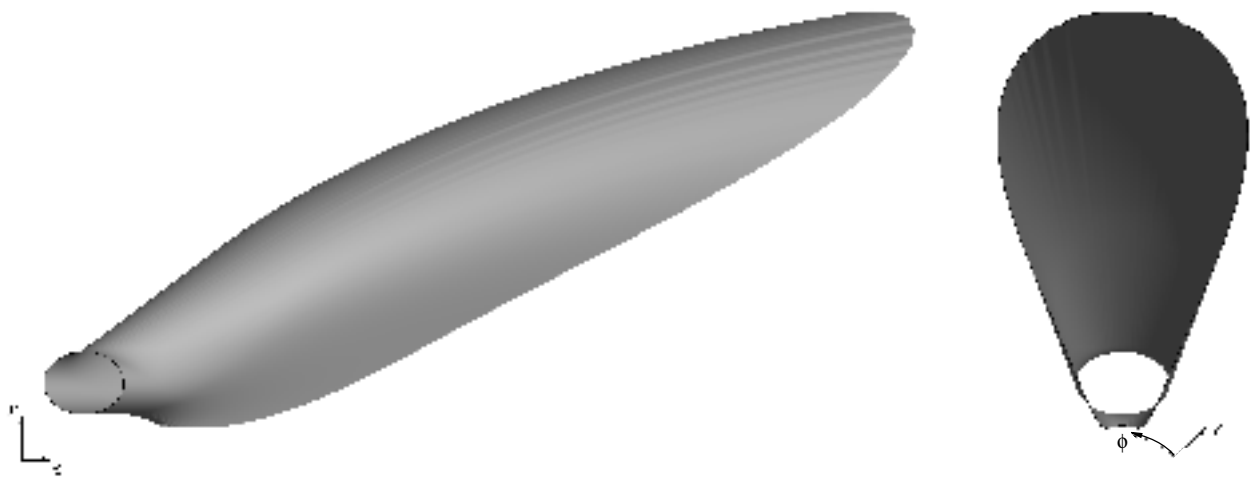


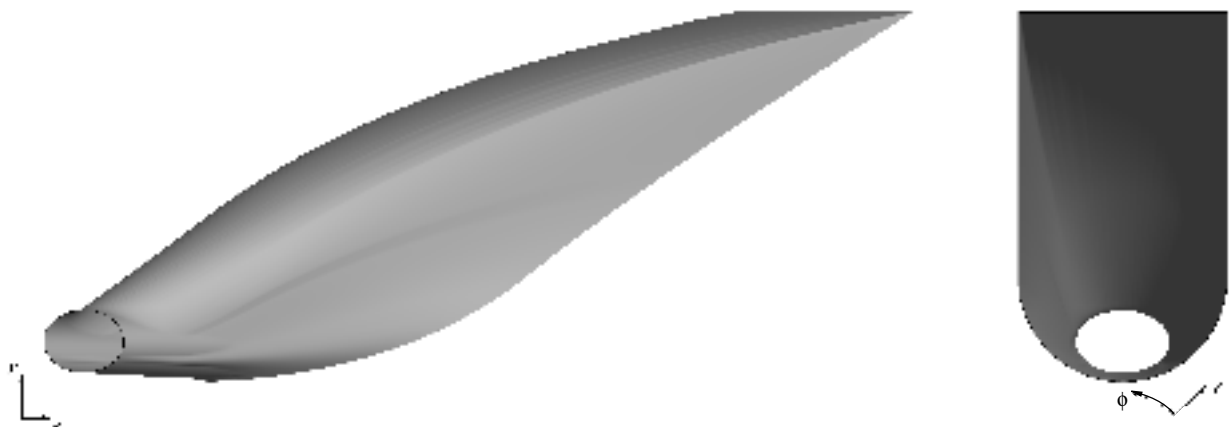
Figure 3.14: The elliptical combustor exit cross-section streamline traced through the parent flowfield.

is more advantageous to preserve the parent flowfield's properties or to make use of the entire base area of the model, two shape transition nozzles were designed and compared. The two nozzles are

shown in Figure 3.15. Nozzle 1 preserves the cowl-side features of the combustor nozzle as much



(a) Nozzle 1



(b) Nozzle 2

Figure 3.15: A comparison of two shape transition nozzles with different exit shapes. Nozzle 1 reproduces the parent flowfield's expansion waves very accurately by avoiding a shape transition at the cowl-side of the engine. Nozzle 2 fills the entire base area of the scramjet model.

as possible and Nozzle 2 fills the entire base area of the scramjet model. A different parent flowfield was used for each nozzle to reduce the amount of necessary shape transition to a minimum. As a consequence Nozzle 2 is longer than Nozzle 1, in addition to having a bigger area ratio. The Centre for Hypersonics' in-house finite volume CFD solver eilmer4 (Jacobs and Gollan, 2016) was used to run inviscid simulations of both nozzles. Table 3.7 shows a comparison of the two nozzle's metrics. The inviscid forces were calculated by integrating the pressure on the nozzle wall over the respective area. Inviscid thrust per unit length and total thrust produced were used as the pivotal metrics in determining to use Nozzle 2 over Nozzle 1. It should be noted that Nozzle 2, even though the centre body radius of the parent flowfield was carefully chosen, contained drag surfaces before it was merged

Table 3.7: A comparison of Nozzle's 1 and 2.

	l , mm	AR	T , N	T/l , Nm $^{-1}$	L , N
Nozzle 1	361.5	14	27.4	75.8	151.1
Nozzle 2	395.9	16	30.0	75.9	168.1

with the combustor extension. The cowl-side surfaces of N_{cb} and N_v were too different to be blended smoothly while ensuring a diverging nozzle at the same time.

3.4.2 CFD Analysis of the Parent Flowfield Capture

A discussion of the simulation of Nozzle 2, performed with eilmer4, is presented hereinafter. eilmer4's explicit time stepping solver for unstructured grids was used in the present analysis. A second order spatial reconstruction in conjunction with an HLLE flux calculator was used. The computational grid was unstructured with approximately 1.6 million cells and was created with Pointwise®'s T-Rex mesher. A T-Rex mesh consists of structured hexahedral cells at prescribed boundaries that grow in size normal to the boundary. The interior of the mesh is then filled with unstructured cells (tetrahedrals, pyramids and prisms) as required. The simulation was run inviscidly and all walls were assigned a free slip boundary condition. The exhaust gas was simulated as a perfect gas. Its composition was determined with cycle analysis. The far field downstream of the control surface was designed such that no interactions with the internal nozzle flow occurred. Due to its symmetry about the x - r -plane for $\phi = 90^\circ$, only one half of the nozzle was simulated. It was run on the University of Queensland's Tinaroo cluster. The computational grid is displayed in Figure 3.16. To check for grid convergence, the simulation was repeated on two other grids containing approximately 1.2 and 2 million cells respectively. It was found that, although the pressure distribution showed small differences between the 1.2 and the 1.6 million cell grids, the thrust and lift forces only varied by 0.3 % and 1.2 % respectively. The coarse grid was therefore deemed sufficient for determining integral quantities. No noticeable differences were observed between the flow solutions of the 1.6 and the 2 million cell grids.

The average inflow conditions were the same as the ones presented in Table 3.6. The velocity vector in each cell of the inflow plane was rotated to create a diverging inflow that follows the combustor wall while preserving its magnitude. The complete set of inflow conditions and the simulated gas properties, determined with cycle analysis, are listed in Table 3.8.

Table 3.8: The inflow conditions and gas properties used in the inviscid simulation of the shape transition nozzle.

M_A	p_A , kPa	T_A , K	γ	R_A , Jkg $^{-1}$ K $^{-1}$
2.52	56.2	1979	1.28	375.7

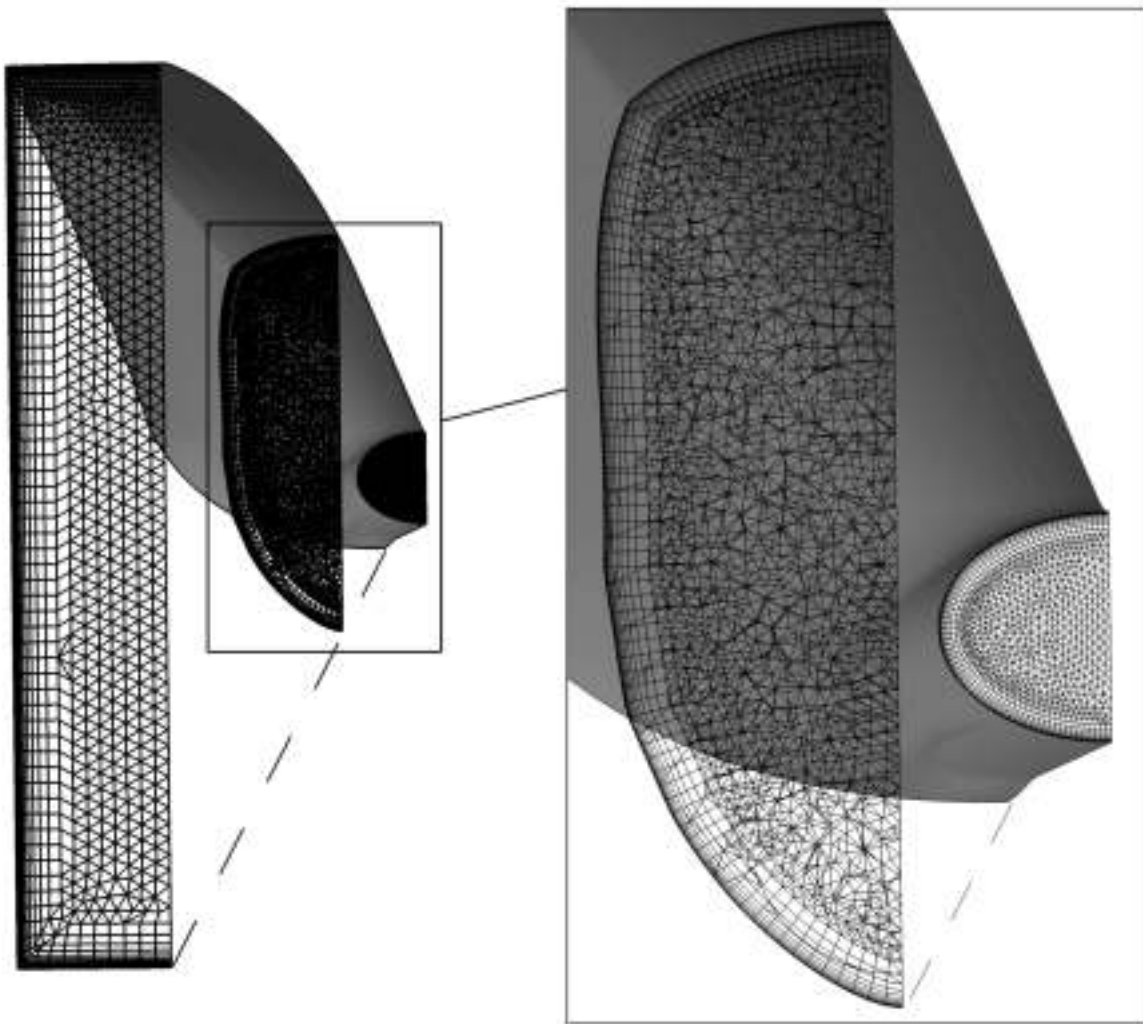


Figure 3.16: The unstructured computational mesh for the simulation of Nozzle 2.

Below is presented a comparison between the parent flowfield and that of the shape transition nozzle. Figure 3.17 shows plots of Mach number and pressure contours of the CFD solution at the symmetry plane of the shape transition nozzle. For reference, they are displayed inside the parent flowfield wall contour. In comparing Figures 3.17 and 3.13, it is apparent that the flowfields, while overall similar, are different as a result of the shape transition and merging the nozzle with the combustor. The main deviation can be seen along the centre body wall. This can be explained by the diverging combustor wall. Since the parent flowfield is designed with a uniform inflow, the extension of the combustor intersects the centre body downstream of the first expansion waves created on the centre body in the parent flowfield. The intersection is referred to as point B' . Hence, the cowl-side part of the shape transition nozzle only creates expansion waves downstream of point B' . The lack of these cowl-side expansion waves causes compression waves to be created on the nozzle wall from around $x/r_A = 3$. The wall pressure at $x/r_A > 3$ is thus larger than it is in the parent flowfield while the Mach number on the wall is smaller. The reduced pressure and increased Mach number of the

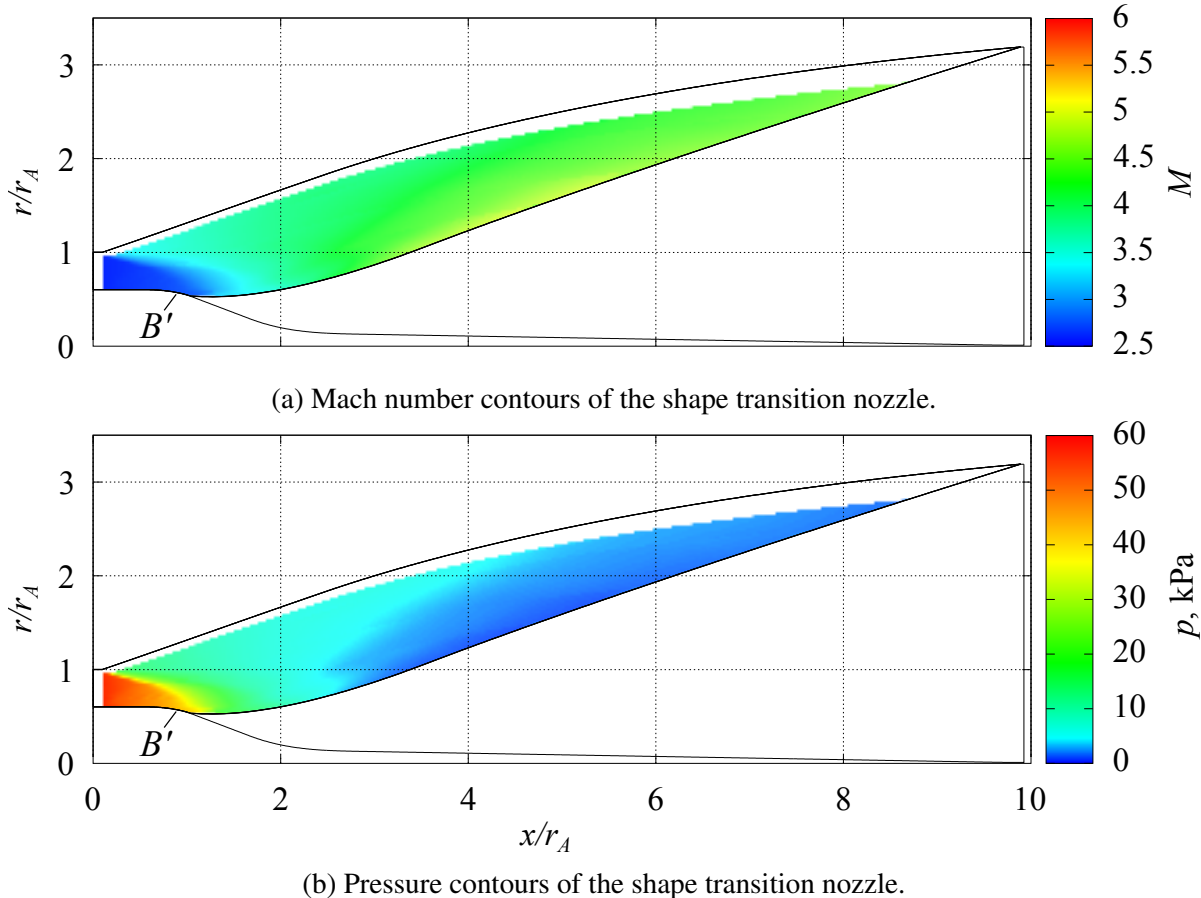


Figure 3.17: The shape transition nozzle flowfield at the symmetry plane as calculated with eilmer4.

shape transition nozzle flow at the start of the nozzle, i.e. $x/r_A < 1$, is a combined effect of the shape transition and the combustor geometry. While the parent flowfield shows no expansion in that area, the shape transition nozzle expands laterally from $x/r_A = 0$. Therefore, the pressure inside the shape transition nozzle is lower than it is in the parent flowfield and the Mach number is higher.

For a quantitative analysis of the differences between the shape transition nozzle and the parent flowfield, the local relative difference of Mach number and pressure was calculated for six slices of the CFD solution. The local relative differences were defined as

$$\Delta M_n = \frac{\Delta M}{M_{PF}} = \frac{M_{ST} - M_{PF}}{M_{PF}} \quad \text{and} \quad (3.22)$$

$$\Delta p_n = \frac{\Delta p}{p_{PF}} = \frac{p_{ST} - p_{PF}}{p_{PF}}, \quad (3.23)$$

where the index PF designates quantities of the parent flowfield and the index ST those of the shape transition nozzle.

Given the axisymmetric nature of the parent flowfield, slices of the CFD solution through the x -axis and the r -axis for any given ϕ can be compared directly to the parent flowfield. The results for slices at intervals of $\Delta\phi = 5^\circ$ are shown in Figures 3.18 and 3.19. Note that the scales of the two

plots are different due to the difference in magnitude of the relative differences. The slices shown

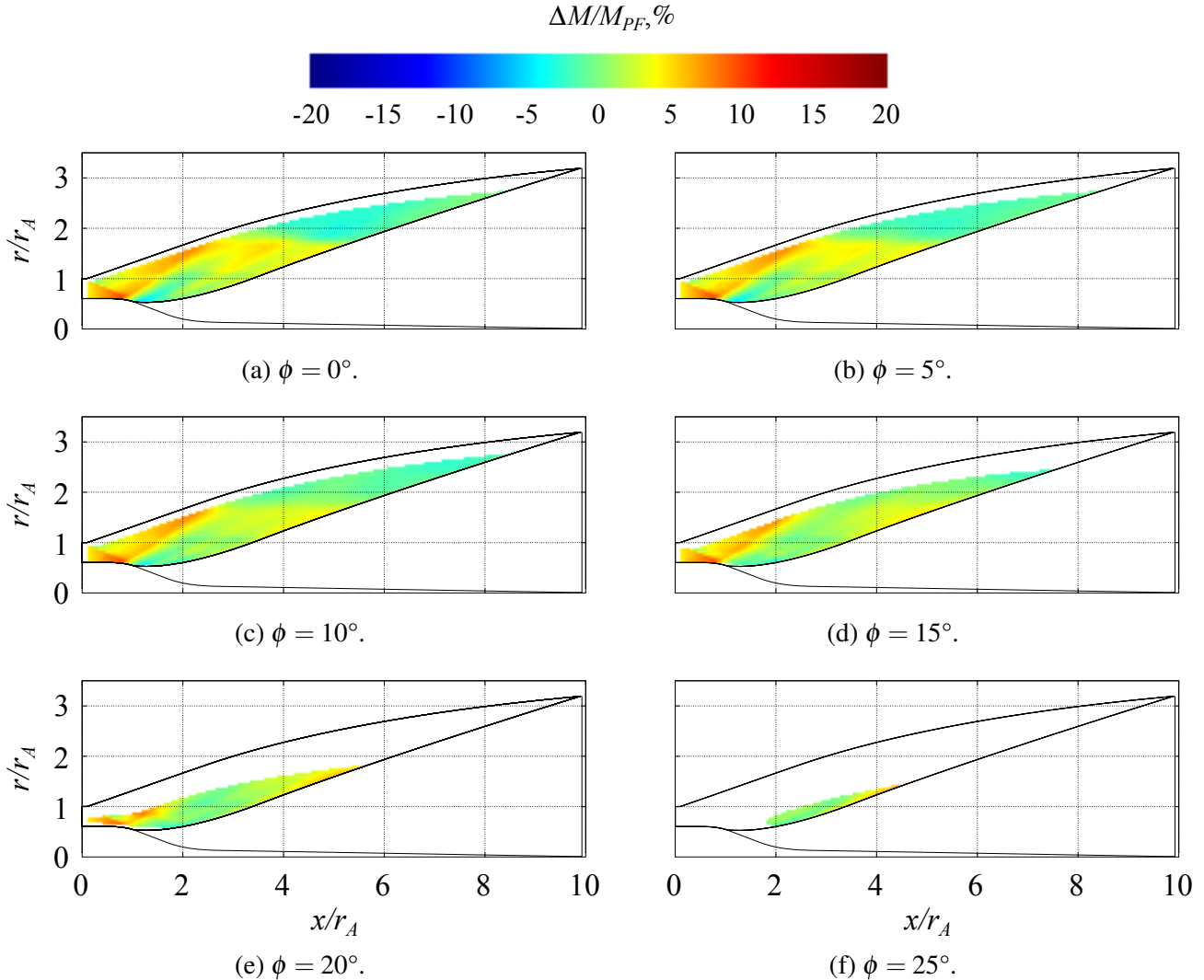


Figure 3.18: Contours of the difference in Mach number between the parent flowfield and the CFD solution of the shape transition nozzle at intervals of $\Delta\phi = 5^\circ$. At each point the difference is normalised by the local Mach number of the parent flowfield.

confirm the observations made in the previous paragraphs. Additionally, it is evident that the slices with $\phi = 25^\circ$ deviate the most from the parent flowfield. This is to be expected considering that the combustor and vehicle nozzle vary strongly from one another in that region.

In general, the Mach number distributions show small to moderately large deviations from the parent flowfield. While this implies that the expansion waves of the parent flowfield are not perfectly reproduced, it suggests that the flow inside the shape transition nozzle closely resembles that of the parent flowfield.

The relatively large values in Figure 3.19 for $x/r_A > 3$ are due to the magnitude of pressure downstream of most of the expansion waves. The pressure does not exceed 5 kPa in this region. Variations of Δp_n in excess of 50 % thus only indicate an absolute difference of approximately 2.5 kPa

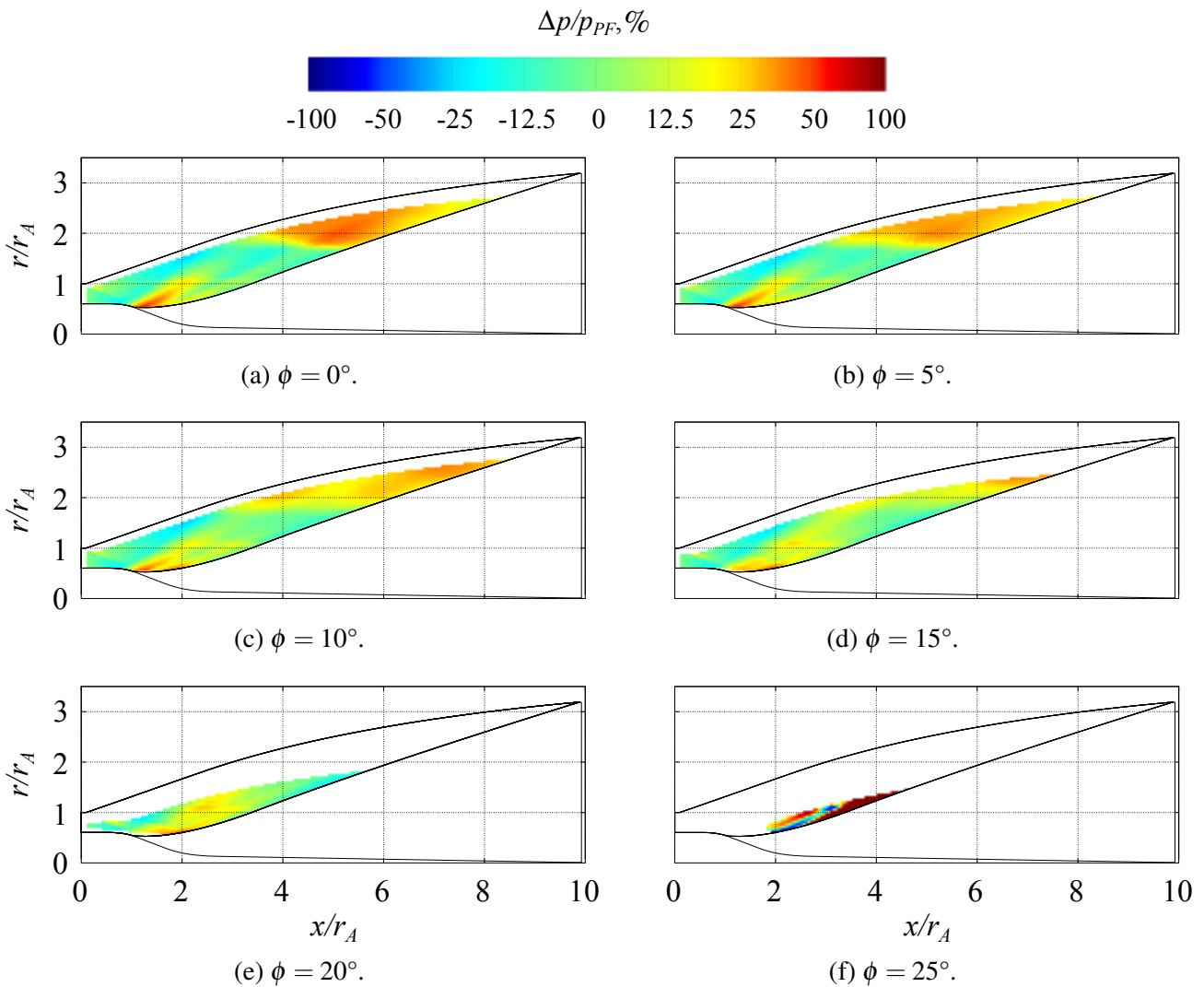


Figure 3.19: Contours of the difference in pressure between the parent flowfield and the CFD solution of the shape transition nozzle at intervals of $\Delta\phi = 5^\circ$. At each point the difference is normalised by the local pressure of the parent flowfield.

to 4 kPa. Table 3.9 lists the average relative difference for both Mach number and pressure in percent as well as one standard deviation and the minimum and maximum relative difference. As expected, the two flowfields show differences where the geometry deviates from a streamline traced shape. However, most of the major features of the parent flowfield were successfully captured.

Considering that thrust production is the main objective, it is of interest to analyse the distribution of thrust production in comparison with the parent flowfield. Figure 3.20 shows thrust normalised by the product of the combustor exit pressure and the nozzle inflow area, i.e. $T/(p_A \cdot A_A)$, versus normalised nozzle length for both the shape transition nozzle and the parent flowfield. As evidenced in Figure 3.20, the shape transition nozzle performs better than the parent flowfield in terms of thrust production. It is postulated that this is due to the lateral expansion added by the shape transition and the combustor extension. While the only thrust producing surface for $x/r_A < 0.6$ in the parent

Table 3.9: Relative differences in the Mach number and the pressure distribution of the parent flowfield and the shape transition nozzle.

$\phi, {}^\circ$	Quantity	Unit	Mean	σ	Min	Max
0	ΔM_n	%	2.0	3.2	-8.0	10.1
		%	2.1	3.1	-7.6	9.9
		%	2.1	2.9	-8.6	9.6
		%	2.5	2.5	-6.8	9.6
		%	2.1	2.6	-5.4	9.7
		%	2.6	3.0	-11.2	11.1
5	Δp_n	%	7.4	19.6	-25.3	88.9
		%	6.8	18.4	-24.8	89.9
		%	7.2	17.0	-25.9	115.4
		%	4.3	14.0	-23.7	89.3
		%	6.1	16.1	-29.8	66.2
		%	314	397	-1743	1303

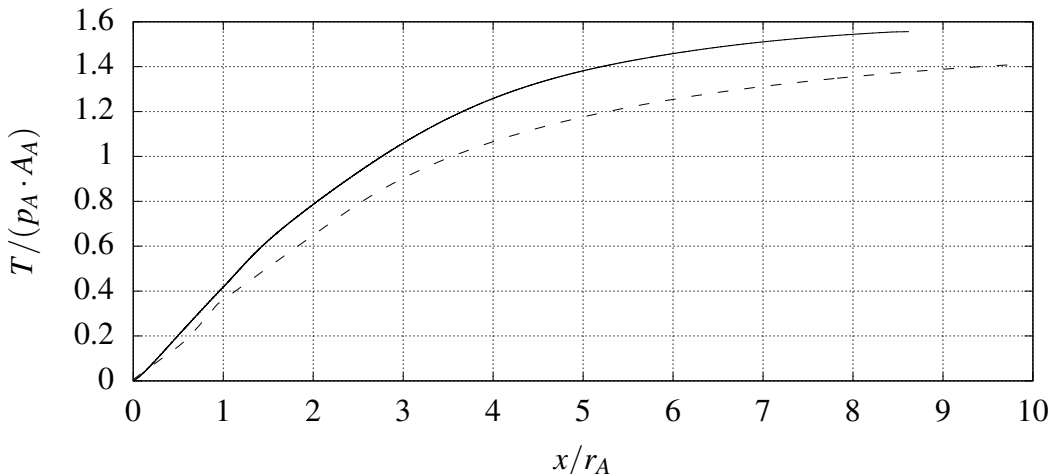


Figure 3.20: The normalised thrust distribution for the shape transition nozzle (—) and the parent flowfield (---).

flowfield is the outer wall, the shape transition nozzle is diverging from $x/r_A = 0$, i.e. every part of its surface contributes to the thrust produced. Given that the combustor extension accounts for a significant part of the shape transition nozzle surface at its start, the nozzle surface is largely tangential to the combustor. Thus, as opposed to the parent flowfield, no expansion waves are created here and the static pressure remains high. It is this high pressure region that explains the surplus in normalised thrust. In the parent flowfield on the other hand, the exhaust gases have to pass through the expansion waves created by the nozzle wall and centre body before the orientation of the nozzle surface allows them to produce thrust.

In nozzle design, it is of interest to analyse the thrust and lift contribution of each part of the nozzle, in particular the last third. The first third of the shape transition nozzle contributes the majority of

both thrust and lift. This is to be expected given the high wall pressure and the orientation of the nozzle surface. Given that the shape transition nozzle is based on an optimised flowfield but is not optimised itself, a comparison with the parent flowfield is warranted. It is postulated that if the last third of the shape transition nozzle produces a similar fraction of the total thrust as the last third of the parent flowfield produces of its total thrust a truncation of the shape transition nozzle does not yield a performance benefit despite not being optimised. In Table 3.10 the contribution of each third of the shape transition nozzle as well as the parent flowfield to the normalised forces is listed. Note that the parent flowfield is axisymmetric and therefore does not produce lift. The data presented

Table 3.10: A streamwise breakdown of the forces produced by the shape transition nozzle and the parent flowfield.

(a) Normalised absolute and relative forces produced by the shape transition nozzle.

	Quantity	Unit	1 st Third	2 nd Third	3 rd Third	Total
Absolute	$\frac{T_{ST}}{p_A \cdot A_A}$	-	1.00	0.43	0.12	1.56
Relative	$\frac{T_{ST}}{p_A \cdot A_A}$	%	64.4	27.8	7.8	100
Absolute	$\frac{L_{ST}}{p_A \cdot A_A}$	-	6.19	1.57	0.97	8.73
Relative	$\frac{L_{ST}}{p_A \cdot A_A}$	%	70.9	18.0	11.1	100

(b) Normalised absolute and relative forces produced by the parent flowfield.

	Quantity	Unit	1 st Third	2 nd Third	3 rd Third	Total
Absolute	$\frac{T_{PF}}{p_A \cdot A_A}$	-	0.94	0.35	0.12	1.41
Relative	$\frac{T_{PF}}{p_A \cdot A_A}$	%	66.5	24.6	8.8	100

demonstrates that the last third of the shape transition nozzle produces significant thrust. The fraction of the total thrust is comparable to that of the last third of the parent flowfield. A further truncation of the shape transition nozzle is therefore not warranted. However, the analysis presented here is based on the assumption of inviscid flow. Further investigation, including viscous effects and external flow, is required to conclusively determine the contribution of each nozzle segment to the net forces.

CHAPTER 4

EXPERIMENTAL DESIGN

The current chapter introduces the facility in which the experimental part of the present study was conducted, the experimental model as well as the diagnostic hardware employed in the experimental campaign. The aim of the experimental campaign was to measure the net forces on a full airframe integrated scramjet. To date, there are three methods that provide the means to do so in impulse facilities; the stress wave force balance, accelerometers and image tracking based force measurements (Robinson et al., 2006; Tanno et al., 2009; Laurence and Karl, 2010).

As stated in Chapter 1, the method of choice used in the present study was image tracking. A requirement for this method is that the model is either completely unrestrained or restrained such that the motion of the model during the test time is not affected. Here, the model was initially suspended by two strands of fishing line. Following the design by Hannemann et al. (2014), the starting flow of the facility pushes each strand backwards onto a razor blade, which cuts the fishing line and releases the model. Fishing line is well suited for this application, as it is rated to a specific weight. The strands can therefore easily be tailored to suit the model. Two steel supports catch the model after the flow terminates. The Mach 12 REST scramjet model used in present study is shown suspended on fishing line inside the T4 test section in Figure 4.1. The supports do not touch the model while it is suspended and allow for sufficient motion in every direction to avoid interference. Details of the catch and release mechanism are covered in Section 4.2. Since the model is too large to be visualised through the test section windows, a tracking object is installed on top of it. The motion of the model can be inferred from the motion of the tracking object using rigid body motion analysis.

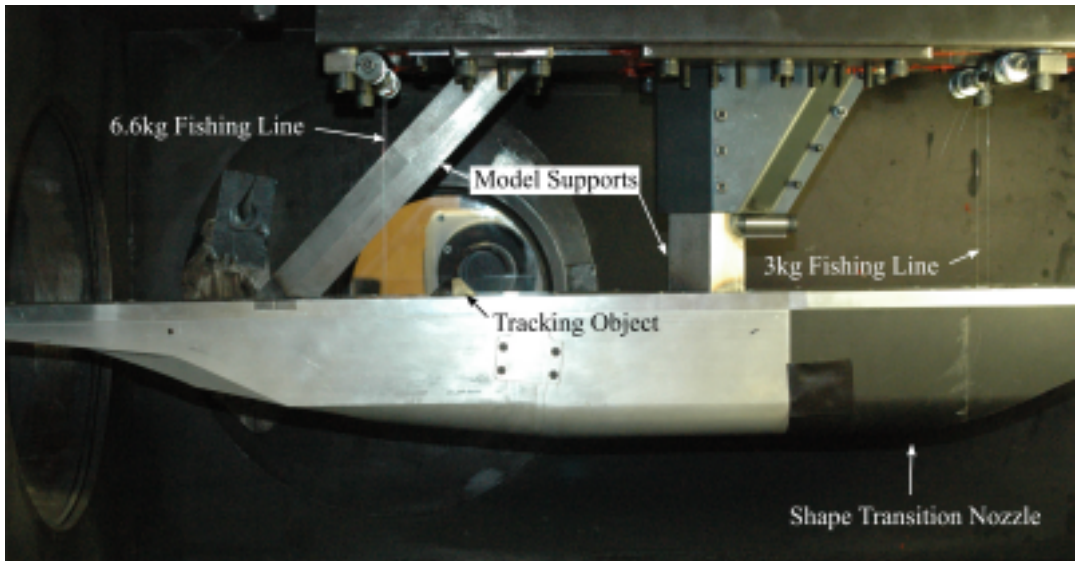


Figure 4.1: The Mach 12 REST scramjet model inside the T4 test section. The direction of flow is from left to right.

4.1 Experimental Facility

The T4 shock tunnel was commissioned in 1987 and has since been used for over 12000 experiments, commonly referred to as 'shots'. T4 is a free piston driven reflected shock tunnel, also known as a Stalker tube after their inventor Ray Stalker (Stalker, 1967). Test conditions over a range of Mach numbers (4 to 10) and stagnation enthalpies ($<3 \text{ MJ kg}^{-1}$ to 15 MJ kg^{-1}), with the maximum stagnation pressure exceeding 90 MPa, are attainable for test times on the order of a few milliseconds. T4 consists of six sections: the high pressure reservoir, the compression tube, the shock tube, the convergent-divergent nozzle, the test section and the dump tank, as shown in Figure 4.2.

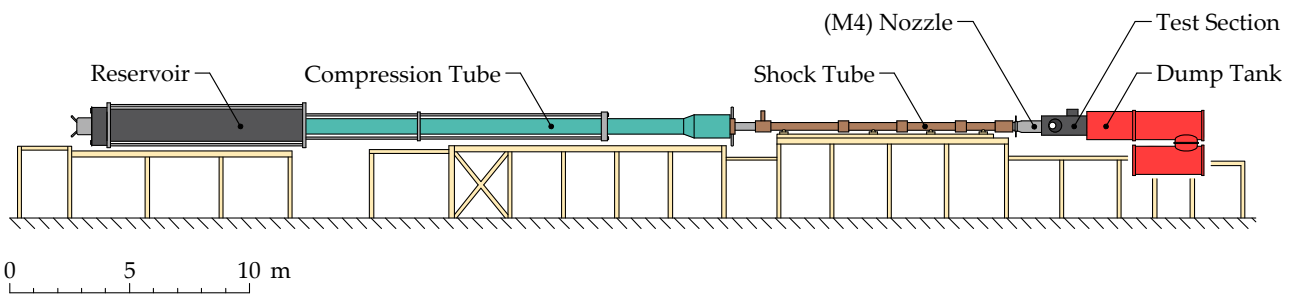


Figure 4.2: A schematic of the T4 shock tunnel at the University of Queensland. The graphic is adapted from Doherty (2014).

The compression tube has a length of 26 m and a diameter of 230 mm. The shock tube is 10 m long and has a diameter of 76 mm. The overall length of the facility exceeds 40 m. Before a shot, the reservoir and compression tube are separated by a 90.5 kg piston. A steel diaphragm, the thickness of which depends on the desired stagnation pressure, isolates the compression tube from the shock

tube and a thin Mylar[®] diaphragm separates the shock tube from the nozzle, test section and dump tank. The steel and Mylar[®] diaphragms are also referred to as the primary and secondary diaphragms respectively. Each section is individually evacuated to below 1 torr (133 Pa) to avoid contamination with moisture and other pollutants. Once the required pressure is reached in every component, the shock tube is filled with the test gas or driven gas, in the current experiments dry air. The compression tube is then filled with the driver gas. Traditionally, only argon, helium or a combination of the two was used. However, test conditions using nitrogen or combinations of argon and nitrogen as the driver gas have recently been added (Whitside et al., 2019). Finally, the reservoir is filled with high pressure air.

A shot is started by allowing the reservoir gas to fill the piston space, a small cavity behind the piston. The piston is thus accelerated towards the primary diaphragm by the force generated from the difference in pressure between the compression tube and the reservoir. The magnitude of this force causes the entire facility to recoil. Once the piston has sufficiently compressed the driver gas, compression ratios of 60 and 40 are available in T4, the primary diaphragm bursts and an unsteady shock wave travels into the shock tube. This process compresses the test gas and accelerates it towards the facility nozzle. The shock is then reflected at the secondary diaphragm, stagnating and further compressing the test and driver gases. The hot and high pressure test gas causes the secondary diaphragm to burst. This allows the test gas to expand through the convergent-divergent nozzle into the test section, thus creating the test condition. The test time is terminated once the pressure upstream of the nozzle falls below a certain threshold, in the present study this was taken to be 90 % of its average. The wave processes in the compression and shock tube, under the assumption of one dimensional flow and starting with the opening of the primary diaphragm, are shown in Figure 4.3. A set of initial conditions, that results in the contact surface between driver and test gas to be stagnated during the test time, as is the case in Figure 4.3, is referred to as a tailored condition. It should be noted, however, that this represents an idealisation. In a real shock tube, the starting process of the nozzle involves an unsteady expansion, which accelerates the previously stagnated test gas, and hence the contact surface, towards the nozzle. The tailored interface is therefore not achieved when the contact surface is stagnant for the duration of the test time, but when the pressure of the driver gas and the test gas is the same after being processed by the reflected shock. The test time is generally terminated by expansion waves being reflected on the front face of the piston. Following the opening of the primary diaphragm, an unsteady expansion fan starts to reduce the pressure in the compression tube. However, the piston is generally still moving when the primary diaphragm opens and keeps compressing the driver gas. If the piston velocity is such, that it displaces the same volume of driver gas as is leaving the compression tube through the opening in the diaphragm, a steady state is reached and the expansion and compression waves cancel each other out. This is referred to as the tuned piston velocity. Once the piston slows down further the expansion waves reflect and reduce the pressure in the test gas, terminating the test time. In practice, it has been found that overdriving the piston,

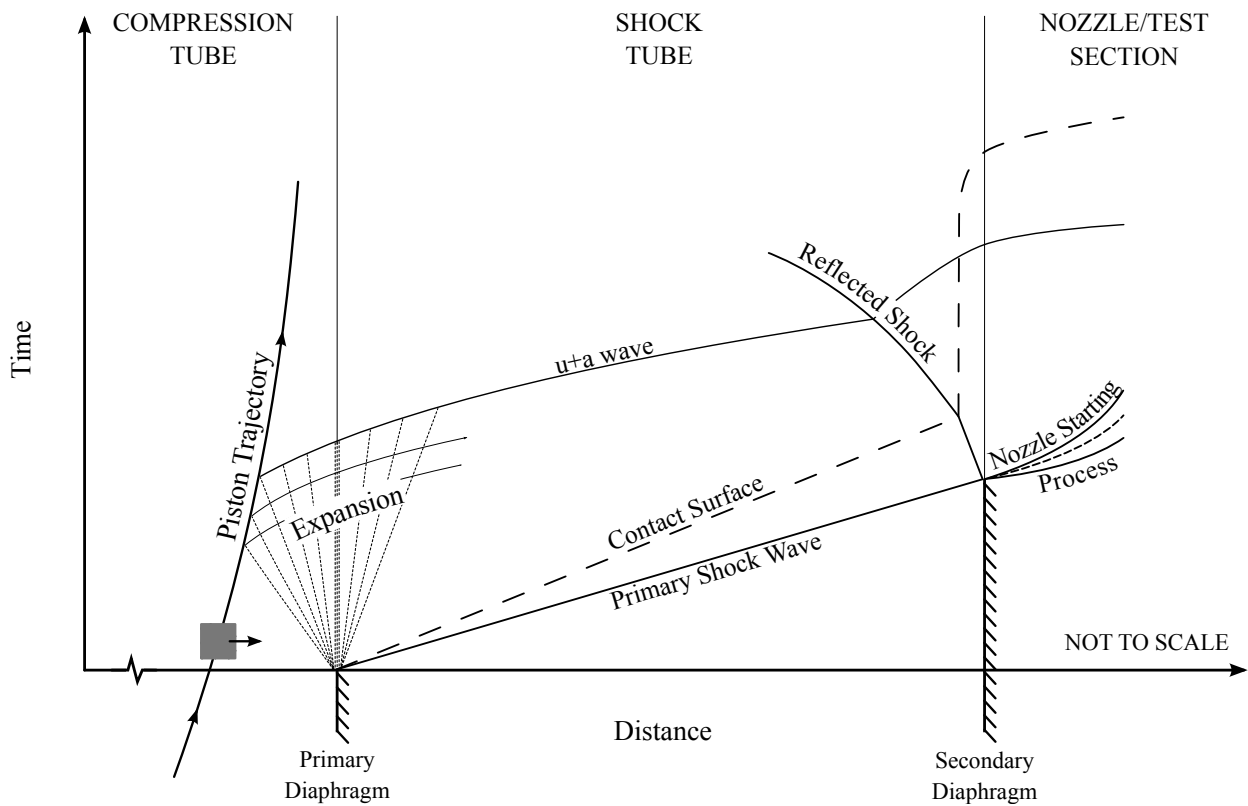


Figure 4.3: The wave processes in the compression and shock tube from the opening of the primary diaphragm assuming one dimensional flow. The graphic is adapted from Doherty (2014).

i.e. a piston velocity that increases the pressure in the driver gas by about 10 % above the rupture pressure of the primary diaphragm, can result in a longer test time (Gildfind et al., 2011). This is a consequence of three dimensional and non-ideal effects in the shock tube. The losses incurred during the processing of the test gas and upon shock reflection cause the test gas pressure to drop early if the piston is ideally tuned. Compression waves from overdriving the piston can, however, counteract these losses and create an approximately constant pressure during the test time.

4.1.1 Facility Instrumentation

The facility instrumentation serves to monitor its performance and provides the measurements that are required to calculate the flow condition that it produces. The facility recoil is measured by a Measurement Specialties™ (now TE Connectivity) DC-EC 5000 linear variable displacement transducer. Since the recoil is initiated upon launching the piston it can be used to trigger diagnostics and other systems that need to be triggered before the test flow starts, for instance the fuel system. Since the test section and experimental model have a fixed position, measuring the recoil allows for an accurate determination of the model position with respect to the facility nozzle. The recoil signal for shot 12199 is shown in Figure 4.4. As is evident, the test time roughly coincides with the maximum recoil

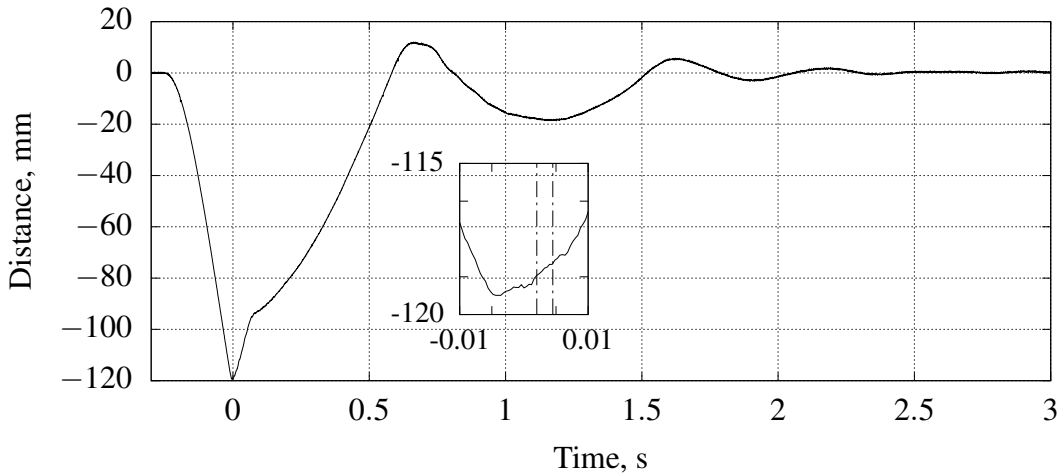


Figure 4.4: The recoil signal for shot 12199. The time axis has been shifted such that $t = 0$ aligns with the reflection of the primary shock at the end of the shock tube. The start and finish of the test time are indicated by -----.

of the facility.

Five PCB® Piezotronics^{Inc} piezoelectric pressure transducers are installed along the shock tube. The first three, models 112A22, 112A23 and 111A23 respectively, are referred to as the shock timing stations. They are placed at intervals of 2.003 m. Their primary use is to measure the speed of the primary shock as it travels along the tube. The shock speed is used in the calculation of the stagnation enthalpy of the test gas after shock reflection. As the primary shock is subject to losses along the tube and its speed decreases as it propagates along the tube, the pressure rise across the shock decreases. The value for the shock speed, that is used to calculate the test condition, is taken as the average shock speed between the second and third shock timing station, i.e.

$$V_{ss} = \frac{2.003 \text{ m}}{t_{TS,3} - t_{TS,2}}. \quad (4.1)$$

Here, V_{ss} designates the average shock speed and $t_{TS,3}$ and $t_{TS,2}$ designate the time at which the shock passes the respective timing station. The reasoning behind this choice of shock speed is that the part of the test gas that is closest to the nozzle, up to timing station 3, passes through the test section while the test flow is not established yet. The next slug of test gas, between timing stations 3 and 2, passes through the test section during the test time, followed by the remainder of the test and the driver gas after the nozzle supply pressure has dropped below the defined limit. It is therefore postulated that this choice of shock speed provides the best estimate of the enthalpy of the test flow (Stalker and Morgan, 1988; Mee, 1993). It can be shown that this value typically does not deviate much ($\pm 2\%$) from the overall average shock speed (Mee, 1993).

The remaining two pressure transducers are referred to as the stagnation (stag) probes, SPA and SPB (model 108A02). The stag probes are located at the end of the shock tube and are used to measure the nozzle supply pressure and to trigger the data acquisition system (DAQ). The DAQ, in the present

study, was triggered when the pressure measured by SPA exceeded 5.6 MPa. This is referred to as the 'stag trigger'. The time axes of all data plots presented in this study, unless otherwise indicated, are relative to the stag trigger, i.e. $t = 0$ corresponds to the primary shock passing SPA.

The shock speed and nozzle supply pressure are used to calculate the free stream flow properties inside the test section. It is therefore most important that these are measured accurately. While the main uncertainty in the shock speed comes from the fact that it is unsteady (Mee, 1993) and can thus not be improved significantly with more accurate measurements, the uncertainty of the measured nozzle supply pressure can be reduced by a factor of $1/\sqrt{n}$ by using n sensors to measure it. In the present study, every shot, except for shot 12231, has been processed using only SPA. The signal of SPB was subject to too much noise, created by a faulty connector, to be reliable for much of the experimental campaign. SPB was used to process shot 12231 because in this instance SPA measured a highly unsteady nozzle supply pressure while SPB measured a steady one, which was confirmed by the instrumentation on the experimental model.

The T4 DAQ consists of 17 National InstrumentsTM PXI-6133 cards, a PXI-1045 chassis and a PXI-4480 controller. The amplified analogue signals from all sensors are converted to digital at a 1 MHz sampling rate (1 μ s timebase) by the cards and processed by a LabVIEW 2015 virtual instrument (VI) running on the controller. The recoil and the signals that are triggered by the recoil are converted at a 2.5 kHz sampling rate (400 μ s timebase) to reduce the data size on disk. Finally, the data is stored on a local hard drive and a network file server.

4.1.2 Test Condition

Scramjets are generally designed to operate at free stream dynamic pressures between 50 kPa and 100 kPa. The Mach 12 REST scramjet used here was designed to accelerate from Mach 6 to Mach 12 (Suraweera and Smart, 2009). In the present study, a Mach 8 enthalpy condition, at a free stream dynamic pressure of 80 kPa, was used. This condition produced a steady test time of approximately 2.5 ms and was deemed suitable for the image tracking based thrust measurements. The configuration of the facility to achieve this condition is detailed in Table 4.1. The nozzle exit and stagnation

Table 4.1: The facility configuration for the Mach 8 test condition used in the experiments described in the present study.

Component	Setting	Symbol	Value	Unit
Reservoir	Pressure	p_R	2.6	MPa
Compression Tube	Pressure	p_{CT}	40.2	kPa
	Gas Mixture	-	100 % Ar	-
Primary Diaphragm	Thickness	d_D	3	mm
Shock Tube	Pressure	155	p_{ST}	kPa
Nozzle	Mach Number	M_N	7.6	-

conditions are calculated using the in house code Non-Equilibrium Nozzle Flow reloaded (NENZFr) (Jacobs et al., 2011). It consists of a range of python scripts that combine various codes to calculate the flow properties in the test section from the initial state of the shock tube, the shock speed and the nozzle supply pressure. Equilibrium Shock Tube Calculation junior (ESTCj) (Jacobs et al., 2014) is used to calculate the nozzle supply conditions assuming one dimensional flow and thermal and chemical equilibrium. The shock tube fill pressure and temperature and the measured primary shock speed and nozzle supply pressure are used as the inputs to calculate the conditions after shock reflection. The equilibrium gas properties are calculated using the NASA CEA2 data base (McBride et al., 2002). The post shock reflection conditions are then expanded isentropically to the measured nozzle supply pressure to account for the nozzle starting process. A further expansion to Mach 1 provides the nozzle throat conditions for the nozzle calculation with eilmer3 (Gollan and Jacobs, 2013). For stagnation enthalpies $< 3 \text{ MJ kg}^{-1}$ ESTCj can be used to calculate a good approximation of the flow conditions inside the test section. However, at about 3 MJ kg^{-1} non-equilibrium chemistry, viscous effects and multi dimensional expansion processes become too significant for a one dimensional calculation to be sufficient. Thus, eilmer3's block-marching mode is used to perform an axisymmetric viscous calculation of the nozzle flow.

Since a single run of NENZFr for the Mach 7.6 nozzle can take in excess of 24 h on eight cores of the University of Queensland's Tinaroo cluster and it is useful to know the test flow conditions immediately after a shot, a response surface is created from nine individual NENZFr runs. To account for typical variations, the nominal shock speed is perturbed by $\pm 5\%$ and the nominal nozzle supply pressure by $\pm 15\%$. The properties inside the test section can then be interpolated from the response surface, i.e. a plane fitted to the nine data points. The response surface for the static pressure is displayed in Figure 4.5. As evident, the nine data points coincide almost perfectly with the best fit

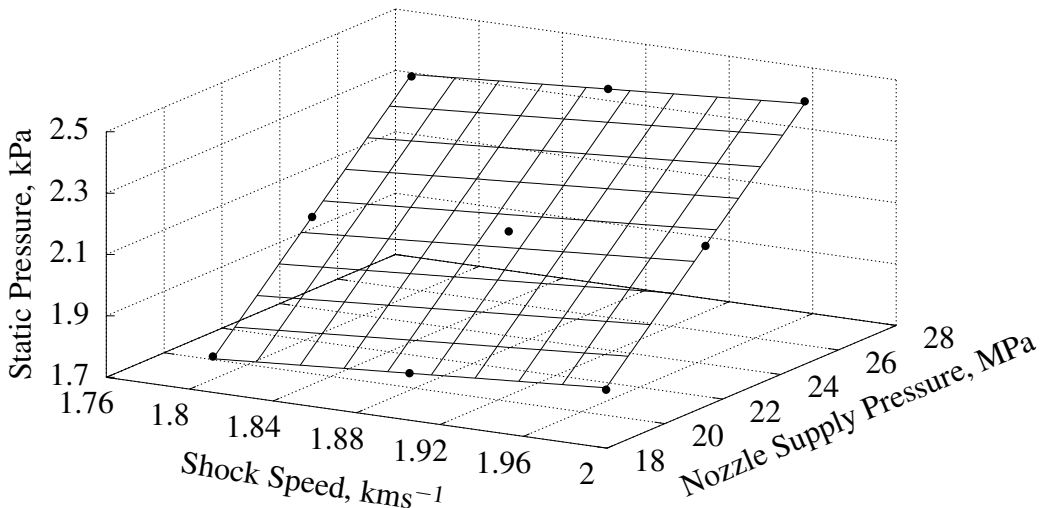


Figure 4.5: The NENZFr response surface for the static pressure inside the T4 test section at the given test condition.

plane. The assumption of linearity over the given range of shock speeds and nozzle supply pressures is therefore warranted.

The average stagnation conditions and primary shock speed from all shots of the experimental campaign are listed in Table 4.2. The uncertainties quoted are the experimental uncertainties for a

Table 4.2: The average stagnation conditions and primary shock speed from all shots of the experimental campaign. The quoted uncertainties are for a single shot.

Property	Symbol	Value	Unit
Nozzle Supply Pressure	p_s	22.1 ± 0.7	MPa
Shock Speed	V_{ss}	1.85 ± 0.10	km s^{-1}
Nozzle Supply Enthalpy	H_s	3.16 ± 0.25	MJ kg^{-1}
Nozzle Supply Temperature	T_s	2829 ± 165	K
Nozzle Supply Density	ρ_s	27.1 ± 1.7	kg m^{-3}

single shot. The calculation of the uncertainties for the derived quantities, i.e. H_s , T_s and ρ_s follows the procedure detailed in Mee (1993). SPA had an uncertainty of 3.2 % and the shock speed was assumed to be accurate to within 5.5 % of the measured value.

The repeatability of the condition is shown in Figure 4.6 by depicting the measured primary shock speeds and nozzle supply pressures of all shots together with their average. It can be seen that the size

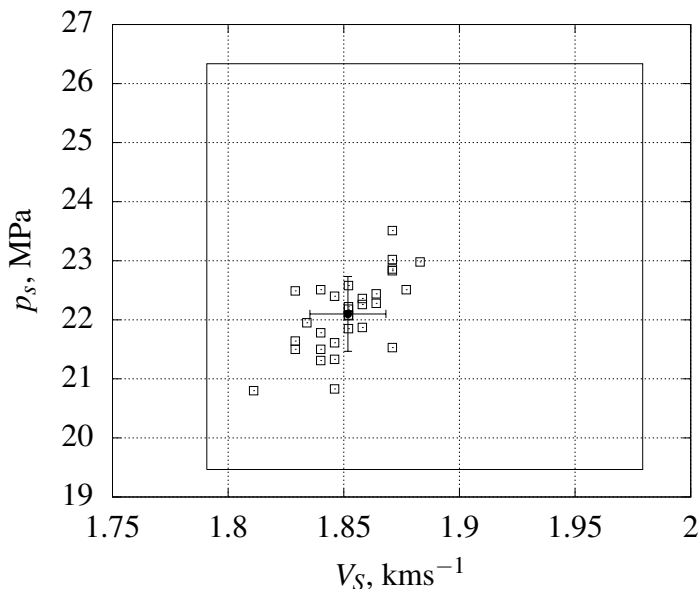


Figure 4.6: The repeatability of the Mach 8 test condition. Each \square symbolises a single shot. The nominal condition with one standard deviation for both shock speed and nozzle supply pressure is indicated by \bullet . The large rectangle designates the extent of the NENZFr response surface created for the condition.

of the NENZFr response surface was sufficient to be used for every shot.

The mean free stream conditions from all shots of the experimental campaign are listed in Table 4.3a. The associated free stream test gas composition and properties are shown in Table 4.3b. The composition is given in the form of species mass fractions. It should be noted that the mass fraction

Table 4.3: The free stream conditions and test gas properties as calculated with NENZFr for the average shock speed and nozzle supply pressure and the nominal shock tube fill conditions. The quoted uncertainties are for a single shot.

(a) The free stream properties.

Property	Value	Unit
M_0	7.56 ± 0.07	-
p_0	2010 ± 80	Pa
T_0	271 ± 23	K
ρ_0	0.0258 ± 0.0017	kg m^{-3}
u_0	2497 ± 82	m s^{-1}
q_0	80.3 ± 7.5	kPa
$Re_{u,0}$	$(3.77 \pm 0.38) \times 10^6$	-
$\rho_0 u_0$	64.3 ± 4.8	$\text{kg s}^{-1} \text{m}^{-2}$

(b) The test gas composition and properties.

Property	Value	Unit
R_0	288 ± 33	$\text{J kg}^{-1} \text{K}^{-1}$
γ_0	1.40 ± 0.16	-
Y_{N_2}	0.756 ± 0.003	-
Y_{O_2}	0.220 ± 0.003	-
Y_{NO}	0.024 ± 0.006	-
Y_{O}	$(0.27 \pm 0.16) \times 10^{-3}$	-

for atomic oxygen, i.e. Y_{O} , is a result of the 5 species gas model, accounting only for N_2 , O_2 , NO, N and O, used by NENZFr (Vanyai, 2018, Section 2.4.5). It was found that a 6 species gas model predicts the formation of NO_2 , which consumes all of the atomic oxygen. CFD simulations of the experiments conducted by Vanyai agreed much better with experimental data when using the 6 species gas model than the simulation results obtained with the 5 species model. Atomic nitrogen, i.e. N, was not predicted by either gas model and is therefore omitted in Table 4.3b.

In order to verify that the nozzle throat was in good working order and to determine the core flow diameter, i.e. the cross-section of the free stream where conditions are approximately constant, a pitot survey was conducted by Dr. Tristan Vanyai. The throats of the T4 nozzles are subject to high mechanical loads as well as impacts from pieces of the primary diaphragm and need replacing periodically. The T4 pitot rake inside the test section is shown in Figure 4.7. The rake can be configured to hold a maximum of 33 PCB® pressure transducers. For the pitot survey presented herein, mea-



Figure 4.7: The T4 pitot rake inside the test section. The end of the Mach 7.6 nozzle can be seen on the left hand side.

surements were taken at 23 locations. It should be noted that a pressure transducer in the free stream will cause a normal shock to form upstream of the sensing surface. Thus, the pressure measured by the pitot probes is that of the stagnated free stream after being processed by a normal shock. Figure 4.8 shows the nozzle exit flow conditions, as calculated by NENZFr, together with the pitot pressure data from shots 12264 and 12269. The good agreement suggests that the nozzle throat was in good condition and a core flow diameter of approximately 90 mm can reasonably be assumed. The deviation at $r > 120$ mm is due to the fact, that NENZFr calculates the flow properties at the nozzle exit plane and the pitot rake was located approximately 150 mm further downstream. Figure 4.9 shows a CAD representation of the Mach 12 REST model inside the T4 test section. The outline of the core flow created by the Mach 7.6 nozzle was determined experimentally (Basore, 2015) and is indicated by

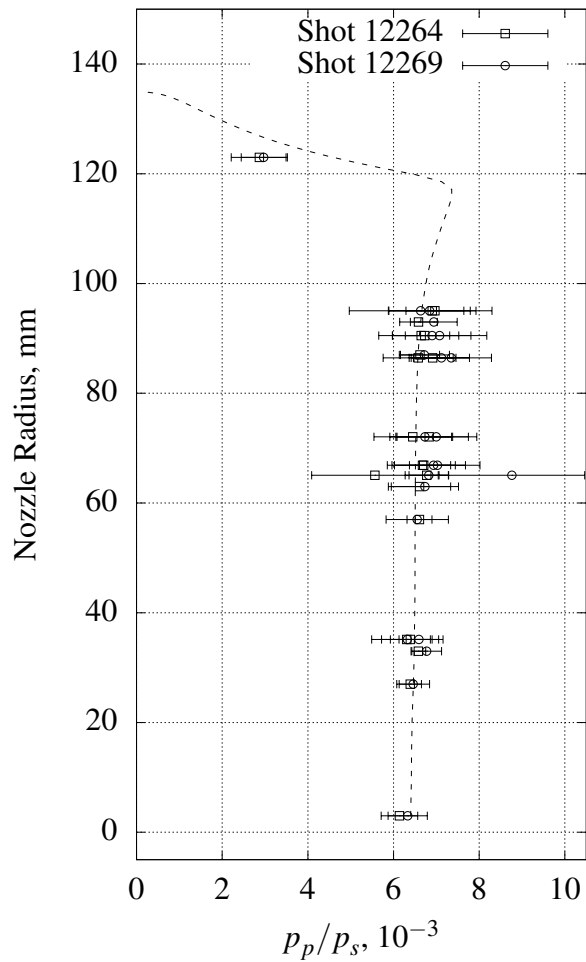


Figure 4.8: A comparison of two pitot survey shots at the Mach 8 condition with the nozzle exit flow, as calculated by NENZFr, (---). The error bars indicate one standard deviation of the average pitot pressure during the test time.

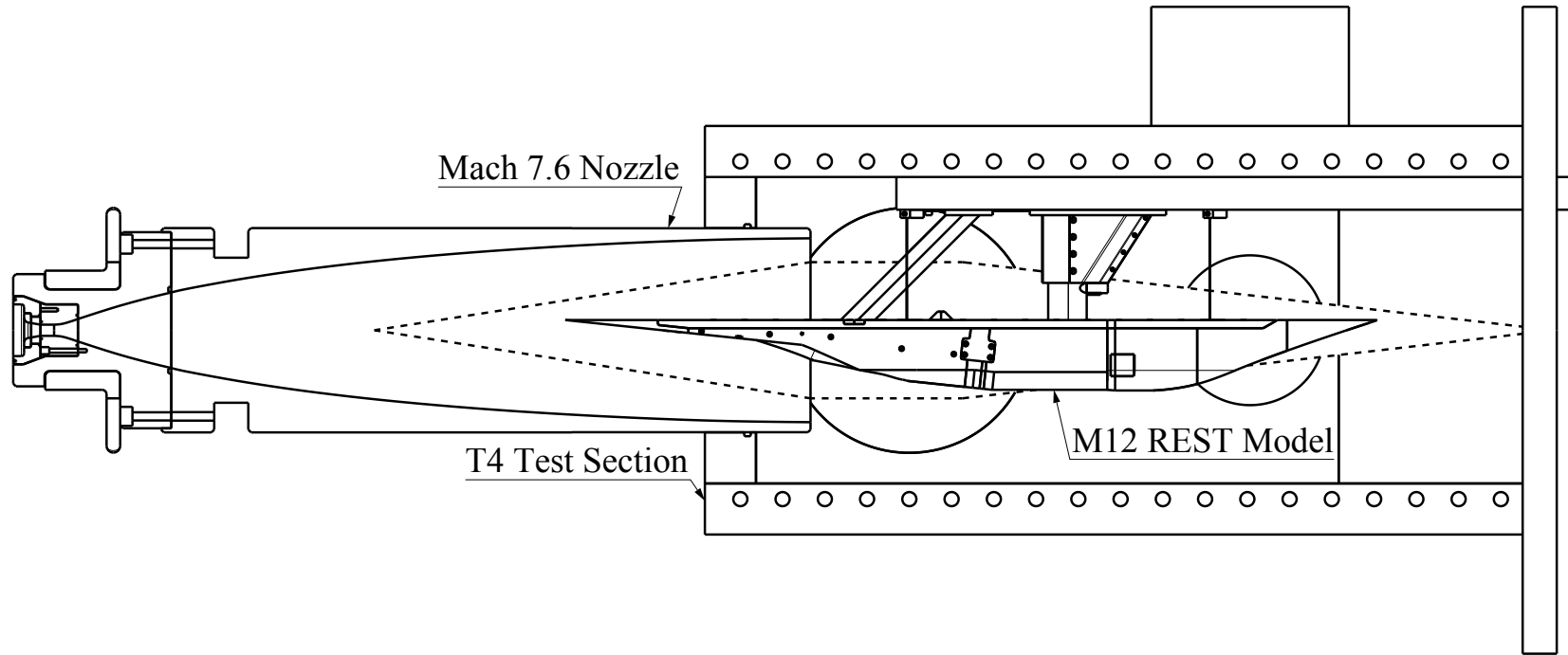


Figure 4.9: A CAD representation of the Mach 12 REST model inside the T4 test section. The extent of the core flow is indicated by ---.

4.1.3 Determination of Test Time

As stated in Section 4.1, the extent of the test time is determined by the steadiness of the nozzle supply pressure. The processes following shock reflection on the secondary diaphragm are as follows: The secondary diaphragm bursts due to the high pressure and temperature of the test gas and flow through the nozzle commences. The unsteady expansion that starts the nozzle flow creates a drop in nozzle supply pressure. Once steady flow is established the nozzle supply pressure remains approximately constant. The test time begins as soon as steady flow is achieved inside the test section and over the full length of the experimental model. For experiments involving combustion, approximately 3.3 flow lengths are commonly used as the time required for steady conditions to establish on the model (Jacobs et al., 1992; East et al., 1980), i.e.

$$t_{fs} = 3.3 \cdot \frac{l}{u_0}, \quad (4.2)$$

where l designates the length of the experimental model. In the present study, it was assumed that, given the small scale of the model, the static pressure measurements are a good indication for the establishment of the core flow as well as the boundary layer. Hence, the model flow was assumed to be steady as soon as the static pressure normalised by the nozzle supply pressure reached an approximately constant value. As stated in Section 4.1, the test flow finishes once the nozzle supply pressure drops below a pre-defined threshold. Generally, $\pm 5\%$ of the average nozzle supply pressure is used as the upper and lower threshold for the test time. In the present study, however, the test time was extended to approximately $\pm 10\%$ of the average. This was done to achieve a longer effective test time and therefore reduce the uncertainty of the mean value of the thrust measurements. In Section 6.2.1 it is demonstrated that the variation of the flow conditions does not significantly affect the measurement of the average thrust during the test time and that the assumption of constant acceleration is justified.

Figure 4.10 shows the normalised signals of four pressure transducers together with the nozzle supply pressure from shot 12224. The time axis of each plot is shifted such that $t = 0\text{s}$ aligns with the reflected shock passing the stag probes. Note that, given the main objective of the experimental campaign was to measure the installed forces on the model, the same test window was used on each transducer rather than accounting for the time delays between individual transducers and tracing a slug of gas through the model. Consequently, the pressure signal from each transducer is normalised by a different part of the nozzle supply pressure signal. The delay in between the forebody sensor and the last sensor in the combustor was approximately 0.469 ms. Therefore, the nozzle supply pressure signal in the time interval from 2 ms to 4.5 ms is used to normalise the signal of the forebody sensor and the interval from 1.531 ms to 4.031 ms is used to normalise the last combustor sensor's signal. It is evident that the normalised pressure traces are all steady at $t = 2\text{ms}$. The pressure in the combustor appears to be increasing towards the end of the test time. This is due to the fact that the fuel mass flow rate was approximately constant over the test time but the nozzle supply pressure decreased. The

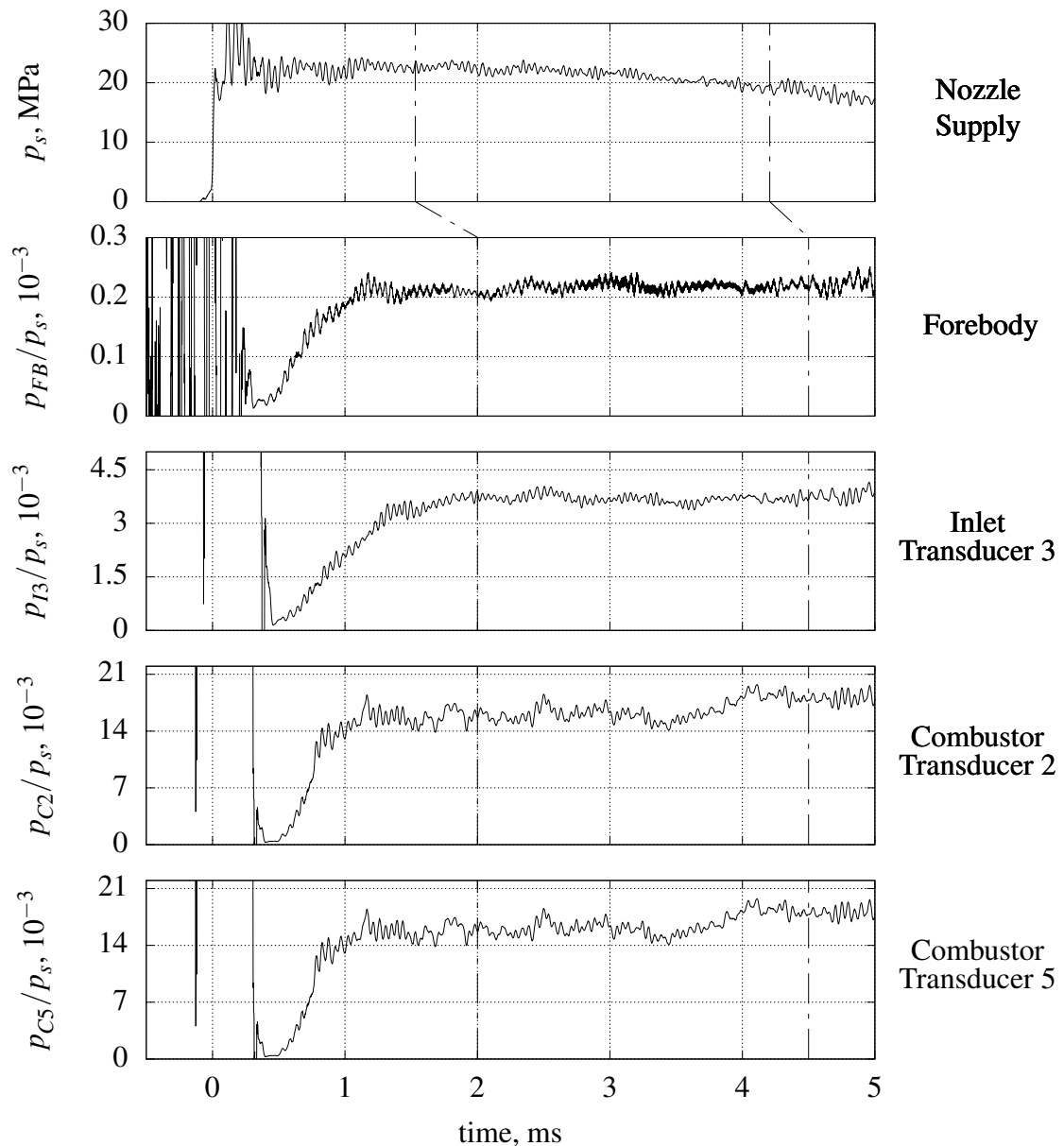


Figure 4.10: Time histories of the nozzle supply pressure and four engine pressure transducer signals normalised by p_s from shot 12224. The test time is indicated by ——. Since the supply pressure is only quasi steady, each transducer has been normalised by a different time interval of the nozzle supply signal.

equivalence ratio therefore increased over the test time and caused the pressure to rise.

4.2 Experimental Model

The experimental model used in the present study was designed and tested by Doherty et al. (2015). It is an airframe integrated and downscaled adaptation of the flowpath developed and tested by Suraweera and Smart (2009). The size of the model was chosen such that it fits into the core flow of

the Mach 10 nozzle of T4. Based on the capture width of the engines of the SPARTAN (Preller and Smart, 2017), the scale of the model is 1/13.5 of a flight scale vehicle. The model was modified to suit the free-flight tests conducted for the present study. It was furthermore fitted with a nozzle designed with the methodology introduced in Chapter 3. In this section, only the manufacturing aspects of the nozzle design are discussed.

A 6° planar forebody with a sharp leading edge is followed by a REST inlet with a design point of Mach 12 and a geometric contraction ratio of 6.61. The inlet has an overall length of 339.8 mm and includes a short isolator downstream of the elliptical throat. The capture width of the inlet is 48mm. Two fuelling stations are used in the model. The first one is located in the inlet, approximately 163 mm downstream of its start. It consists of three portholes of a 1.3 mm diameter, angled at 45° with respect to the local inlet surface. The second fuelling station is located downstream of the isolator. 24 portholes of 0.65 mm are evenly spaced around the circumference of a backward facing step of a height of 0.8 mm. Each porthole is angled at 15° with respect to the axis of the isolator. Following the step injector is an elliptical combustor, which is rotated by 6° with respect to the isolator to realign the flow with the free stream. It consists of a constant area and a divergent section, 103 mm and 77.4 mm in length respectively. The walls of the divergent section are angled at 1.6° with respect to the combustor axis. The area ratio of the combustor exit cross-section to that of the inlet throat is 2.0. This results in an elliptical combustor exit cross section with a major half-axis of 12.9 mm and an aspect ratio of 1.5. Overall, the forebody, inlet and combustor parts have a width of 57.6 mm and a total height of 102.5 mm (Doherty, 2014, Section 3.4.1, Figure 3.8).

The centre of mass of the model with the fuel system and all instrumentation installed is situated 551.5 mm behind and 30 mm below the leading edge. The tracking object was installed 5 mm upstream of the centre of mass of the model and 32.5 mm above it and it has a trapezoidal silhouette. Its edge was blunted to allow for higher precision in the manufacturing process. Generally, a sharp edge is preferable for the technique used in this project. However, difficulties with manufacture and handling of the tracking object required the change to a blunt edge. Figure 4.11 shows the tracking object. The reference point used to define its position is indicated by (x_{TO}, y_{TO}) .

4.2.1 Nozzle

The nozzle was made using a Markforged Mark Two composite material 3D printer. It can print objects of a maximum size of $320 \times 132 \times 154$ mm using onyx, nylon reinforced with short unordered segments of carbon fibre, as a matrix. Various types of fibre, for instance carbon fibre, fibreglass and kevlar fibre, are available for reinforcement of the printed parts. Carbon fibre reinforced parts exhibit a similar flexural modulus, a higher tensile strength and a higher flexural strength when compared to machined Aluminium. Fibreglass reinforced onyx on the other hand has a flexural modulus of about 40 % of that of Aluminium. The tensile strength is larger than that of Aluminium while the flexural

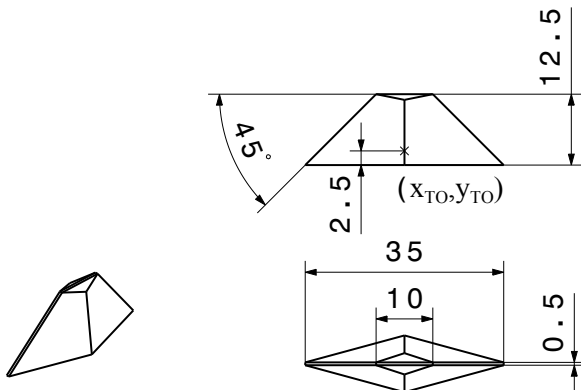


Figure 4.11: The tracking object used to determine the model's motion with the image tracking technique introduced in Chapter 5.

strength is less than half of that of Aluminium. The nozzle part has a total length of 393 mm. In order for the printer to be able to print the trailing edges of the nozzle, where the wall thickness is $\ll 1$ mm, the part had to be wider and taller than the other parts. Thus, the nozzle part has a total width of 58.6 mm and a total height of 103.5 mm. With the new nozzle the model is 1187 mm long.

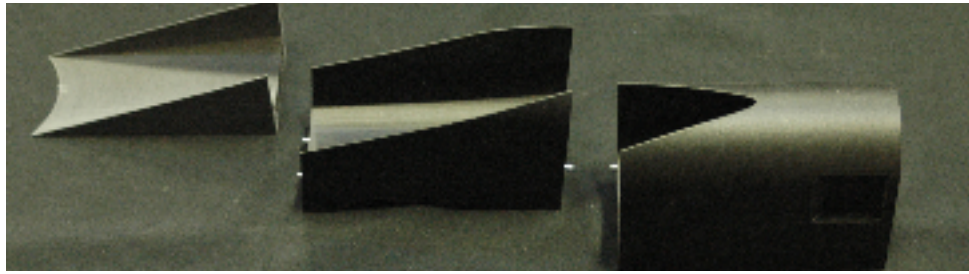
Due to the size constraints given by the print bed and to be able to investigate the contribution of the tail end of the nozzle to the overall thrust, it was manufactured in three parts. The first part was reinforced with carbon fibre, the second and third part using fibreglass. Given that the first section of the nozzle experiences the highest heat and structural loads, the higher cost of the carbon fibre was warranted. Fibreglass was deemed sufficiently strong for the other two parts. Figure 4.12 shows the three nozzle parts and, for comparison, the old aluminium nozzle of the Mach 12 REST scramjet next to the assembled shape transition nozzle. McMaster-Carr® tapered heat-set brass inserts were used to add threads to the printed parts. In Figure 4.13 the second nozzle part is shown with one brass insert already installed and a second one positioned for installation. The complete model with the newly designed shape transition nozzle is displayed in Figure 4.14.

4.2.2 Catch and Release Mechanisms

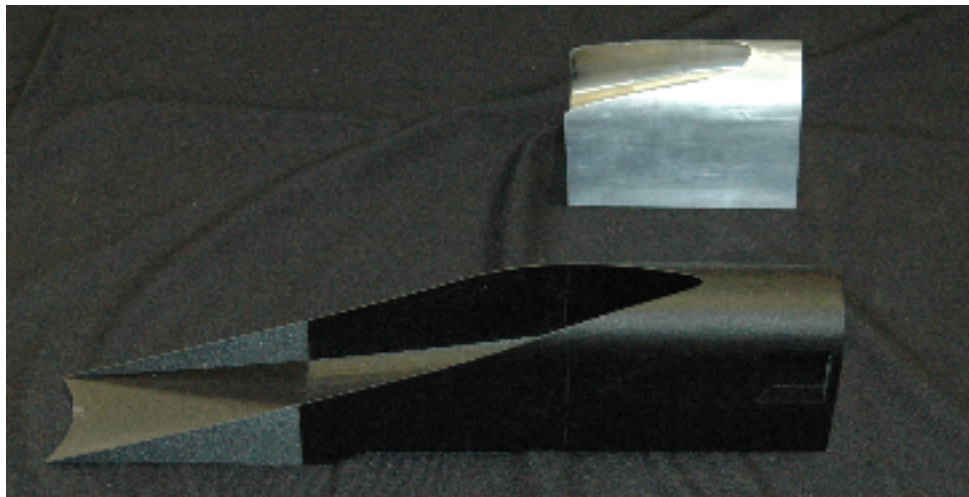
For free-flying experiments to be possible a number of requirements must be met:

1. a release mechanism has to ensure that the model is unrestrained during the test time.
2. The fuel system and transducer cables must not interfere with the motion of the model and have to be shielded from the free stream.
3. The model has to be caught after the test flow ends.

As described in the introduction to this chapter, point one is met by initially suspending the model on two strands of fishing line. Razor blades installed on the model cut the strands as they are pushed



(a) The individual parts of the shape transition nozzle.



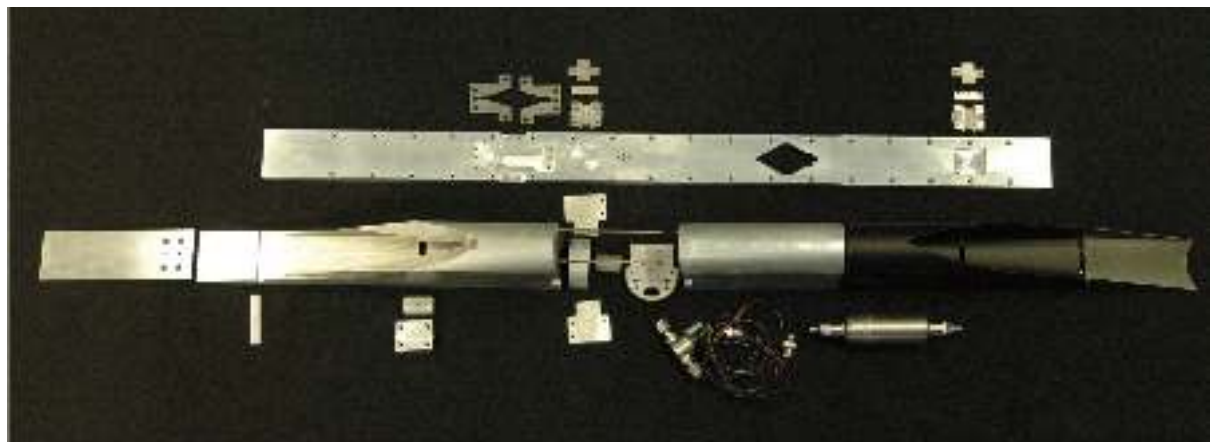
(b) The assembled nozzle in comparison with the one designed by Doherty.

Figure 4.12: Photographs of the 3D printed shape transition nozzle.



Figure 4.13: The middle part of the shape transition nozzle during the installation of the heat-set brass thread inserts.

downstream by the test gas. Figure 4.15 displays a partially exploded CAD representation of the Mach 12 REST model with the catch and release mechanisms.



(a) The individual parts of the complete Mach 12 REST model.



(b) The assembled Mach 12 REST model.

Figure 4.14: Photographs of the Mach 12 REST model.

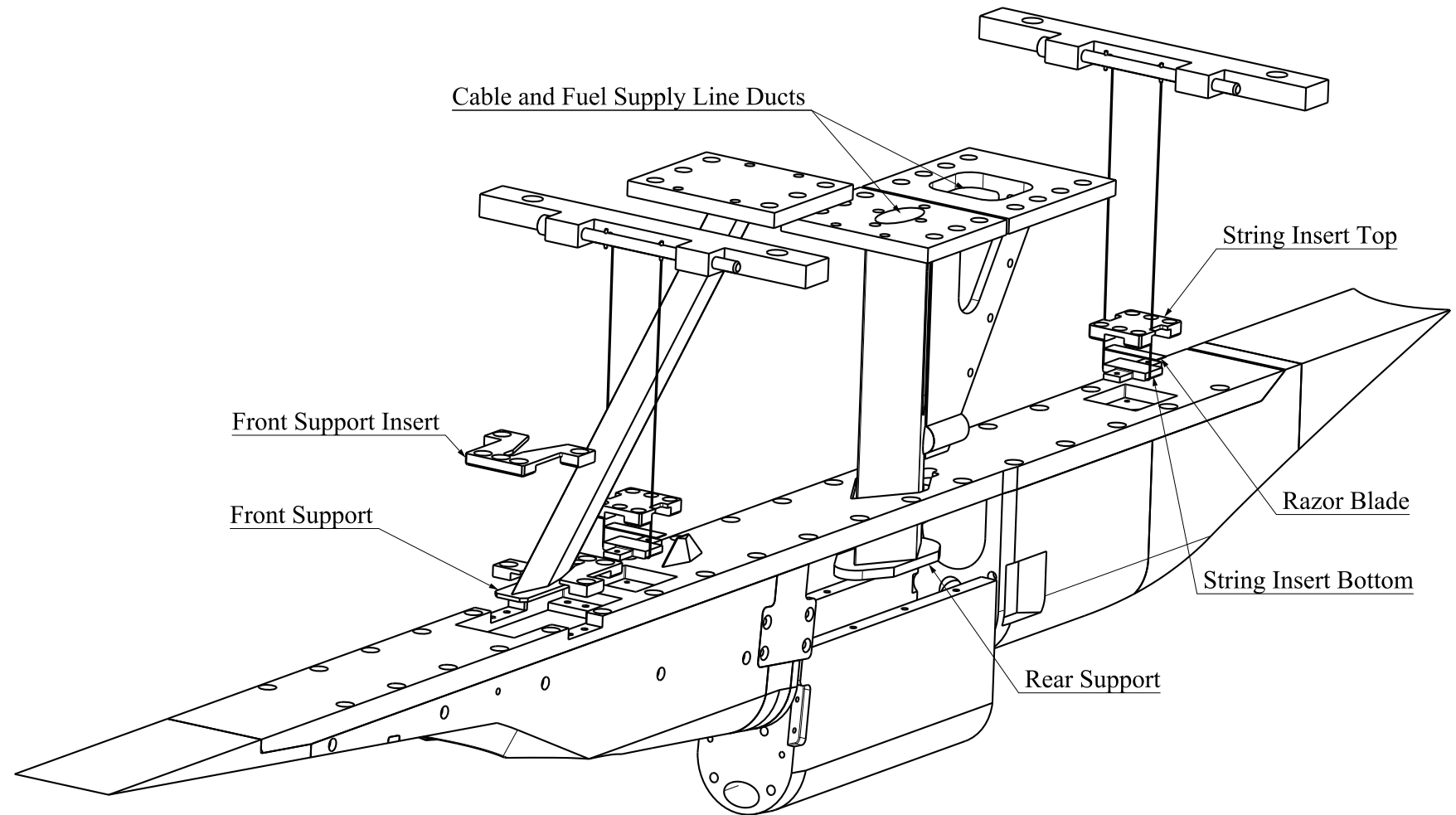


Figure 4.15: A partially exploded CAD representation of the Mach 12 REST model with focus on the catch and release mechanisms. The leading edge of the model is in the bottom left corner, the direction of flow is from bottom left to top right.

Before a shot, each strand of fishing line was wound up such that the top of the model was horizontal. The razor blade was clamped in between the top and bottom of the string insert. The fishing line wrapped around the bottom. It was determined experimentally that both strands of fishing line consistently break before the start of the test time (at $t < 2\text{ ms}$).

The catching mechanism consists of the front and the rear support. They are designed such that there are 3 mm of clearance for motion in the vertical and the streamwise direction. For lateral motion 2 mm of clearance were deemed sufficient.

In addition to catching the model, the rear support serves to shield the transducer and solenoid cables and the fuel supply line as shown in Figure 4.16.

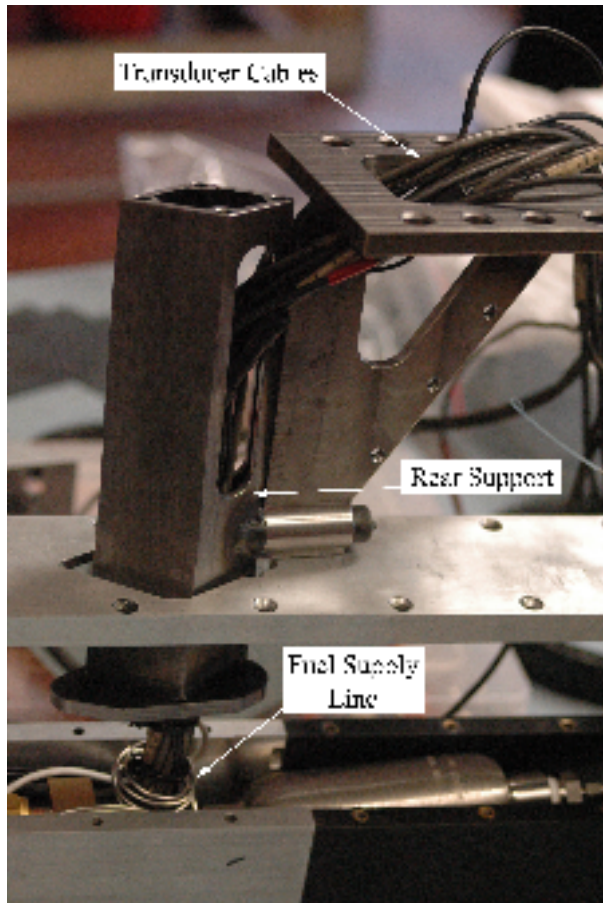


Figure 4.16: The rear support of the experimental model.

4.2.3 Instrumentation

Nine Kulite® piezoresistive pressure transducers were installed along the flowpath. An additional Kulite® was used to measure the pressure in each fuel plenum respectively. Figure 4.17 shows a cut through the symmetry plane of the Mach 12 REST model. Transducer locations are indicated by labels P1 through P9 and FP1 and FP2 for the fuel plenum sensors.

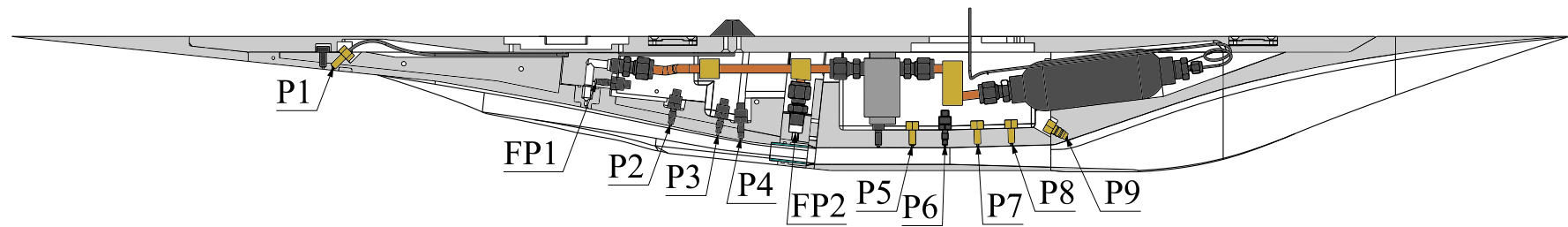


Figure 4.17: A cut through the symmetry plane of the Mach 12 REST engine. Pressure transducers in the engine flowpath are labeled P1 through P9. The fuel plenum pressure transducers are designated FP1 and FP2.

The forebody and nozzle pressure, P1 and P9, were measured using model XCEL-100 miniature Kulite® transducers with a measurement range of 5 psi . Three model XTEL-190S Kulite® transducers with a range of 25 psi were installed in the inlet. The combustor pressure was measured using transducers with a range of 100 psi. Model XCEL-100 was used for transducers P5, P7 and P8; model XTEL-190S at location P6. The fuel plenum pressures were measured with model XTEL-190S transducers with a 500 psi (FP1) and a 600 psi (FP2) measurement range. Note that the presented configuration only allows for four pressure transducers to be installed in the combustor instead of five (compare Doherty, 2014, Section 3.4.4). The fifth transducer location, upstream of P5, was obstructed by the solenoid valve of the on-board fuel system. Hence, it was sealed to avoid flow leakage.

4.2.4 Fuel System

The design of the fuel system was constrained by the requirement of the model to be unrestrained during the test time. Fuel lines with a large enough internal diameter to provide a sufficient fuel mass flow rate to the fuel plenums were too rigid to be used in the present study. It was thus necessary to install a fuel tank and a solenoid valve on-board the Mach 12 REST engine. Figure 4.18 shows a schematic of the fuel system used in the experiments described in the present study. Before a shot, the on-board fuel tank was filled to the desired pressure with hydrogen and the manual isolation valve closed. The fuel valve was then triggered by the facility recoil such that the fuel plenum pressures were approximately constant during the test time. Swagelok® 1/16” stainless steel tube was used for the fuel supply line connecting the on-board tank to the test section wall. It was formed into a coil in several locations to reduce its stiffness. Through the rear support, the fuel line was directed into the model and to the on-board fuel tank. A section of the fuel supply line can be seen in Figure 4.19. Downstream of the tank, Swagelok® 1/4” copper tubing connected the fuel supply to a solenoid valve, three brass manifolds and the fuel plenums. The fuel valve was a Gems™ A2014 solenoid valve. The brass manifolds were used instead of standard Swagelok® fittings to account for the space constraints of the experimental model. Downstream of the solenoid valve, the fuel mass flow was split in two to supply both fuel plenums. The configuration presented here created a fuel split of approximately 40/60 by fuel mass flow rate between the inlet and the combustor plenum. Photographs of the fuel system before and after being installed on the model are shown in Figure 4.20.

Calibration

In order to evaluate the performance of a scramjet engine, it is important to calculate the fuel equivalence ratio during an experiment. Assuming sonic conditions at the injector holes and quasi-steady

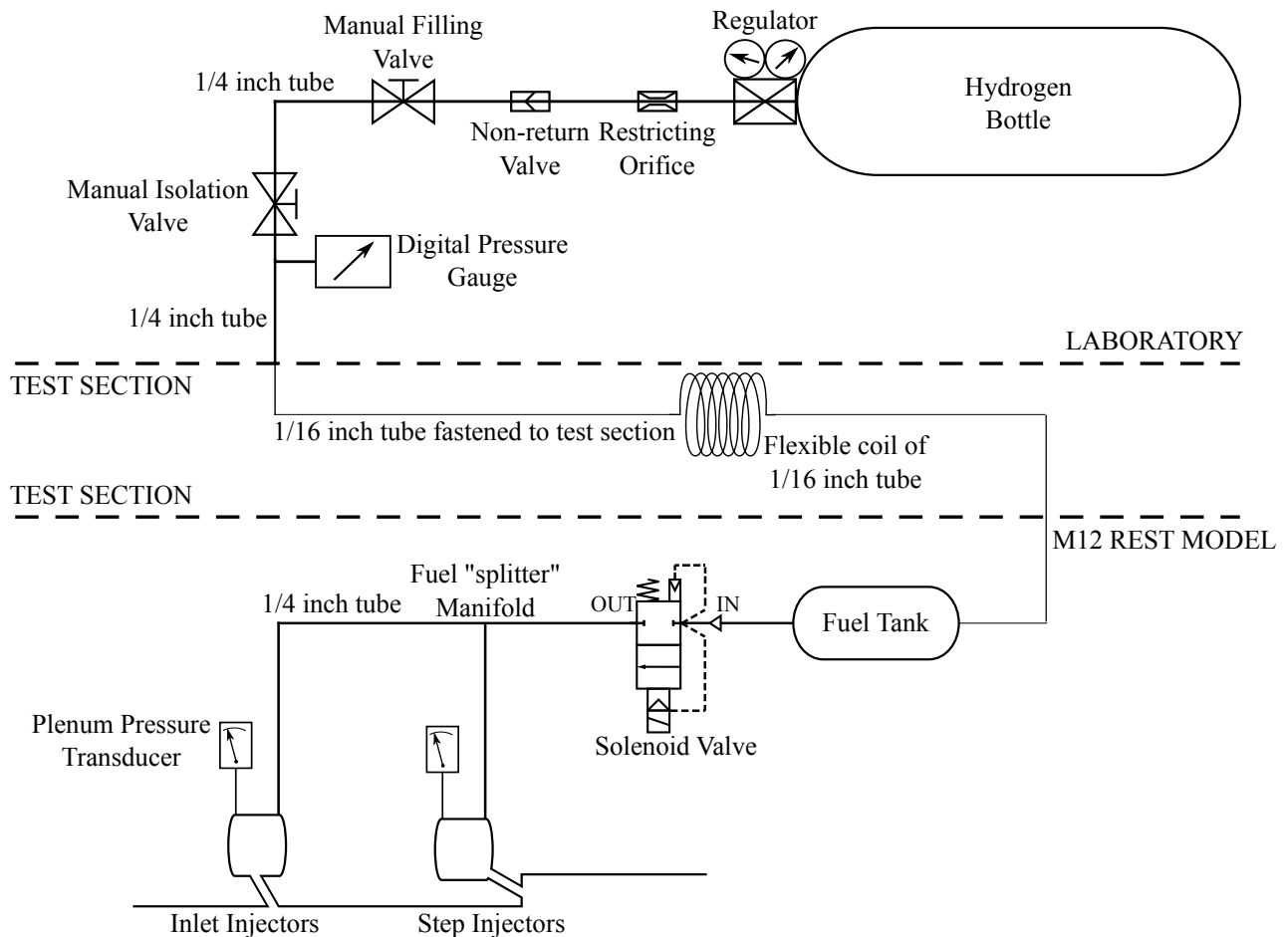


Figure 4.18: A Schematic of the fuel system used in the experiments described in the present study. The graphic was adapted from Doherty (2014).

pressure in the plenums, the fuel mass flow rate can be calculated as

$$\dot{m}_{H2} = \sqrt{\frac{\gamma}{RT} \left(\frac{2}{\gamma+1} \right)^{\frac{\gamma+1}{\gamma-1}} \cdot (C_{d,IP} A_{IP} p_{IP} + C_{d,CP} A_{CP} p_{CP})}. \quad (4.3)$$

Here, $C_{d,IP}$ and $C_{d,CP}$ designate the discharge coefficients of the inlet and the combustor plenum respectively. A_{IP} and A_{CP} respectively indicate the cross-sectional area of the inlet and the combustor injectors. The quasi stagnated pressure in either plenum is denominated p_{IP} and p_{CP} , respectively. Razzaqi et al. (2014) found that the static temperature inside the fuel plenums is commonly equal to room temperature despite the expansion from the fuel tank.

The discharge coefficients have to be determined by calibrating each set of injectors individually. However, due to the complexity of assembling the Mach 12 REST model, only the combustor plenum was calibrated individually. The discharge coefficient of the inlet plenum was then calculated from a simultaneous calibration of both plenums.



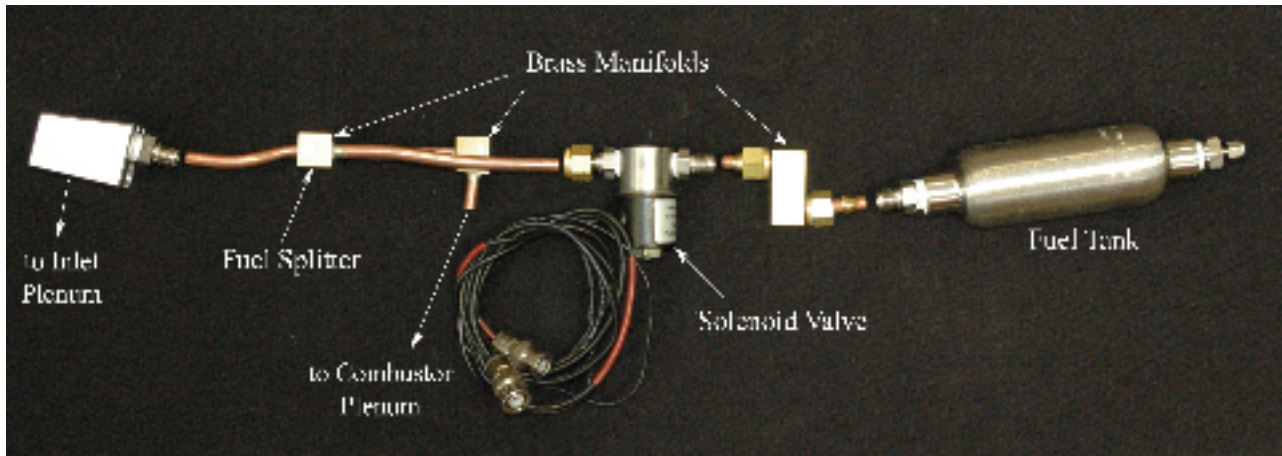
Figure 4.19: A part of the Swagelok® 1/16 " fuel supply line in the T4 test section.

To calibrate the fuel system, first its volume must be determined. For this purpose a 1 l Swagelok® sample cylinder was connected to the fuel system upstream of the manual filling valve, replacing the hydrogen bottle (compare Figure 4.18). The setup can be seen in Figure 4.21. Two additional valves were installed to be able to isolate the sample cylinder from the inert calibration gas and the fuel system. The combined volume of the sample cylinder and the attached flexible fuel lines was measured first by filling it with distilled water and weighing the added mass. Once connected to the fuel system, the sample cylinder was filled with Helium. The pressure was measured using a GE™ Unik 5000 pressure transducer. The fuel system was then filled section by section from the sample cylinder, recording the pressure after opening each valve. Sufficient time was allowed for the temperature to settle to a steady value.

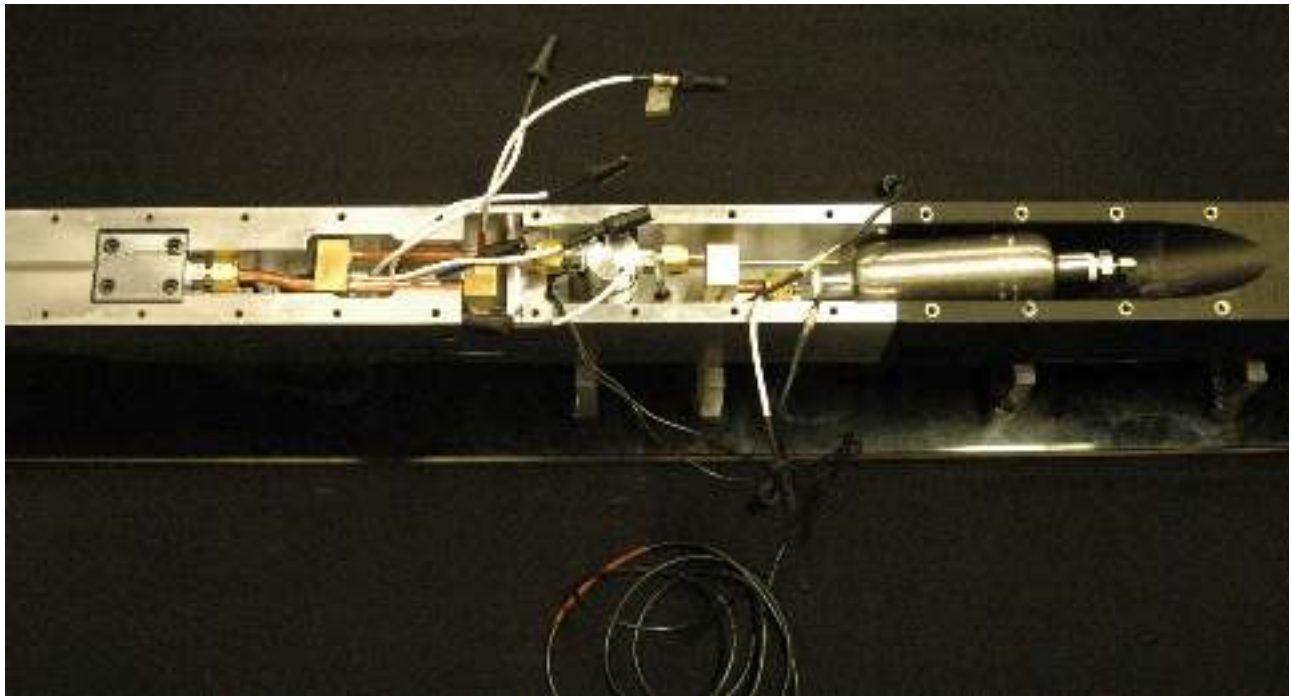
With the volume known, the total mass of fuel discharged during a calibration can be calculated from the ideal gas law. The discharge coefficient can then be calculated by integrating and rearranging equation (4.3). Table 4.4 lists the properties thus determined.

Table 4.4: The properties of the Mach 12 REST on-board fuel system.

Property	Symbol	Value	Unit
Volume	V_{FS}	151 ± 4	ml
Inlet Injectors Discharge Coefficient	$C_{d,IP}$	0.477 ± 0.015	-
Combustor Injectors Discharge Coefficient	$C_{d,CP}$	0.594 ± 0.010	-



(a) The components of the on-board fuel system.



(b) The fuel system installed on-board the Mach 12 REST model.

Figure 4.20: Photographs of the Mach 12 REST on-board fuel system.

4.3 Motion Tracking Apparatus

This section introduces the optical setup used to track the motion of the Mach 12 REST scramjet. It consisted of six components: the LED driver, a Thorlabs 100 mm focal length lens with an achromatic coating, a planar mirror, a spherical mirror, a combination of three Thorlabs lenses with achromatic coating to focus the image onto the camera sensor and a Phantom® v611 high speed camera. It forms one half of a Z-type Schlieren setup, i.e. the light beam was collimated by the spherical mirror but rather than being decollimated by a second spherical mirror after passing through the test section it was directly focussed onto the camera sensor. A schematic of the optical setup is shown in Figure

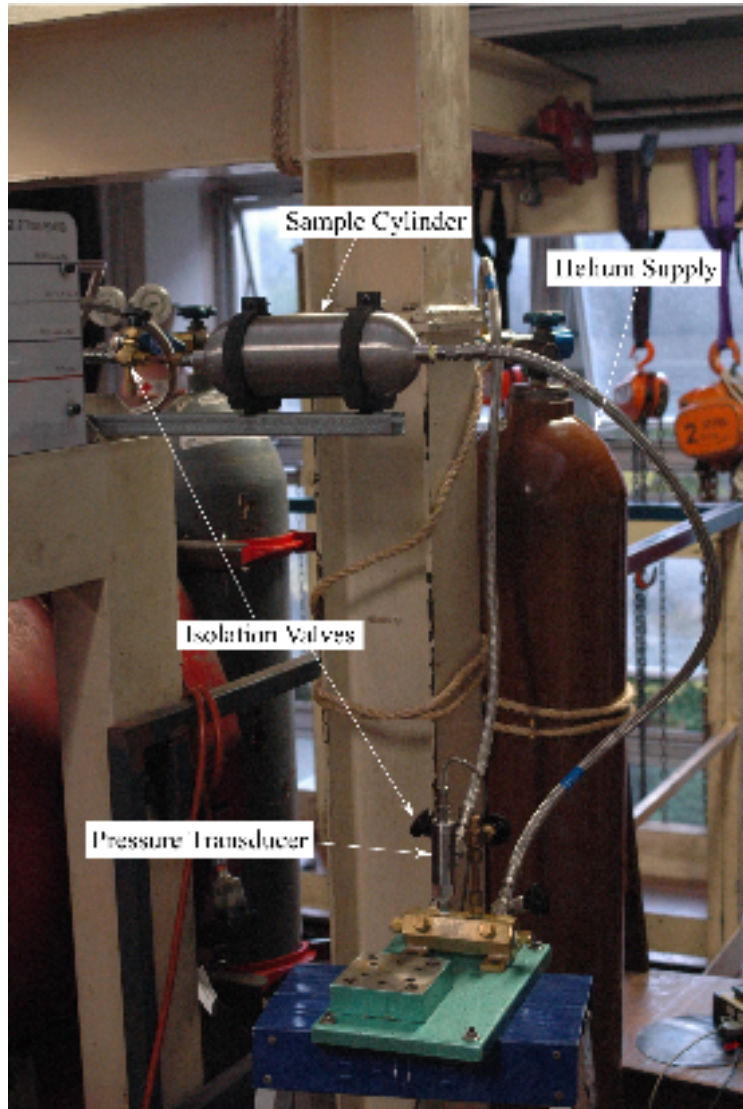


Figure 4.21: The sample cylinder, gas supply and instrumentation used to measure the fuel system volume.

4.22.

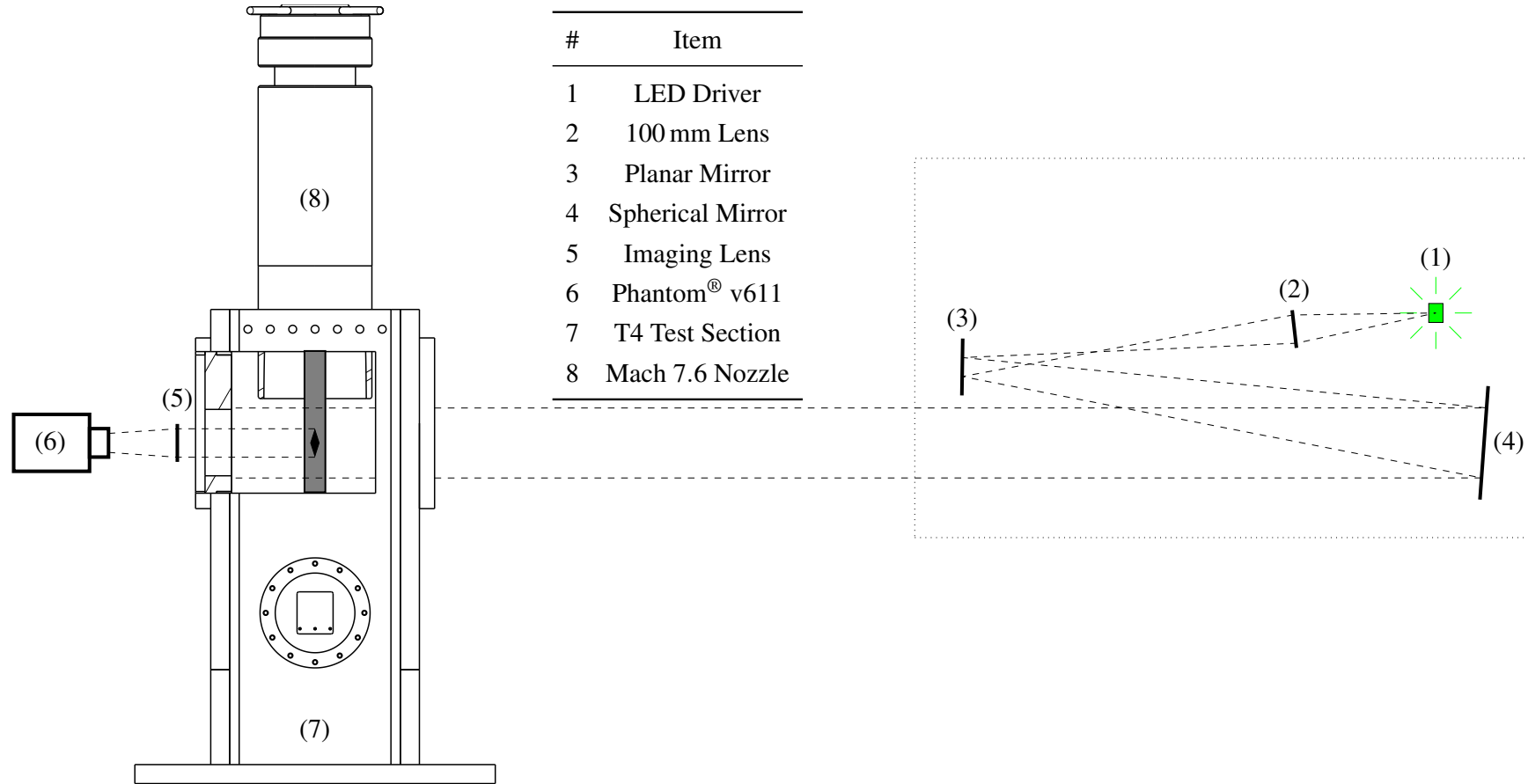


Figure 4.22: A schematic of the optical setup used for tracking the motion of the Mach 12 REST engine. ----- indicates the light path.

The LED driver is an in-house design of Mr. Barry Allsop. It uses a green PhlatLight™ PT121 projection chipset LED and can be run in either continuous or a variety of pulsed modes. The pulsed modes are designed to be used in conjunction with the high speed cameras currently in use at the Centre for Hypersonics; a Phantom® v611 and a Shimadzu HPV-1.

Table 4.5 lists the different modes that are available with the LED driver. The purpose of the

Table 4.5: List of the modes the LED driver can be run in.

Mode #	Operation	# of Flashes	Flash Length, μs	Flash Period, μs	I_{max}, A	U_{nom}, V
1	Continuous	-	-	-	17	5.75
2	Pulsed	1	1000	-	38	8
3	Pulsed	1	300	-	75	11.5
4	Pulsed	100	2	4	70	11
5	Pulsed	100	2	8	97	13.3
6	Pulsed	100	2	16	135	16.5
7	Pulsed	100	2	50	135	16.5
8	Pulsed	100	2	150	135	16.5

100 mm lens was to increase the intensity of the light that illuminates the tracking object. Before the light beam is collimated, its intensity is proportional to $1/r^2$. By refocussing the light beam with an appropriate lens, the divergence angle of the beam could be reduced and the intensity increased. The spherical mirror then collimated the light beam and reflected it towards the test section. This part of the apparatus is referred to as the source side and the components are shown in Figure 4.23. The remaining components are referred to as the image side. It consisted of the imaging lens and the Phantom® v611 high speed camera. The Phantom® v611 is capable of recording 12 bit images at resolutions ranging from 128×8 px to 1280×800 px. The maximum recording frequency (frame rate) is dependent on the resolution. At the minimal resolution the maximum frame rate is 1000000 s^{-1} . Exposure times as low as $0.3 \mu\text{s}$ are possible. For the experiments described here, the camera was set to a resolution of 512×160 px, a frame rate of 66225 s^{-1} and an exposure time of $0.3 \mu\text{s}$. Both the imaging lens and the camera were mounted on an aluminium frame, which was bolted to the test section. In order to isolate the optics from vibrations of the facility, two Mackay Industrial M10202555 Multicushions and a M12201855 Multibuffer were installed in between the test section and the aluminium frame. The components of the image side are shown in Figure 4.24.



(a) The LED driver and the 100 mm lens.

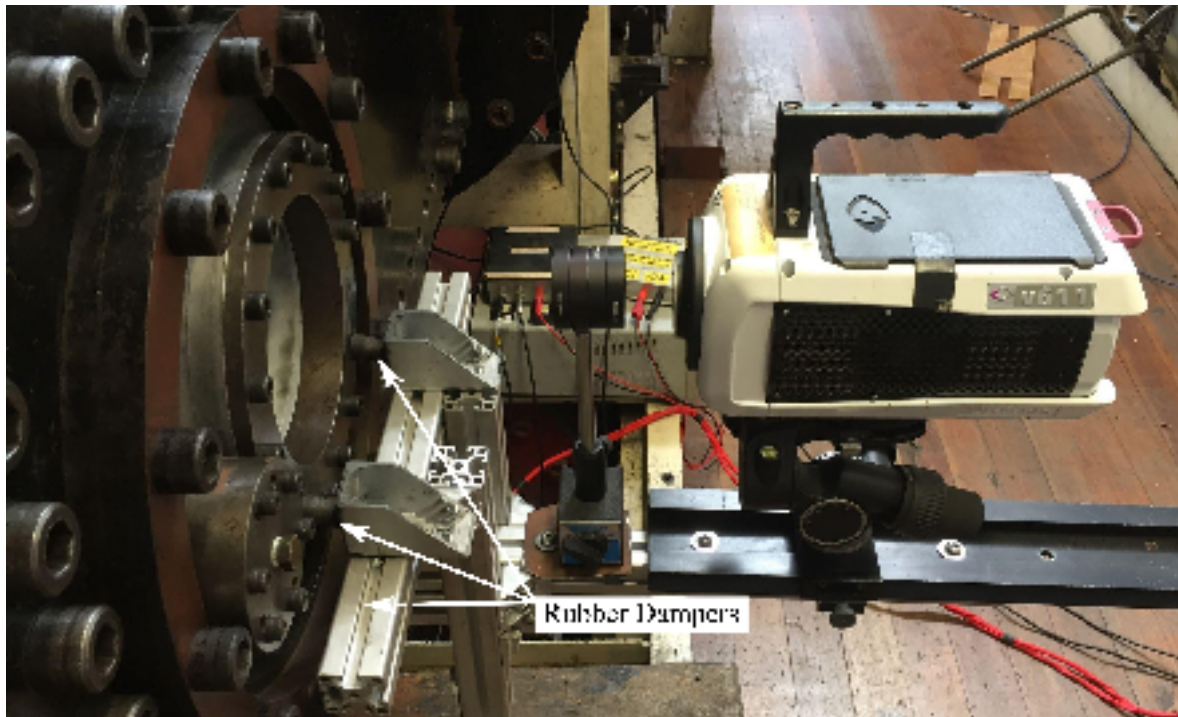


(b) The planar mirror.



(c) The spherical mirror.

Figure 4.23: Photographs of the source side components of the optical apparatus.



(a) The camera and the imaging lens on the aluminium frame that is mounted on the test section.



(b) A close-up view of the Multibuffer.



(c) The three rubber dampers, two Multi-cushions with the custom made M10 studs and a Multibuffer.

Figure 4.24: Photographs of the image side components of the optical apparatus.

CHAPTER 5

IMAGE TRACKING BASED FORCE MEASUREMENT TECHNIQUE

This chapter introduces the force measurement technique used in the experimental analysis part of the present study. A few general remarks are followed by a detailed explanation of the technique and its limitations. The last part details the calibration of the apparatus discussed in Section 4.3.

Image tracking based force measurements are characterised by recording an image sequence of a free-flying or weakly restrained model in a wind tunnel. The images are then used to track the motion of the experimental model. Trajectories in the streamwise (x) and the vertical direction (y) as well as a rotational trajectory about the z -axis, i.e. the pitch angle (α), with respect to time are calculated by comparing the position of the model in subsequent images. Assuming constant acceleration during the steady test time, quadratic polynomials are fitted to the trajectories. Thrust and lift forces and the pitching moment can then be calculated as:

$$T = m \cdot a_x = m \cdot 2 \cdot C_{x,1}, \quad (5.1)$$

$$L = m \cdot a_y = m \cdot 2 \cdot C_{y,1} \quad \text{and} \quad (5.2)$$

$$M_z = I_z \cdot a_\alpha = I_z \cdot 2 \cdot C_{\alpha,1}, \quad (5.3)$$

respectively. $C_{x,1}$ designates the first coefficient in the quadratic polynomial that has been fitted to the trajectory in x , i.e.

$$x_{fit}(t) = C_{x,1} \cdot t^2 + C_{x,2} \cdot t + C_{x,3}. \quad (5.4)$$

5.1 Edge Detection with Sub-Pixel Accuracy

In order to determine the location of the model, the edge of the tracking object has to be found in each image. This is achieved in a two step process:

1. detect the edge with pixel level accuracy, i.e. find every pixel that the edge crosses.
2. Improve the accuracy of the edge position with a sub-pixel edge detection routine.

A Canny edge detection algorithm (Canny, 1986) is used for step one. To reduce the influence of noise, it employs a Gaussian blur filter which recalculates the intensity of every pixel based on a weighted average of its neighbours' intensity first. In a second step the intensity gradients in both the vertical and the horizontal direction are calculated for each pixel. Additionally, the orientation of the edge is calculated from the gradients. Where multiple non-zero gradients are encountered in adjacent pixels, i.e. the edge is blurred across a few pixels, the pixel containing the local gradient maximum is chosen as the one containing the edge. To further eliminate noise effects, edge pixels are split into three categories: strong edge pixels, weak edge pixels and suppressed edge pixels. The categories are defined by user-defined intensity gradient thresholds, that need to be chosen empirically. Where the intensity gradient is smaller than the lower threshold the edge is suppressed, that is, the edge pixel is disregarded. Strong edge pixels are assumed to always indicate true edges whereas weak edge pixels can result from noise as well as true edges. To determine whether a weak edge pixel is part of a true edge, a check is carried out to ascertain that it is connected to a strong edge pixel. If none of the eight adjacent pixels are a strong edge pixel the weak edge pixel is suppressed.

The intensity of a pixel is the sum of all light that it registers during the exposure time of the camera sensor. In a black and white image the intensity is translated into a shade of gray, where an intensity value of 0 corresponds to a black pixel and maximum intensity corresponds to a white one. Pixels that are partially covered by an object receive a shade of gray corresponding to the fraction of the total pixel area that is covered. Consider for instance the image shown in Figure 5.1. Evidently, the illuminated region (top and left) is not uniform. Where the tracking object blocks light from reaching the camera sensor the image appears to be uniformly black. However, that area is also subject to noise and the intensity values vary from pixel to pixel. The Phantom® v611 has a 12 bit sensor with a noise level of approximately 1 % of the maximum pixel intensity, i.e. the standard deviation of all black pixel intensities in Figure 5.1 is $0.01 \cdot I_{max} = 41$, with $I_{max} = 2^{12}$, assuming no other sources of error. The edge appears to be blurred across two to three pixels and there are pixels in the illuminated part of the image that are considerably darker than the average. In shock tunnel experiments it is near impossible to avoid all contamination of the test gas and particles appearing in the image must be expected. The Gaussian blur filter removes noise and small artifacts from the image. As stated above, each pixel's intensity is recalculated using a weighted average of the surrounding pixels. Since images are two dimensional, the weights are determined using a Gaussian surface; a Gaussian bell curve that

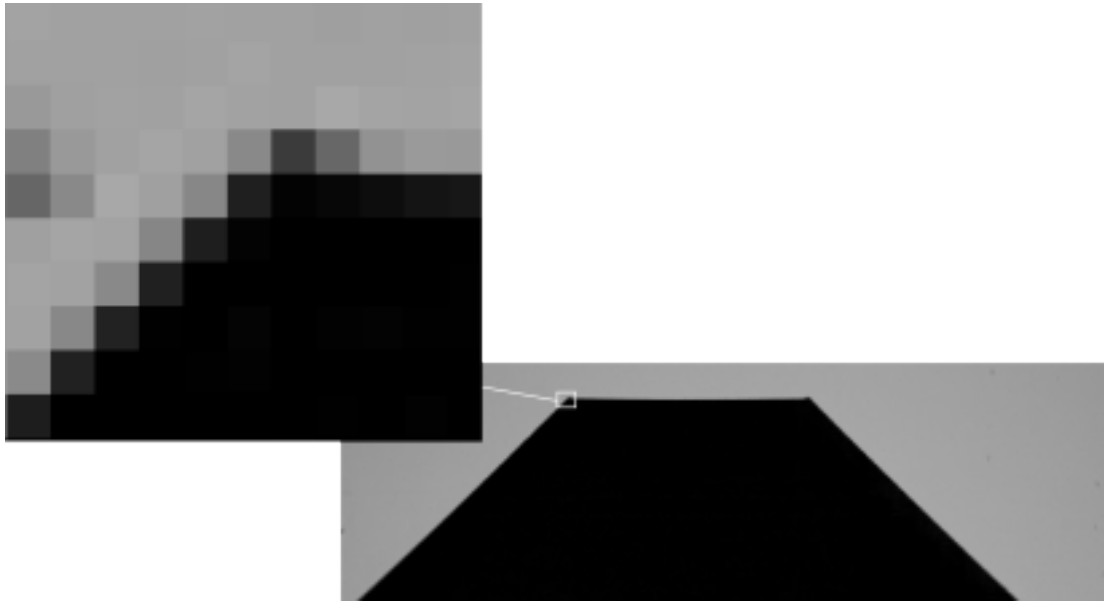


Figure 5.1: The first image in the image series of shot 12235 with a close-up of the edge of the tracking object.

is revolved about its origin. It has its maximum at the origin, i.e. at the pixel whose intensity is being recalculated, and its contours are concentric circles around the origin. For a Gaussian blur filter of size 5×5 px the weights can be calculated according to

$$H_{ij} = \frac{1}{2\pi\sigma_G^2} \cdot \exp\left(-\frac{(i-3)^2 + (j-3)^2}{2\sigma_G^2}\right); 1 \leq i, j \leq 5. \quad (5.5)$$

σ_G denotes the standard deviation of the Gaussian surface. For the images analysed in the present study $\sigma_G = 1$ was found to be appropriate. i and j respectively designate the horizontal and vertical image coordinate. With the weights calculated, the image can be smoothed using a convolution operation:

$$\mathbf{I}_s = H_{ij} * \mathbf{I}. \quad (5.6)$$

\mathbf{I} denotes the matrix containing the pixel intensities of the original image and \mathbf{I}_s designates the intensity matrix of the smoothed image.

In the next step, the intensity gradients of the smoothed image in i and j are calculated separately using the Sobel operator:

$$\frac{\partial \mathbf{I}_s}{\partial i} = \begin{bmatrix} -1 & 0 & 1 \\ -2 & 0 & 2 \\ -1 & 0 & 1 \end{bmatrix} * \mathbf{I}_s \quad \text{and} \quad (5.7)$$

$$\frac{\partial \mathbf{I}_s}{\partial j} = \begin{bmatrix} -1 & -2 & -1 \\ 0 & 0 & 0 \\ 1 & 2 & 1 \end{bmatrix} * \mathbf{I}_s. \quad (5.8)$$

Edge angles and the total edge gradient can easily be derived from the vertical and horizontal gradients, i.e.

$$\Theta = \arctan \left(\frac{\partial \mathbf{I}_s}{\partial j} \cdot \left(\frac{\partial \mathbf{I}_s}{\partial i} \right)^{-1} \right) \quad \text{and} \quad (5.9)$$

$$\mathbf{G}_e = \sqrt{\frac{\partial \mathbf{I}_s^2}{\partial i} + \frac{\partial \mathbf{I}_s^2}{\partial j}}. \quad (5.10)$$

Once all gradients and edge directions have been calculated the above steps can be carried out to detect the edge to an accuracy of one pixel.

To further refine the edge location, Laurence and Karl (2010) have introduced sub-pixel accuracy edge detection. Using the gradient matrix calculated with the Canny edge detector, the distance of the true edge to the centre of a pixel can be calculated by fitting a quadratic polynomial to the pixel containing the edge and the two adjacent pixels normal to the edge and finding its maximum. For vertical and horizontal edges this yields

$$d_s = 0.5 \cdot \frac{G^+ - G^-}{G^+ - 2G_0 + G^-}. \quad (5.11)$$

Here, G^+ and G^- designate the intensity gradient of the adjacent pixels and G_0 the intensity gradient of the pixel containing the edge. For diagonal edges, however, the intensity of a pixel does not change linearly but quadratically with a change in position, i.e.

$$\Delta I \propto \Delta s^2 + 2 \cdot (\sin(45^\circ) \cdot w_{px} - d_{s,0}) \cdot \Delta s. \quad (5.12)$$

Δs is an incremental change in position normal to the edge, w_{px} designates the width of a pixel and $d_{s,0}$ is the distance from the center of the pixel to the edge before the change in position. The following correction is hence applied to diagonal edges:

$$d_{s,diag} = f \cdot d_s^* + (1 - f) \cdot d_s, \quad (5.13)$$

where

$$d_s^* = \text{sgn}(d_s) \cdot (0.5 - 2(|d_s| - 0.5)^2), \quad (5.14)$$

$$f = \frac{1}{0.7} \cdot \frac{G_0 - 0.5(G^+ + G^-)}{G_0} \quad (5.15)$$

and $\text{sgn}(x)$ designates the signum function, i.e.

$$\text{sgn}(x) = \begin{cases} -1 & \text{if } x < 0, \\ 0 & \text{if } x = 0, \\ 1 & \text{if } x > 0. \end{cases} \quad (5.16)$$

Laurence and Karl report the attainable accuracy of the sub-pixel edge detection to be on the order of 1/1000 of a pixel under ideal visualisation conditions.

5.2 Calculation of the Model Trajectory

To determine the trajectory of the model, the linearised edge tracking method described in Laurence (2012, Section 2.3) was employed. It is characterised by calculating the relative movement of the detected edge in between images. This technique is especially useful if only a part of the model outline can be visualised or optical distortion prohibits a comparison with an analytical description of the model geometry (Laurence, 2012, Section 2.1). The most important distinction between the two methods is that the analytic tracking method determines the absolute position and orientation of the tracking object in each image whereas the edge tracking method determines the relative motion between two images.

For each edge point in the first of two images, referred to as the reference image, the closest edge point in the second image, referred to as the displaced image, is determined. Note, that the closest point does not necessarily correspond to the same point on the model geometry. Hence, for each point pair, the range of possible motions must be deduced. A least squares fit over the movement space of the combined possible motions of all points is then used to calculate the most likely motion between the two images.

Consider, for instance, the motion displayed in Figure 5.2, where only one edge point was detected on each edge segment and the motion was purely translational ($\Delta x = 0.5 \text{ px}$; $\Delta y = 0$; $\Delta\alpha = 0$). (x_e, y_e) designates the coordinates of the edge point in the reference image and (x'_e, y'_e) the coordinates of the closest edge point in the displaced image. φ denotes the local edge angle. Assuming φ is the same for both points in each point pair, the displacement $(\Delta x, \Delta y)$ of the edge point must satisfy the following equation:

$$\Delta x \sin(\varphi) - \Delta y \cos(\varphi) = (x'_e - x_e) \sin(\varphi) - (y'_e - y_e) \cos(\varphi). \quad (5.17)$$

The range of possible motions derived from each point pair in the absence of any errors is shown in the bottom left plot of Figure 5.2. However, real images are always subject to noise and the subpixel edge detection has a maximum attainable accuracy. Accounting for these unavoidable errors, the plot in the bottom right of Figure 5.2 shows a more realistic representation of the possible motions determined

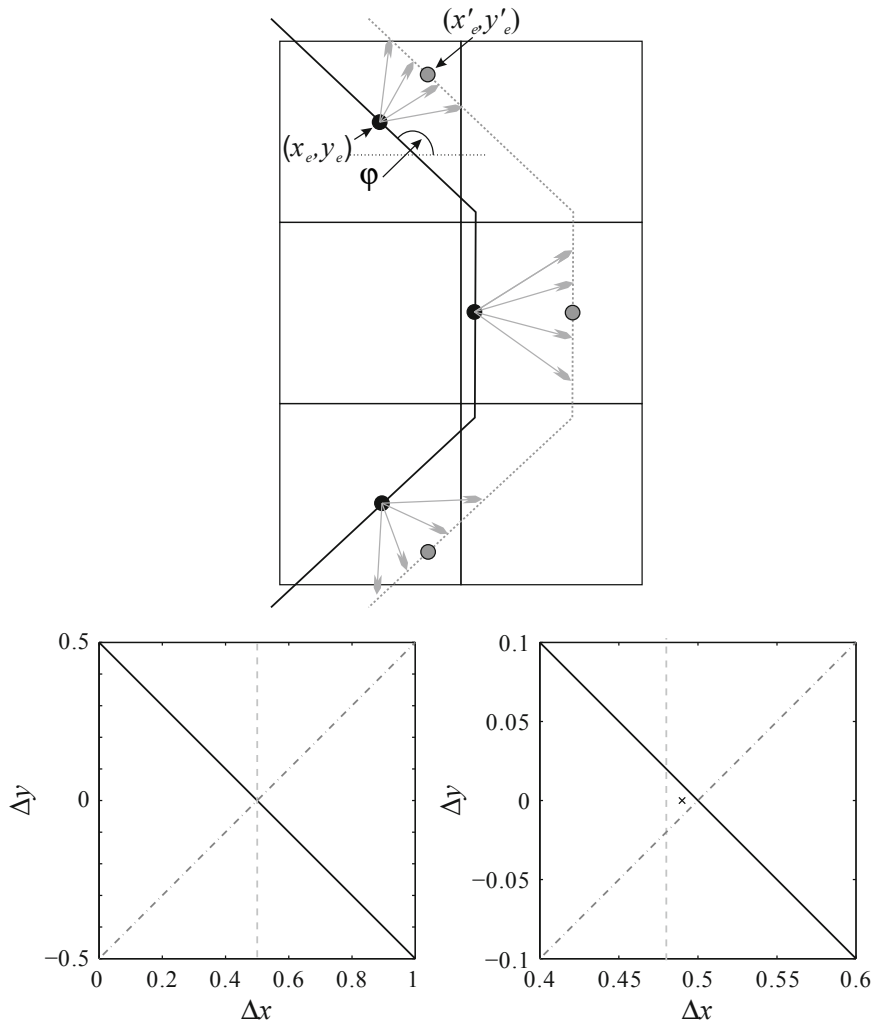


Figure 5.2: The contour detected in the reference and the displaced image for a translation of the model of $\Delta x = 0.5 \text{ px}$. The bottom plots show the range of possible motions assuming edge detection without errors (left) and with errors (right). The graphic was adapted from Laurence (2012).

for the three point pairs shown. It is evident that a least squares fit is necessary to determine the most likely overall displacement. Assuming the same uncertainty in determining the position of each edge point, the result is more accurate the more edge pixels are contained in an image.

Considering the more general case, which allows for rotation about the z -axis as well as translation in x and y , the edge tracking equation can be expressed as

$$\Delta x \cdot \sin(\varphi + \Delta\alpha) - \Delta y \cdot \cos(\varphi + \Delta\alpha) = \sin(\varphi + \Delta\alpha) \cdot x^* - \cos(\varphi + \Delta\alpha) \cdot y^*. \quad (5.18)$$

where

$$x^* = x'_e - x_e \cdot \cos(\Delta\alpha) + y_e \cdot \sin(\Delta\alpha) \quad \text{and} \quad (5.19)$$

$$y^* = y'_e - y_e \cdot \cos(\Delta\alpha) - x_e \cdot \sin(\Delta\alpha). \quad (5.20)$$

Here, $\Delta\alpha = \varphi' - \varphi$ denotes the rotation between the reference and the displaced image. To solve Equation (5.18), Laurence recommends using a form to which a linear fit can be applied to determine $\Delta\alpha$, i.e.

$$\Delta x \cdot \sin(\varphi) - \Delta y \cdot \cos(\varphi) - \sin(\Delta\alpha) \cdot c' = (x'_e - x_e) \cdot \sin(\varphi) - (y'_e - y_e) \cdot \cos(\varphi), \quad (5.21)$$

where

$$c' = x'_e \cdot \cos(\varphi) + y'_e \cdot \sin(\varphi). \quad (5.22)$$

Equation (5.21) can be derived from Equation (5.18) by assuming that $\Delta\alpha \ll 1$ and Δx and Δy are much smaller than x'_e and y'_e . The assumptions can be justified by the fact that the displacements between images in impulse facilities are generally very small. Laurence states that, while Equation (5.21) is very good in determining small $\Delta\alpha$, it is limited in accurately finding Δx and Δy .

With $\Delta\alpha$ known and the rotation applied to the edge points in the reference image, either Equation (5.17) or Equation (5.18) can be used to calculate Δx and Δy using a linear least squares approach. Figure 5.3 graphically summarises the approach. The detected edge is first rotated by $\Delta\alpha$ about a known centre of rotation, commonly the centre of mass of the experimental model, the translation is then calculated for the rotated edge.

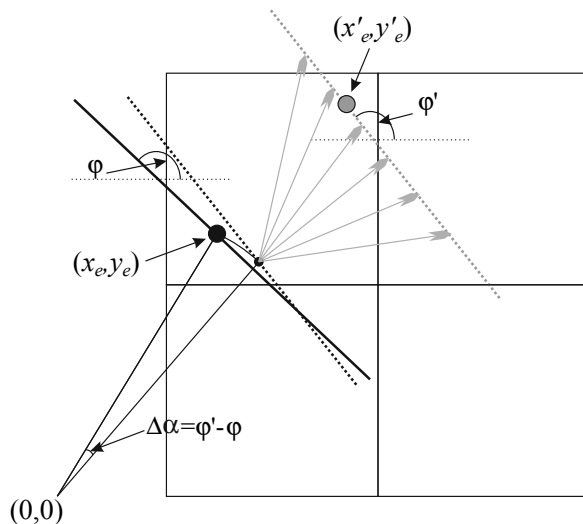


Figure 5.3: The generalised edge tracking approach including rotation. The detected edge is first rotated about the centre of mass of the experimental model by $\Delta\alpha$, the translation of the edge is then determined by computing the range of possible motions of all edge points. The image was adapted from Laurence (2012).

A limitation of this technique is that it cannot be used to determine the scale of the images relative to the experimental model. This is, however, required to transform the determined trajectory from the image coordinate system to physical coordinates. The analytic tracking technique described in Laurence (2012, Section 2.1) is thus applied to the first image. A comparison of the edge detected in

the first image to an analytic description of the tracking object yields the required scale. Given that the analytic tracking itself was found to be inadequate to determine the acceleration in the experiments presented herein, the error that is introduced by this step was estimated. It was found that neither blur nor noise nor small variations in the starting point of each of the three edges significantly affected the scale ($< 0.2\%$). However, in Section 5.4.3 the distortion of the experimental images is estimated and it is shown that distortion does have a significant effect on the scale factor and hence the measured acceleration.

5.3 Calibration

To calibrate the apparatus described in Section 4.3, the Mach 12 REST engine was dropped under gravity inside the T4 test section. It was suspended from a single strand of 22.7 kg fishing line. A 10Ω resistor was attached to the strand. Using a trigger signal generated by the T4 DAQ, the resistor was connected to a power supply via a relay. A few seconds after the trigger signal, the heat generated by the resistor melted the fishing line and the model dropped. The Phantom® v611 has an internal trigger circuit. It can be triggered by either applying a 5 V step signal or simply by shorting the BNC trigger input port. If the trigger port is shorted when the camera is armed opening the circuit will also trigger the camera. Here, a closed circuit was opened by attaching one of its cables to the test section roof and the other one to the experimental model. As soon as the model dropped, the cables were separated and the camera triggered. A schematic of the two circuits used in the calibration setup is displayed in Figure 5.4. The images were recorded at a frame rate of $66\,225\text{ s}^{-1}$ and an exposure time

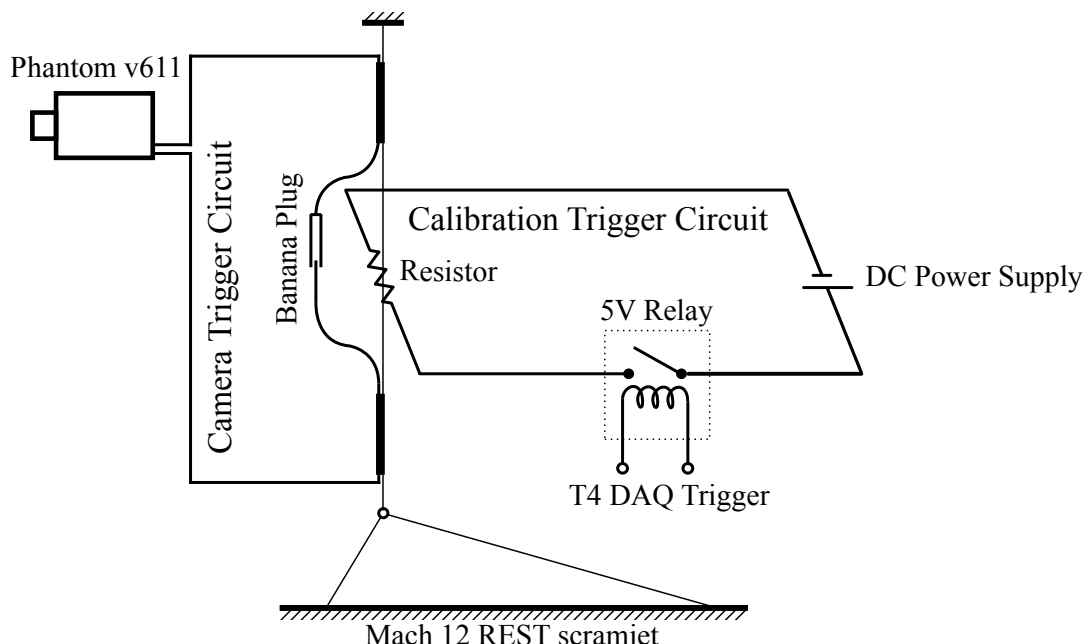


Figure 5.4: A schematic of the trigger mechanism used for the calibration.

of $0.3 \mu\text{s}$. Photographs of the calibration can be seen in Figure 5.5.

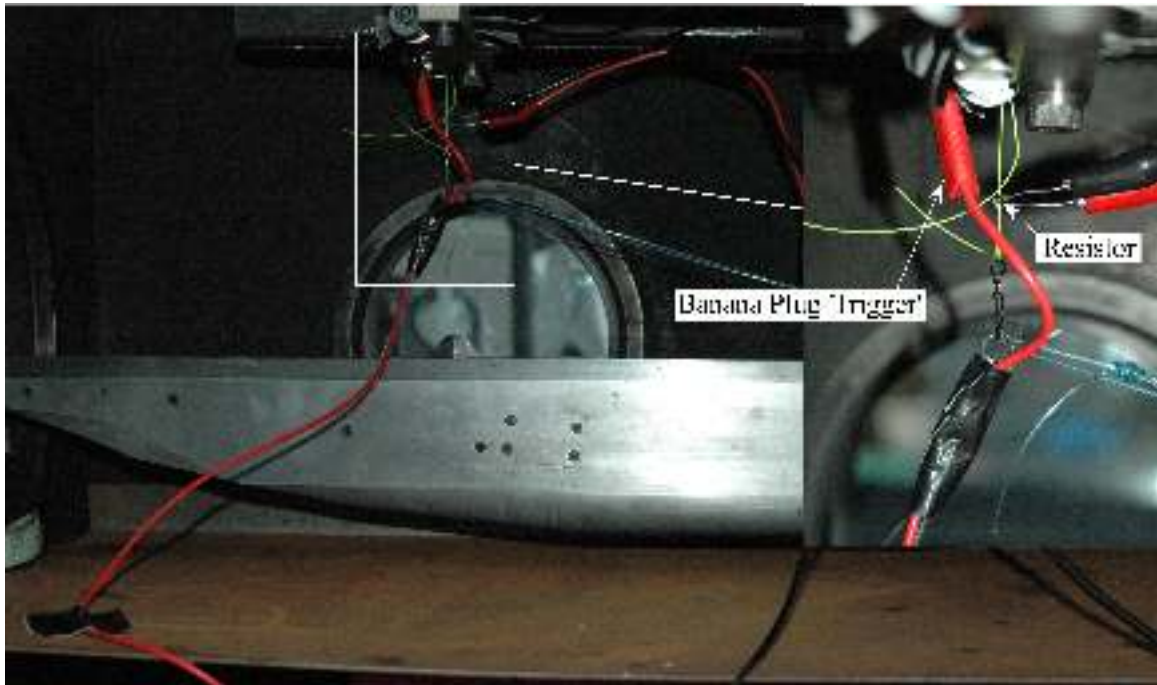


Figure 5.5: Photographs of the experimental setup used for the calibration.

The recorded trajectories for four calibration runs are shown in Figure 5.6.

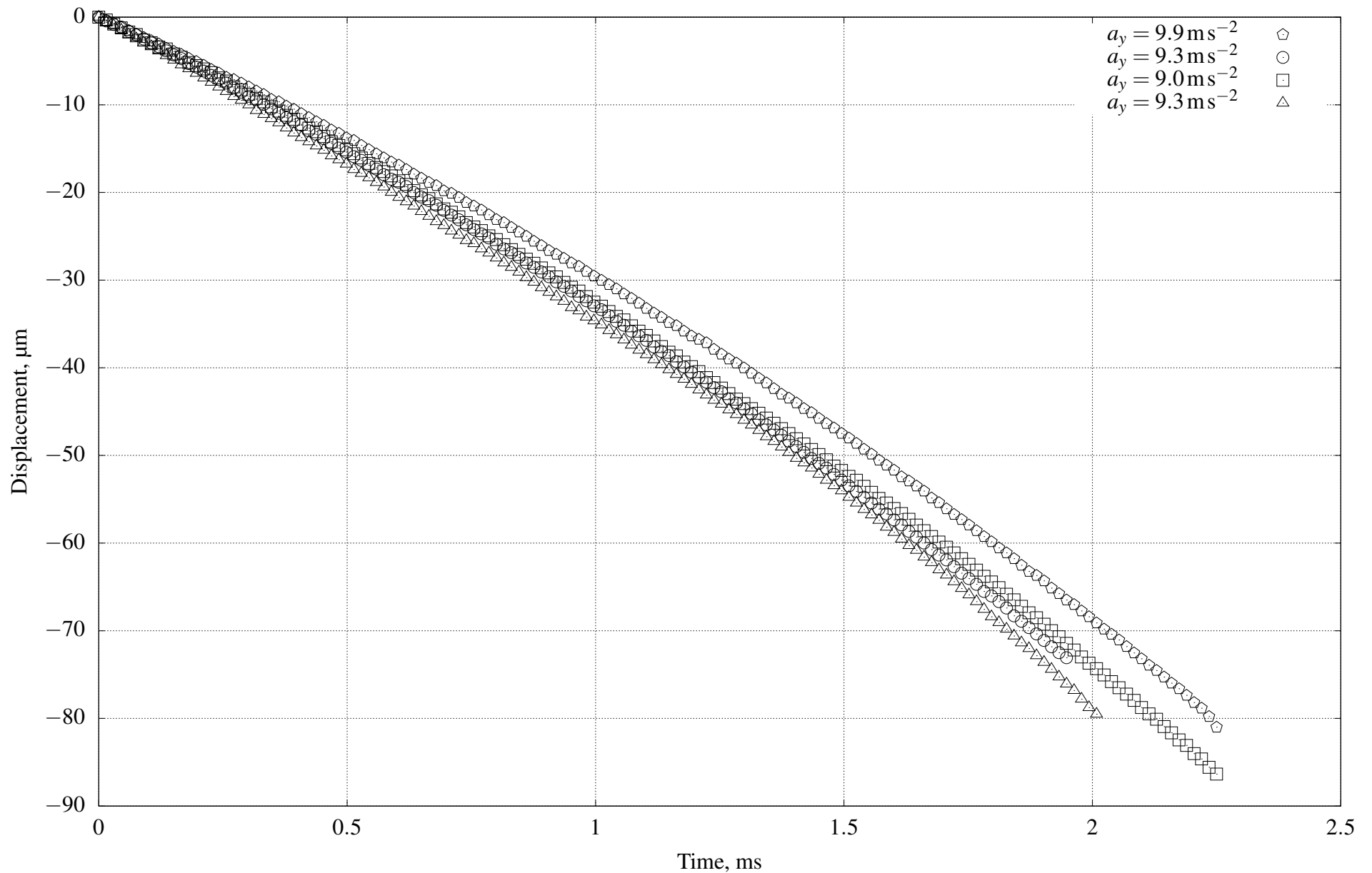


Figure 5.6: The trajectories of the Mach 12 REST model dropping in the T4 test section. The legend shows the obtained acceleration from fitting a quadratic curve to each trajectory.

The divergence of the trajectories at their beginning can be attributed to small differences in the time that it took for the camera to be triggered. Consequentially, the velocity and, thus, the trajectories' slopes at $t = 0$ are different from one trajectory to the other. The mean acceleration and the associated uncertainty of the calibrations are presented in Table 5.1. Comparing the obtained value

Table 5.1: The mean acceleration measured during the calibration experiments. The quoted uncertainty represents one standard deviation of the measured data.

a_y	Unit
9.4 ± 0.4	ms^{-2}

to the gravitational acceleration, i.e. $g = 9.81 \text{ ms}^{-2}$, it can be stated that gravity could be measured successfully within the quoted uncertainty. In the following section, artificially created images are used to better quantify the experimental uncertainty of the method.

5.4 Error Analysis Using Artificial Images

In this section, the influence of a number of variables on the accuracy of the measurement technique is presented. For this purpose, artificial images, depicting the tracking object and simulating ideal visualisation conditions, were created and analysed with the described technique. Simulated trajectories were calculated using constant values of acceleration in x , y and α . Using the artificial images, it is possible to isolate individual variables and determine their effects on the measured acceleration.

Unless otherwise specified, the default camera settings and engine forces used to create the artificial images were the ones listed in Table 5.2. The forces were determined using viscous CFD of the

Table 5.2: The default camera settings, engine forces and engine mass used for the artificial images.

Quantity	Symbol	Magnitude	Unit
Streamwise Acceleration	a_x	12.3	ms^{-2}
Vertical Acceleration	a_y	-2.9	ms^{-2}
Rotational Acceleration	a_α	103.5	rad s^{-2}
Mass	m	7.15	kg
Mass Moment of Interia	I_z	0.427	kg m^2
Frame Rate	-	66 225	s^{-1}
Resolution	-	512×208	px
Exposure	-	0.3	μs
Test Time	t_t	2.5	ms
Scale	S_i	0.072 27	mm px^{-1}

full scramjet engine model, see 6.1.1. The model mass was measured with the entire instrumentation and the fuel system installed.

The error analysis follows that presented in Laurence and Karl (2010). Assuming that the position in each image was determined with the same level of accuracy and that the acceleration is constant over the measured time period, the error in the acceleration can be expressed as

$$S_a = \frac{6\sqrt{5} \cdot (n-1)^2}{\sqrt{(n-3) \cdot (n-2) \cdot n \cdot (n+1) \cdot (n+2)}} \cdot \frac{2s}{(t_n - t_1)^2}. \quad (5.23)$$

Here, n designates the number of images taken and s the accuracy with which the position of the model was determined.

5.4.1 Artificial Images

In order to create the artificial images, the simulated trajectories were calculated first. All intersections of the edges of the tracking object with pixel boundaries were then determined for each image. With the edge coordinates known, the intensity of each pixel could be calculated. Pixels that were completely covered by the tracking object were assigned the intensity value 0 and pixels that were fully exposed to light were assigned the value 1. Edge pixels were assigned the intensity value that corresponds to the fraction of the pixel area that was exposed to light, i.e.

$$I_h = \frac{A_{exp}}{A_{px}} = 1 - \frac{A_{cov}}{A_{px}}, \quad (5.24)$$

where A_{exp} designates the area exposed to light, A_{cov} the area covered by the tracking object and A_{px} the total area of the pixel. For instance, if the tracking object covered 30 % of a pixel it was assigned the normalised intensity value 0.7. To convert the resulting normalised intensity matrix \mathbf{I}_N to an image file, Gaussian blur was added with $\sigma_G = 0.5$, see Equation (5.5). Gaussian noise was also added at a noise level of 1 % of the maximum intensity of the Phantom® v611 camera sensor. Finally, \mathbf{I}_N was scaled by I_{max} and the 12 bit data was stored in a 16 bit TIFF image format, as is the case with the Phantom® v611.

Given the small exposure times during the experiments of $0.3\mu\text{s}$, motion induced blur was assumed to be negligible. With a constant acceleration of $a_x = 12.5\text{ m/s}^2$, the expected maximum as estimated from CFD, see Section 6.1.1, the maximum velocity at the end of the test time, i.e. at $t = 4.5\text{ ms}$, reaches 56.25 mm s^{-1} . In the given exposure time, the tracking object thus moves less than 17 nm. Converting motion of that magnitude to a change in pixel intensity yields $\Delta I = 0.94$, which is equivalent to 0.024 % of I_{max} .

One of the artificial images is shown in Figure 5.7. The magnified view of the corner of the tracking object demonstrates that the edges are blurred across two to three pixels and that the chosen level of noise has only a small effect. Comparing the artificial image to the experimental image in Figure 5.1 shows that the chosen levels of noise and blur are a good approximation of the experimental

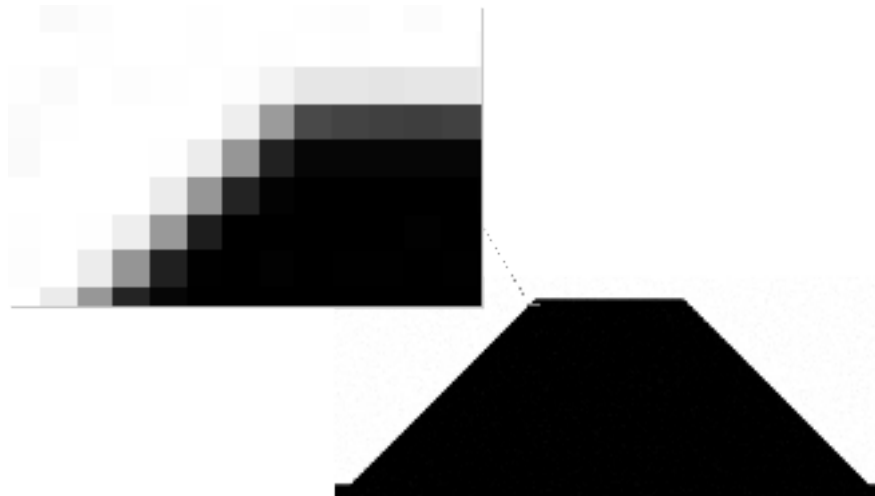


Figure 5.7: One of the artificial images created with the described method.

levels.

To be able to account for potential effects resulting from the initial position of the tracking object within an image, 100 image series of the same trajectories were created where the initial position of the tracking object was varied by $\Delta x = 0.01w_{px}$ in between image series. Figure 5.8 shows the error in absolute acceleration in x , y and α for each of the 100 image series. The magnitude of the error was obtained by subtracting the forces listed in Table 5.2 from the result of the motion tracking algorithm. The error evidently varies periodically with the starting position of the tracking object within the image. Given that the trajectories in x and y depend on that in α , it is postulated that the determination of the angle is the cause of the uncertainty. However, it is not clear why the determined angle changes so drastically with the starting position of the tracking object. A possible explanation is that the attainable resolution for diagonal edges changes with its position within a pixel. A diagonal edge that is close to the corner of a pixel needs to move further to change the intensity of a pixel by a given increment ΔI than a diagonal edge that is close to the centre of a pixel, see Figure 5.9 and Equation (5.12). It is therefore possible that small displacements Δs don't result in a change in intensity for pixels where the edge is close to a corner whereas the same displacement causes a significant change in intensity in pixels where the edge is close to the centre of the pixel. It should be emphasised, however, that the images analysed here represent ideal visualisation conditions. In a real image this effect will likely be less pronounced. However, the average error, taken as the mean of the 100 values, and its associated standard deviation are considered to give a reasonable estimate of the uncertainty of the technique.

5.4.2 Resolution, Frame Rate and Magnitude of Acceleration

It is of interest to determine the level of accuracy that is attainable with the Phantom® v611. Every frame rate setting is associated with a maximum resolution, the higher the frame rate is the lower is the

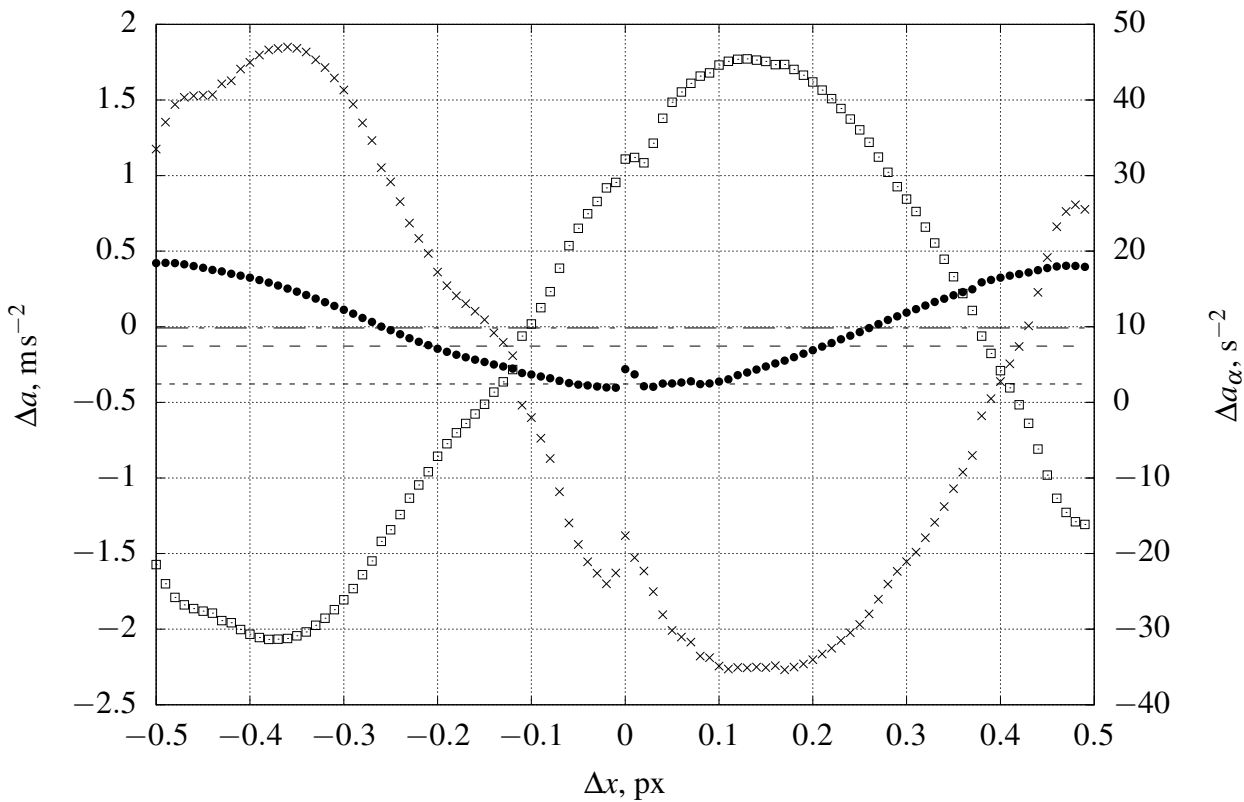


Figure 5.8: The error in the acceleration for each of the 100 image series with respect to the shift in starting position. \square denotes the error in a_x and $- - -$ the associated average. \bullet designates the error in a_y and $- - -$ the associated average. The error in the angular acceleration is denoted by \times ; the associated mean by $- - -$

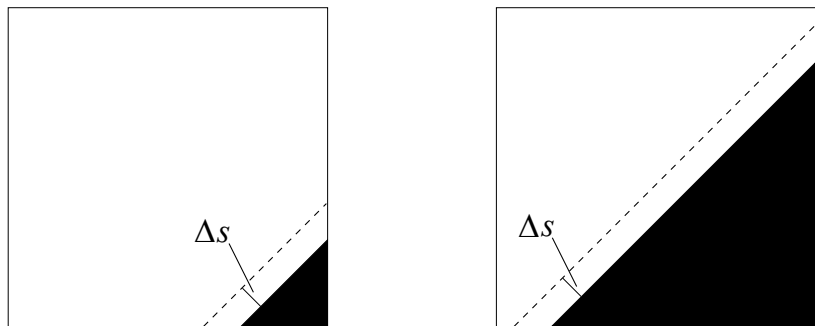


Figure 5.9: The difference in attainable resolution from a single pixel containing a diagonal edge. The same displacement results in a different change in intensity. If the edge is close to the corner of a pixel a small displacement Δs may not be resolvable whereas the same Δs for an edge at the centre of the pixel results in a significant ΔI .

maximum resolution. Figure 5.10 shows a plot of the accuracy with which the position of the model could be determined against the frame rate of the camera for different settings. Lines of constant error are displayed as well as a line indicating the approximate performance of the Phantom® v611 at the maximum resolution for a given frame rate. The performance curve was obtained by fitting an exponential function to the given data points. From the data in Figure 5.10, one can conclude that

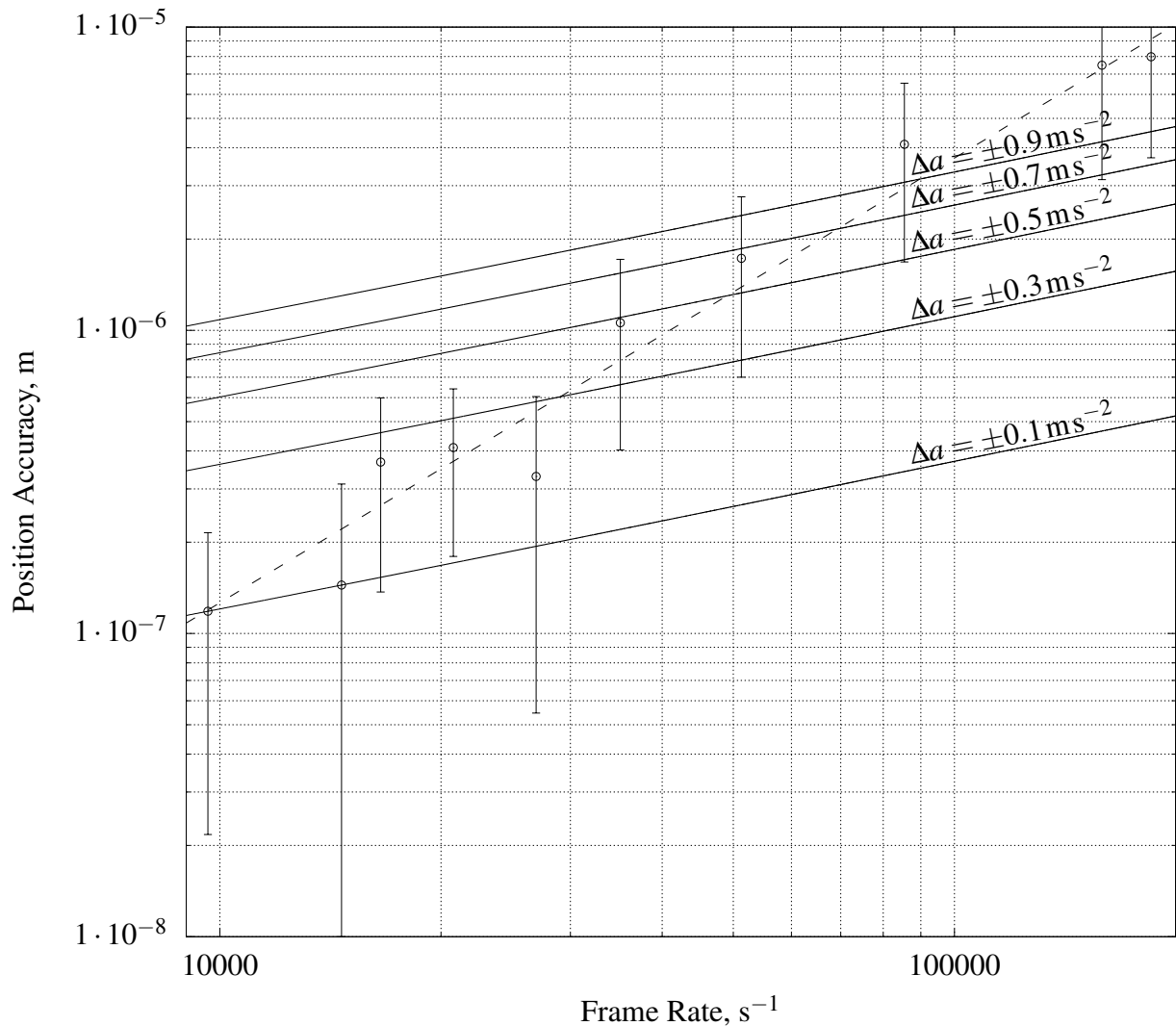


Figure 5.10: A performance curve of the Phantom® v611 showing the minimum attainable error for a given frame rate at the standard condition shown in Table 5.2.

under ideal visualisation conditions increasing the resolution will yield a larger increase in accuracy than an increase in frame rate.

One should note that the accuracy of the method is dependant on the measured acceleration. Figure 5.11 shows the average absolute error and associated standard deviation for image series with varying acceleration in the streamwise direction. The acceleration in y and α was set to zero, i.e. $a_y = a_\alpha = 0$, for the data presented in Figure 5.11. It is evident that the inherent error of the method reduces with increasing acceleration. This is easily explained by the change in intensity associated with a larger velocity. Significant ΔI , in excess of the noise level of the sensor, results in higher certainty in determining the angle and the displacement of the model, whereas small changes in position in between two images may not be detectable at all.

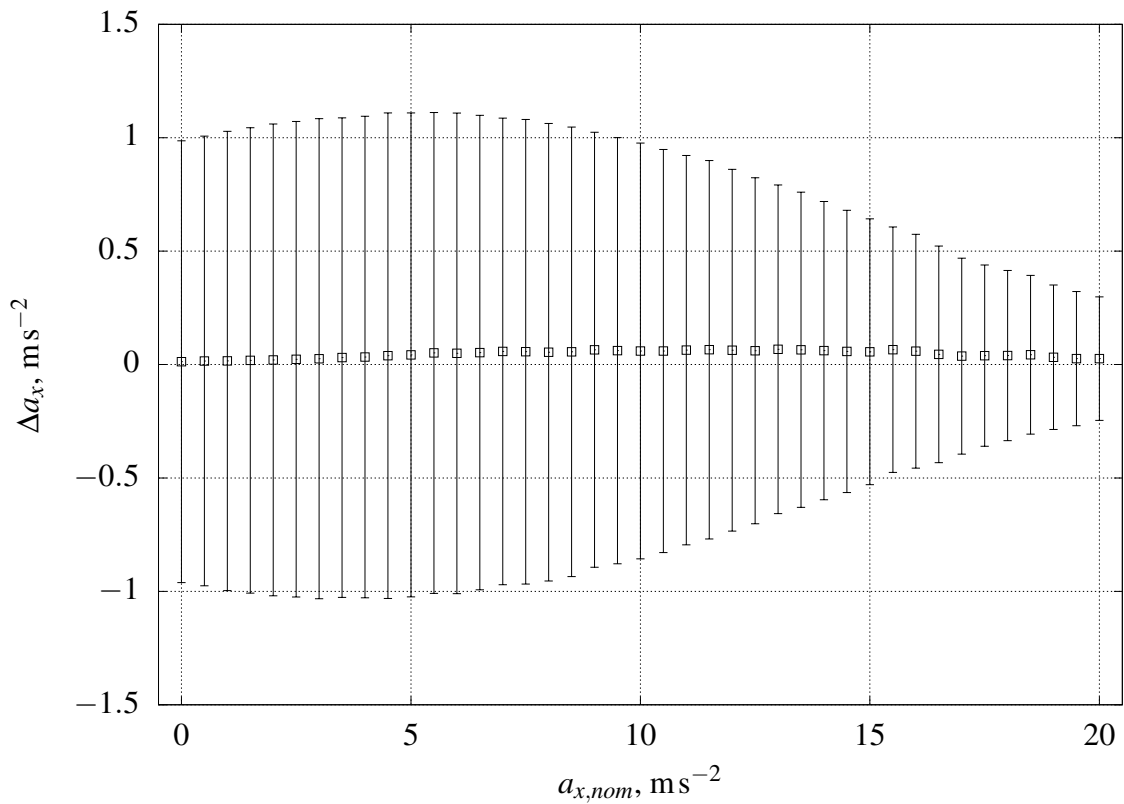


Figure 5.11: The mean error in the acceleration in x for $0 \leq a_x \leq 20 \text{ m s}^{-2}$.

5.4.3 Optical Distortion

Close investigation of the images from the experimental campaign yielded that the tracking object contour was distorted by the optical components. In Figure 5.12 the edge detected with the sub-pixel edge detection is shown together with the undistorted edge of the tracking object. Obvious distortion

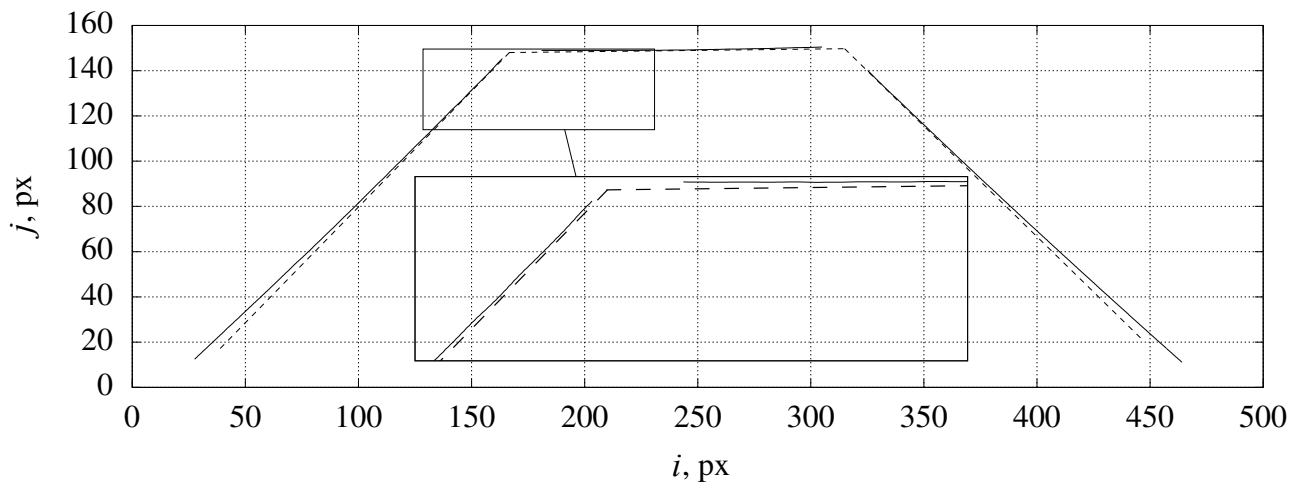


Figure 5.12: A comparison of the edges detected by the sub-pixel edge detection routine (—) with the undistorted contour of the tracking object (---).

can be seen at the ends of each of the three edge segments. Each of the segments appears to be

concave. This effect is characteristic of pin-cushion distortion.

Pin-cushion distortion is characterised by an increase in magnification of the image with distance from the optical axis of the lens creating the image. Analytically, this can be expressed as

$$r_d = r_u + r_u^3 \cdot \xi, \quad (5.25)$$

where r_u is the distance from a given point to the optical axis, r_d is the distance after applying the distortion and ξ designates the distortion factor; which defines the magnitude of the effect. The optical axis was assumed to be at the centre of the tracking object. In Figure 5.13 the edge detected in an image which was taken during the calibration of the apparatus is overlayed with the edge detected in an artificial image with added pin-cushion distortion with $\xi = 1.5 \times 10^{-6}$. This qualitative compar-

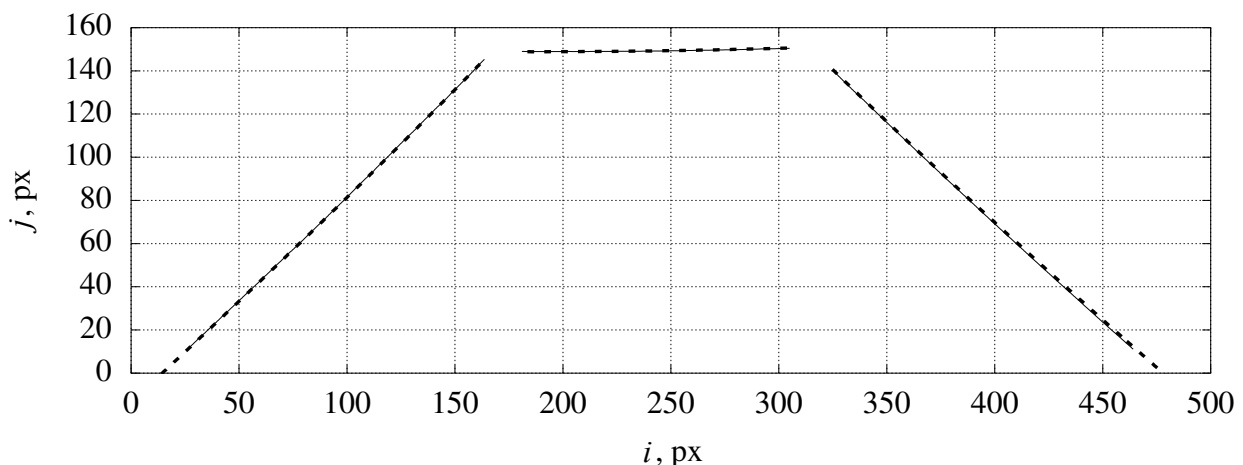


Figure 5.13: A comparison of the edges detected in a distorted artificial image (----) with the edges detected during the calibration of the optical apparatus (—).

ison suggests that the distortion is indeed of the pin cushion type and that $\xi = 1.5 \times 10^{-6}$ is a good estimate for the magnitude of the effect.

The scale detected by the analytic tracking technique for the distorted artificial image was $0.06684 \text{ mm px}^{-1}$. Comparing this value to the nominal scale listed in Table 5.2 yields that the added distortion reduced the detected scale by 7.5 %. Given that the measured acceleration is directly proportional to the scale, it is reasonable to assume that the measured acceleration in the calibration experiments was too low. Correcting the values presented in the previous section for the effects of distortion results in $a_y = 10.1 \pm 0.4 \text{ m s}^{-2}$.

Due to time constraints it was not possible to perform an experimental investigation of the nature of the encountered distortion and its effects on the measurements. It should be noted that Equation (5.25) demonstrates that the contour of the tracking object will be distorted in a different manner for each image. This can result in further measurement error and should be considered when evaluating the experimental results presented in Chapter 6. Further analysis of the effects of the distortion on the

measured acceleration using the artificial images yielded that the effects are not limited to the error in determining the scale of the images. However, it was not possible to quantify this.

CHAPTER 6

EXPERIMENTAL RESULTS

Three experimental campaigns were conducted over the course of the present study. The first campaign, shots 11928 to 11951, served to validate the unfuelled operation of the engine at a Mach 8 condition, to ensure the catch and release mechanisms were working as expected and to measure the drag force of the Mach 12 REST model. However, vibrations and difficulties with the optical components rendered the force measurements useless. In the second campaign, shots 12112 to 12123, the source of the vibrations was identified and the first reproducible drag measurements produced. With the lessons from the first and second campaign, the vibrations could be addressed and a fuel system was installed on-board the Mach 12 REST model for the third test campaign, shots 12197 to 12235. The engine was tested at two different test conditions during the third campaign. Only the results of the condition presented in Chapter 4 are discussed in this chapter. The second test condition and the corresponding pressure data are presented in Appendix A. A summary of all shots is given in Appendix D.

Hereinafter are presented the results from shots 12198, 12199 and 12223 to 12235 of the third experimental campaign in the T4 shock tunnel. The other shots were excluded from the following analysis for one or multiple of the reasons listed below:

1. the engine unstarted or did not start during the test time,
2. the 2 mm test condition (details presented in Section A.1) was used or
3. notable oscillations of the imaging lens obscured the image tracking data too much to be used.

Any reference to all shots in the following sections only refers to those 15 shots.

The main purpose of the experiments was to measure the net forces, i.e. thrust, lift and the pitching moment, on an airframe integrated scramjet model using the image tracking technique. The campaign consisted of two parts. In the first one, the full shape transition nozzle was attached to the Mach 12

REST engine. For the second part, the tail third of the nozzle was removed to investigate its contribution to the engine forces. Tests were performed at various different fuelling ratios with gaseous hydrogen as well as without fuel injection. The contribution of the fuel mass flow rate to the net thrust was calculated analytically.

In the first section of this chapter, experimental pressure data is compared to fuel-off CFD of the Mach 12 REST model. Section 6.2 shows the data obtained with the image tracking technique. It is further demonstrated in Section 6.2.1 that the thrust measurements are not significantly affected by the varying conditions in the chosen test time. The presence of facility vibrations, which affected the image tracking data, is shown in Section 6.2.2 and the process used to quantify their influence presented. It was not possible to entirely isolate the optical components from the vibrations of the facility in the available time frame.

In order to evaluate any of the data collected during the experimental campaign it had to be established that the engine was started and unrestrained during the test time. Figure 6.1 shows a schlieren photograph of the cowl closure point of the Mach 12 REST model. The shocks from the leading edge

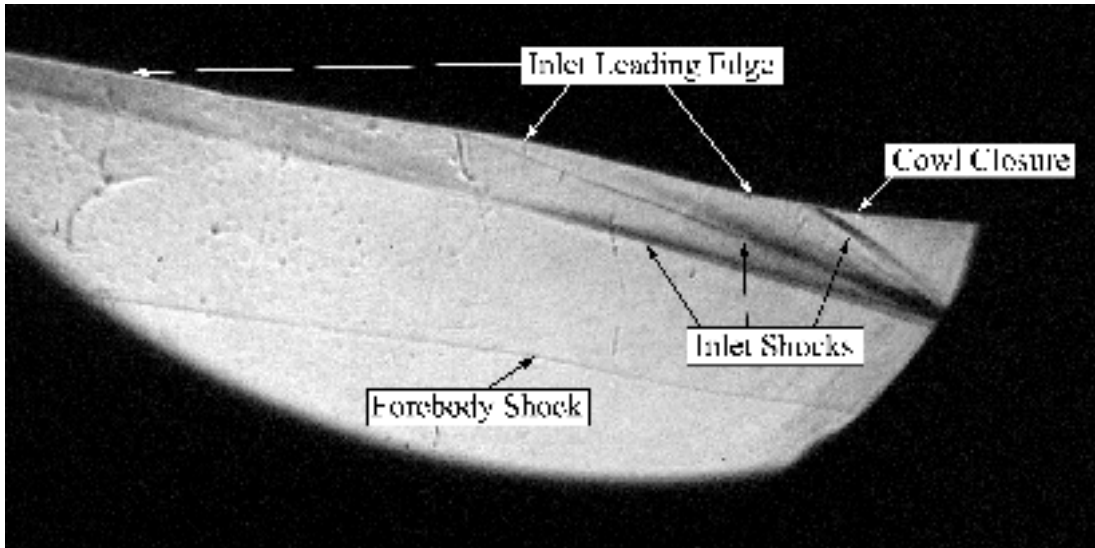


Figure 6.1: A schlieren photograph showing part of the inlet and the cowl closure point of the Mach 12 REST model. The contrast has been enhanced to aid visualisation.

and the inlet are clearly visible. It is evident that there is some spillage from the inlet as the shocks are not focussed on the cowl closure point but the engine is started. In subsequent shots it was verified that both strands of fishing line break before the start of the test time. Figure 6.2 shows an image from shot 12198. The image shows the tracking object at $t = 1.28\text{ ms}$; well before the start of the test time. The cut strand of fishing line that supported the front of the model can be seen at the left hand border of the image. Due to low image quality, the image demonstrating that the rear fishing line broke ahead of the test time too, is not shown here. However, given that the established freestream takes approximately $180\text{ }\mu\text{s}$ longer to reach the rear fishing line and it was considerably weaker than



Figure 6.2: An image from shot 12198. One end of the cut front strand of fishing line is clearly visible. Shown is frame number 86, i.e. $t = 1.28\text{ ms}$.

the front one, it can be concluded that the experimental model was released at $t < 2\text{ ms}$.

6.1 Pressure Data and CFD Results

The first main part of this chapter concerns itself with the pressure data obtained during the experimental campaign. The results from a fuel-off CFD simulation are presented in Section 6.1.1. A comparison of the pressure distribution along the body-side wall of the engine with the measured pressure is presented thereafter. While evaluating pressure data was not the main objective of the experimental campaign, it provides valuable insight into the operation of the engine. It is demonstrated in the following that, in agreement with Figure 6.1, the engine started at the Mach 8 test condition and that robust combustion was achieved at various equivalence ratios.

All pressure data was normalised using the pressure recorded by P1 and then averaged over the test time. The signal from P1 was filtered with a $20\text{ }\mu\text{s}$ moving average filter to reduce its noise level before the normalisation. During shots 12225 and 12226, P1 did not record any data. The pressure data from these two shots was hence normalised by the signal recorded with SPA. In order to compare them to the other shots, the ratio of p_s/p_1 was interpolated by fitting a linear curve to p_s/p_1 over p_s from the remaining shots. The interpolated value of p_s/p_1 was then used to scale the normalised pressure for shots 12225 and 12226.

Note that both P2 and P9 did not record any useable data throughout the campaign. They were therefore omitted in the analysis. The cause of this could not be determined during the campaign.

6.1.1 Fuel-off CFD Simulation

CFD simulations without fuel are useful for a number of reasons. They can serve to validate the pressure measurements of fuel-off shots, demonstrate the pressure rise from combustion in fuelled experiments and provide a breakdown of the aerodynamic forces acting on the individual engine components. The mass capture of the inlet can also be evaluated.

The NASA code VULCAN (White and Morrison, 1999) was used for the simulation presented here. It was run on a structured grid containing approximately 13.3 million cells. Turbulent flow was assumed in the entire computational domain and was modelled using the 1998 Wilcox $k-\omega$ model. All walls were ascribed a no-slip boundary condition at a constant temperature of 300 K. The assumption of a constant temperature wall is reasonable for shock tunnel experiments, given the length of test time.

The freestream conditions assumed for the simulation presented are shown in Table 6.1.

Table 6.1: The freestream conditions used for the fuel-off CFD simulation.

Quantity	Value	Unit
p_0	2100	Pa
M_0	7.53	-
ρ_0	0.026	kg m^{-3}
T_0	280.6	K
u_0	2532	m s^{-1}
q_0	83.2	kPa

The top surface of the engine was not modeled in the simulation. Its contribution to the forces is calculated analytically below. Due to time constraints the tail end of the nozzle was omitted too. Its contribution to the net forces was not considered in the following analysis.

Engine Flowfield

Figure 6.3 shows the computed wall pressure at the body-side wall of the Mach 12 REST engine normalised by the forebody pressure (Figure 6.3a) as well as pressure contours of the internal and part of the external flowfield (Figure 6.3b). As can be expected, the flowfield is dominated by shocks being created and reflected throughout the engine. Given that the engine's design point is Mach 12, the forebody shock and the shock at the start of the inlet sit well beneath the cowl of the engine. This causes significant flow spillage. The capture area at the given test condition is found to be

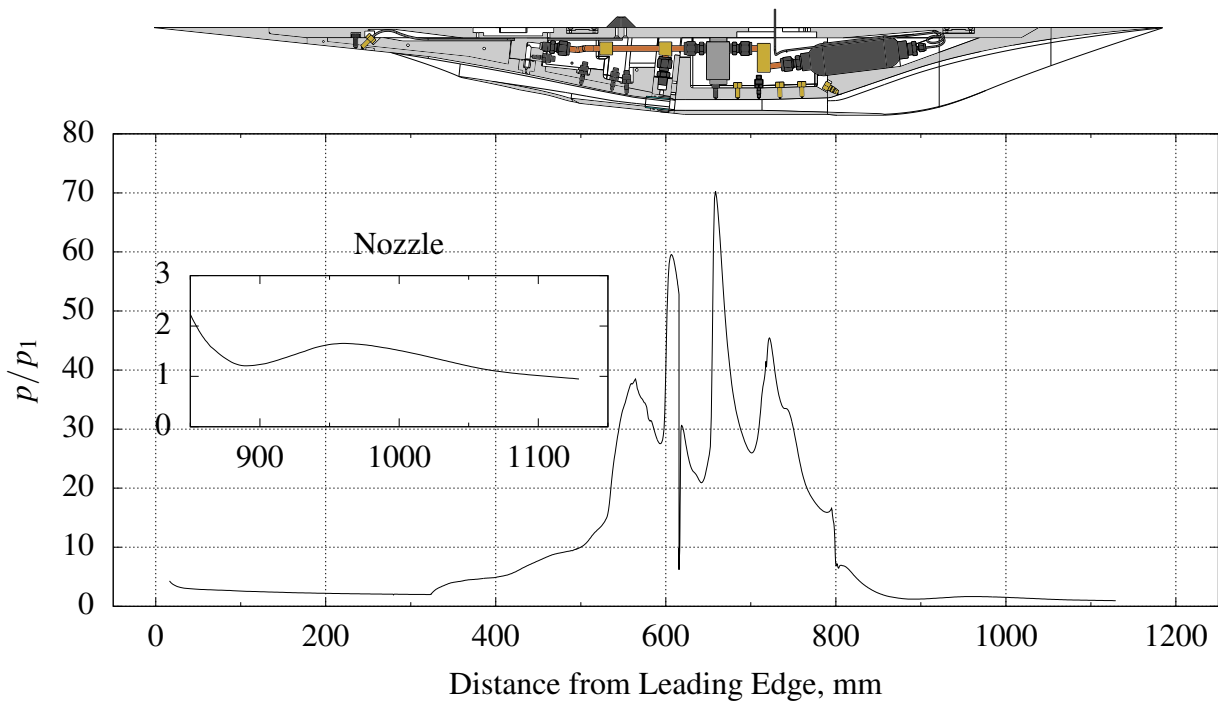
$$A_c = 1495 \text{ mm}^2. \quad (6.1)$$

The mass flow rate through the engine can hence be calculated according to

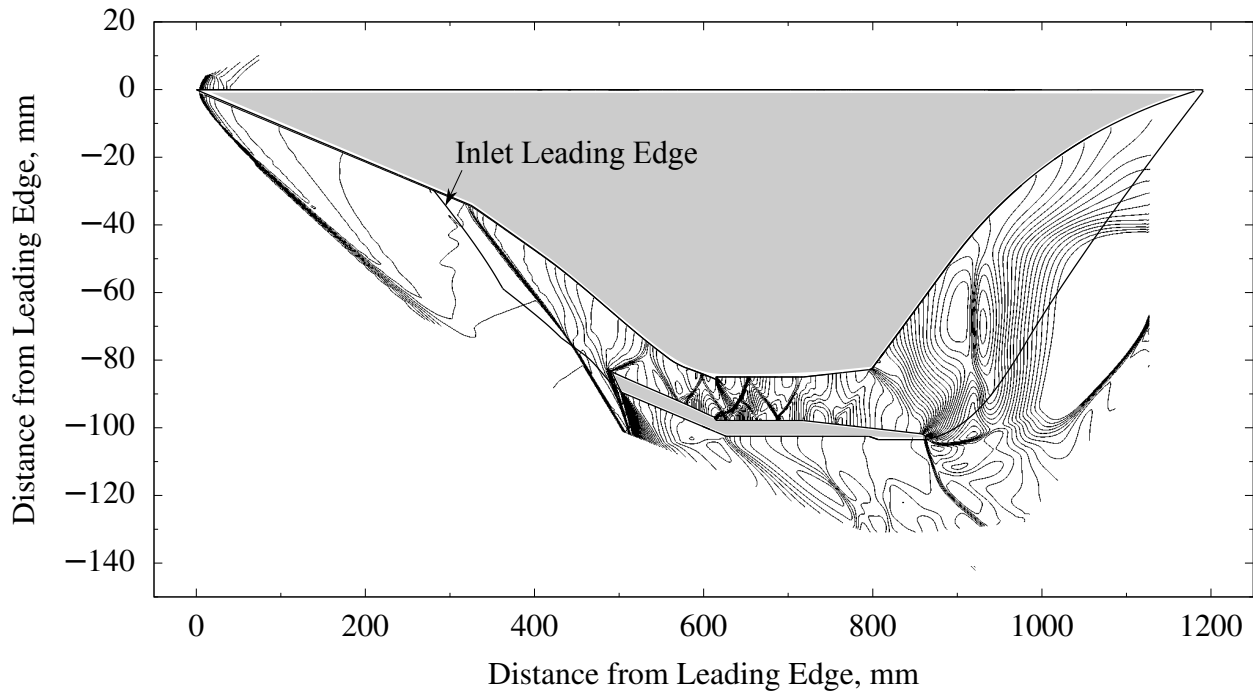
$$\dot{m}_0 = \rho_0 u_0 A_c. \quad (6.2)$$

Defining the mass capture performance as a fraction of the maximum attainable capture area yields

$$\eta_{\dot{m}} = \frac{A_c}{A_{c,max}} = 0.45, \quad (6.3)$$



(a) The pressure distribution along the body-side wall at the symmetry plane of the Mach 12 REST engine normalised by the forebody pressure.



(b) Pressure contours of the CFD solution. Contour levels are shown as $\log_{10}(p)$ from 2.70 to 5.36 at increments of 0.054. The scale of the y-axis has been increased to enhance visualisation.

Figure 6.3: The flowfield of the Mach 12 REST model without fuel.

where $A_{c,max} = 3308 \text{ mm}^2$ (see Doherty (2014) Section 5.4 for the definition of $A_{c,max}$ and η_m for different conditions).

Forces on the Mach 12 Model

The contribution of the components of the Mach 12 REST model to the aerodynamic drag, lift and pitching moment is shown in the following. For this purpose the engine surfaces are split into two categories: flowpath surfaces and airframe surfaces. The flowpath surfaces are all surfaces that directly contribute to the operation of the engine, i.e. the leading edge, the underside of the forebody and the internal surfaces of the inlet, the combustor and the nozzle. All other surfaces are considered part of the airframe.

Given that the top surface was not modelled in the simulation, its contribution to the forces was calculated analytically. Assuming constant pressure, the contribution to the lift can be calculated using

$$L_{TS} = -A_{TS} \cdot p_0 = -143.9 \text{ N}. \quad (6.4)$$

Here, A_{TS} designates the surface area of the top surface. The area occupied by the supports of the experimental model was 3.7 % of the top surface. The viscous drag of the top of the model was calculated using the reference temperature method by Meador and Smart (2005). Assuming an entirely turbulent boundary layer the drag force on the top surface was found to be

$$D_{TS} = 3.6 \text{ N}. \quad (6.5)$$

Table 6.2 shows the total drag, lift and pitching moment about the centre of mass of the engine. A breakdown into the contribution of skin friction and pressure to each force and the pitching moment are also provided.

Table 6.2: The total forces and pitching moment acting on the Mach 12 REST model according to fuel-off CFD.

	D, N	L, N	M_z, Nm
Skin Friction	63.7	47.7	47.0
Pressure	28.0	-2.8	-2.7
Total	91.7	44.9	44.3

In Table 6.3a the contribution of the flowpath surfaces is summarised and in Table 6.3b that of the airframe surfaces is listed. The same breakdown as above, into skin friction and pressure drag, is provided.

One should note that the flowpath of the engine was designed for a modular propulsion system. That is, if applied to a vehicle, multiple modules would be mounted side by side. Given that the skin friction drag of the side walls is the same for any number of engine modules, the analysis of only a single module integrated with an airframe exaggerates the contribution of the side walls to the total

Table 6.3: The forces acting on the flowpath and the airframe.

(a) The flowpath forces.

	D , N	L , N	M_z , Nm
Skin Friction	40.3	-1.1	-2.5
Pressure	9.6	99.8	39.5
Total	49.9	98.7	37.0

(b) The airframe forces.

	D , N	L , N	M_z , Nm
Skin Friction	23.3	-1.7	-0.2
Pressure	18.4	-52.1	7.5
Total	41.7	-53.8	7.3

drag. In the simulation presented herein, the skin friction drag on the side walls constitutes 14 % of the total drag force acting on the model. Assuming two engine modules under the same conditions, the contribution of the side walls reduces to 7 %. Table 6.4 shows the relative contribution of the side walls to the total drag of the engine for up to 6 engine modules mounted side by side. The number of modules is denoted by n_M .

Table 6.4: The relative contribution of the side walls to the total drag force for multiple engine modules.

n_M	1	2	3	4	5	6
D_{SW}/D , %	14	7	5	4	3	3

6.1.2 Fuel-Off Shots

Fuel-off experimental pressure data is presented in this section. Figure 6.4 compares the body-side wall pressure from CFD to four fuel-off shots. The data was normalised by the pressure recorded by P1 on the forebody. It is evident that, overall, the experimental data agrees well with the CFD solution. As stated in the introduction to this section, this confirms that the engine started at the Mach 8 condition. The most notable difference between the simulation and the experimental data can be seen in P6 at 714 mm from the leading edge. The signals recorded by P6 suggest that a shock impinged on the body-side wall where it was located. This explains the difference between shot 12223 and the other three in Figure 6.4. A small shift in position of the shock changed the recorded pressure drastically.

With the unfuelled operation of the engine validated, the data from fuelled experiments can be interpreted.

6.1.3 Fuel-On Shots

Pressure data from fuelled shots is presented hereinafter. All shots with an equivalence ratio of $\phi < 0.7$ are shown in Figure 6.5. The higher equivalence ratio shots are shown in Figure 6.6. The fuel used was gaseous hydrogen in all cases. It was injected through the inlet and combustor plenums at a fuel

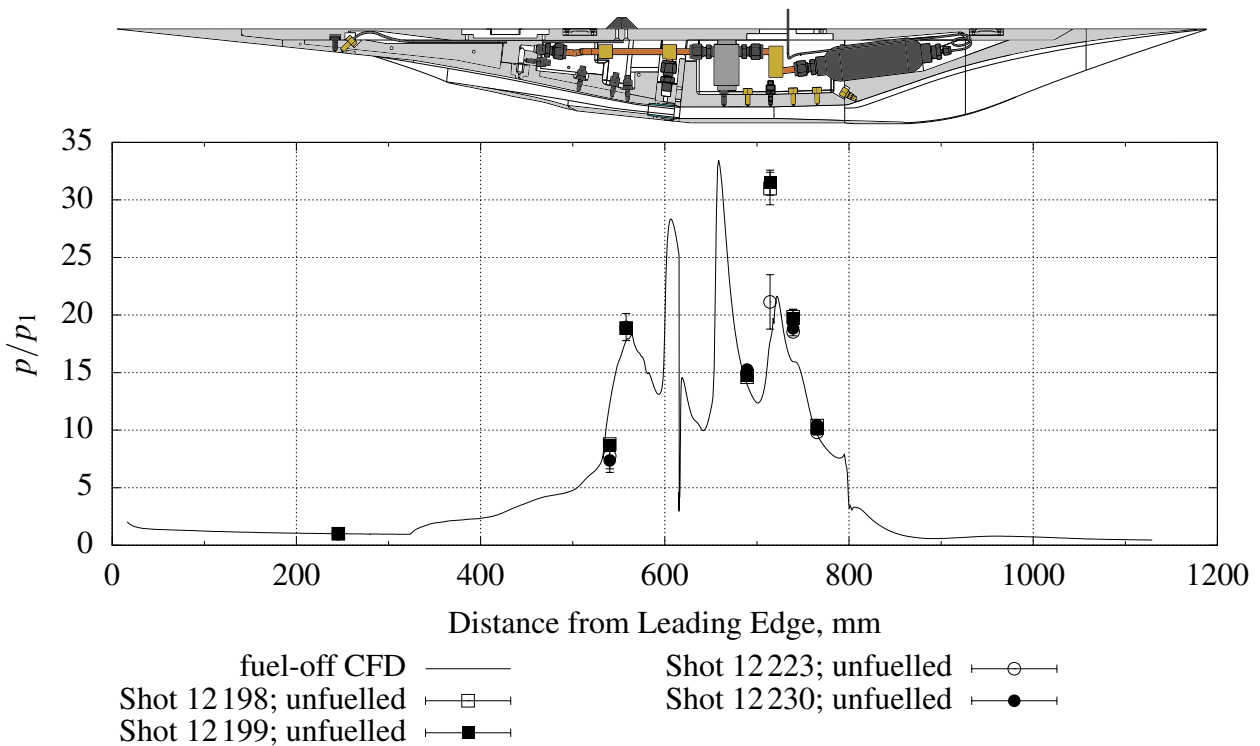


Figure 6.4: Normalised pressure data from four fuel-off shots in comparison with that of the CFD solution. The error bars show one standard deviation of the variation of pressure during the test time.

split of 40/60 by fuel mass flow rate. A distinct combustion induced pressure rise over the unfuelled pressure data is clearly visible in the signals of transducers P5 to P8 for all fuelled shots. The pressure measured by P3 is also consistently higher than in the unfuelled shots. This can be explained by the fuel injected into the inlet. Following inlet injection, a bow shock forms ahead of the injector and changes the pressure distribution inside the inlet. It is interesting to note that P4 recorded slightly lower pressures when fuel was injected than without fuel injection.

Figures 6.5 and 6.6 show that the magnitude of the recorded pressures in the combustor increased with an increase in the fuel equivalence ratio. From the data presented it can be concluded that the engine worked as expected at the Mach 8 test condition.

6.2 Image Tracking Data

In this second main part of the presentation of the experimental results, the image tracking data is shown. In the previous sections of this chapter it was established that the engine started, combustion occurred and the model was free-flying during the test time. As stated in Section 4.1.3, the test time used for the present study was extended to reduce the uncertainty associated with the image tracking based measurements. It is therefore first demonstrated in Section 6.2.1 that the assumption of constant acceleration is still valid for the extended test time. The facility vibrations encountered during the experiments are then discussed before the data from the force measurements is shown in the last

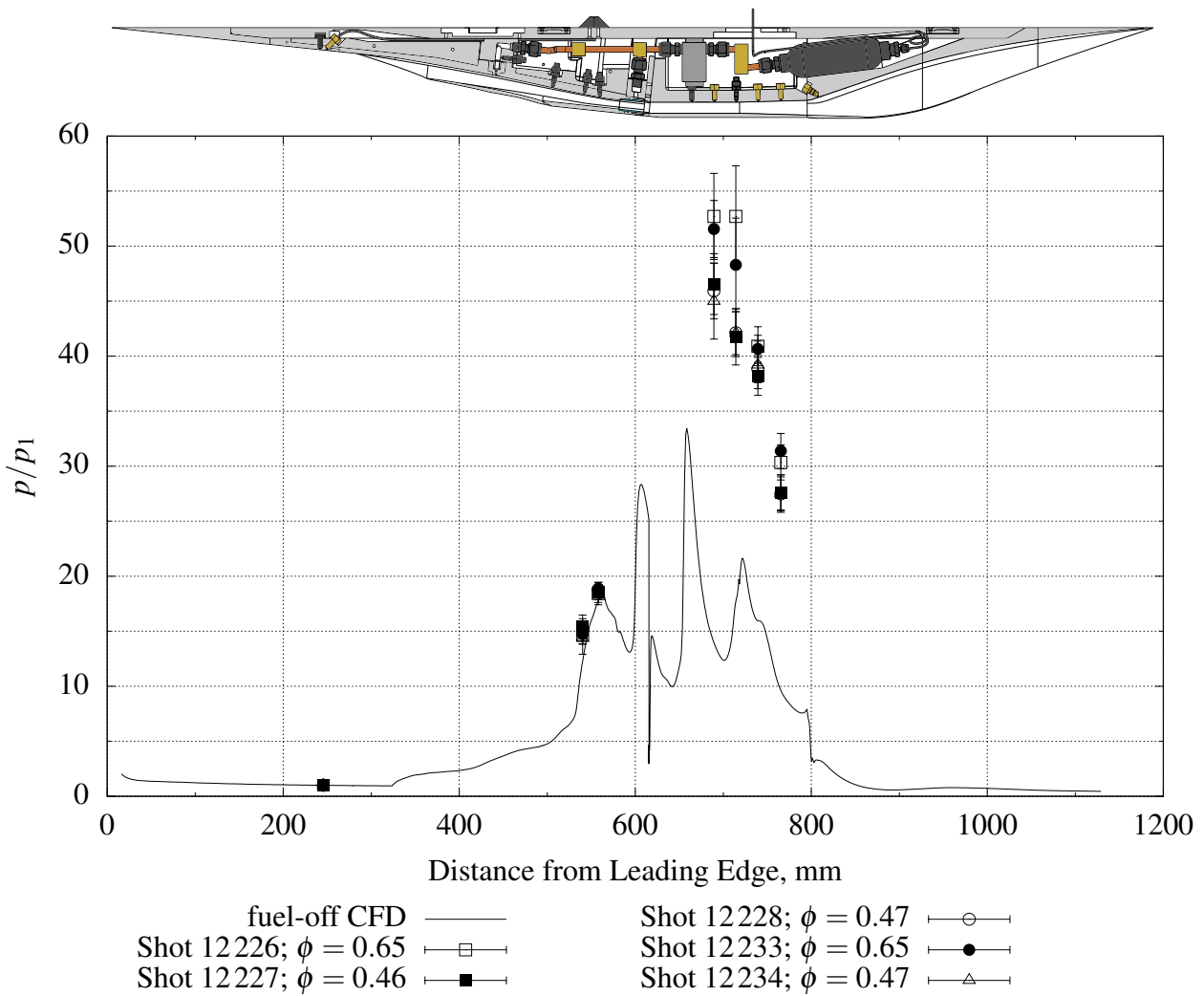


Figure 6.5: Normalised pressure data from the low equivalence ratio shots ($\phi < 0.7$) in comparison with CFD. The error bars show one standard deviation of the variation of pressure during the test time.

section.

The coordinate system used here had its origin at the centre of mass of the experimental model. The coordinate directions are chosen such that positive x corresponds to movement upstream and positive y corresponds to upwards motion. Positive α therefore indicates nose-up rotation to complete a right-handed cartesian coordinate system.

The data analysis is demonstrated for the data recorded for shot 12224. All other shots were processed in the same fashion. No images were recorded for shot 12227 and it is thus omitted from the following analysis.

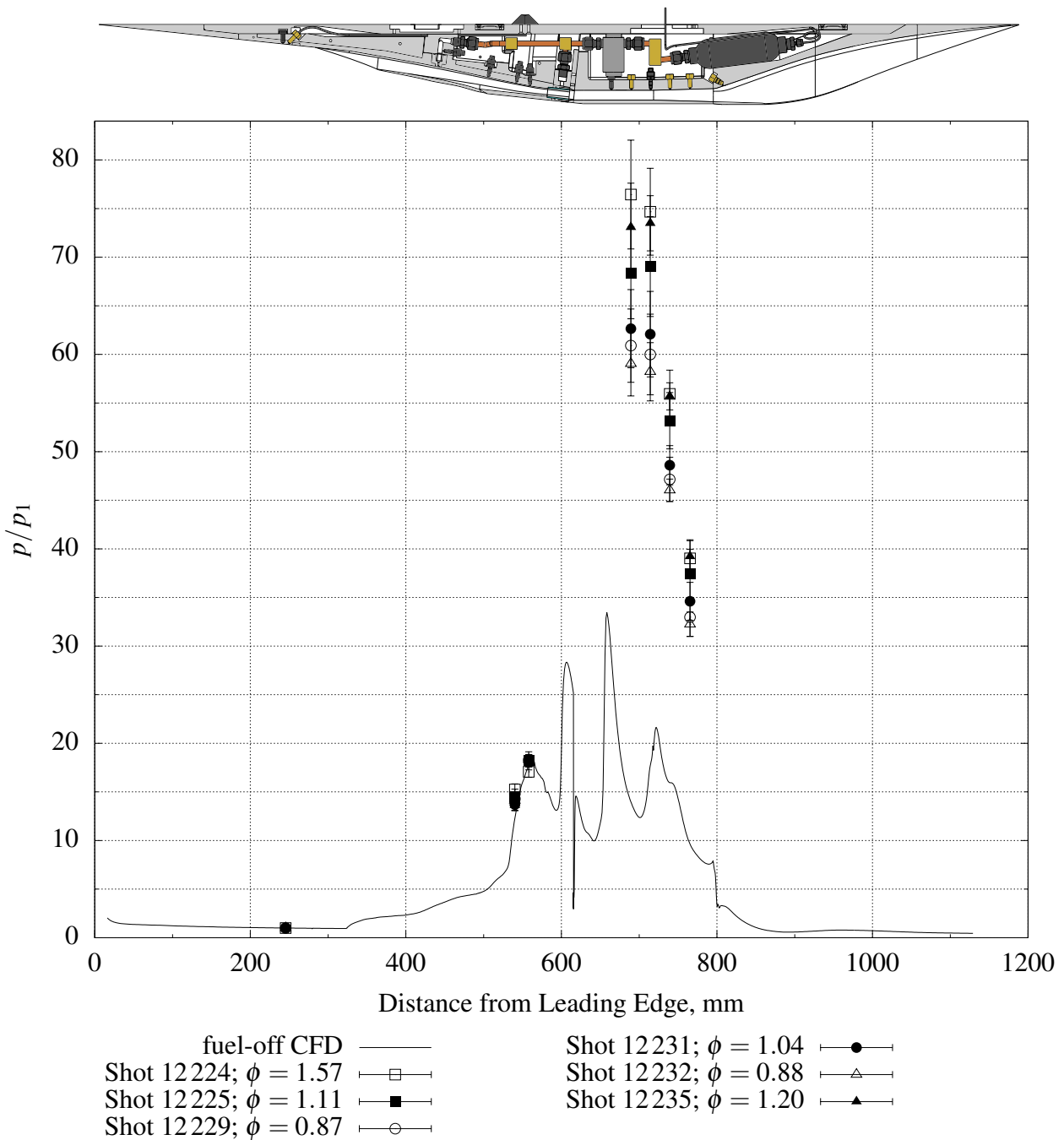


Figure 6.6: Normalised pressure data from the high equivalence ratio shots ($\phi > 0.8$) in comparison with CFD. The error bars show one standard deviation of the variation of pressure during the test time.

6.2.1 Cycle Analysis

As described in Section 4.1.3, the test time is chosen such that the error of the acceleration measurements is minimised. According to Equation (5.23), all other settings being equal, increasing the test time from 1.5 ms to 2.5 ms reduces the error S_a by a factor of approximately 3.6. However, as can be seen from the pressure traces in Figure 6.7, the longer the test time the greater the variation in nozzle

supply pressure as well as the fuel plenum pressures during a shot. For shot 12224, the pressure

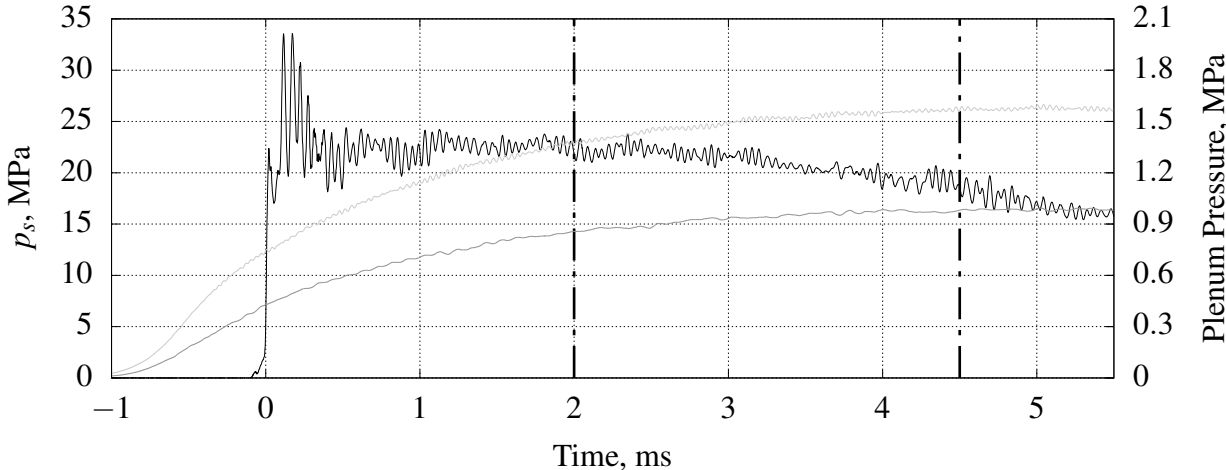


Figure 6.7: The nozzle supply pressure trace (—), the combustor plenum pressure (—) and the inlet plenum pressure (—) from shot 12224. ----- indicates the start and finish of the test time.

in both fuel plenums increases consistently over the test time. At the same time, the nozzle supply pressure is dropping. It follows that the mass flow rate of test gas through the engine drops while the mass flow rate of fuel and hence the equivalence ratio increases. Furthermore, the dynamic pressure and therefore the aerodynamic drag force reduces with time. Given these variations, the net engine forces were not constant during the test time.

To demonstrate that the variation in nozzle supply pressure and fuelling conditions does not significantly affect the measured acceleration and the assumption of constant acceleration is valid, 1D scramjet cycle analysis (Smart, 2007) and the fuel-off CFD results presented in Section 6.1.1 were used to estimate the development of the net engine thrust during each shot. Model trajectories were then calculated by twice integrating the determined thrust. Finally, a quadratic polynomial was fitted to each trajectory and its second derivative with respect to time was compared to the mean acceleration determined with cycle analysis. The comparison yields an estimate for how accurately the mean acceleration during the test time can be predicted by a quadratic fit.

Estimating the drag force for a given set of freestream conditions is straightforward. Assuming that

$$D_{nom} = q_{0,nom} \cdot C_D \cdot A \quad \text{and} \quad (6.6)$$

$$C_D = \text{const.}, \quad (6.7)$$

where C_D designates the drag coefficient of the Mach 12 REST engine and A its projected frontal area, the total drag determined in Section 6.1.1, designated D_{nom} , can be scaled directly with the freestream dynamic pressure, i.e.

$$D = \frac{q_0}{q_{0,nom}} \cdot D_{nom}. \quad (6.8)$$

Cycle analysis can be used to estimate the effects of varying the equivalence ratio on the gross engine thrust. Since CFD is more accurate in predicting the complex compression processes occurring on the forebody and inside the inlet, the conditions at the inlet throat were determined from the CFD solution presented in Section 6.1.1. The processes downstream of the throat, i.e. inside the combustor and the nozzle, are then calculated with cycle analysis.

The net thrust of the internal flowpath is thus calculated as

$$T_c = p_{10}A_{10} + \dot{m}_{10}u_{10} - (p_0A_c + \dot{m}_0u_0), \quad (6.9)$$

where

$$\dot{m}_{10} = \dot{m}_0 + \dot{m}_{H2}. \quad (6.10)$$

The fuel mass flow rate is calculated based on the equivalence ratio recorded during the respective shot:

$$\dot{m}_{H2} = \phi \cdot \dot{m}_{H2,\text{stoich}} = \phi \cdot X_{O2} \cdot A_c \rho_0 u_0 \cdot \frac{2 \cdot M_H}{M_O}. \quad (6.11)$$

Here, X_{O2} designates the mass fraction of the available oxygen in the freestream calculated by

$$X_{O2} = Y_O + Y_{O2} + \frac{M_O}{M_O + M_N} \cdot Y_{NO}. \quad (6.12)$$

M_H , M_O and M_N denote the molar mass of hydrogen, oxygen and nitrogen respectively. The ratio of the molar masses of hydrogen and oxygen in Equation (6.11) follows from the chemical reaction for the combustion of hydrogen:



Using the fuel mass flow rate, the forces resulting from fuel injection were calculated according to

$$T_{fi} = \dot{m}_{H2,I} \cdot \sqrt{R_{H2} \cdot T_{H2}} \cdot \left(\sqrt{\gamma_{H2}} + \frac{1}{\sqrt{\gamma_{H2}}} \right) \cdot \cos(57^\circ) \quad (6.14)$$

for the inlet injection and

$$T_{fc} = \dot{m}_{H2,C} \cdot \sqrt{R_{H2} \cdot T_{H2}} \cdot \left(\sqrt{\gamma_{H2}} + \frac{1}{\sqrt{\gamma_{H2}}} \right) \cdot \cos(15^\circ) \cdot \cos(6^\circ) \quad (6.15)$$

for the fuel injection in the combustor.

The gross engine thrust was calculated by subtracting the drag of the internal engine surfaces obtained with CFD, T_{fi} and T_{fc} from T_c . To account for the effects of varying freestream pressure, it was assumed that, over the range of conditions encountered during a single shot, gross thrust scales

linearly with static pressure, i.e.

$$T_g = \frac{p_0}{p_{0,nom}} \cdot T_{g,nom}. \quad (6.16)$$

The experimentally determined fuel thrust from the respective shot was then added to the scaled gross thrust and the net thrust could be calculated by subtracting the scaled drag force D .

Figure 6.8 shows the estimated drag, gross thrust and net thrust over time for shot 12224. They were calculated for 21 points at regular time intervals, with $\Delta t = 0.125$ ms during the test time. As

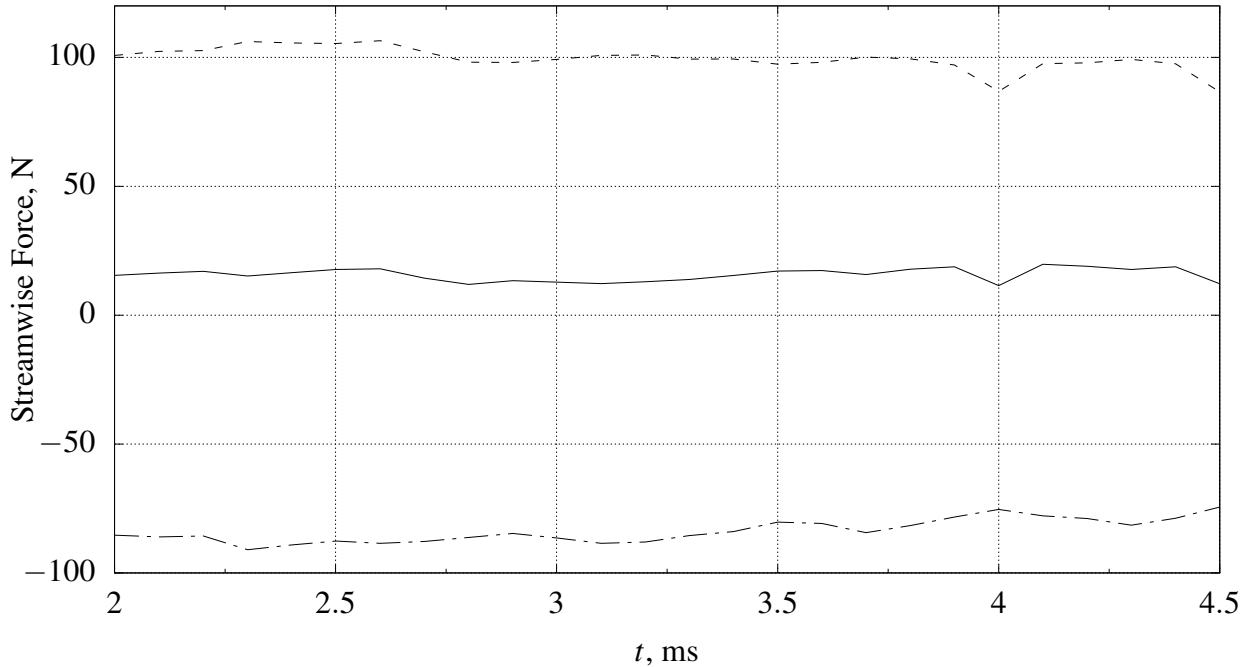


Figure 6.8: The estimated streamwise force development for shot 12224. — designates the net thrust, - - - the gross thrust and - · - the drag.

can be expected, given that the dynamic pressure drops during the test time, the magnitude of the drag force becomes consistently smaller over time. The gross thrust, however, is the result of two competing effects: an increase because of the rising equivalence ratio and a decrease following from the lower static pressure. For the case shown in Figure 12224 the increasing equivalence ratio does not result in a significant increase in gross thrust given that the equivalence ratio is above 1. However, the increasing fuel thrust partially counteracts the loss of gross thrust from the reducing static pressure. Owed to the fact that the drag decreases faster than the gross thrust the net thrust increases throughout the test time.

With the net thrust known, the estimated trajectory for shot 12224 can be calculated. The integration constants $u(t = 0)$ and $x(t = 0)$ were assumed to equal zero. Neither constant was found to affect the fitted quadratic polynomial. The calculated trajectory is shown in Figure 6.9 together with the fitted polynomial. It is evident that the curve fit is a good approximation of the calculated trajectory.

The mean acceleration, calculated from the thrust data, and the acceleration obtained from the

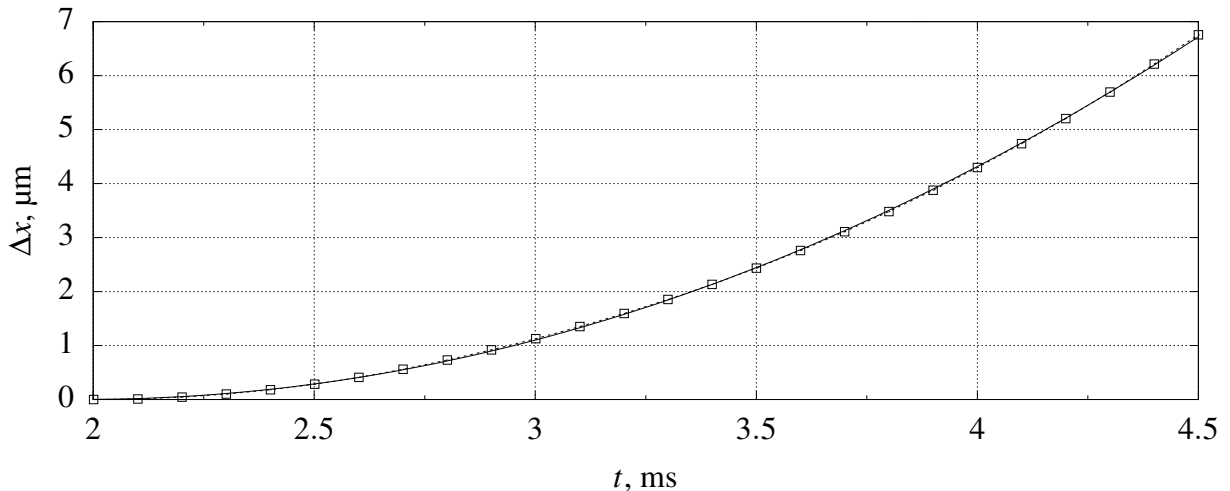


Figure 6.9: The trajectory estimate (□) together with the fitted quadratic polynomial (—) for shot 12224.

curve fit are compared in Table 6.5. From the data in Table 6.5 it can be concluded that the ex-

Table 6.5: The estimated average acceleration and the acceleration from the curve fit for all shots from the experimental campaign.

(a) Shots with the complete nozzle.

shot	\bar{a}_x , m s^{-2}	$a_{x,fit}$, m s^{-2}	Δa , m s^{-2}
12198	-12.5	-12.6	0.1
12199	-12.2	-12.3	0.1
12223	-12.1	-12.2	0.1
12224	2.20	2.12	0.08
12225	1.29	1.30	0.01
12226	-1.90	-1.94	0.04
12228	-3.7	-3.8	0.1
12229	-0.14	-0.16	0.02

(b) Shots with the tail third of the nozzle removed.

Shot	\bar{a}_x , m s^{-2}	$a_{x,fit}$, m s^{-2}	Δa , m s^{-2}
12230	-11.9	-12.0	0.1
12231	0.71	0.81	0.1
12232	-0.29	-0.32	0.03
12233	-2.19	-2.24	0.05
12234	-3.9	-3.9	0.0
12235	1.16	1.18	0.02

tended test time does not significantly affect the thrust measurements and the assumption of constant acceleration is warranted.

6.2.2 Facility Vibrations

As was stated in the introduction to this chapter, the image tracking measurements were affected by vibrations of the experimental facility. This section explains their cause and provides a general estimate of the expected error based on the frequencies present. The approach used to correct for the vibrations is demonstrated and discussed.

When vibrations are present the measured trajectory becomes a superposition of the motion of the experimental model and the motion of the measurement hardware. The dampers described in Section 4.3 were installed to reduce the effects of the vibrations on the measurements. However, even though the amplitude of the vibrations reduced and the dominant frequencies were lowered, the dampers were not sufficient to eliminate the vibrations altogether. A more sophisticated approach was not possible within the time frame of the present study.

Vibrations of the experimental model itself due to stress waves induced by the flow or the release of the model were assumed to be negligible. Assuming a speed of sound of $a_{Al} = 3040 \text{ ms}^{-1}$ in aluminium yields that the lowest possible frequency for vibrations resulting from stress waves occur at

$$f_{sw} = \frac{a_{Al}}{2 \cdot l} = 1280 \text{ Hz}, \quad (6.17)$$

where l designates the length of the experimental model. No such vibrations were observed in any of the signals recorded.

It was assumed in this analysis that the three trajectories of the model did not show any oscillatory behaviour given the relative steadiness of the recorded pressure signals. Obvious oscillatory features were therefore attributed to vibrations.

Detection and Analysis of the Vibrations

In order to capture the vibrations, 20 000 images (equivalent to 0.302 s) were recorded ahead of the stag trigger. Any motion detected in these images can be attributed to motion of the measurement hardware, given that the experimental model was stationary.

The vibrations begin when the tunnel starts recoiling, as Figure 6.10 demonstrates. When the piston is accelerated by the reservoir gas, stress waves begin travelling down the shock tunnel. Once they reach the test section and the camera, these begin to vibrate. Note that, regardless of the vibrations, the onset of the test flow can be seen in all traces by a distinct change in slope at $t = 0$. It is furthermore evident that the pitch angle is more sensitive to vibrations than the displacements in x and y . The pitch angle signal changes as soon as T4 is accelerated, while the displacement signals remain at rest for approximately 0.04 s longer.

Although the signals shown demonstrate that the vibrations were unsteady, the dominant frequencies, i.e. those with the largest amplitude, could be identified using a fast Fourier transform on the data for $t < 0$. Table 6.6 lists the dominant frequencies in each signal for shot 12 224. The vibrations

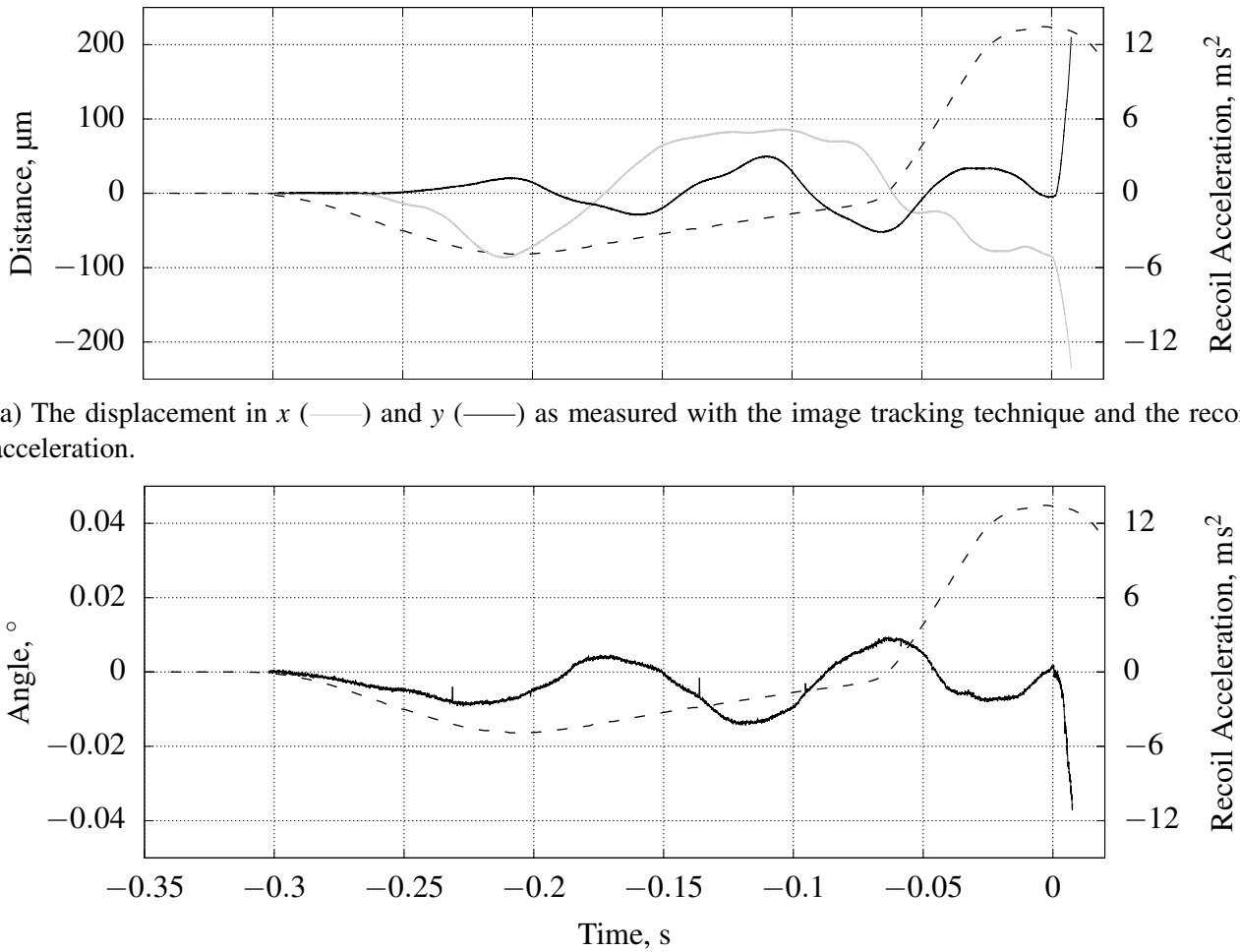


Figure 6.10: Image tracking data from shot 12224 overlayed with the acceleration experienced by T4 during a shot (---). $t = 0$ corresponds to the stag trigger.

Table 6.6: The dominant components of the vibrations detected in the trajectories from shot 12224

(a) The composition of the vibrations in x and y .

Variable	Frequency 1		Frequency 2		Frequency 3	
	A , μm	f , Hz	A , μm	f , Hz	A , μm	f , Hz
x	57.2	3.3	7.9	19.9	36.4	2
y	26.6	9.9	2.9	33.1	-	-

(b) The composition of the vibrations in α .

Variable	Frequency 1		Frequency 2		Frequency 3	
	A , 10^{-3} °	f , Hz	A , 10^{-3} °	f , Hz	A , 10^{-3} °	f , Hz
α	6.4	9.9	0.4	33.1	0.2	46.4

from all shots analysed in this chapter are presented in Tables B.1 and B.2 in Appendix B. Between two and four different frequencies could be identified from the recorded signals.

The dominant frequency in x consistently was 3.3 Hz. The amplitude, however, varied from 41.5 μm (shot 12229) to 114.2 μm (shot 12198). The amplitude in y was significantly lower and ranged from 9.6 μm (shot 12234) to 30.3 μm (shot 12225). The dominant frequency varied from 3.3 Hz (shot 12226) to 13.3 Hz (shot 12198). The pitch angle traces show a lot of high frequency oscillations. However, given the high frequency and small amplitude these were not taken into account. The dominant frequency of the pitch angle traces varied from 3.3 Hz (shots 12198, 12199, 12223, 12230, 12232 and 12233) to 9.9 Hz (shots 12226 and 12229). The measured amplitude ranged from $18.5 \times 10^{-3}\text{ }^\circ$ (shot 12198) to $4.2 \times 10^{-3}\text{ }^\circ$. It appears that the vibrations varied from shot to shot. They thus need to be analysed individually.

Once the flow starts and the experimental model begins to move it is very difficult to distinguish vibrations of the apparatus from the motion of the model. Figure 6.11 shows the signals recorded for x , y and α from the stag trigger for shot 12224. Note that the signals for x and y appear to be smooth

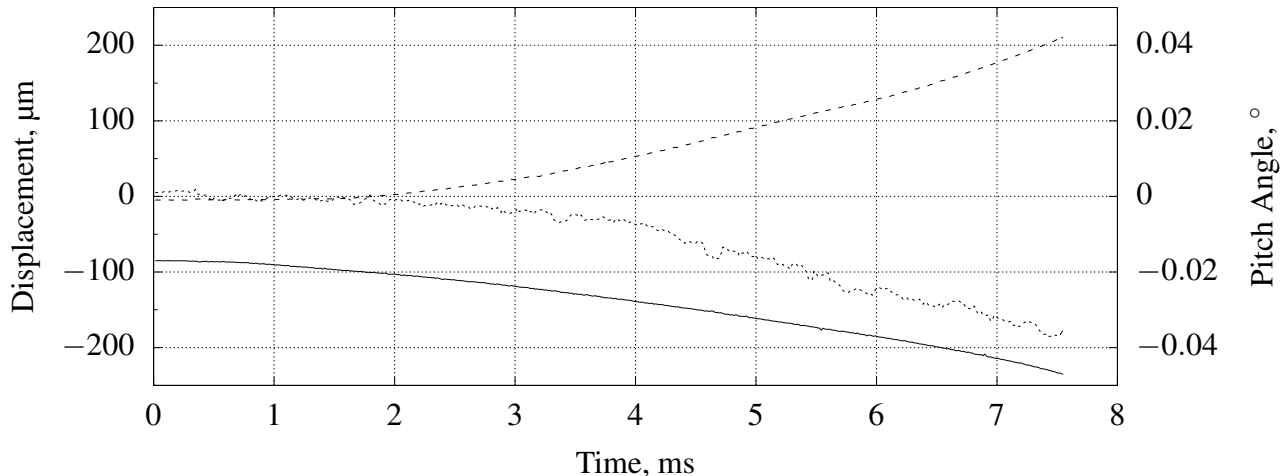


Figure 6.11: The displacement in x (—) and y (---) and the pitch angle (.....) as measured with the image tracking technique for $t > 0$.

and free of oscillations with significant amplitudes. The pitch angle signal, however, is very unsteady even though a clear trend can be identified. It must be emphasised that it is impossible to determine whether frequencies other than the ones listed in Table 6.6 affect the measurements during the test time. However, Figure 6.11 demonstrates that for the signals in x and y high frequency oscillations are either not present or of a very small amplitude. The presence of vibrations with $f \leq 132\text{Hz}$, which corresponds to one period in the length of signal shown in Figure 6.11, cannot be ruled out.

Error Estimate

The error introduced by harmonic vibrations of a single frequency and a single amplitude can be estimated by fitting quadratic polynomials to constant acceleration trajectories superposed with a sinusoidal oscillation at varying phase angles. The resulting trajectories can be described by

$$x_\varphi(t) = \frac{a_x}{2} \cdot t^2 + A \cdot \sin(2\pi f t + \varphi), \quad (6.18)$$

where A designates the amplitude of the vibration, f designates its frequency and φ denotes the phase angle of the vibration. By varying φ from 0 to 2π in increments of $\Delta\varphi = 0.002\pi$ and fitting quadratic polynomials to each trajectory $x_\varphi(t)$, the error of a given amplitude and frequency can be calculated as

$$\sigma_a = \sqrt{\frac{1}{n-1} \sum_{i=1}^n (a_x - a_\varphi)^2}. \quad (6.19)$$

Here, a_φ designates the acceleration determined from a curve fit to $x_\varphi(t)$ where the phase angle is calculated by $\varphi = (i-1) \cdot \Delta\varphi$. σ_a represents one standard deviation of the thus calculated accelerations.

The results of Equations (6.18) and (6.19) for $1 \mu\text{m} < A < 300 \mu\text{m}$ and $1 \text{Hz} < f < 10000 \text{Hz}$ are shown in Figure 6.12. It was found that for the frequencies and amplitudes considered the error was independent of the nominal acceleration a_x . Figure 6.12 demonstrates that there is a maximum at $f = 400 \text{Hz}$ irrespective of the amplitude of the oscillation. $f = 400 \text{Hz}$ corresponds to a period of $T = 2.5 \text{ms}$ which is equal to the length of the test time. Within the frequency range of $0.15 \cdot t_t^{-1} < f < 5 \cdot t_t^{-1}$ amplitudes as low as $1 \mu\text{m}$ cause errors larger than 0.1 m s^{-2} and need to be avoided.

To illustrate the cause for this effect, consider fitting a quadratic polynomial to a quadratic trajectory with $x(t) = 6.25 \cdot t^2$ superposed with a sinusoidal oscillation of $f = 400 \text{Hz}$ with $A = 10 \mu\text{m}$, as is shown in Figure 6.13. The fitted quadratic polynomial clearly has a vastly different curvature than the original quadratic trajectory. Given that exactly one period fits into the test time of 2.5 ms, the curve fit is too short to filter the oscillations. At a higher frequency a filtering effect occurs because of the periodicity of the sinusoid and the error reduces. Lower frequencies of the same amplitude have a smaller curvature and thus do not affect the measured acceleration as much.

While Figure 6.12 provides insight into the sensitivity of the measurements to different frequencies and the error caused by a single sinusoidal vibration, the effect of combining multiple frequencies still needs to be determined. This can be estimated using a modified version of Equation (6.18):

$$x(t) = \frac{a_x}{2} + \sum_{i=1}^n A_i \cdot \sin(2\pi f_i t + \varphi_i). \quad (6.20)$$

The phase angles φ_i were varied in increments of $\Delta\varphi = 0.02\pi$ and trajectories for all possible combinations of phase angles calculated. The best estimate for the error caused by the combination of a given set of sinusoidal vibrations could then be calculated using Equation (6.19). The error esti-

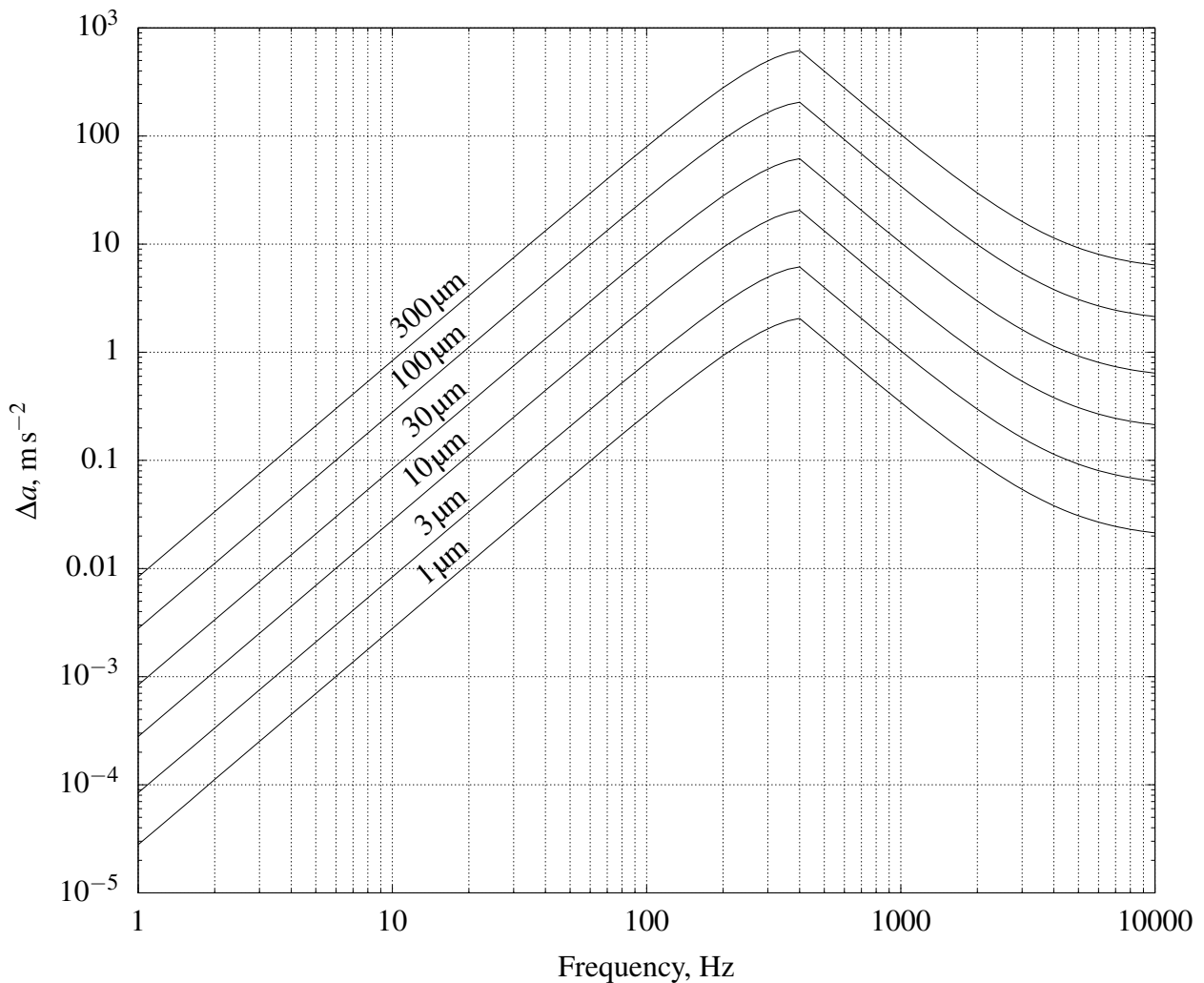


Figure 6.12: An estimate of the measurement error introduced by a single harmonic vibration depending on its amplitude and frequency. — indicates lines of constant amplitude.

mate for all three trajectories from shot 12224 is shown in Table 6.7. The interaction of multiple

Table 6.7: The error caused by the vibration of the measurement hardware during shot 12224 calculated using Equations (6.20) and (6.19).

Variable	σ_a	Unit
x	0.12	m s^{-2}
y	0.11	m s^{-2}
α	24.4	${}^\circ \text{s}^{-2}$

frequencies is clearly more complex than a simple addition of the errors induced by each frequency individually, although it is still independent of the nominal acceleration. However, the analysis shown suggests that the best estimate for the error caused by the detected vibrations is small compared to the inherent error of the image tracking technique presented in Section 5.4.2. The errors calculated with

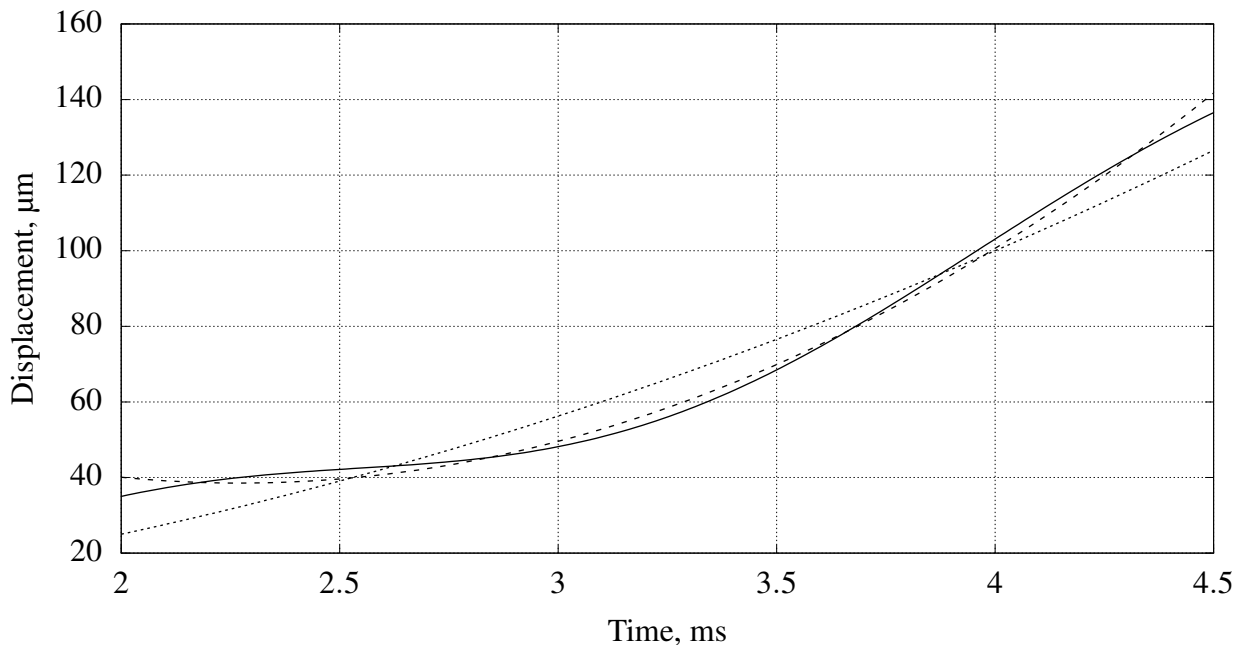


Figure 6.13: A quadratic trajectory superposed with a sinusoidal oscillation of $f = 400\text{ Hz}$ and $A = 10\mu\text{m}$. — indicates the resulting trajectory, - - - a quadratic polynomial fit to the trajectory and the original quadratic trajectory.

Equation (6.20) for all shots are shown in Appendix B.

Extrapolation using Fourier Series

In the following, the approach to correct the measured trajectories for the detected vibrations is explained. While the analysis in the previous section demonstrates that the errors introduced by mechanical vibrations are likely small, the values can be exceeded in individual cases. It is therefore warranted to attempt to correct for the vibrations.

Fourier series were fit to the measured signals up to the onset of flow and used to extrapolate the motion of the experimental apparatus into the test time. The extrapolated motion was then subtracted from the measured trajectory and the quadratic fit applied.

A Fourier series consists of a number of sine and cosine functions superposed to approximate a given curve, i.e.

$$S_{x,n}(t) = \frac{a_0}{2} + \sum_{i=1}^n \left(a_i \cdot \cos \left(\frac{2\pi i t}{T_F} \right) + b_i \cdot \sin \left(\frac{2\pi i t}{T_F} \right) \right). \quad (6.21)$$

Here, $S_{x,n}$ denotes a Fourier series fit to a signal $x(t)$ using n terms. T_F designates the sample window, i.e. the length of time the Fourier series is fit to. a_i and b_i respectively indicate the amplitudes of the

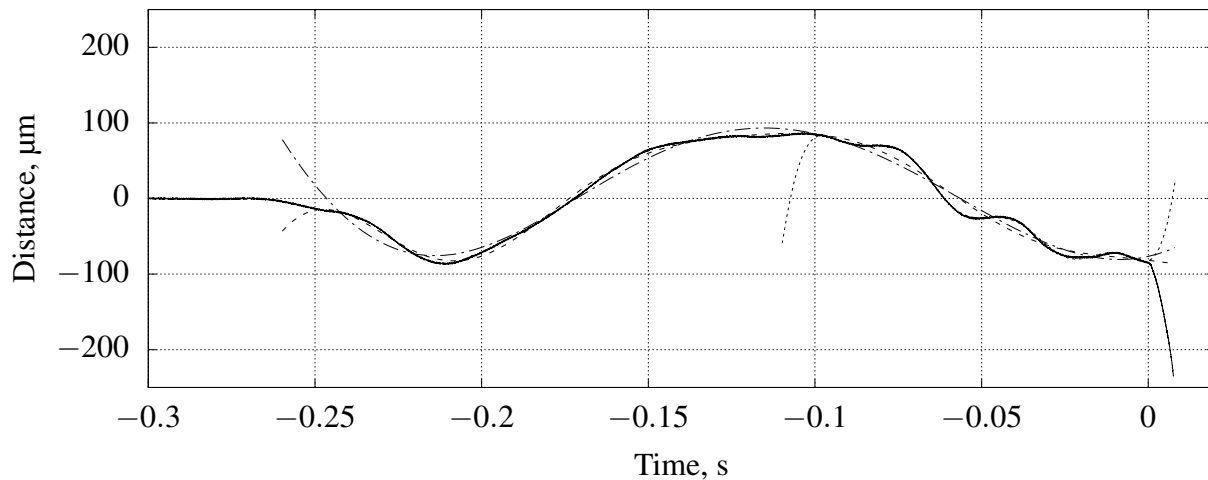
cosine and sine functions with frequency i/T_F . They can be calculated using

$$a_i = \frac{2}{T_F} \int_{t_{f,s}}^{t_{f,s}+T_F} x(t) \cdot \cos\left(2\pi t \frac{i}{T_F}\right) dt \quad \text{and} \quad (6.22)$$

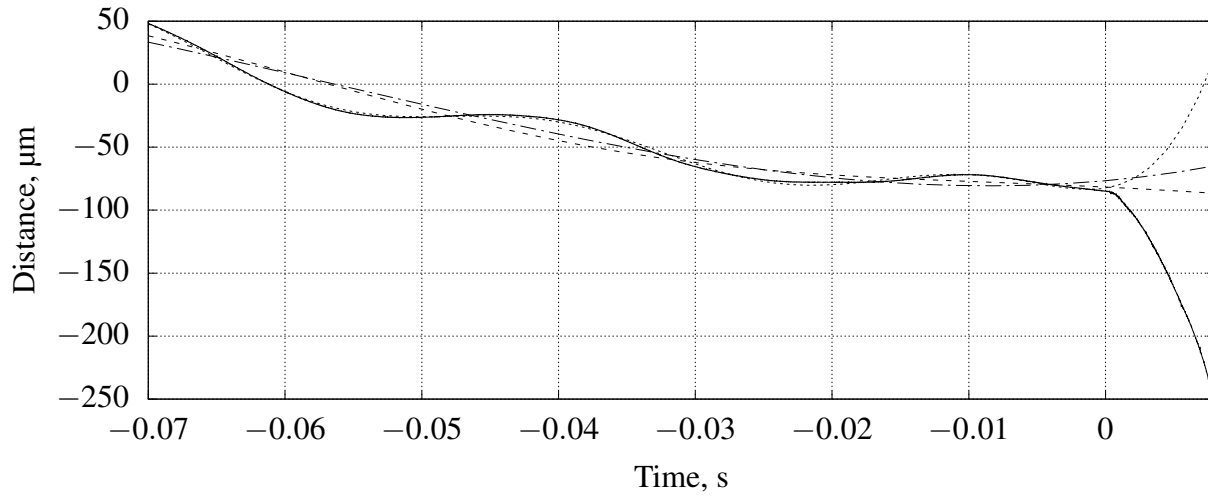
$$b_i = \frac{2}{T_F} \int_{t_{f,s}}^{t_{f,s}+T_F} x(t) \cdot \sin\left(2\pi t \frac{i}{T_F}\right) dt, \quad (6.23)$$

where $t_{f,s}$ designates the start of the sample window.

Regardless of T_F and n , the fit was applied to the data points from $t_{f,s}$ to $t = 0.2$ ms; the test gas reaches the test section at approximately $t = 0.3$ ms. Figure 6.14 shows three different Fourier series that were fit to the image tracking data in x of shot 12224. The first Fourier series, with $T_F = 100$ ms



(a) The complete recorded signal with the three Fourier series.



(b) A detailed view of $-0.07 \text{ s} < t < 0.008 \text{ s}$.

Figure 6.14: Three different Fourier series fit to the displacement data in x of shot 12224. The first, with $T_F = 100$ ms and $n = 5$, is indicated by ..., the second, with $T_F = 250$ ms and $n = 5$, is indicated by - - - and the third, with $T_F = 250$ ms and $n = 3$, is indicated by - · -.

and $n = 5$, reproduces the displacement signal from $t = -0.1$ s very accurately. However, it deviates strongly from the general trend of the signal from $t \approx 0$. It can therefore not be used to provide an estimate of the vibrations during the test time. The second and third Fourier series, with $T_F = 250$ ms and $n = 5$ and $T_F = 250$ ms and $n = 3$ respectively, do not capture as much detail as the first one. They do, however, reproduce the general trend of the displacement signal much more accurately for $t \approx 0$. In the process of choosing a Fourier series to extrapolate the vibrations for a given signal, priority was assigned to the general trend of the signal, i.e. the Fourier series had to capture the low frequency oscillation with the largest amplitude. Higher frequency oscillations were given lower priority. The second Fourier series shown in Figure 6.14 was therefore used for the displacement in x of shot 12224.

The measured acceleration in x during the test time changed by $\Delta a_x = 0.14 \text{ m s}^{-2}$ due to the correction. This is consistent with the estimate given in Table 6.7. The effect of the correction for the other shots is given in Table B.4 in Appendix B.

Note that the correction presented here can only account for the general trend of the signals recorded before each shot. The signals themselves were unsteady and different frequency oscillations appear in different locations of the signal. Changes in the vibration signals, in particular in the frequency range below 132 Hz, could not be ruled out or accounted for. The dampers used were effective at dampening vibrations of higher frequencies.

6.2.3 Force Measurement Data

The results of the image tracking technique are presented in the following. As in the previous sections, the data are presented using the example of shot 12224. At the end of this section plots of net acceleration against the fuel equivalence ratio are shown for all variables using all shots covered here. Note that, unlike in Section 6.2.2, the x and y displacement traces have been zeroed to the model position at the stag trigger.

The correction discussed in Section 6.2.2 was applied to all data shown except for shot 12231. A data storage fault made the images prior to the stag trigger unusable.

Figure 6.15 displays all three trajectories, in x , y and α , for shot 12224. The quadratic polynomials used to determine the mean acceleration are shown as well. The trajectories with their respective fits for the other shots are shown in Appendix C.

The quality of the fits can be evaluated using Equation (5.23). Where the position uncertainty s is calculated as one standard deviation of the difference between the measured data points and the fit, i.e. $\Delta x(t) = x_{fit}(t) - x(t)$. As was demonstrated in the remainder of Section 6.2 and Section 5.4, this must not be confused with the total measurement error. The quality of the fit merely indicates how closely the measured data points resemble a quadratic curve. However, both the position uncertainty s and the corresponding acceleration uncertainty S_a can help to gain valuable insight into the data. Large values of s relative to the total displacement or change in pitch angle during the test time indicate a

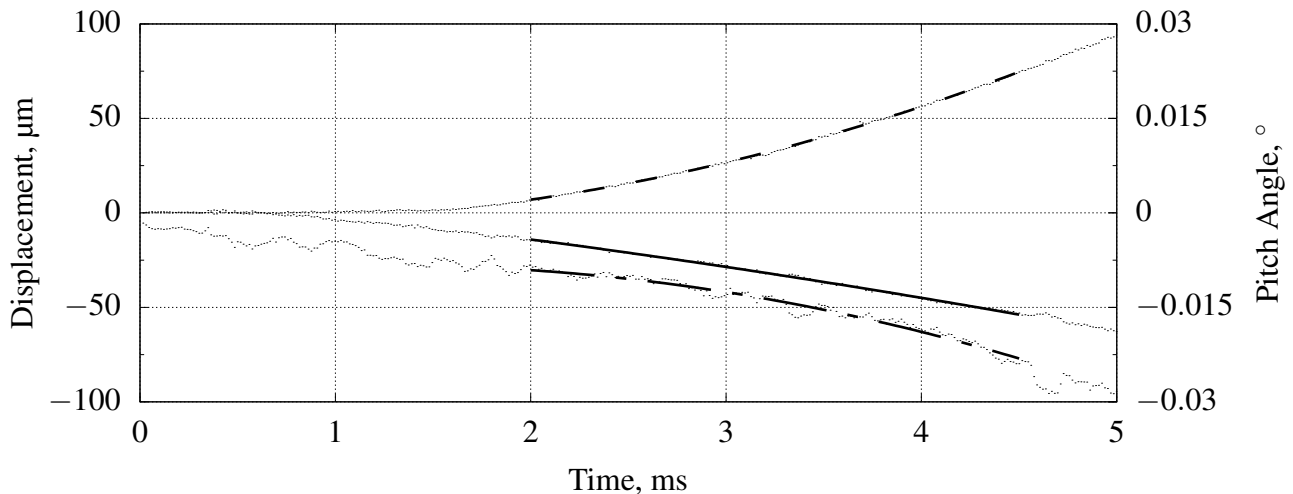


Figure 6.15: The corrected signals in x , y and α from shot 12224. The fitted quadratic polynomials in x (—), y (---) and α (-·-) are overlayed with the respective signal.

large deviation from a constant acceleration trajectory and therefore that the assumption of constant acceleration is not valid. Thus, while the fit quality by itself cannot indicate a reliable measurement, it can be used to identify unreliable data points.

Table 6.8 compares s with the total displacement or change in pitch angle, respectively, for all three variables for the data shown in Figure 6.15. The magnitude of s_α relative to the total change in

Table 6.8: The quality of the curve fits for shot 12224.

Variable	s	Unit	Δ	Unit	$s/\Delta, \%$
x	0.529	μm	37.3	μm	1.4
y	0.447	μm	67.2	μm	0.67
α	0.670	10^{-3} °	15.4	10^{-3} °	4.8

pitch angle can be attributed to the unsteady nature of the signal. The total measurement error in α is therefore likely larger than the analysis of the previous sections alone predicts. The fit quality in x and y suggests a near quadratic trajectory. It is thus reasonable to assume that the total measurement error in x and y does not significantly exceed that calculated in the previous sections. The fit quality of the displacement in x is consistently good, i.e. $s_x/\Delta x \leq 1.9\%$, for the shots analysed. With the exception of shots 12232 ($s_y/\Delta y = 4.9\%$) and 12233 ($s_y/\Delta y = 12.6\%$), the fit quality of the displacement in y is very good, i.e. $s_y/\Delta y \leq 1.3\%$. The fit quality of the pitch angle trajectories is consistently lower, i.e. $4.4\% \leq s_\alpha/\Delta \alpha \leq 13.7\%$. It is therefore postulated that the measurements of the pitching moment are less reliable than those of the lift and drag force for the data presented here. The fit quality of all shots is shown in Appendix C.

Figure 6.16 shows the measured acceleration against the fuel equivalence ratio of all shots. The errorbars indicate the sum of the uncertainty of the method presented in Section 5.4.2, the error introduced by the distortion of the images and the error resulting from the vibrations of the facility.

The shown trend lines are linear curves fit to the data points. Three points were excluded from the fits

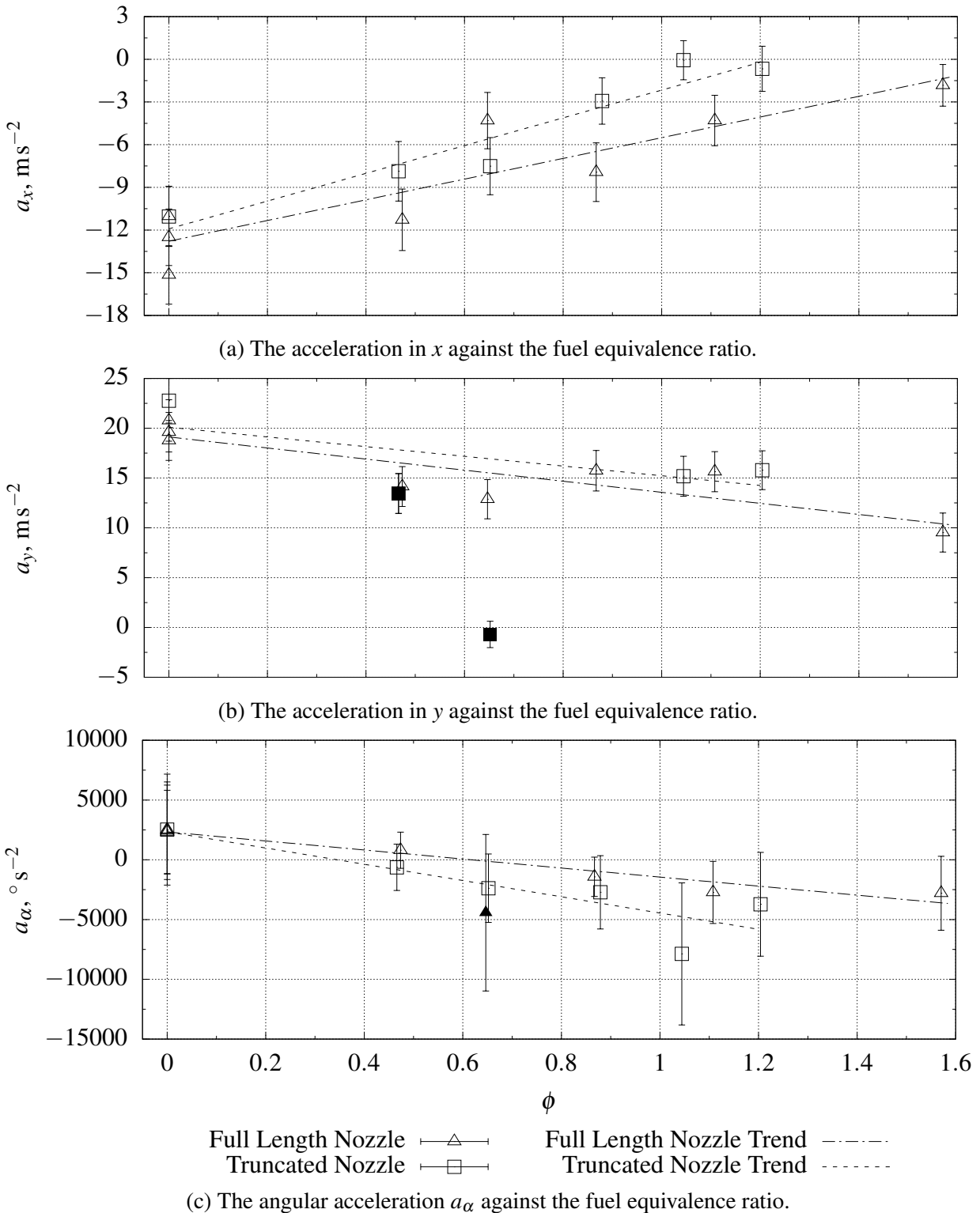


Figure 6.16: The measured acceleration from all shots against the fuel equivalence ratio. The trend lines were obtained by fitting a linear curve to the data points. Filled symbols were excluded from the fit.

given their low fit quality (see Table C.1). For a_y shots 12232 and 12233 were excluded from the fit. Shot 12226 was excluded from the trend line fit for a_α . No shots were excluded for a_x .

Clear trends can be identified for all three accelerations. As is expected, a_x increases with the fuel equivalence ratio. The surplus of thrust of the truncated nozzle over the full length nozzle does not exceed the experimental uncertainty. It must therefore be concluded that the effect of the last third of the nozzle on thrust production could not be determined in the experiments. The same applies to the question of whether the engine produced net thrust at high equivalence ratios. Net thrust lies within the measurement uncertainty and further analysis is necessary to refine the results. The analysis in Section 6.2.1 suggests that net thrust should have been achieved during shots 12224, 12225, 12234 and 12235. Considering that the drag force predicted by CFD could be matched in the experiments, it is postulated that the combustion efficiency was overpredicted in the cycle analysis. It is conceivable that the small scale of the model adversely affects combustion and thus causes the discrepancy.

The measurements suggest that the Mach 12 REST model produced significant positive lift over the entire range of operation. A negative trend with increasing equivalence ratio is notable. However, the prediction from CFD suggests that the model does not produce enough lift to overcome the force of gravity. No explanation for this could be found during the present study.

The recorded pitch angle trajectories, as shown, were subject to unsteady oscillations during the test time. Whether they were due to the limitations of the image tracking technique or physical vibrations of the apparatus could not be determined. A precise evaluation of the measurement uncertainty was thus impossible. The error bars presented are clearly insufficient. However, while the magnitude of the measured acceleration is questionable due to the unknown uncertainty, the identifiable trend is physically sound. Fuelled operation of the engine results in higher static pressure within the nozzle than unfuelled operation. The resulting force, due to the large distance from the nozzle to the centre of mass, creates a significant negative (nose down) pitching moment.

In Table 6.9 the measured net thrust from each shot is shown together with the gross thrust produced by the engine and the contribution of the fuel injection. The mean drag for each shot was calculated with the analysis presented in Section 6.2.1. The measured lift and the total lift force produced by the engine, i.e. the weight of the engine subtracted from the measured lift, are also listed. The pitching moment is not listed due to the uncertainty of the measurements.

Table 6.9: The net and gross thrust and the thrust from fuel injection for all shots as well as the measured lift and the total produced lift.

(a) Shots with the complete nozzle.

Shot	T , N	T_g , N	T_f , N	L , N	L_g , N
12198	-78.9 ± 15.1	-	-	134.0 ± 14.3	204.0 ± 14.3
12199	-108.4 ± 14.7	-	-	140.0 ± 14.2	210.0 ± 14.2
12223	-89.4 ± 14.2	-	-	149.0 ± 14.9	219.0 ± 14.9
12224	-13.1 ± 10.5	70.6 ± 10.5	7.5 ± 0.2	68.0 ± 14.0	138.0 ± 14.0
12225	-30.8 ± 12.7	53.4 ± 12.7	5.4 ± 0.1	112.0 ± 14.4	182.0 ± 14.4
12226	-30.8 ± 14.2	52.9 ± 14.2	3.1 ± 0.1	92.0 ± 14.1	162.0 ± 14.1
12228	-80.7 ± 15.5	4.3 ± 15.5	2.3 ± 0.1	101.0 ± 14.3	171.0 ± 14.3
12229	-56.7 ± 14.7	27.1 ± 14.7	4.2 ± 0.1	113.0 ± 14.5	183.0 ± 14.5

(b) Shots with the tail third of the nozzle removed.

Shot	T , N	T_g , N	T_f , N	L , N	L_g , N
12230	-79.0 ± 15.1	-	-	163.0 ± 16.0	233.0 ± 16.0
12231	-0.5 ± 9.8	88.5 ± 9.8	5.3 ± 0.1	109.0 ± 14.3	179.0 ± 14.3
12232	-20.9 ± 11.7	61.1 ± 11.7	4.1 ± 0.1	83.0 ± 14.6	153.0 ± 14.6
12233	-53.7 ± 14.3	32.2 ± 14.3	3.2 ± 0.1	-5.0 ± 9.5	65.0 ± 9.5
12234	-56.3 ± 15.0	29.3 ± 15.0	2.3 ± 0.1	96.0 ± 14.3	166.0 ± 14.3
12235	-4.8 ± 11.3	81.6 ± 11.3	5.9 ± 0.1	113.0 ± 14.0	183.0 ± 14.0

CHAPTER 7

CONCLUSIONS

The aim of the present study was to create a design method for 3D scramjet nozzles with a shape transition and to investigate the performance of a scramjet engine fitted with a nozzle designed with the proposed method in the T4 shock tunnel.

The design is based on the REST inlet design method by Smart (1999). An axisymmetric parent flowfield, optimised with the method by Rao (1958), is designed first. With the parent flowfield the flow properties of the nozzle are defined. Using a streamline tracing technique, a part of the parent flowfield is reproduced in a nozzle that interfaces with the combustor exit of the given scramjet engine. A second nozzle, which allows for a modular propulsion system and interfaces with the vehicle body is also created through streamline tracing. In blending these two nozzles, a shape transition nozzle that reproduces a part of the parent flowfield is created. The relative simplicity of the individual steps, only 2D axisymmetric calculations are required, allows for a quick design process; a complete shape transition nozzle can be designed in a matter of minutes.

For the design process, a type of parent flowfield with a contoured centre body was developed. The flowfield allows for the design flexibility of the centre body while mitigating the inherent creation of drag surfaces associated with non-contoured centre bodies in the streamline tracing process. It is thus possible to tailor the shape transition nozzle to a variety of combustor and vehicle shapes. Limitations of the design were explored and are due to the axisymmetric nature of the parent flowfield.

A nozzle was designed for the Mach 12 REST scramjet model designed by Doherty et al. (2015) with the proposed method. The comparison of the parent flowfield with flow inside the shape transition nozzle yielded that, as was postulated, they differ from one another where the shape transition nozzle deviates from a streamline traced geometry.

Experiments in the T4 shock tunnel were conducted at a Mach 8 test condition with a dynamic pressure of approximately 80 kPa. It was observed that the engine started and robust combustion could be achieved at various fuel equivalence ratios.

To measure the forces produced by the engine, the image tracking based force measurement technique by Laurence and Karl (2010) was employed. Free flight was achieved consistently during the test time. Thrust and lift forces were successfully measured on the unrestrained Mach 12 REST scramjet model. Although vibrations of the camera caused by the experimental facility affected the measurements, it was found that they only had a small effect on the measured forces. The pitching moment, however, could not be determined accurately.

In the two following sections the findings of the present study and recommendations for future work are listed. For clarity, they are categorised into those concerning the nozzle design, those concerning the experimental investigation and those concerning the image tracking technique. The experimental category is further split into technical and scientific findings, where technical findings and recommendations refer to the experimental design and scientific findings refer to the operation of the engine.

7.1 Findings of the Present Study

7.1.1 Nozzle Design

An axisymmetric parent flowfield with a contoured centre body can be used to create a shape transition nozzle without drag surfaces. The main objective of the present study was to develop a shape transition nozzle design methodology. Previous work has demonstrated that axisymmetric flowfields with centre bodies offer great design flexibility but can suffer from large drag surfaces (Kunze, 2014). In introducing the dual expansion nozzle with a contoured centre body, the flexibility could be retained while drag surfaces were eliminated from the design.

The introduced parent flowfield is limited to large centre body radii at useful nozzle area ratios. It was found that the centre body radius required to eliminate the drag surfaces increases with the area ratio of the parent flowfield. The larger the area ratio the more limited the design therefore becomes. For the flow conditions used in the present study, the centre body radius had to be at least $r_B/r_A = 0.67$ to achieve an area ratio of 10.

Allowing for small drag surfaces in early stages of the design opens up the design space. Small drag surfaces from streamline tracing may be acceptable because the blending process can be used to eliminate them. This allows for the centre body radius to be reduced and opens up the design space to a larger variety of nozzle shapes.

An interface to a diverging combustor can be added to the shape transition nozzle. While it is impossible to create a nozzle that is tangential to a diverging combustor with the presented method, a

diverging combustor can be extended and merged with the shape transition nozzle. It is acknowledged that this adjustment affects the nozzle flow. However, the alternative of creating shock waves at the nozzle start is postulated to be worse given the loss of total pressure.

The main parent flowfield properties could be captured in the designed shape transition nozzle. Despite the shape transition and the addition of the diverging combustor exit to the designed nozzle, the produced flowfield was similar to that of the parent flowfield. As was expected, the main differences existed where the nozzle was merged with the combustor.

The relative contribution to the inviscid thrust of the designed nozzle is similar to that of the parent flowfield. Rao's optimisation creates a nozzle that produces optimum thrust for a given length at the given inflow conditions. The relative contribution of each third of the parent flowfield to its total thrust can therefore be used as a guideline to determine whether the shape transition nozzle is close to an optimum itself. The rear third of the shape transition nozzle contributes 7.8 % of thrust to the nozzle's total thrust. The rear third of the parent flowfield contributes 8.8 % of its total thrust. It can therefore be concluded that, despite not being optimised itself, the designed nozzle shows good performance characteristics.

7.1.2 Image Tracking

Artificial images are a useful tool to gain insight into the image tracking technique. In the present study, artificial images were used to determine the uncertainty of the image tracking technique. It was found that the noise level of the sensor does not significantly contribute to the uncertainty. The change of attainable resolution for diagonal edges with their position within a pixel resulted in a large measurement error, particularly for small accelerations. Blurring of the images was found to contribute significantly to the error too.

The error associated with different settings of the Phantom[®] v611 could be quantified and it was determined that the image resolution has a bigger influence on the error than the frame rate of the camera.

7.1.3 Experimental

Scientific

Successful engine operation at the Mach 8 test condition. The engine consistently started at the Mach 8 test condition. Robust combustion was achieved at a range of equivalence ratios ($0.45 \leq \phi \leq 1.6$). The measured pressure of the unfuelled shots agreed well with the prediction from CFD.

The observed combustion induced pressure rise in the combustor was proportional to the equivalence ratio.

The tested Mach 12 REST engine module does not produce net thrust at the Mach 8 condition. Although net thrust was within the measurement uncertainty of the measured forces of shots 12234 and 12235 and the results from cycle analysis and CFD suggest that the engine module produces net thrust at the tested condition, the data from shots 12224 and 12225 shows that net thrust could not be achieved in the experiments. The discrepancy between the prediction from cycle analysis and the experimental results is postulated to be caused by the small scale of the Mach 12 REST model. At this size, viscous effects are likely to be disproportionately large, thus causing a disproportionate amount of skin friction drag and affecting combustion. It is, furthermore, emphasised that the viscous drag of the side walls of the module has the same magnitude for any number of engine modules. Its relative contribution to the total drag therefore reduces with the number of engine modules.

Positive net lift was observed despite negative lift being predicted by CFD. The force data from CFD presented in 6.1.1 suggests that the engine does not produce net lift. However, the measured lift force was distinctly positive for all shots. The cause for this discrepancy is not clear at this stage.

A change from a nose-up pitching moment for unfuelled operation of the engine to a nose-down pitching moment at fuelled conditions was observed. While the magnitude of the measured pitching moment is questionable due to the unsteady nature of the signals, the observed trend is physically sound. A higher pressure in the nozzle can result in a large change in pitching moment given the long lever with respect to the centre of mass.

The mass capture of the engine was equivalent to approximately 45 % of the maximum capture area. Significant flow spillage was observed at the Mach 8 test condition. It should be noted that, as is the case with the drag caused by the side walls, flow spillage on the forebody is expected to be the same for one engine module as it is for any number of modules.

Engine operation at the 2 mm test condition was limited by the amount of fuel in the inlet. Equivalence ratios above 0.9 could not be achieved at the 2 mm test condition. It was found that the fuel in the inlet ignited, which unstarted the engine. In some cases the starting shock of the facility ignited the fuel in the inlet when the fuelling started too early. In other cases the fuel air mixture self-ignited during the test time. Unstarts originating from the combustor were not observed in either condition.

Technical

Successful force measurements using the image tracking technique. The present study marked the first time that forces on a free-flying scramjet engine were measured in the T4 shock tunnel. While several difficulties were encountered, the image tracking technique proved reliable in measuring the gravitational acceleration during the calibrations and thrust and lift forces of the unrestrained scramjet model during shots. The measurements of the pitching moment, however, were not found to be satisfactory.

The catch and release mechanisms worked reliably and the model was consistently free-flying during the test time. The catch and release mechanisms underwent multiple design iterations over the course of the present study. The latest version, shown in Figure 4.15, allowed for easy installation of the fishing line and model alignment. It was found that it is beneficial to wind up both ends of one strand of fishing line simultaneously as opposed to separately. The inserts, holding the razor blades, were altered to ensure the fishing line cannot catch on the insert before coming into contact with the razor blade. It was furthermore important to change the razor blade after every shot to ensure that the fishing line broke ahead of the test time. Concerning the rear support, it was most important to create enough space for all cables, connectors and the fuel line to be fitted inside with enough spare room to be without tension. The instrumentation and fuel supply line were not found to affect the motion of the model.

Varying freestream and fuelling conditions did not significantly affect the force measurements. Extending the test time to 2.5 ms was found useful in reducing the uncertainty of the image tracking technique. Using cycle analysis, it could be demonstrated that the assumption of constant acceleration during the test time was warranted and did not introduce significant error.

The dampers were effective in reducing the amplitude and frequency of the observed vibrations. In comparison with the second experimental campaign, the amplitude and frequency of the vibrations was reduced significantly. It was furthermore possible to clearly identify the start of model motion in the trajectories despite the vibrations. This was not the case in the second test campaign. However, the dampers did not isolate the camera and imaging lens entirely from the vibrations.

Low frequency vibrations are manageable. While it should be the aim to isolate the camera and imaging lens from vibrations entirely, it was found that the effect of the low frequency vibrations encountered in the third experimental campaign could be quantified and did not exceed the inherent uncertainty of the measurement technique. Using the Fourier series to extrapolate the measured signal can provide a means to remove vibrations from the measured signal. Vibrations at frequencies in the

range of $0.15 \cdot t_t^{-1} < f < 5 \cdot t_t^{-1}$ must be avoided at all cost since they cause the largest measurement errors.

The fit quality can predict bad data points reliably. It is again emphasised that the fit quality (see Section 6.2.3) does not quantify the uncertainty of the measurements. However, it was found that it can be used as a tool to identify bad data points.

The on-board fuel system was adequate. The 75 ml Swagelok® sample cylinder was large enough to supply enough fuel for approximately constant plenum pressures for about 3 ms at all fuelling conditions. The Gems™ A2014 solenoid valve opened sufficiently fast and provided a large enough fuel mass flow rate for constant fuelling conditions. Although its opening time changed during the experimental campaign, it was consistent before and after the change. It is postulated that wear on the spring that resets the valve when it is de-energised caused the change. This should be taken into consideration if the valve is reused.

Using brass manifolds to connect different pieces of tubing instead of standard fittings allowed for the fuel system to fit inside the Mach 12 REST model.

The Mach 12 REST model does not fit into the core flow diamond of the Mach 7.6 facility nozzle. In Section 4.1.2 it was shown that the Mach 12 REST model does not fit into the core flow diamond of the Mach 7.6 facility nozzle. The effects of this are not entirely clear. It is conceivable that this affects the engine forces.

3D printing is an adequate manufacturing method for scramjet nozzles for shock tunnel experiments. The 3D printed nozzle was found to be of satisfactory quality. Both the surface quality of the nozzle as well as the fit to the combustor were good. No obvious signs of wear were observed over the course of the experimental campaign. The relative ease with which complex parts can be manufactured as well as the low cost are clear advantages over machined parts.

7.2 Recommendations

7.2.1 Nozzle Design

Further explore the limits of the design methodology. In the present study, nozzle were only designed for one set of inflow and ambient conditions. It is of interest to gain a more thorough understanding of the limits of the parent flowfield. For this purpose, different flow conditions should be investigated.

Investigate the possibility of a 3D parent flowfield. The limiting factor of the proposed design is the axisymmetry of the parent flowfield. A three dimensional parent flowfield could allow for nozzles that are not possible with the proposed method and for instance account for non-uniform inflows. The main trade-off would be the increased time it takes to design a nozzle.

7.2.2 Image Tracking

Several improvements of the image tracking technique are possible. The first step in improving the image tracking based measurements should be the isolation of the imaging side from all vibrations. For this purpose the hardware should be moved to a suitable optics table. This would also allow the use of a lens with a longer focal length. The observed distortion of the images was due to the lens required to focus the image onto the camera sensor; which was less than 500 mm away from the test section window. The removal of distortions would also allow for the use of the analytic tracking technique as opposed to the edge tracking technique. An experimental evaluation of possible distortion should nonetheless be performed at the beginning of an experimental campaign using the technique. The light intensity of the LED driver can be increased by using an appropriate combination of lenses on the source side. A more intense light source increases the magnitude of the intensity gradients at the edge location and should reduce the effect noise and artifacts in the flow have. At the Mach 10 test condition flow luminosity has been found to obscure images. A high intensity light source is therefore a requirement for image tracking based force measurements at the Mach 10 condition.

The shape of the tracking object can be improved for small accelerations. Considering that the diagonal edges were the main source of error at small accelerations, other shapes should be considered for the tracking object. Any edge angle other than 45° should improve the accuracy of the technique. Artificial images can be used to find the optimum shape.

7.2.3 Experimental

Scientific

The nozzle was designed for a Mach 10 condition. Given that the nozzle was not tested at its design condition, experiments at a Mach 10 flight condition are of interest. These would allow a comparison to the experiments conducted and the nozzle designed by Doherty. However, it is acknowledged that the Mach 10 test condition of the T4 shock tunnel produces a much shorter test time than the Mach 8 condition used in the present study. The difficulties experienced with the image tracking technique thus need to be addressed for the engine forces to be measured accurately.

Technical

Changes to the fuel system. For future experiments the fuel system should be changed to create a more suitable fuel split.

REFERENCES

- Anderson, G. Y., C. McClinton, and J. P. Weidner (2001). “Scramjet Performance”. In: *Scramjet Propulsion*. Ed. by E. T. Curran and S. N. B. Murthy. Progress in astronautics and aeronautics ; v. 189. Reston ,VA: American Institute of Aeronautics and Astronautics, pp. 369–446. ISBN: 1563473224. DOI: 10.2514/5.9781600866609.0369.0446. URL: <http://arc.aiaa.org/doi/10.2514/5.9781600866609.0369.0446>.
- Anderson, J. D. (2003). *Modern Compressible Flow*. third. McGraw-Hill. ISBN: 978-0-07-242443-0.
- Andrews, E. H. and E. A. Mackley (1994). *NASA’s Hypersonic Research Engine Project: A Review*. TM 107759. NASA.
- Barger, R. L. (1981). *A procedure for designing forebodies with constraints on cross-section shape and axial area distribution*. Tech. rep. NASA-TP-1881, L-14516. NASA Langley Research Center; Hampton, VA, United States.
- Basore, K. (2015). *2015 M8 Pitot Survey*. Tech. rep. School of Mechanical and Mining Engineering, The University of Queensland, pp. 1–22.
- Beck, W., G. Eitelberg, T. McIntyre, J. Baird, J. Lacey, and H. Simon (1991). “The High Enthalpy Shock Tunnel in Göttingen (HEG)”. In: *Proceedings of the 18th International Symposium on Shock Waves*, pp. 677–682.
- Bernstein, L. (1975). *Force Measurements in Shot-Duration Hypersonic Facilities*. Tech. rep. November. Advisory Group for Aerospace Research and Development, North Atlantic Treaty Organization, p. 224.
- Buttsworth, D. R. (2010). “Ludwieg tunnel facility with free piston compression heating for supersonic and hypersonic testing”. In: *Proceedings of the 9th Australian Space Science Conference*. National Space Society of Australia Ltd., pp. 153–162.
- Cain, T. (2010). “Scramjet Nozzles”. In: *AVT-185 RTO AVT/VKI Lecture Series*. Gas Dynamics LTD Farnborough (United Kingdom). Hampshire.

REFERENCES

- Canny, J. (1986). “A Computational Approach to Edge Detection”. In: *IEEE Transactions on Pattern Analysis and Machine Intelligence* PAMI-8.6, pp. 679–698. ISSN: 0162-8828. DOI: 10.1109/TPAMI.1986.4767851. URL: <http://ieeexplore.ieee.org/lpdocs/epic03/wrapper.htm?arnumber=4767851>.
- Curran, E. T. (2001). “Scramjet Engines: The First Forty Years”. In: *Journal of Propulsion and Power* 17.6, pp. 1138–1148.
- Doherty, L. J. (2014). “An Experimental Investigation of an Airframe Integrated Three-Dimensional Scramjet Engine at a Mach 10 Flight Condition.pdf”. PhD thesis. The University of Queensland. DOI: <https://doi.org/10.14264/uql.2014.382>.
- Doherty, L. J., M. K. Smart, and D. J. Mee (2015). “Experimental Testing of an Airframe-Integrated Three-Dimensional Scramjet at Mach 10”. In: *AIAA Journal* 53.11, pp. 3196–3207. ISSN: 0001-1452. DOI: 10.2514/1.J053785. URL: <http://arc.aiaa.org/doi/10.2514/1.J053785>.
- East, R. A., R. J. Stalker, and J. P. Baird (1980). “Measurements of heat transfer to a flat plate in a dissociated high-enthalpy laminar air flow”. In: *Journal of Fluid Mechanics* 97.4, pp. 673–699. ISSN: 14697645. DOI: 10.1017/S0022112080002753.
- Evvard, J. C. and S. H. Maslen (1952). *Three-Dimensional Supersonic Nozzles and Inlets of Arbitrary Exit Cross Section*. Tech. rep. Cleveland, Ohio: Lewis Flight Propulsion Laboratory. URL: <https://apps.dtic.mil/dtic/tr/fulltext/u2/a380474.pdf>.
- Ferri, A. (1968). “Review of scramjet propulsion technology.” In: *Journal of Aircraft* 5.1, pp. 3–10.
- Gildfind, D. E., R. G. Morgan, M. McGilvray, P. A. Jacobs, R. J. Stalker, and T. N. Eichmann (2011). “Free-piston driver optimisation for simulation of high Mach number scramjet flow conditions”. In: *Shock Waves* 21.6, pp. 559–572. ISSN: 09381287. DOI: 10.1007/s00193-011-0336-9.
- Gollan, R. J. and P. A. Jacobs (2013). “About the formulation, verification and validation of the hypersonic flow solver Eilmer”. In: *International Journal for Numerical Methods in Fluids* 73.1, pp. 19–57. ISSN: 02712091. DOI: 10.1002/fld.3790. arXiv: fld.3790 [DOI: 10.1002]. URL: <http://doi.wiley.com/10.1002/fld.3790>.
- Govinda, A., M. K. K. Devaraj, Y. Singh, N. Thakor, V. R. Kulkarni, S. N. Omkar, and G. Jagadeesh (2017). “Design of Optimized Two-Dimensional Scramjet Nozzle Contour for Hypersonic Vehicle Using Evolutionary Algorithms”. In: *30th International Symposium on Shock Waves 1*. Cham: Springer International Publishing, pp. 119–124. DOI: 10.1007/978-3-319-46213-4_19. URL: [https://doi.org/10.1007/978-3-319-46213-4%7B%5C_%7D19](https://doi.org/10.1007/978-3-319-46213-4%7B%5C_%7D19%20http://link.springer.com/10.1007/978-3-319-46213-4%7B%5C_%7D19).
- Guderley, K. and E. Hantsch (1955). “Beste Formen für achsensymmetrische Überschalldüsen”. In: *Zeitschrift für Flugwissenschaften* 3, pp. 305–313.
- Haney, J. and M. Bradley (1995). “Waverider nozzle integration issues”. In: *33rd Aerospace Sciences Meeting and Exhibit*. Reston, Virginia: American Institute of Aeronautics and Astronautics. DOI: 10.2514/6.1995-847. URL: <http://arc.aiaa.org/doi/10.2514/6.1995-847>.

- Hannemann, K., J. Martinez Schramm, S. Karl, and S. J. Laurence (2017). “Enhancement of Free Flight Force Measurement Technique for Scramjet Engine Shock Tunnel Testing”. In: *21st AIAA International Space Planes and Hypersonics Technologies Conference* 21.March, pp. 1–16. DOI: 10.2514/6.2017-2235. URL: <https://arc.aiaa.org/doi/10.2514/6.2017-2235>.
- Hannemann, K., J. Martinez Schramm, S. J. Laurence, S. Karl, T. Langener, and J. Steelant (2014). “Experimental and Numerical Analysis of the small Scale LAPCAT II Scramjet Flow Path in High Enthalpy Shock Tunnel Conditions”. In: *Space Propulsion* 19, p. 22.
- Heiser, W. H. and D. T. Pratt (1994). *Hypersonic airbreathing propulsion / William H. Heiser, David T. Pratt with Daniel H. Daley and Unmeel B. Mehta*. AIAA education series. Washington, D.C.: American Institute of Aeronautics and Astronautics. ISBN: 1563470357.
- Henry, J. R. and G. Y. Anderson (1973). *Design considerations for the airframe-integrated scramjet*. Tech. rep. NASA-TM-X-2895, L-8152. NASA Langley Research Center; Hampton, VA, United States.
- Herring, D. J. (1992). “Design of an Optimum Thrust Nozzle for a Typical Hypersonic Trajectory Through Computational Analysis”. PhD thesis. Air University.
- Hiraiwa, T., S. Tomioka, S. Ueda, T. Mitani, M. Yamamoto, and M. Matsumoto (1995). “Performance variation of scramjet nozzle at various nozzle pressure ratios”. In: *Journal of Propulsion and Power* 11.3, pp. 403–408. ISSN: 0748-4658. DOI: 10.2514/3.23858. URL: <http://arc.aiaa.org/doi/10.2514/3.23858>.
- Hirschen, C. and A. Gühan (2009). “Influence of Heat Capacity Ratio on Pressure and Nozzle Flow of a Scramjets”. In: *Journal of Propulsion and Power* 25.2, pp. 303–311. ISSN: 0748-4658. DOI: 10.2514/1.39380. URL: [http://arc.aiaa.org/doi/10.2514/1.39380](http://arc.aiaa.org/doi/10.2514/6.2006-8095%20http://arc.aiaa.org/doi/10.2514/1.39380).
- Hoffman, J. D., M. P. Scofield, and H. D. Thompson (1972). “Thrust nozzle optimization including boundary-layer effects”. In: *Journal of Optimization Theory and Applications* 10.3, pp. 133–159. ISSN: 00223239. DOI: 10.1007/BF00934730.
- Hornung, H. G., B. Sturtevant, J. Bélanger, S. Sanderson, and M. Brouillette (1991). “Performance of the new free-piston shock tunnel T5 at GALCIT”. In: *18th Int. Symp. on Shock Waves, Sendai, Japan*. Sendai, Japan: Springer Berlin Heidelberg, pp. 603–610.
- Huang, W., Z. G. Wang, D. B. Ingham, L. Ma, and M. Pourkashanian (2013). “Design exploration for a single expansion ramp nozzle (SERN) using data mining”. In: *Acta Astronautica* 83, pp. 10–17. ISSN: 00945765. DOI: 10.1016/j.actaastro.2012.09.016. URL: <http://dx.doi.org/10.1016/j.actaastro.2012.09.016>.
- Igra, O. and K. Takayama (1991). “Shock Tube Study of the Drag Coefficient of a Sphere in a Non-stationary Flow”. In: *Proceedings of the 18th International Symposium on Shock Waves*. Sendai, Japan: Springer, pp. 491–497.

REFERENCES

- Itoh, K., S. Ueda, H. Tanno, T. Komuro, and K. Sato (2002). “Hypersonic aerothermodynamic and scramjet research using high enthalpy shock tunnel”. In: *Shock Waves* 12.2, pp. 93–98.
- Jacobs, P. A. and C. M. Gourlay (1991). “An interactive method-of-characteristics program for gas-dynamic calculations”. In: *International Journal of Applied Engineering Education* 7.3.
- Jacobs, P. A. and R. J. Gollan (2016). “Implementation of a Compressible-Flow Simulation Code in the D Programming Language”. In: *Applied Mechanics and Materials* 846, pp. 54–60. ISSN: 1662-7482. DOI: 10.4028/www.scientific.net/AMM.846.54. URL: <http://www.scientific.net/AMM.846.54>.
- Jacobs, P. A., R. J. Gollan, D. Potter, F. Zander, D. E. Gildfind, P. Blyton, W. Y. K. Chan, and Do (2014). *Estimation of High-Enthalpy Flow Conditions for Simple Shock and Expansion Processes Using the ESTCj Program and Library*. Tech. rep. Centre for Hypersonics, pp. 1–104. URL: <http://cfcfd.mechmining.uq.edu.au/pdf/estcj.pdf>.
- Jacobs, P. A., R. J. Gollan, and F. Zander (2011). *Still Using NENZF? That's so 1960s*. URL: <http://cfcfd.mechmining.uq.edu.au/pdf/nenzfr-presentation-pj-iwstt-2011.pdf>.
- Jacobs, P. A., R. C. Rogers, E. H. Weidner, and R. D. Bittner (1992). “Flow establishment in a generic scramjet combustor”. In: *Journal of Propulsion and Power* 8.4, pp. 890–899. ISSN: 0748-4658. DOI: 10.2514/3.23566. URL: <http://arc.aiaa.org/doi/10.2514/3.23566>.
- Jain, R., B. Kasturi, B. G. Schunck, R. Kasturi, and B. G. Schunck (1995). *Machine Vision*. Vol. 5. McGraw-Hill, Inc. ISBN: 0-07-032018-7.
- Jegede, O. O. and W. J. Crowther (2016). “Low Order Supersonic Nozzle Design using Superimposed Characteristics”. In: *54th AIAA Aerospace Sciences Meeting* January, pp. 1–13. DOI: AIAA2016-0805.
- Jessen, C. and H. Grönig (1989). “A new principle for a short-duration six component balance”. In: *Experiments in Fluids* 8.3-4, pp. 231–233. ISSN: 0723-4864. DOI: 10.1007/BF00195800. URL: <http://link.springer.com/10.1007/BF00195800>.
- Joarder, R. and G. Jagadeesh (2004). “A new free floating accelerometer balance system for force measurements in shock tunnels”. In: *Shock Waves* 13.5, pp. 409–412. ISSN: 09381287. DOI: 10.1007/s00193-003-0225-y.
- Johnston, P. J., J. M. Cubbage, and J. P. Weidner (1971). “Studies of Engine-Airframe Integration on Hypersonic Aircraft”. In: *Journal of Aircraft* 8.7, pp. 495–501. ISSN: 0021-8669. DOI: 10.2514/3.59129. URL: <http://arc.aiaa.org/doi/10.2514/3.59129>.
- Kanopoulos, N., N. Vasanthavada, and R. L. Baker (1988). “Design of an Image Edge Detection Filter Using the Sobel Operator”. In: *IEEE Journal of Solid-State Circuits* 23.2, pp. 358–367. ISSN: 1558173X. DOI: 10.1109/4.996.
- Kunze, J. (2014). “Entwicklung von dreidimensionalen Düsen mit sich von elliptisch auf rechteckig änderndem Querschnitt”. Diploma Thesis. TU Munich, Germany: Institute for Flight Propulsion. URL: <https://espace.library.uq.edu.au/view/UQ:718148>.

- Kunze, J., M. K. Smart, and R. J. Gollan (2018). “A Design Method for Shape Transition Nozzles for Hypersonic Vehicles”. In: *22nd AIAA International Space Planes and Hypersonics Systems and Technologies Conference*. Reston, Virginia: American Institute of Aeronautics and Astronautics. ISBN: 978-1-62410-577-7. DOI: 10.2514/6.2018-5318. URL: <https://arc.aiaa.org/doi/10.2514/6.2018-5318>.
- Kushida, R., F. Falconer, and D. Seiveno (1964). *Advanced Air Breathing Engine Study*. Tech. rep. Air Force Aero Propulsion Laboratory, Technical Documentary Report No. APL TDR 64-112.
- Laurence, S. J. (2012). “On tracking the motion of rigid bodies through edge detection and least-squares fitting”. In: *Experiments in Fluids* 52.2, pp. 387–401. ISSN: 07234864. DOI: 10.1007/s00348-011-1228-6.
- Laurence, S. J., R. Deiterding, and H. G. Hornung (2007). “Proximal bodies in hypersonic flow”. In: *Journal of Fluid Mechanics* 590.2007, pp. 209–237. ISSN: 00221120. DOI: 10.1017/S0022112007007987.
- Laurence, S. J. and H. G. Hornung (2009). “Image-based force and moment measurement in hypersonic facilities”. In: *Experiments in Fluids* 46.2, pp. 343–353. ISSN: 07234864. DOI: 10.1007/s00348-008-0565-6.
- Laurence, S. J. and S. Karl (2010). “An improved visualization-based force-measurement technique for short-duration hypersonic facilities”. In: *Experiments in Fluids* 48.6, pp. 949–965. ISSN: 0723-4864. DOI: 10.1007/s00348-009-0780-9. URL: <http://link.springer.com/10.1007/s00348-009-0780-9>.
- Le, D. B., C. P. Goyne, R. H. Krauss, and J. C. McDaniel (2008). “Experimental Study of a Dual-Mode Scramjet Isolator”. In: *Journal of Propulsion and Power* 24.5, pp. 1050–1057. ISSN: 0748-4658. DOI: 10.2514/1.32591. URL: <http://arc.aiaa.org/doi/10.2514/1.32591>.
- Lv, Z., J. Xu, and J. Mo (2017a). “Design and analysis on three-dimensional scramjet nozzles with shape transition”. In: *Aerospace Science and Technology* 71, pp. 189–200. ISSN: 12709638. DOI: 10.1016/j.ast.2017.09.025. URL: <http://dx.doi.org/10.1016/j.ast.2017.09.025>.
- (2017b). “Design of a three-dimensional scramjet nozzle considering lateral expansion and geometric constraints”. In: *Acta Astronautica* 141.September, pp. 172–182. ISSN: 00945765. DOI: 10.1016/j.actaastro.2017.09.033. URL: <https://doi.org/10.1016/j.actaastro.2017.09.033>.
- Lv, Z., J. Xu, Y. Yu, and J. Mo (2017c). “A new design method of single expansion ramp nozzles under geometric constraints for scramjets”. In: *Aerospace Science and Technology* 66, pp. 129–139. ISSN: 12709638. DOI: 10.1016/j.ast.2017.03.013. URL: <http://dx.doi.org/10.1016/j.ast.2017.03.013>.
- Martinez, B., M. Bastide, and P. Wey (2014). “Free flight measurement technique in shock tunnel”. In: *AIAA AVIATION 2014 - 30th AIAA Aerodynamic Measurement Technology and Ground Testing Conference June*, pp. 1–12. DOI: 10.2514/6.2014-2523.

REFERENCES

- Martinez, B., P. Wey, M. Libsig, D. Bidino, M. Bastide, J. Juncker, and F. Leopold (2018). “Stereo-vision based determination of aerodynamic coefficients for a wind tunnel model in free rotational motion”. In: *2018 Aerodynamic Measurement Technology and Ground Testing Conference*, pp. 1–12. DOI: 10.2514/6.2018-3804.
- Mattingly, J. D., W. H. Heiser, and D. T. Pratt (2002). *Aircraft Engine Design, Second Edition*. Reston ,VA: American Institute of Aeronautics and Astronautics. ISBN: 978-1-56347-538-2. DOI: 10 . 2514/4.861444. URL: <http://arc.aiaa.org/doi/book/10.2514/4.861444>.
- McBride, B. J., M. J. Zehe, and S. Gordon (2002). *NASA Glenn coefficients for calculating thermodynamic properties of individual species*. Tech. rep. Cleveland, Ohio: NASA Glenn Research Center, p. 287. URL: <https://ntrs.nasa.gov/archive/nasa/ntrs.nasa.gov/20020085330.pdf>.
- Meador, W. E. and M. K. Smart (2005). “Reference Enthalpy Method Developed from Solutions of the Boundary-Layer Equations”. In: *AIAA Journal* 43.1, pp. 135–139. ISSN: 0001-1452. DOI: 10.2514/1.2656. URL: <http://arc.aiaa.org/doi/10.2514/1.2656>.
- Mee, D. J. (1993). *Uncertainty Analysis of Conditions in the Test Section of the T4 Shock Tunnel*. Tech. rep. Brisbane: Department of Mechanical Engineering, The University of Queensland.
- Mo, J., J. Xu, R. Gu, and Z. Fan (2014). “Design of an asymmetric scramjet nozzle with circular to rectangular shape transition”. In: *Journal of Propulsion and Power*.
- Mo, J., J. Xu, Z. Quan, K. Yu, and Z. Lv (2015). “Design and cold flow test of a scramjet nozzle with nonuniform inflow”. In: *Acta Astronautica* 108, pp. 92–105. ISSN: 00945765. DOI: 10.1016/j.actaastro.2014.12.005. URL: <http://dx.doi.org/10.1016/j.actaastro.2014.12.005>.
- Mudford, N. R., S. O’Byrne, A. J. Neely, D. R. Buttsworth, and S. Balage (2014). “Hypersonic wind-tunnel free-flying experiments with onboard instrumentation”. In: *Journal of Spacecraft and Rockets* 52.1, pp. 231–242.
- Naumann, K. W., H. Ende, G. Mathieu, and A. George (1993). “Millisecond aerodynamic force measurement with side-jet model in the ISL shock tunnel”. In: *AIAA Journal* 31.6, pp. 1068–1074. ISSN: 00011452. DOI: 10.2514/3.11730.
- Nickerson, G., S. Dunn, and D. Migdal (1988). “Optimized supersonic exhaust nozzles for hypersonic propulsion”. In: *24th Joint Propulsion Conference*. Reston, Virigina: American Institute of Aeronautics and Astronautics. DOI: 10.2514/6.1988-3161. URL: <http://arc.aiaa.org/doi/10.2514/6.1988-3161>.
- Ogawa, H. and R. R. Boyce (2012). “Nozzle Design Optimization for Axisymmetric Scramjets by Using Surrogate-Assisted Evolutionary Algorithms”. In: *Journal of Propulsion and Power* 28.6, pp. 1324–1338. ISSN: 0748-4658. DOI: 10.2514/1.B34482. URL: <http://arc.aiaa.org/doi/10.2514/1.B34482>.

- Olivier, H. (2016). "The Aachen Shock Tunnel TH2 with Dual Driver Mode Operation". In: *Experimental Methods of Shock Wave Research*. Ed. by O. Igra and F. Seiler. Cham: Springer International Publishing, pp. 111–129. ISBN: 978-3-319-23745-9. DOI: 10.1007/978-3-319-23745-9_5. URL: https://doi.org/10.1007/978-3-319-23745-9%7B%5C_%7D5%20http://link.springer.com/10.1007/978-3-319-23745-9%7B%5C_%7D5.
- Perrier, P., M. Rapuc, P. Rostand, R. Hallard, D. Regard, A. Dufour, and O. Penanhoat (1996). "Nozzle and Afterbody Design for Hypersonic Airbreathing Vehicles". In: *Space Plane and Hypersonic Systems and Technology Conference*. Reston, Virginia: American Institute of Aeronautics and Astronautics. DOI: 10.2514/6.1996-4548. URL: <http://arc.aiaa.org/doi/10.2514/6.1996-4548>.
- Preller, D. and M. K. Smart (2017). "Reusable Launch of Small Satellites Using Scramjets". In: *Journal of Spacecraft and Rockets* 54.6, pp. 1–13. ISSN: 0022-4650. DOI: 10.2514/1.A33610. URL: <https://arc.aiaa.org/doi/10.2514/1.A33610>.
- Rao, G. V. R. (1958). "Exhaust nozzle contour for optimum thrust". In: *Journal of Jet Propulsion* 28.6, pp. 377–382.
- Razzaqi, S. A., W. Y. K. Chan, and M. K. Smart (2014). *Ground Testing of the HIFiRE 7 Scramjet at 75% Scale - Fuel Injector Calibration*. Tech. rep. Brisbane: Centre for Hypersonics, The University of Queensland.
- Riehmer, J. and A. Gühan (2011). "Design of a Scramjet Nozzle with Streamline Tracing Technique and Reference Temperature Method". In: *7th Aerodynamics Symposium on Space Vehicles*. Brugge.
- Robinson, M. J., D. J. Mee, and A. Paull (2006). "Scramjet lift, thrust and pitching-moment characteristics measured in a shock tunnel". In: *Journal of Propulsion and Power* 22.1, pp. 85–95. ISSN: 07484658. DOI: 10.1016/j.aam.2005.05.004.
- Sahoo, N., D. R. Mahapatra, G. Jagadeesh, S. Gopalakrishnan, and K. P. Reddy (2003). "An accelerometer balance system for measurement of aerodynamic force coefficients over blunt bodies in a hypersonic shock tunnel". In: *Measurement Science and Technology* 14.3, pp. 260–272. ISSN: 09570233. DOI: 10.1088/0957-0233/14/3/303.
- (2007). "Design and analysis of a flat accelerometer-based force balance system for shock tunnel testing". In: *Measurement: Journal of the International Measurement Confederation* 40.1, pp. 93–106. ISSN: 02632241. DOI: 10.1016/j.measurement.2006.03.016.
- Salas, M. D. (1976). "Shock Fitting Method for Complicated Two-Dimensional Supersonic Flows". In: *AIAA Journal* 14.5, pp. 583–588. ISSN: 0001-1452. DOI: 10.2514/3.61399. URL: <http://arc.aiaa.org/doi/10.2514/3.61399>.
- Sanderson, S. R. and J. M. Simmons (1991). "Drag balance for hypervelocity impulse facilities". In: *AIAA Journal* 29.12, pp. 2185–2191. ISSN: 00011452. DOI: 10.2514/3.10858.

REFERENCES

- Saravanan, S., G. Jagadeesh, and K. P. Reddy (2009). “Aerodynamic force measurement using 3-component accelerometer force balance system in a hypersonic shock tunnel”. In: *Shock Waves* 18.6, pp. 425–435. ISSN: 09381287. DOI: 10.1007/s00193-008-0172-8.
- Sauerwein, B., R. Hruschka, P. Gnemmi, C. Rey, and M. Bastide (2015). “ISL Shock Tunnel Operation with Contoured Mach-4.5-6-8-10-Nozzles for Hypersonic Test Applications”. In: *29th International Symposium on Shock Waves 1*. Ed. by R. Bonazza and D. Ranjan. Cham: Springer International Publishing, pp. 391–396. ISBN: 978-3-319-16834-0. DOI: 10.1007/978-3-319-16835-7_61. URL: http://link.springer.com/10.1007/978-3-319-16835-7%20http://link.springer.com/10.1007/978-3-319-16835-7%7B%5C_%7D61.
- Schindel, L. (1999). “Effect of Nonuniform Nozzle Flow on Scramjet Performance”. In: *Journal of Propulsion and Power* 15.2, pp. 363–364. ISSN: 0748-4658. DOI: 10.2514/2.5435. URL: <http://dx.doi.org/10.2514/2.5435>.
- Seigel, A. E. (1959). *Millisecond Measurement of Forces and Moments in Hypersonic Flow*. Tech. rep. White Oak, MD: NOL Aeroballistic Research Facilities Dedication and Decennial, pp. 25–26.
- Shyne, R. and T. Keith jr. (1990). “Analysis and design of optimized truncated scarfed nozzles subject to external flow effects”. In: *26th Joint Propulsion Conference*. Reston, Virginia: American Institute of Aeronautics and Astronautics, p. 2222. DOI: 10.2514/6.1990-2222. URL: <http://arc.aiaa.org/doi/10.2514/6.1990-2222>.
- Small, W. J., J. P. Weidner, and P. J. Johnston (1976). *Scramjet Nozzle and Design Analysis as Applied to a Highly Integrated Hypersonic Research Airplane*. Tech. rep. NASA.
- Smart, M. K. (1999). “Design of three-dimensional hypersonic inlets with rectangular-to-elliptical shape transition”. In: *Journal of Propulsion and Power* 15.3, pp. 408–416.
- Smart, M. K. (2007). “Scramjets”. In: *The Aeronautical Journal* 111.1124, pp. 605–619. ISSN: 0001-9240. DOI: 10.1017/S0001924000004796. arXiv: NIHMS150003. URL: https://www.cambridge.org/core/product/identifier/S0001924000004796/type/journal%7B%5C_7Darticle.
- Smart, M. K. and M. R. Tetlow (2009). “Orbital Delivery of Small Payloads Using Hypersonic Air-breathing Propulsion”. In: *Journal of Spacecraft and Rockets* 46.1, pp. 117–125. ISSN: 0022-4650. DOI: 10.2514/1.38784. URL: <https://arc.aiaa.org/doi/10.2514/1.38784>.
- Stalker, R. J. (1967). “A study of the free-piston shock tunnel.” In: *AIAA Journal* 5.12, pp. 2160–2165. ISSN: 0001-1452. DOI: 10.2514/3.4402. URL: <http://arc.aiaa.org/doi/abs/10.2514/3.4402>.
- (1991). “Waves and Thermodynamics in High Mach Number Propulsive Ducts”. In: *High-Speed Flight Propulsion Systems*. Ed. by E. T. Curran and S. N. B. Murthy. Vol. 137. Washington DC: American Institute of Aeronautics and Astronautics, pp. 237–264. ISBN: 978-1-56347-011-0. DOI:

- 10.2514/5.9781600866104.0237.0264. URL: <http://arc.aiaa.org/doi/book/10.2514/4.866104%20http://arc.aiaa.org/doi/10.2514/5.9781600866104.0237.0264>.
- Stalker, R. J. and R. G. Morgan (1988). "The University of Queensland Free Piston Shock Tunnel T4 - Initial Operation and Preliminary Calibration". In: *The University of Queensland Free Piston Shock Tunnel T4 - Initial Operation and Preliminary Calibration*. Adelaide: ational conference publication (Institution of Engineers, Australia), pp. 182–198.
- Stalker, R. J., A. Paull, D. J. Mee, R. G. Morgan, and P. A. Jacobs (2005). "Scramjets and shock tunnels - The Queensland experience". In: *Progress in Aerospace Sciences* 41.6, pp. 471–513. ISSN: 03760421. DOI: 10.1016/j.paerosci.2005.08.002. URL: <https://linkinghub.elsevier.com/retrieve/pii/S0376042105001028>.
- Stalker, R. J., N. K. Truong, R. G. Morgan, and A. Paull (2004). "Effects of hydrogen-air non-equilibrium chemistry on the performance of a model scramjet thrust nozzle". In: *Aeronautical Journal* 108.1089, pp. 575–584. ISSN: 00019240. DOI: 10.1017/S0001924000000403.
- Steelant, J., R. Varvill, C. Walton, S. Defoort, K. Hannemann, and M. Marini (2015). "Achievements obtained for sustained hypersonic flight within the LAPCAT-II project". In: *20th AIAA International Space Planes and Hypersonic Systems and Technologies Conference*, p. 3677.
- Störkmann, V., H. Olivier, and H. Grönig (1998). "Force measurements in hypersonic impulse facilities". In: *AIAA Journal* 36.3, pp. 342–348. ISSN: 00011452. DOI: 10.2514/3.13826.
- Suraweera, M. V. and M. K. Smart (2009). "Shock-tunnel experiments with a mach 12 rectangular-to-elliptical shape-transition scramjet at offdesign conditions". In: *Journal of Propulsion and Power* 25.3, pp. 555–564.
- Takahashi, M., T. Komuro, K. Sato, K. Itoh, H. Tanno, and S. Ued (1999). "Development of a New Force Measurement Method for Scramjet Testing in a High Enthalpy Shock Tunnel Ith Internationa Space Planes and Hypersonic Systems and Technolog .ies . Conference and 3fd Weakly Ionized Gases Workshop 1-5 November 1999 Norfolk , VA". In: *AIAA 9th International Space Planes and Hypersonic Systems and Technologies Conference* November 1999, p. 5. DOI: 10.2514/6.1999-4961.
- Tanimizu, K., D. J. Mee, R. J. Stalker, and P. A. Jacobs (2011). "Thrust Nozzle Design Study for a Quasi-Axisymmetric Scramjet-Powered Vehicle". In: *Journal of Propulsion and Power* 27.1, pp. 40–49. ISSN: 0748-4658. DOI: 10.2514/1.48586. URL: <http://arc.aiaa.org/doi/10.2514/1.48586>.
- Tanno, H., T. Komuro, K. Sato, K. Fujita, and S. J. Laurence (2014). "Free-flight measurement technique in the free-piston high-enthalpy shock tunnel". In: *Review of Scientific Instruments* 85.4, p. 45112.
- Tanno, H., T. Komuro, K. Sato, and K. Itoh (2009). "Aerodynamic force measurement technique with accelerometers in the impulsive facility Hiest". In: *Shock Waves*. Berlin, Heidelberg: Springer Berlin Heidelberg, pp. 471–476. ISBN: 978-3-540-85168-4. DOI: 10.1007/978-3-540-85168-

REFERENCES

- 4_75. URL: http://dx.doi.org/10.1007/978-3-540-85168-4%7B%5C_%7D75%20http://link.springer.com/10.1007/978-3-540-85168-4%7B%5C_%7D75.
- Tanno, H., T. Komuro, M. Takahashi, K. Takayama, H. Ojima, and S. Onaya (2004). “Unsteady force measurement technique in shock tubes”. In: *Review of Scientific Instruments* 75.2, pp. 532–536. ISSN: 00346748. DOI: 10.1063/1.1641156.
- Tanno, H., T. Komuro, K. Sato, and K. Itoh (2015). “Free-flight aerodynamic test of elliptic cone in shock tunnel”. In: *20th AIAA International Space Planes and Hypersonic Systems and Technologies Conference, 2015 July*, pp. 1–6. DOI: 10.2514/6.2015-3655.
- Taylor, T. and D. van Wie (2008). “Performance analysis of hypersonic shape-changing inlets derived from morphing streamline traced flowpaths”. In: *15th AIAA international space planes and hypersonic systems and technologies conference*, p. 2635.
- Turner, J. C. and M. K. Smart (2010). “Application of Inlet Injection to a Three-Dimensional Scramjet at Mach 8”. In: *AIAA Journal* 48.4, pp. 829–838. ISSN: 0001-1452. DOI: 10.2514/1.J050052. URL: <http://arc.aiaa.org/doi/10.2514/1.J050052>.
- Vanyai, T. (2018). “Experimental Investigation of a 3D Thermal Compression Scramjet Using Advanced Optical Techniques”. In:
- Vidal, R. (1956). *Model Instrumentation Techniques for Heat Transfer and Force Measurements in a Hypersonic Shock Tunnel*. Buffalo, NY: Buffalo, N.Y. Cornell Aeronautical Laboratory 1956.
- Warren, W. R. (1959). “Laboratory Experimental Studies in Re-entry Aerothermodynamics”. In: *Xth International Astronautical Congress, London 1959*. Ed. by F. Hecht. London: Springer-Verlag Wien GmbH, pp. 683–704. ISBN: 9783662389614.
- Warren, W. R., E. M. Kaegi, and R. E. Geiger (1961). *Shock Tunnel Experimental Techniques for Force and Moment Surface Flow Direction Measurements*. Tech. rep. 1, pp. 82–83. DOI: 10.2514/8.5388. URL: <http://arc.aiaa.org/doi/10.2514/8.5388>.
- Watanabe, S. (1993). “Scramjet nozzle experiment with hypersonic external flow”. In: *Journal of Propulsion and Power* 9.4, pp. 521–528. ISSN: 0748-4658. DOI: 10.2514/3.23654. URL: <http://dx.doi.org/10.2514/3.23654>.
- Weidner, J. P., W. J. Small, and J. A. Penland (1977). “Scramjet Integration on Hypersonic Research firplane Concepts”. In: *Journal of Aircraft* 14.5, pp. 460–466. ISSN: 0021-8669. DOI: 10.2514/3.58803. URL: <http://arc.aiaa.org/doi/10.2514/3.58803>.
- Wey, P., M. Bastide, B. Martinez, J. Srulijes, and P. Gnemmi (2012). “Determination of aerodynamic coefficients from shock tunnel free flight trajectories”. In: *28th AIAA Aerodynamic Measurement Technology, Ground Testing, and Flight Testing Conference 2012 June*, pp. 1–9. DOI: 10.2514/6.2012-3321.
- White, J. and J. Morrison (1999). “A pseudo-temporal multi-grid relaxation scheme for solving the parabolized Navier-Stokes equations”. In: *14th Computational Fluid Dynamics Conference*.

- Vol. 122. 8. Reston, Virigina: American Institute of Aeronautics and Astronautics, pp. 2065–2069.
DOI: 10.2514/6.1999-3360. URL: <http://arc.aiaa.org/doi/10.2514/6.1999-3360>.
- Whitside, R. W., W. Y. K. Chan, D. E. Gildfind, M. K. Smart, and P. A. Jacobs (2019). “Nitrogen Driver for Low-Enthalpy Testing in Free-Piston Driven Shock Tunnels”. In: *32nd International Symposium on Shock Waves*. Singapore.
- Zhu, M., L. Fu, S. Zhang, and Y. Zheng (2017). “Design and optimization of three-dimensional supersonic asymmetric truncated nozzle”. In: *Proceedings of the Institution of Mechanical Engineers, Part G: Journal of Aerospace Engineering* 0.0, p. 095441001771856. ISSN: 0954-4100.
DOI: 10.1177/0954410017718567. URL: <http://journals.sagepub.com/doi/10.1177/0954410017718567>.

APPENDIX A

SUPPLEMENTAL EXPERIMENTAL DATA

In this Appendix the pressure data from shots 12197 and 12200 to 12222 are presented. These shots were excluded from the analysis in Chapter 6 for one or both of the reasons listed below:

1. the engine unstarted or did not start during the test time or
2. notable oscillations of the imaging lens obscured the image tracking data too much to be used.

A.1 The 2 mm Test Condition

In addition to the test condition presented in Section 4.1.2, the Mach 12 REST engine was tested at a 50 kPa dynamic pressure condition in the present study. ‘2 mm’ refers to the thickness of the diaphragm used in the test condition. Unfortunately, the imaging lens was vibrating throughout the 2 mm shots and the image tracking data was not usable. The pressure data, however, provides insight into the operation of the engine at a lower dynamic pressure.

The facility configuration for the 2 mm condition is shown in Table A.1, the average stagnation conditions and the average primary shock speed are listed in Table A.2 and the freestream conditions and test gas properties and composition are shown in Tables A.3a and A.3b. The repeatability of the condition is shown in Figure A.1. Note that shot 12207 was not included in the calculation of the average condition, since a scored diaphragm was used for that shot and the shock speed was lower than expected. Figure A.1 shows that the NENZFr response surface was adequately sized to predict the free stream conditions of the 2 mm condition.

APPENDIX A SUPPLEMENTAL EXPERIMENTAL DATA

Table A.1: The facility configuration for the 2 mm test condition used in the experiments described in the present study.

Component	Setting	Symbol	Value	Unit
Reservoir	Pressure	p_R	1.6	MPa
Compression Tube	Pressure	p_{CT}	27.4	kPa
	Gas Mixture	-	100 % Ar	-
Primary Diaphragm	Thickness	d_D	2	mm
Shock Tube	Pressure	p_{ST}	100	kPa
Nozzle	Mach Number	M_N	7.6	-

Table A.2: The average stagnation conditions and primary shock speed from all 2 mm shots. The quoted uncertainties are for a single shot.

Property	Symbol	Value	Unit
Nozzle Supply Pressure	p_s	13.3 ± 0.4	MPa
Shock Speed	V_{ss}	1.79 ± 0.10	km s^{-1}
Nozzle Supply Enthalpy	H_s	2.97 ± 0.23	MJ kg^{-1}
Nozzle Supply Temperature	T_s	2697 ± 156	K
Nozzle Supply Density	ρ_s	17.2 ± 1.1	kg m^{-3}

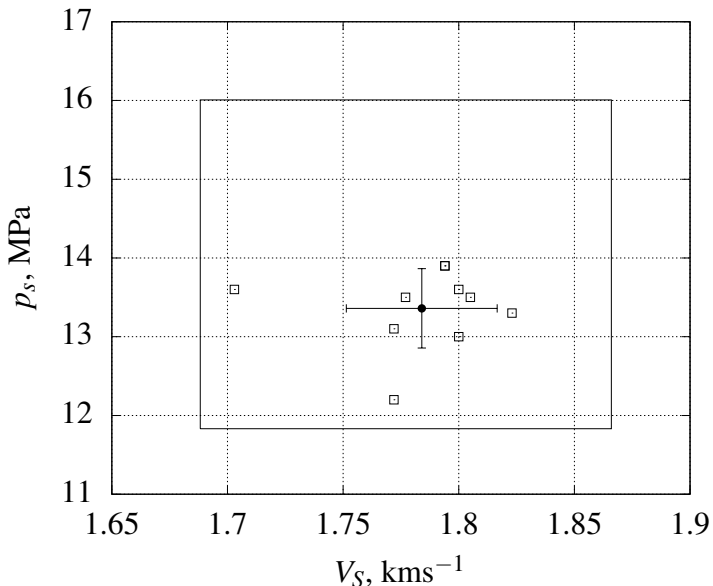


Figure A.1: The repeatability of the 2 mm condition. Each \square symbolises a single shot. The nominal condition with one standard deviation for both shock speed and nozzle supply pressure is indicated by \bullet . The large rectangle designates the extent of the NENZFr response surface created for the condition.

A.2 Supplemental Pressure Data

The normalised pressure data of the shots excluded from the analysis in Chapter 6 is shown below. Figure A.2 shows the unfuelled shots, Figure A.3 the fuelled shots with $\phi < 1$ and Figure A.4 shows

Table A.3: The free stream conditions and test gas properties as calculated with NENZFr for the average shock speed and nozzle supply pressure and the nominal shock tube fill conditions. The quoted uncertainties are for a single shot.

(a) The free stream properties.

Property	Value	Unit
M_0	7.60 ± 0.07	-
p_0	1220 ± 49	Pa
T_0	253 ± 21	K
ρ_0	0.0168 ± 0.0011	kg m^{-3}
u_0	2422 ± 80	m s^{-1}
q_0	49.2 ± 4.6	kPa
$Re_{u,0}$	$(2.52 \pm 0.25) \times 10^6$	-
$\rho_0 u_0$	40.6 ± 3.0	$\text{kg s}^{-1} \text{m}^{-2}$

(b) The test gas composition and properties.

Property	Value	Unit
R_0	288 ± 33	$\text{J kg}^{-1} \text{K}^{-1}$
γ_0	1.40 ± 0.16	-
Y_{N2}	0.758 ± 0.003	-
Y_{O2}	0.220 ± 0.003	-
Y_{NO}	0.019 ± 0.005	-
Y_O	$(0.24 \pm 0.14) \times 10^{-3}$	-

the fuelled shots with $\phi > 1$.

The pressure data of the unfuelled shots demonstrates that the engine started at the 2 mm condition as well. The CFD solution predicts the pressure distribution equally well for the 2 mm and the 3 mm test condition. Shot 12213 was included in Figure A.2 because fuel injection only started during the test time. Ignition was only observed after the test time. Shot 12213 was therefore effectively unfuelled during the test time as is confirmed by the pressure data.

Figure A.3 demonstrates the combustion induced pressure rise for $\phi < 1$. Referring to shot 12207, it should be noted that late fuel injection and an increasing equivalence ratio caused ignition in the combustor to occur during the test time. A pressure rise was only observed in the signal of P8.

It is interesting to note that for $\phi > 1$, refer to Figure A.4, the 2 mm condition appears to produce a larger normalised pressure rise than the 3 mm condition.

A.2.1 Unstart Behaviour

During a number of shots the engine unstarted. It was found that all of the unstarts originated in the inlet. Figure A.5 shows the normalised pressure signals of all shots where an unstart was observed.

APPENDIX A SUPPLEMENTAL EXPERIMENTAL DATA

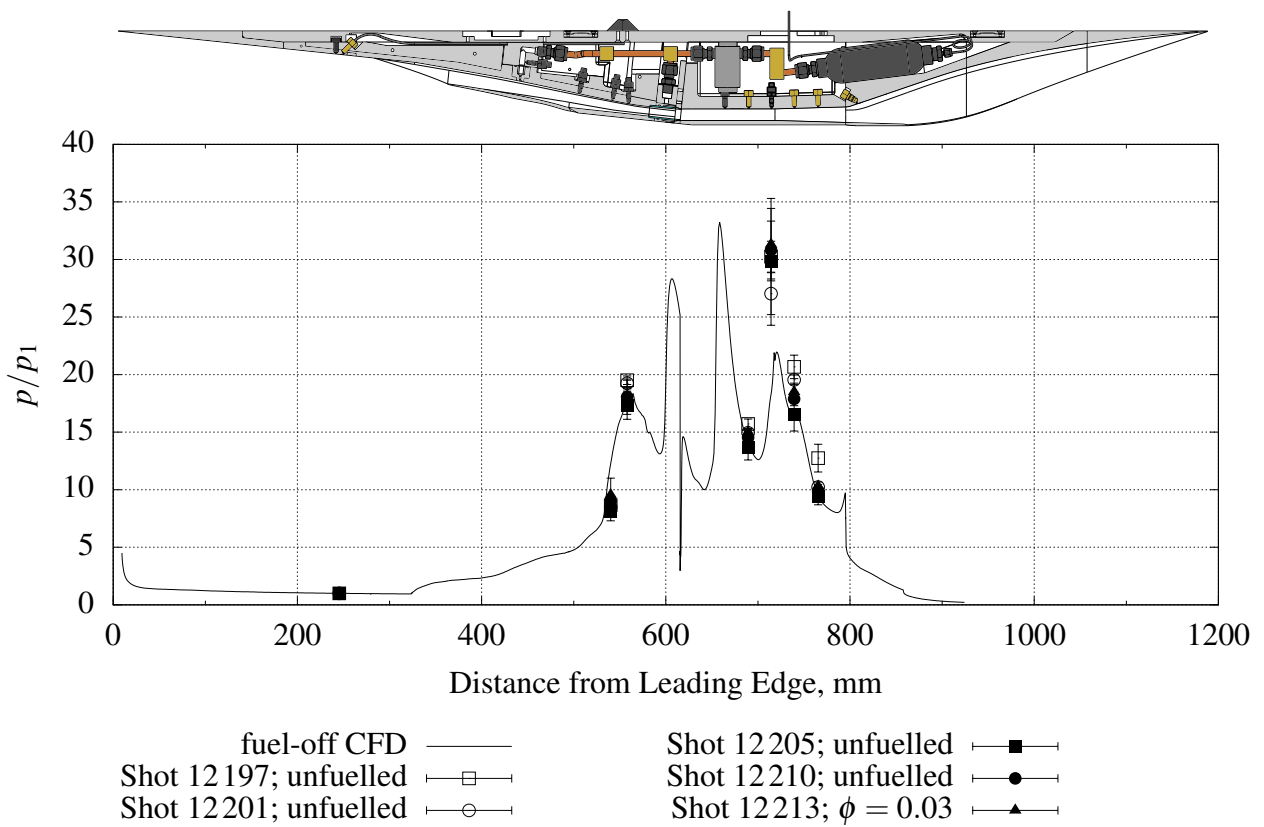


Figure A.2: Normalised pressure data from the remaining fuel-off shots in comparison with that of the CFD solution. The error bars show one standard deviation of the variation of pressure during the test time. Filled symbols designate the 2 mm condition, open symbols the 3 mm condition.

In his investigation of the Mach 12 REST model, Doherty (2014, Appendix H.3) found that a large amount of fuel in the inlet before the onset of flow causes the inlet to unstart. The starting shock of the facility can ignite the fuel in the inlet and the associated pressure rise causes the unstart. In the present study it was found that, in addition to the effect observed by Doherty, a high equivalence ratio in the inlet can cause self ignition during the test time and lead to an unstart.

It is obvious that the equivalence ratio in the 2 mm shots that unstarted was much higher than is practical. This was due to a miscalculation of the capture area and therefore the mass flow rate of air going through the engine. Nonetheless, the unstarts originated in the inlet.

The unstart observed at shot 12215 was caused by badly timed fuel injection. Fuel was injected early, consequentially it accumulated in the inlet before the start of the shot. It was then ignited by the starting shock of the facility.

Shot 12222 marked the upper limit of fuel injection at the 3 mm condition. The fuel plenum pressures were rising during the test time. Ignition inside the inlet was observed at $t \approx 3.7$ ms. The equivalence ratio at this time was $\phi = 1.65$, which corresponds to an equivalence ratio in the inlet of $\phi_I = 0.67$. A drop in pressure in the combustor, caused by the unstart, was only observed at $t > 4$ ms.

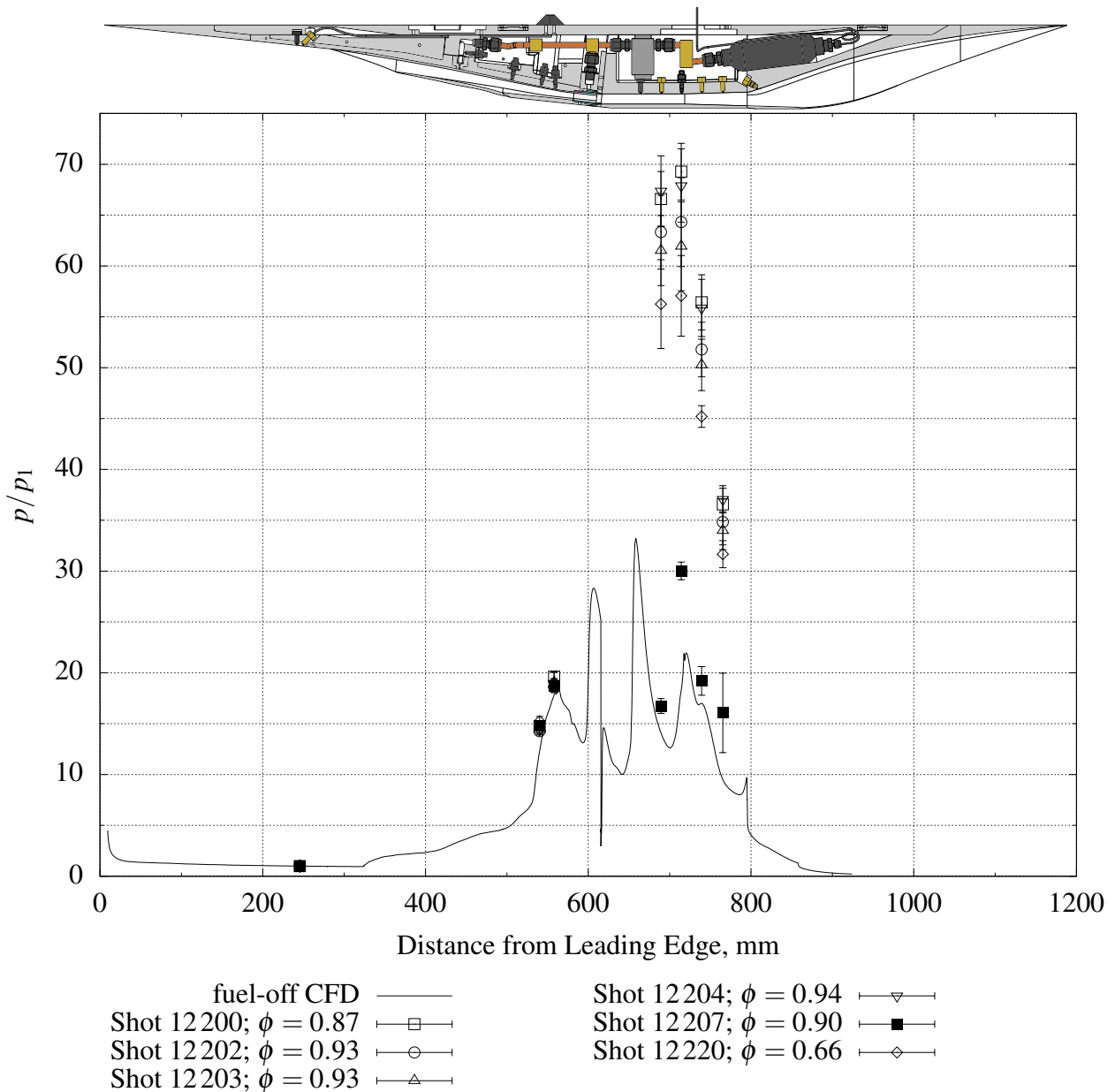


Figure A.3: Normalised pressure data from the remaining fuelled shots with $\phi < 1$ in comparison with that of the CFD solution. The error bars show one standard deviation of the variation of pressure during the test time. Filled symbols designate the 2 mm condition, open symbols the 3 mm condition.

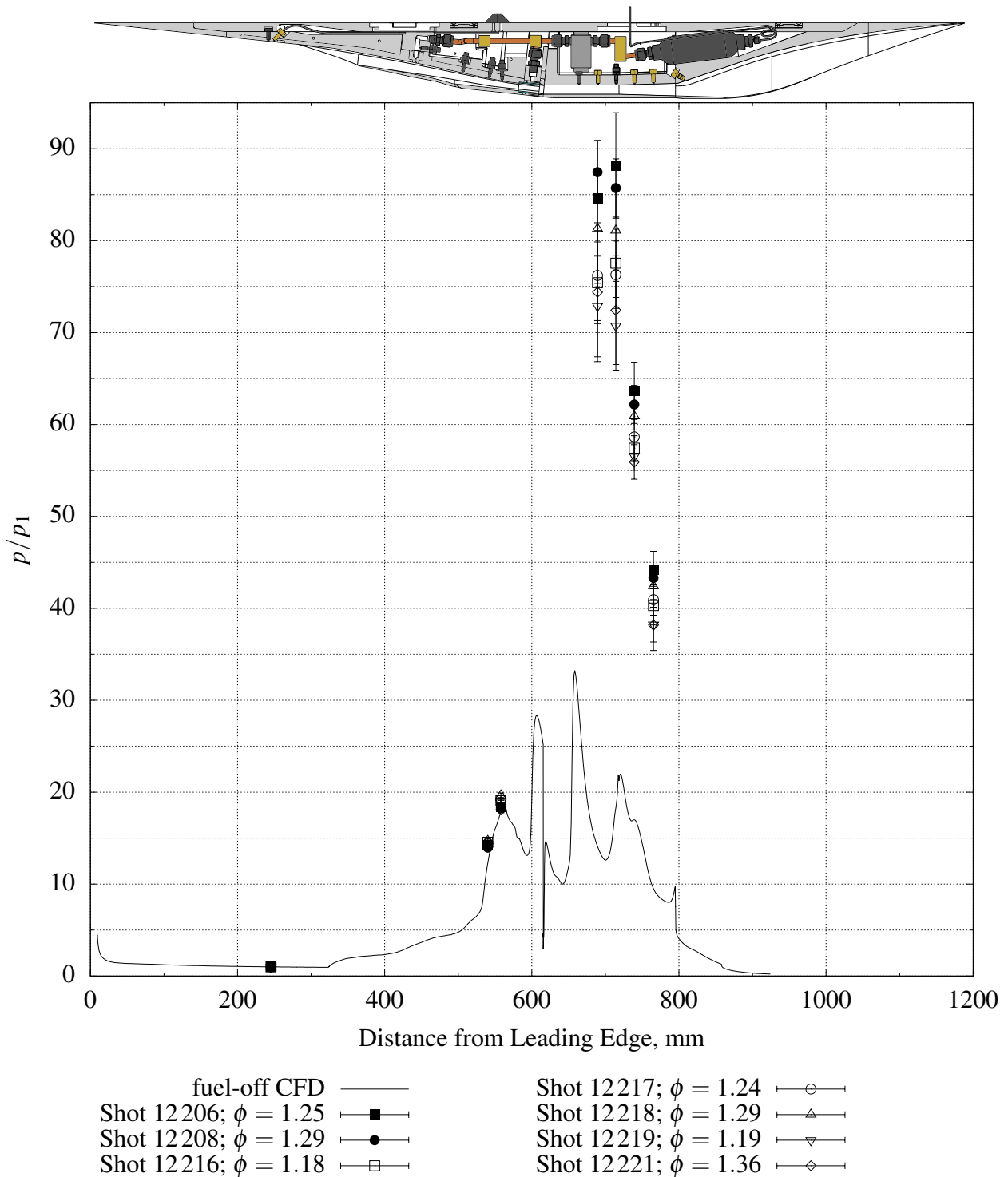


Figure A.4: Normalised pressure data from remaining fuelled shots with $\phi > 1$ in comparison with that of the CFD solution. The error bars show one standard deviation of the variation of pressure during the test time. Filled symbols designate the 2 mm condition, open symbols the 3 mm condition.

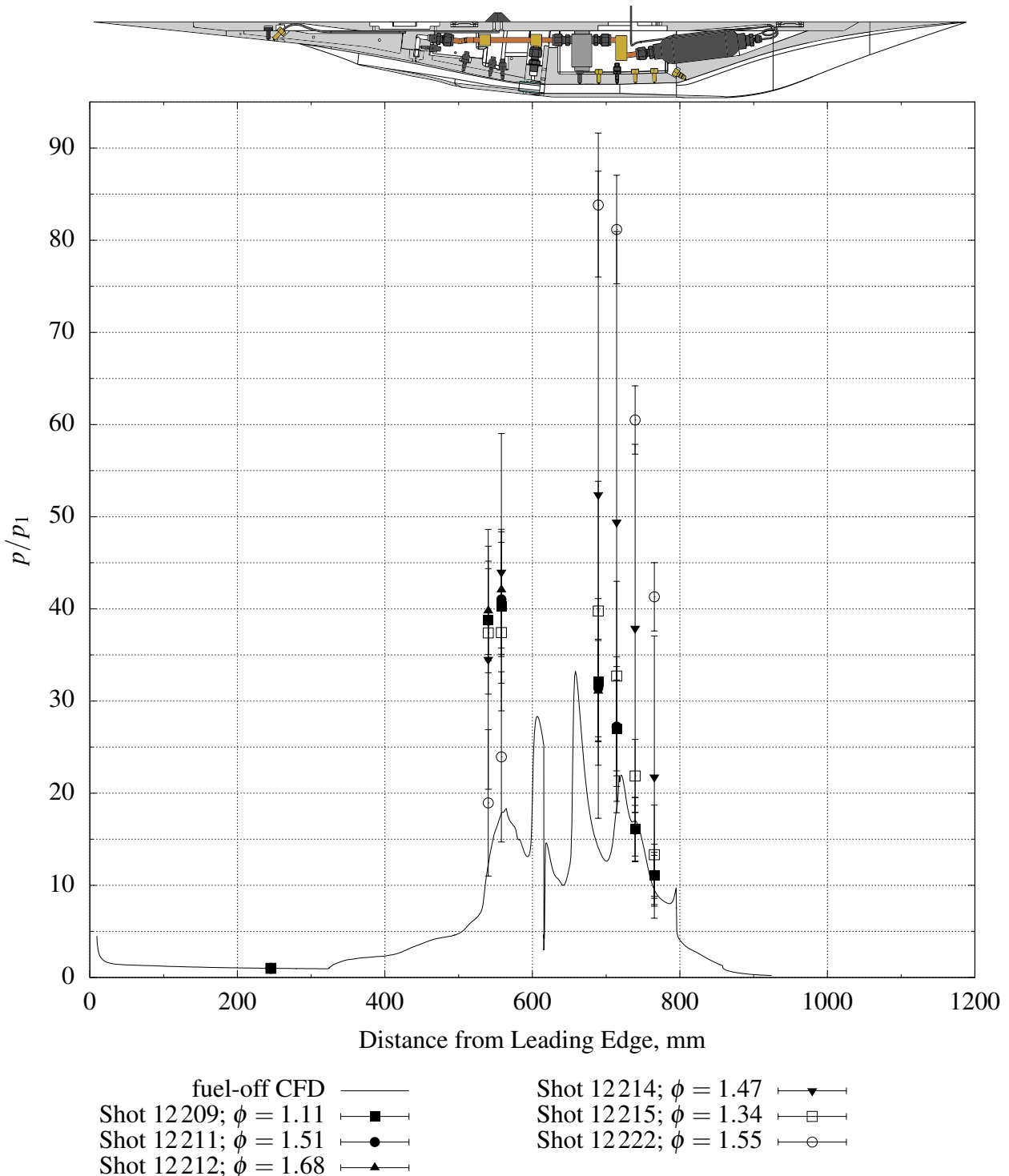


Figure A.5: Normalised pressure data from all shots that unstarted during the third experimental campaign in comparison with that of the CFD solution. The error bars show one standard deviation of the variation of pressure during the test time. Filled symbols designate the 2 mm condition, open symbols the 3 mm condition.

APPENDIX B

VIBRATION DATA

In this appendix are presented the vibrations from all shots used in the analysis in Chapter 6 as well as the Fourier series used to extrapolate the vibrations into the test time. The amplitudes and frequencies listed were determined using a fast fourier transform of 20000 images before the stag trigger. The first frequency listed corresponds to the lowest one identified for the respective shot.

The attainable frequency resolution of a fast fourier transform can be calculated using

$$\Delta f = \frac{1}{\Delta t \cdot n}, \quad (\text{B.1})$$

where Δt is the time interval between images and n designates the number of images used. For $\Delta t = 15.1 \mu\text{s}$ and $n = 20000$ this yields $\Delta f = 3.3 \text{Hz}$.

Tables B.1 and B.2 show the dominant frequencies in x , y and α of all shots analysed in Chapter 6.

In Table B.3 the errors estimated using Equations (6.20) and (6.19) for all shots are listed. Table B.4 shows the Fourier series used to extrapolate the vibration signals into the test time for each variable of each shot. T_F indicates the sample window used for the fit and n the number of terms of the Fourier series. Δa designates the change in acceleration due to the correction using the Fourier series.

Table B.1: The dominant components of the vibrations detected in the trajectories in x and y from all shots discussed in Chapter 6.

Shot	Variable	Frequency 1		Frequency 2		Frequency 3	
		A, μm	f, Hz	A, μm	f, Hz	A, μm	f, Hz
12198	x	114.2	3.3	19.6	13.3	5.7	36.4
	y	16.6	13.3	2.8	36.4	-	-
12199	x	72.6	3.3	10.1	19.9	3.6	33.1
	y	14.8	9.9	3.1	26.5	0.5	39.7
12223	x	99.3	3.3	4.1	23.2	2.6	33.1
	y	29.5	9.9	2.3	23.2	0.8	46.4
12224	x	57.2	3.3	7.9	19.9	2.0	46.4
	y	26.6	9.9	2.9	33.1	-	-
12225	x	54.6	3.3	11.2	19.9	4.2	36.4
	y	30.3	9.9	3.1	29.8	1.3	36.4
12226	x	48.4	3.3	19.6	26.5	2.4	46.4
	y	5.6	3.3	18.1	9.9	1.8	23.2
12228	x	58.5	3.3	14.3	19.9	3.0	36.4
	y	20.5	9.9	2.4	33.1	0.4	53.0
12229	x	41.5	3.3	17.1	26.5	1.5	46.4
	y	19.8	9.9	4.7	33.1	2.2	36.4
12230	x	110.3	3.3	14.3	23.2	1.5	46.4
	y	21.2	9.9	6.4	19.9	0.9	43.1
12232	x	107.5	3.3	8.0	26.5	1.5	46.4
	y	17.9	6.6	8.6	19.9	3.9	29.8
12233	x	111.6	3.3	13.6	23.2	1.6	46.4
	y	13.0	6.6	3.7	33.1	0.4	53.0
12234	x	58.1	3.3	17.8	23.2	2.1	43.1
	y	9.6	6.6	4.3	29.8	1.0	46.4
12235	x	58.3	3.3	19.1	26.5	1.6	43.1
	y	12.8	9.9	2.0	29.8	1.8	36.4

Table B.2: The dominant components of the vibrations detected in the pitch angle signals from all shots discussed in Chapter 6.

Shot	Variable	Frequency 1		Frequency 2		Frequency 3	
		A, $10^{-3}\circ$	f, Hz	A, $10^{-3}\circ$	f, Hz	A, $10^{-3}\circ$	f, Hz
12198	α	18.5	3.3	5.6	13.3	1.6	26.5
12199	α	6.0	3.3	3.4	13.3	1.1	26.5
12223	α	12.8	3.3	1.9	26.5	0.7	43.1
12224	α	6.4	9.9	0.4	33.1	0.2	46.4
12225	α	6.8	6.6	0.4	26.5	0.3	36.4
12226	α	4.2	9.9	1.6	26.5	1.0	33.1
12228	α	6.1	6.6	1.3	19.9	0.9	26.5
12229	α	4.6	9.9	1.4	23.2	0.2	43.1
12230	α	9.5	3.3	1.0	19.9	1.1	33.1
12232	α	10.4	3.3	0.8	26.5	0.5	36.4
12233	α	10.7	3.3	0.9	26.5	0.2	43.1
12234	α	5.9	6.6	1.1	23.2	0.3	56.3
12235	α	6.7	6.6	1.7	23.2	0.2	39.8

Table B.3: The estimated errors caused by the detected vibrations from all shots discussed in Chapter 6.

Shot	Variable	σ_a	Unit	Shot	Variable	σ_a	Unit
12198	x	0.23	ms^{-2}	12229	x	0.27	ms^{-2}
	y	0.13	ms^{-2}		y	0.13	ms^{-2}
	α	41.8	$^{\circ}\text{s}^{-2}$		α	26.4	$^{\circ}\text{s}^{-2}$
12199	x	0.16	ms^{-2}	12230	x	0.23	ms^{-2}
	y	0.08	ms^{-2}		y	0.10	ms^{-2}
	α	31.5	$^{\circ}\text{s}^{-2}$		α	35.5	$^{\circ}\text{s}^{-2}$
12223	x	0.10	ms^{-2}	12232	x	0.18	ms^{-2}
	y	0.10	ms^{-2}		y	0.15	ms^{-2}
	α	51.6	$^{\circ}\text{s}^{-2}$		α	24.1	$^{\circ}\text{s}^{-2}$
12224	x	0.12	ms^{-2}	12233	x	0.23	ms^{-2}
	y	0.11	ms^{-2}		y	0.12	ms^{-2}
	α	24.6	$^{\circ}\text{s}^{-2}$		α	20.6	$^{\circ}\text{s}^{-2}$
12225	x	0.20	ms^{-2}	12234	x	0.29	ms^{-2}
	y	0.12	ms^{-2}		y	0.12	ms^{-2}
	α	16.0	$^{\circ}\text{s}^{-2}$		α	31.5	$^{\circ}\text{s}^{-2}$
12226	x	0.41	ms^{-2}	12235	x	0.38	ms^{-2}
	y	0.09	ms^{-2}		y	0.09	ms^{-2}
	α	57.3	$^{\circ}\text{s}^{-2}$		α	28.1	$^{\circ}\text{s}^{-2}$
12228	x	0.30	ms^{-2}				
	y	0.10	ms^{-2}				
	α	24.1	$^{\circ}\text{s}^{-2}$				

Table B.4: The Fourier series used to extrapolate the vibrations to the test time from all shots discussed in Chapter 6 and the resulting change in acceleration.

Shot	Variable	T_F , ms	n	Δa	Unit	Shot	Variable	T_F , ms	n	Δa	Unit
12198	x	15	2	1.28	ms^{-2}	12229	x	250	8	0.21	ms^{-2}
	y	50	4	0.08	ms^{-2}		y	250	7	0.003	ms^{-2}
	α	70	2	1.55	$^{\circ}\text{s}^{-2}$		α	220	5	0.39	$^{\circ}\text{s}^{-2}$
12199	x	60	2	0.92	ms^{-2}	12230	x	15	2	0.59	ms^{-2}
	y	100	6	0.10	ms^{-2}		y	35	5	1.45	ms^{-2}
	α	45	3	0.55	$^{\circ}\text{s}^{-2}$		α	40	6	46.6	$^{\circ}\text{s}^{-2}$
12223	x	15	2	4.00	ms^{-2}	12232	x	150	3	0.21	ms^{-2}
	y	270	5	0.58	ms^{-2}		y	150	5	0.018	ms^{-2}
	α	250	8	124	$^{\circ}\text{s}^{-2}$		α	150	1	0.09	$^{\circ}\text{s}^{-2}$
12224	x	270	8	0.14	ms^{-2}	12233	x	270	5	1.50	ms^{-2}
	y	250	5	0.23	ms^{-2}		y	30	5	0.05	ms^{-2}
	α	250	8	3.87	$^{\circ}\text{s}^{-2}$		α	120	6	3.47	$^{\circ}\text{s}^{-2}$
12225	x	270	3	0.04	ms^{-2}	12234	x	50	2	1.16	ms^{-2}
	y	270	1	0.13	ms^{-2}		y	50	5	0.03	ms^{-2}
	α	270	8	0.22	$^{\circ}\text{s}^{-2}$		α	200	8	0.10	$^{\circ}\text{s}^{-2}$
12226	x	225	8	0.49	ms^{-2}	12235	x	50	2	0.06	ms^{-2}
	y	50	5	0.17	ms^{-2}		y	270	2	0.48	ms^{-2}
	α	250	5	0.89	$^{\circ}\text{s}^{-2}$		α	270	7	0.43	$^{\circ}\text{s}^{-2}$
12228	x	270	5	0.07	ms^{-2}						
	y	250	1	0.33	ms^{-2}						
	α	250	8	0.21	$^{\circ}\text{s}^{-2}$						

APPENDIX C

IMAGE TRACKING DATA

In this appendix the remainder of data from the image tracking analysis is shown. The fit quality of all shots is shown in Table C.1. All recorded trajectories with their respective quadratic fits are shown in Figures C.1 to C.14.

Table C.1: The quality of the curve fits for all shots.

Shot	Variable	s	Unit	Δ	Unit	$s/\Delta, \%$
12198	x	0.668	μm	115.8	μm	0.58
	y	0.406	μm	87.3	μm	0.47
	α	0.968	10^{-3}°	18.0	10^{-3}°	5.3
12199	x	0.719	μm	130.8	μm	0.55
	y	0.422	μm	135.1	μm	0.31
	α	1.163	10^{-3}°	17.1	10^{-3}°	6.8
12223	x	0.597	μm	98.0	μm	0.61
	y	0.443	μm	70.9	μm	0.62
	α	0.974	10^{-3}°	18.0	10^{-3}°	5.4
12224	x	0.529	μm	37.3	μm	1.4
	y	0.447	μm	67.2	μm	0.67
	α	0.670	10^{-3}°	15.4	10^{-3}°	4.8
12225	x	0.746	μm	47.8	μm	1.6
	y	0.506	μm	98.2	μm	0.52

Table C.1: (continued)

Shot	Variable	s	Unit	Δ	Unit	$s/\Delta, \%$
12226	α	0.928	$10^{-3}\circ$	15.4	$10^{-3}\circ$	6.0
	x	0.941	μm	61.1	μm	1.5
	y	0.494	μm	68.2	μm	0.72
12228	α	1.753	$10^{-3}\circ$	12.8	$10^{-3}\circ$	13.7
	x	0.628	μm	81.3	μm	0.77
	y	0.448	μm	94.2	μm	0.48
12229	α	0.980	$10^{-3}\circ$	13.8	$10^{-3}\circ$	7.1
	x	0.583	μm	64.1	μm	0.91
	y	0.666	μm	98.7	μm	0.67
12230	α	0.922	$10^{-3}\circ$	11.8	$10^{-3}\circ$	7.8
	x	0.603	μm	114.3	μm	0.53
	y	0.474	μm	67.9	μm	0.70
12231	α	0.974	$10^{-3}\circ$	18.0	$10^{-3}\circ$	5.4
	x	0.603	μm	34.4	μm	1.8
	y	0.495	μm	59.0	μm	0.84
12232	α	0.745	$10^{-3}\circ$	14.0	$10^{-3}\circ$	5.3
	x	0.545	μm	55.8	μm	0.98
	y	1.785	μm	36.4	μm	4.9
12233	α	1.014	$10^{-3}\circ$	23.0	$10^{-3}\circ$	4.4
	x	0.597	μm	70.8	μm	0.84
	y	0.391	μm	3.1	μm	12.6
12234	α	1.043	$10^{-3}\circ$	18.7	$10^{-3}\circ$	5.6
	x	0.638	μm	69.7	μm	0.92
	y	0.518	μm	59.0	μm	0.88
12235	α	0.963	$10^{-3}\circ$	14.9	$10^{-3}\circ$	6.5
	x	0.678	μm	35.6	μm	1.9
	y	0.924	μm	70.5	μm	1.3
	α	1.278	$10^{-3}\circ$	17.7	$10^{-3}\circ$	7.2

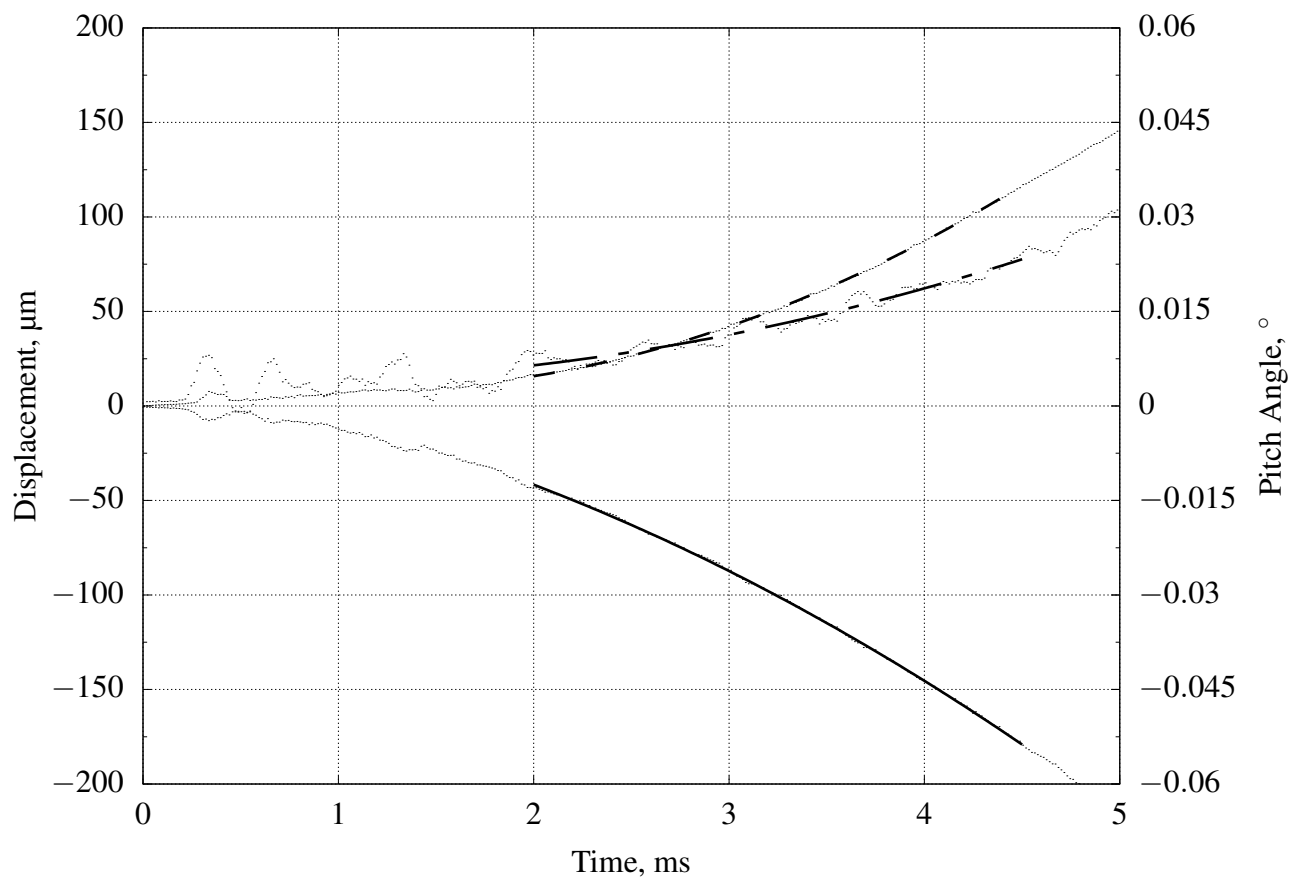


Figure C.1: The measured trajectories with their respective fit from shot 12198.

APPENDIX C IMAGE TRACKING DATA

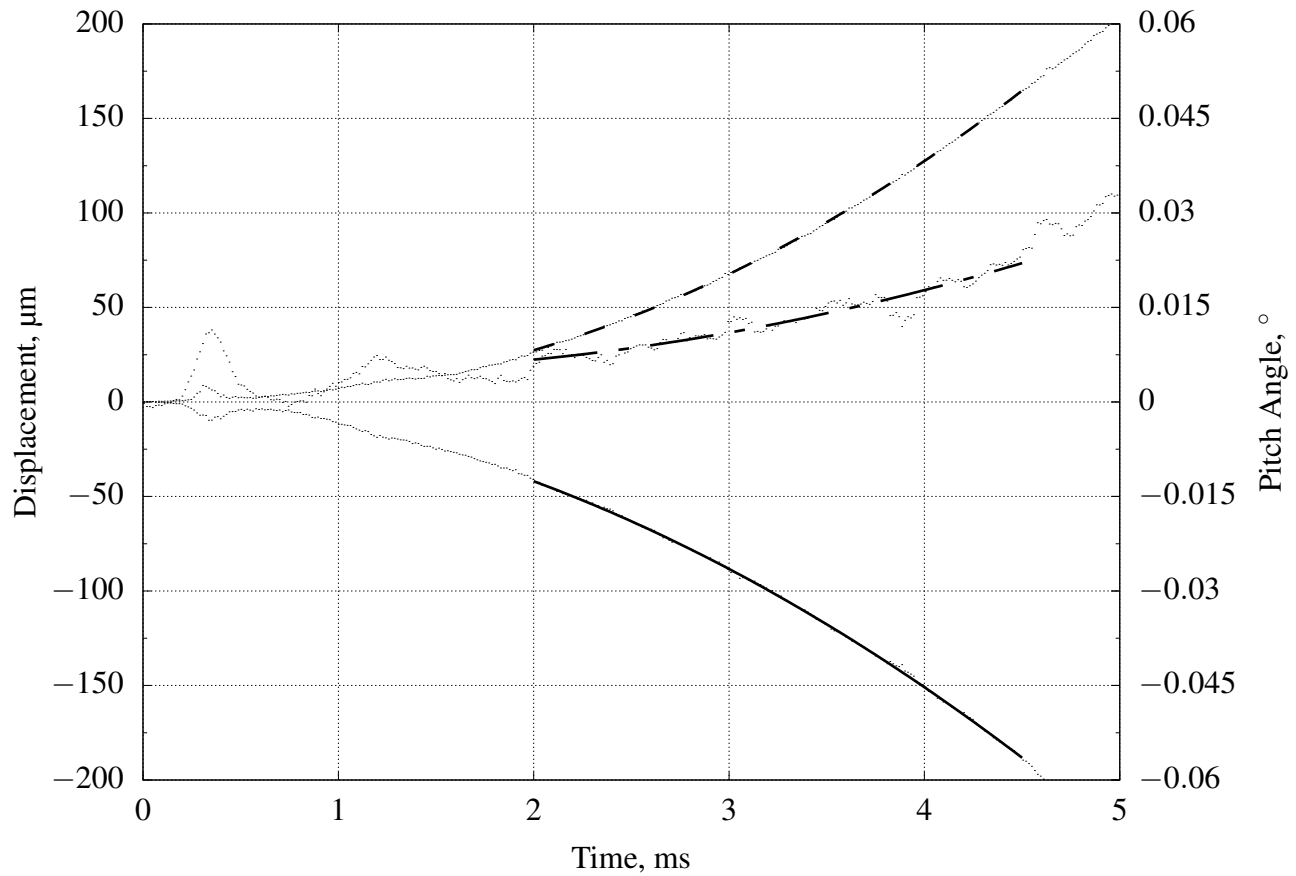


Figure C.2: The measured trajectories with their respective fit from shot 12199.

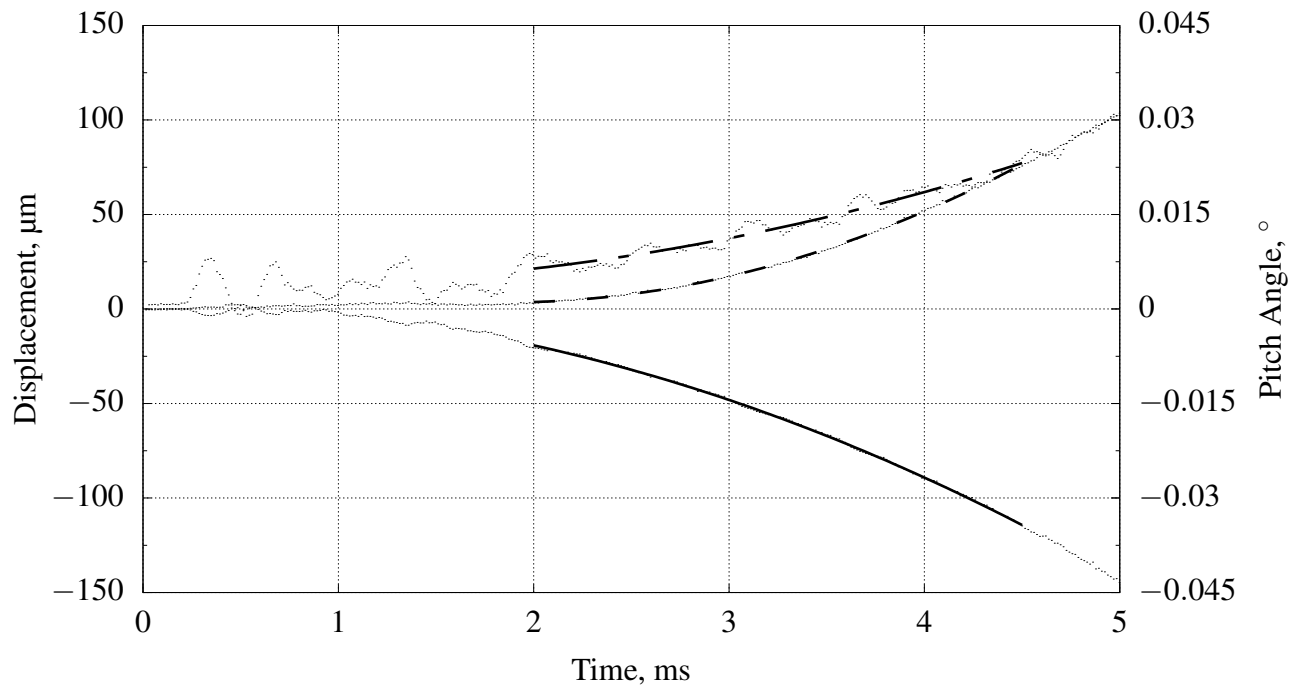


Figure C.3: The measured trajectories with their respective fit from shot 12223.

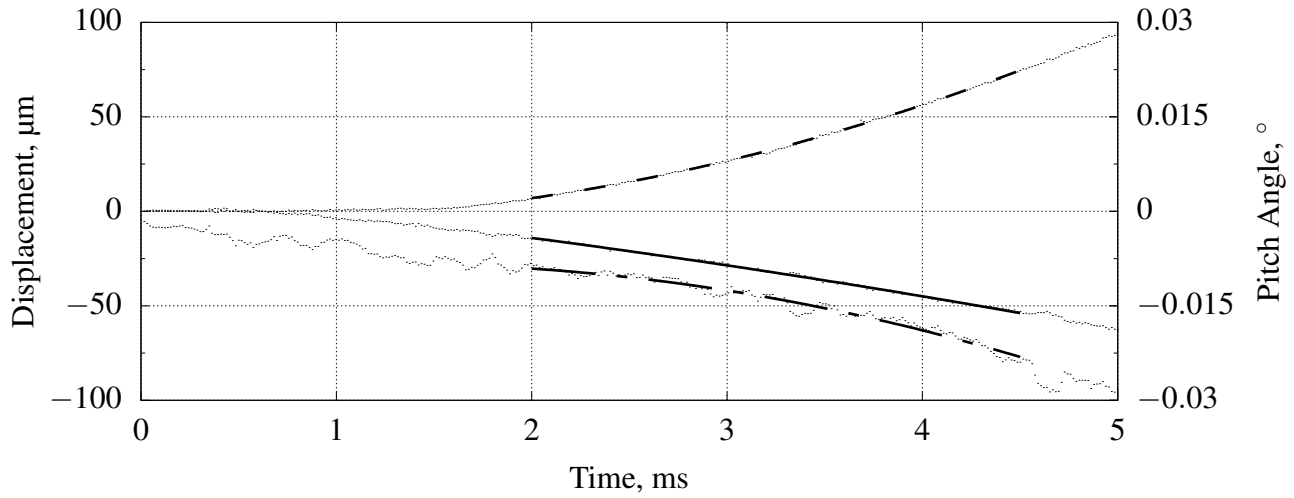


Figure C.4: The measured trajectories with their respective fit from shot 12224.

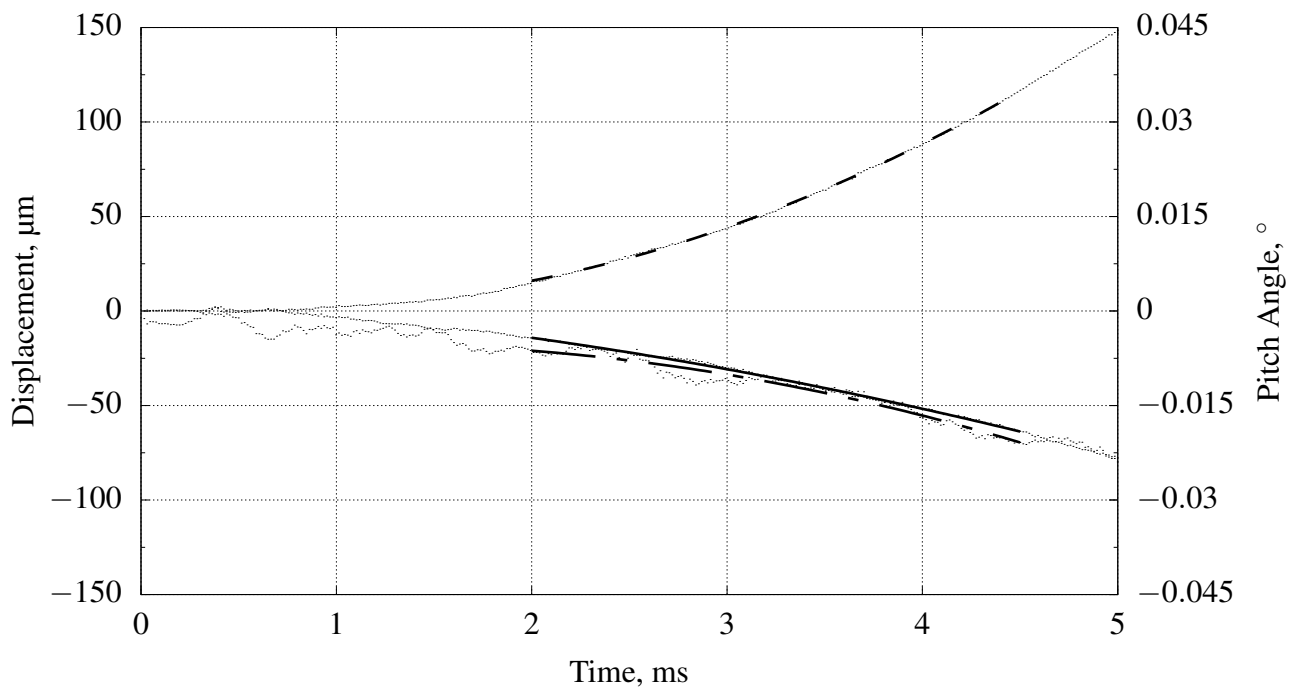


Figure C.5: The measured trajectories with their respective fit from shot 12225.

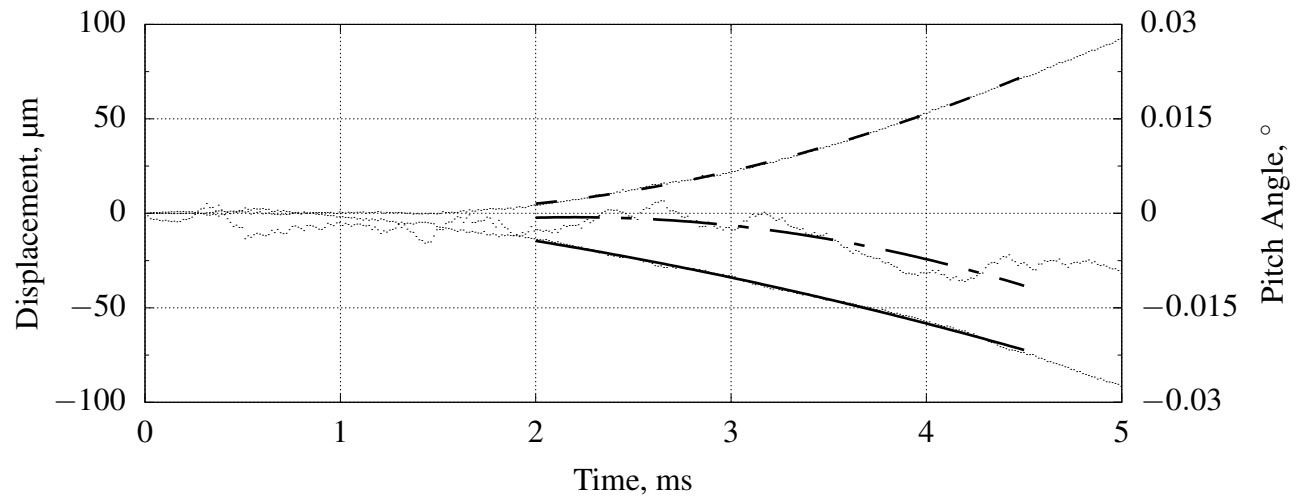


Figure C.6: The measured trajectories with their respective fit from shot 12226.

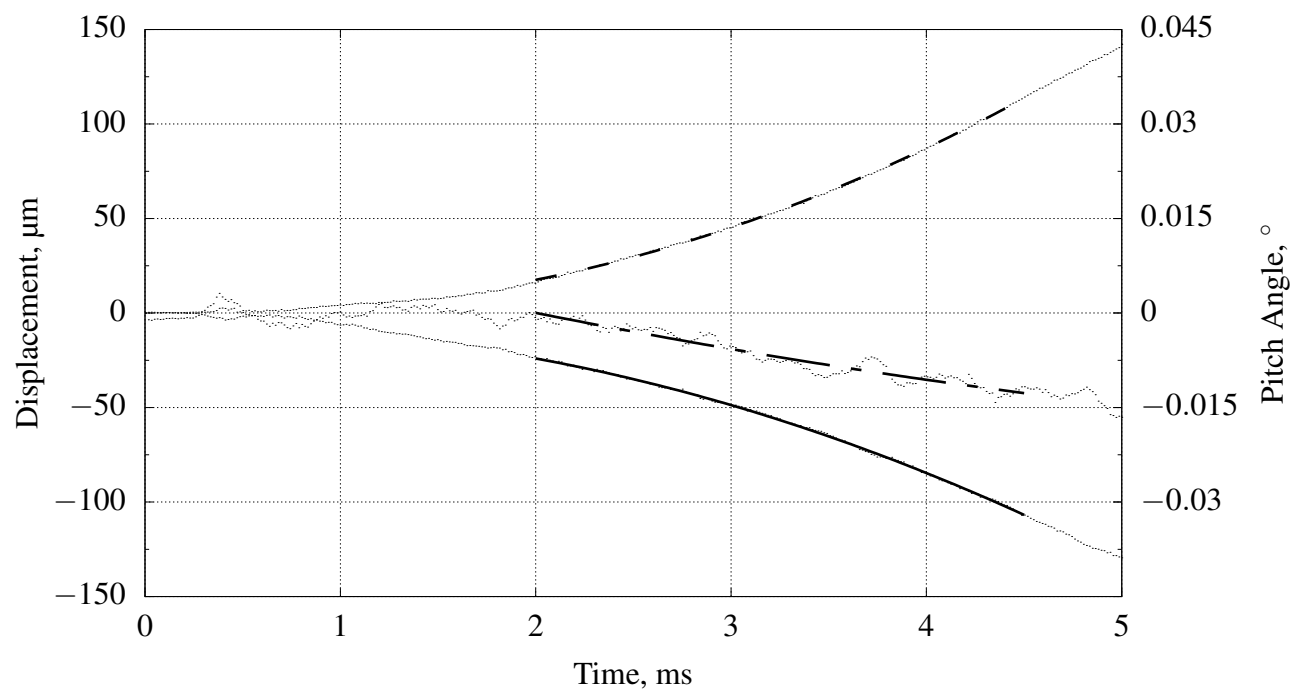


Figure C.7: The measured trajectories with their respective fit from shot 12228.

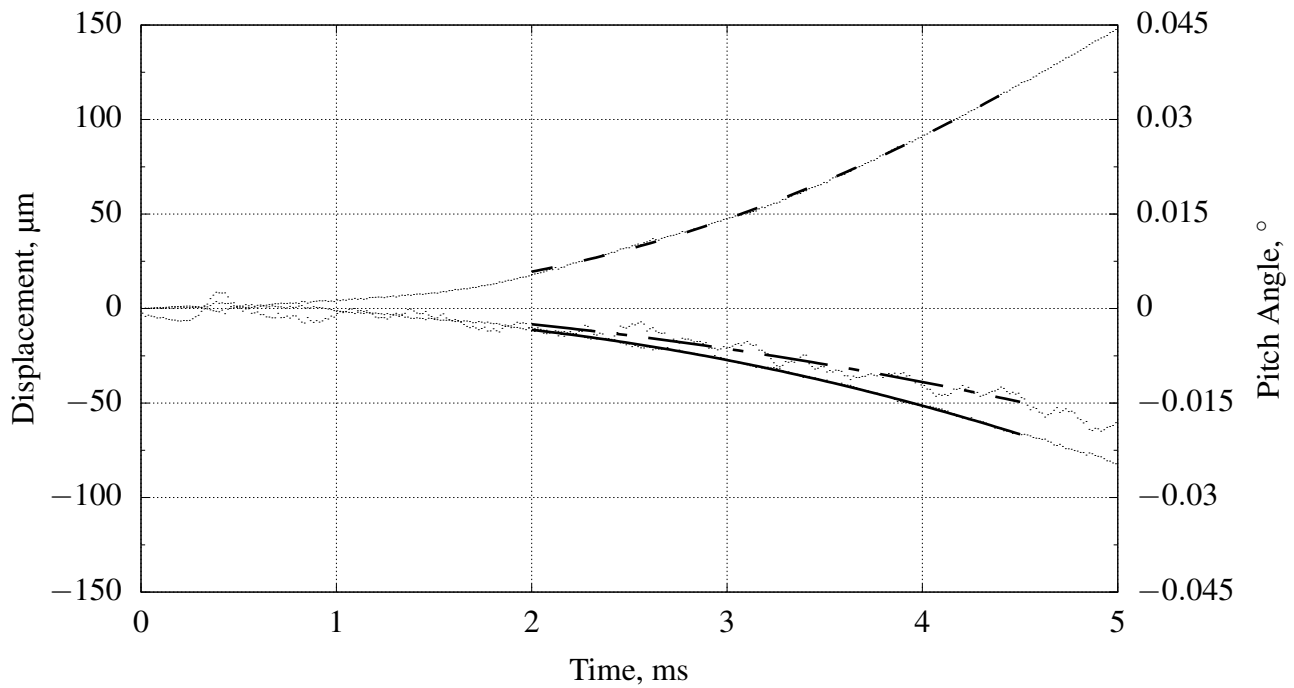


Figure C.8: The measured trajectories with their respective fit from shot 12229.

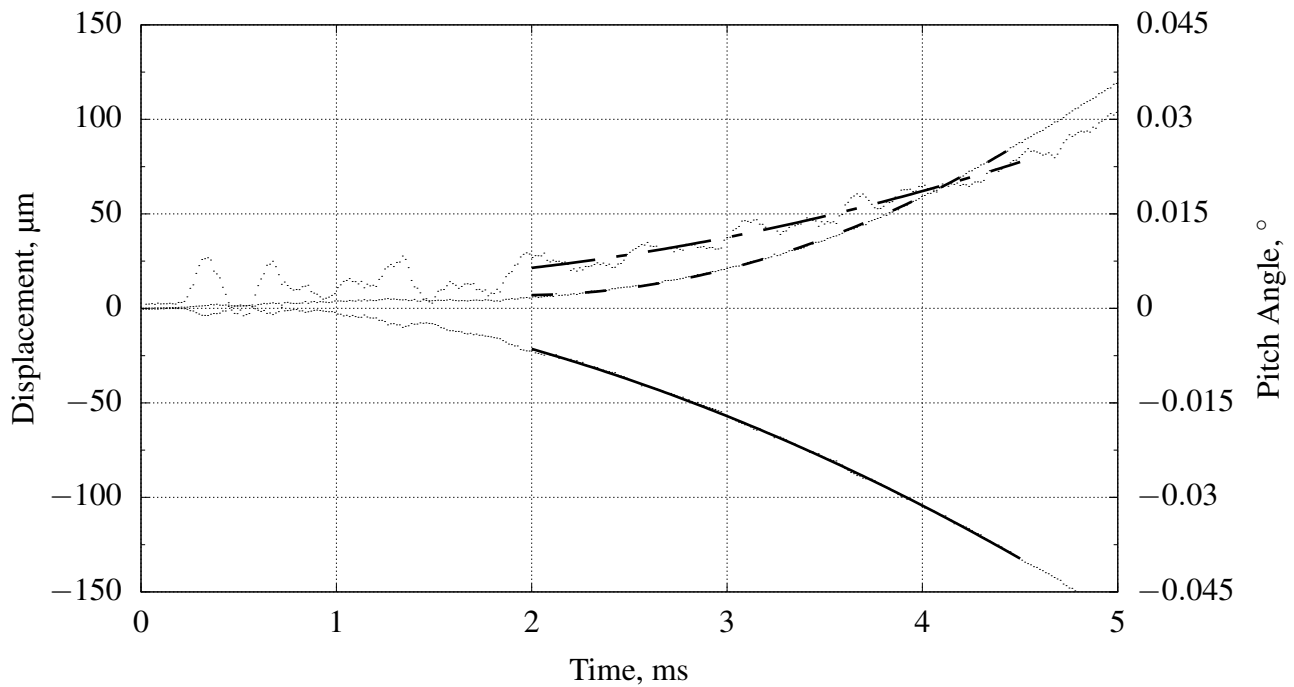


Figure C.9: The measured trajectories with their respective fit from shot 12230.

APPENDIX C IMAGE TRACKING DATA

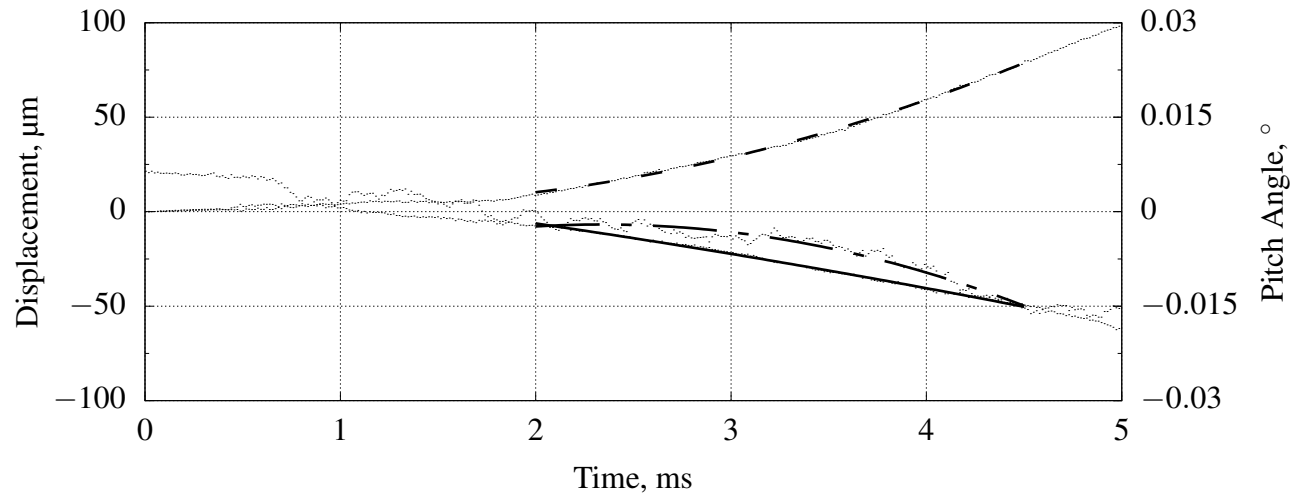


Figure C.10: The measured trajectories with their respective fit from shot 12231.

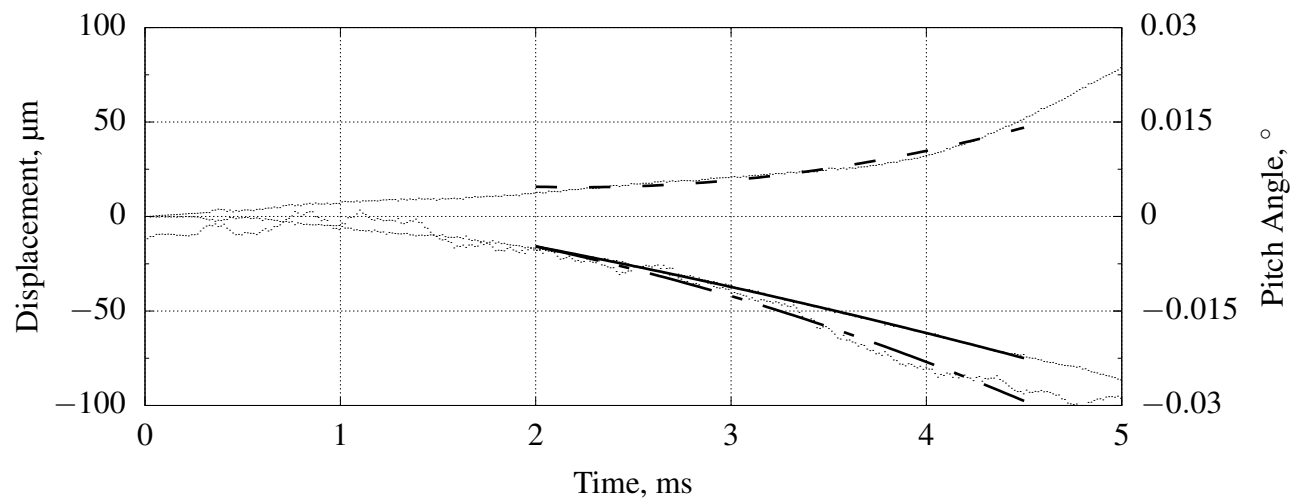


Figure C.11: The measured trajectories with their respective fit from shot 12232.

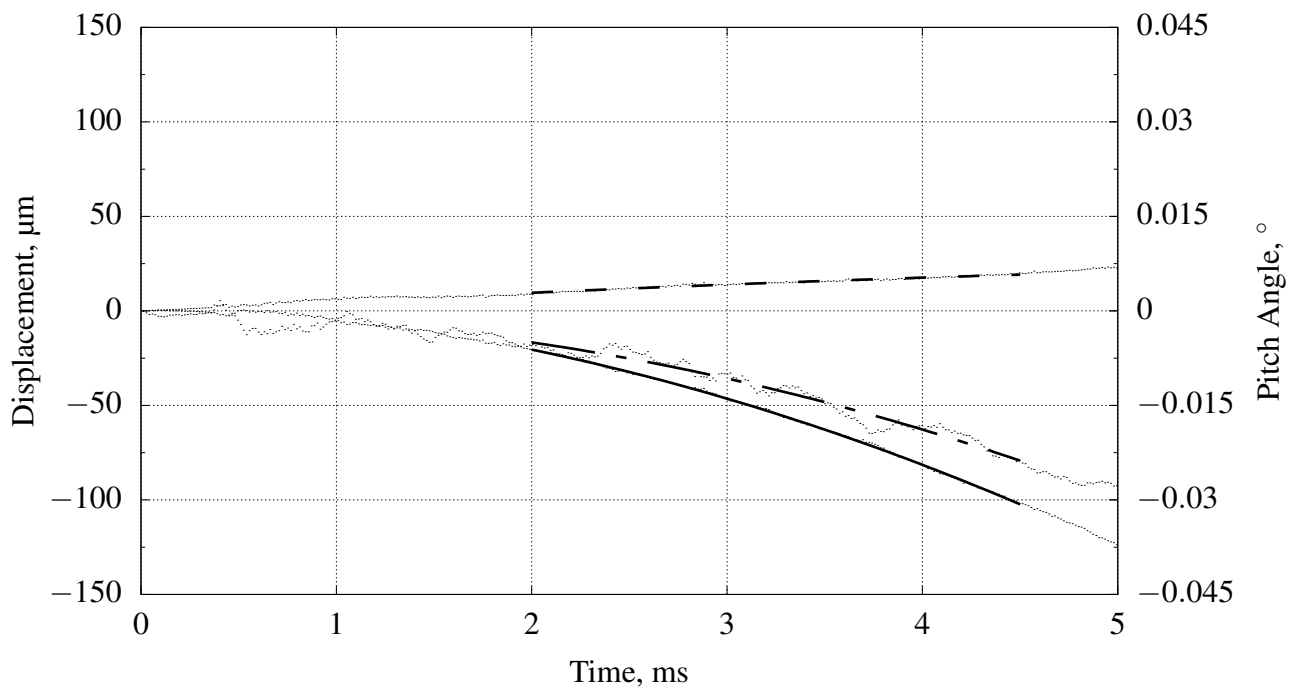


Figure C.12: The measured trajectories with their respective fit from shot 12233.

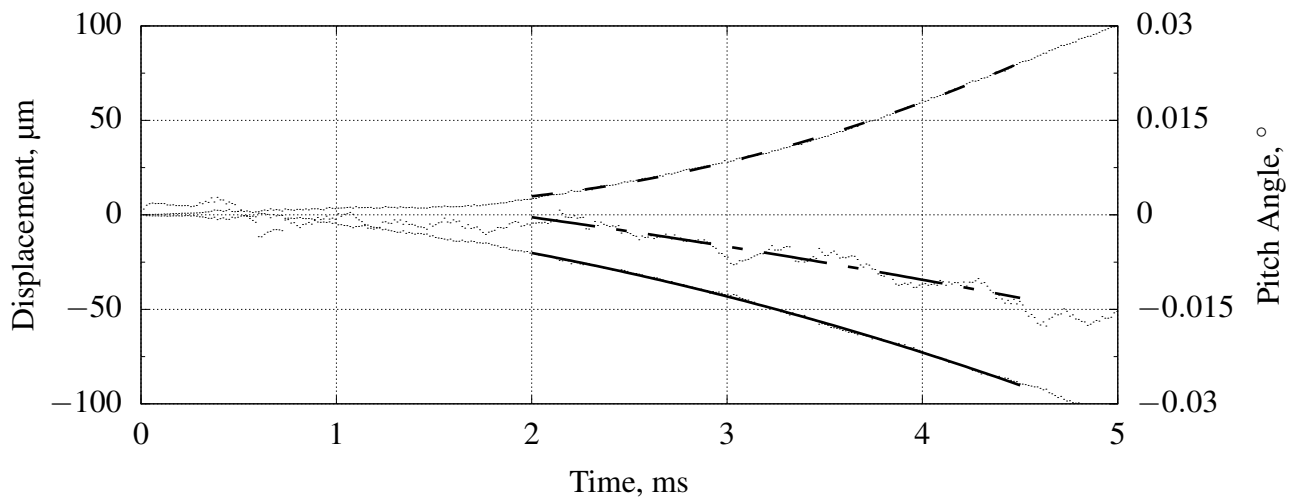


Figure C.13: The measured trajectories with their respective fit from shot 12234.

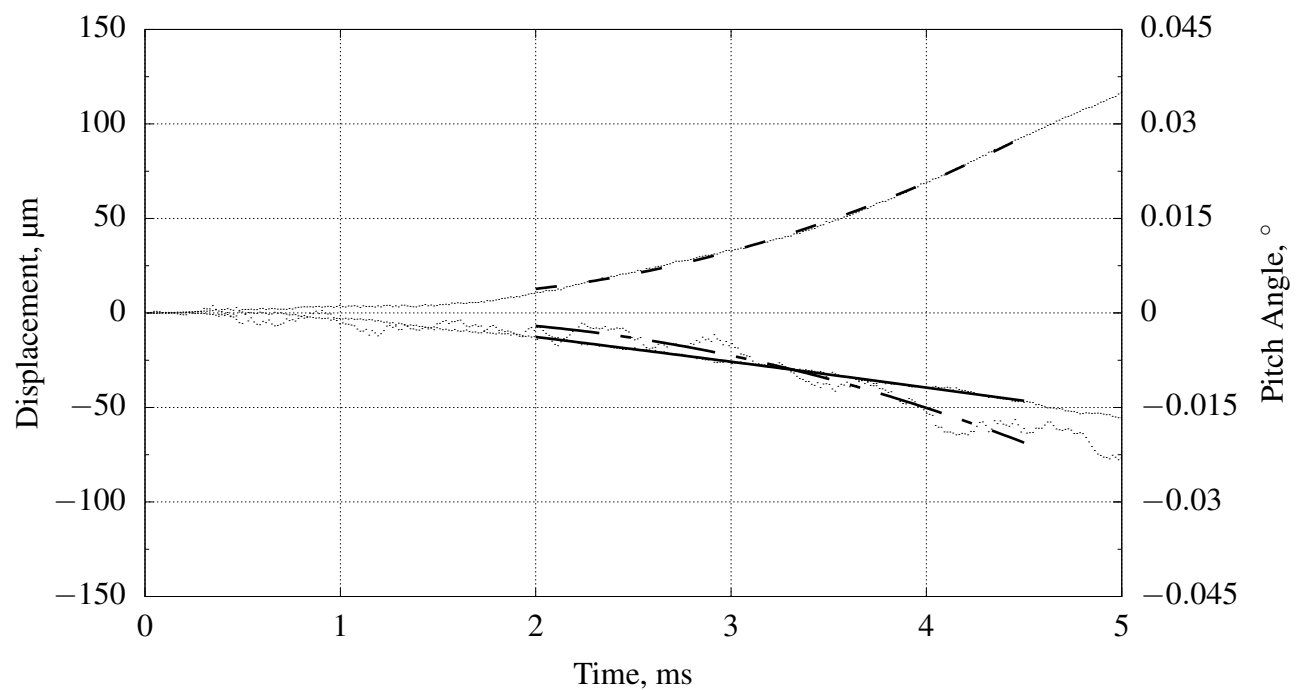


Figure C.14: The measured trajectories with their respective fit from shot 12235.

APPENDIX D

SHOT SUMMARY

The tables presented in the following list all shots performed as part of the present study. Table D.1 lists the fill condition of T4 and the corresponding nozzle supply conditions. Table D.2 lists the freestream conditions and the test gas composition of all shots. The nozzle supply conditions and the freestream conditions of all shots up to shot 12197 were calculated using ESTCj. The freestream conditions of all shots from shot 12197 were calculated using a NENZFr response surface.

The fill temperature of all components was assumed to be 300 K.

Table D.1: The initial tunnel fill and nozzle supply conditions of all shots.

Shot	Res.	Compression Tube		Shock Tube		Facility Motion			Nozzle Supply Conditions				
		p_R MPa	p_{CT} kPa	Driver Gas	p_{ST} kPa	Test Gas	d_D mm	Recoil mm	Over Run mm	V_{ss} km s^{-1}	p_s MPa	T_s K	ρ_s kg m^3
<i>Campaign 1</i>													
11928	2.6	40.2	Argon	202	Air	3				<i>Data System Error, no Data Recorded</i>			
11929	2.6	40.2	Argon	202	Air	3	-119	11	1772	22.1	2576	29.9	2.8
11930	2.6	40.2	Argon	202	Air	3	-120	11	1658	22.4	2408	32.4	2.5
11931	2.6	40.2	Argon	202	Air	3	-120	11	1788	22.0	2597	29.4	2.8
11932	2.6	40.2	Argon	192	Air	3	-120	11	1800	20.1	2597	27.0	2.8
11933	2.6	40.2	Argon	187	Air	3	-120	11	1805	22.3	2671	29.0	2.9
11934	2.6	40.2	Argon	185	Air	3			<i>Xenon Arc Lamp Triggered DAQ, no Data Recorded</i>				
11935	2.6	40.2	Argon	185	Air	3			<i>Xenon Arc Lamp Triggered DAQ, no Data Recorded</i>				
11936	2.6	40.2	Argon	185	Air	3	-120	11	1829	22.8	2726	29.1	3.0
11937	2.6	40.2	Argon	183	Air	3	-120	11	1766	22.5	2627	29.8	2.8
11938	2.6	40.2	Argon	183	Air	3	-120	11	1840	22.4	2740	28.4	3.0
11939	2.6	40.2	Argon	178	Air	3	-120	11	1817	21.6	2686	27.8	3.0
11940	2.6	40.2	Argon	178	Air	3	-119	11	1817	21.0	2672	27.3	2.9
11941	2.6	40.2	Argon	175	Air	3	-119	11	1840	21.6	2732	27.4	3.0
11942	2.6	40.2	Argon	175	Air	3	-120	11	1794	23.0	2706	29.6	3.0
11943	2.6	40.2	Argon	175	Air	3	-120	11	1858	22.3	2792	27.9	3.1
11944	2.6	40.2	Argon	175	Air	3	-	-	1829	22.1	2740	28.1	3.0
11945	2.7	40.2	Argon	175	Air	3	-	-	1864	23.6	2832	29.0	3.1
11946	2.7	40.2	Argon	175	Air	3	-121	11	1852	23.4	2807	29.0	3.1

Table D.1: (continued)

Shot -	Res.	Compression Tube		Shock Tube		Facility Motion			Nozzle Supply Conditions				
		p_R MPa	p_{CT} kPa	Driver Gas	p_{ST} kPa	Test Gas	d_D mm	Recoil mm	Over Run mm	V_{ss} km s ⁻¹	p_s MPa	T_s K	ρ_s kg m ⁻³
11947	2.7	40.2	Argon	175	Air	3	-121	11	1834	23.3	2776	29.2	3.1
11948	2.7	40.2	Argon	175	Air	3	-	-	1734	22.9	2601	30.6	2.8
11949	2.7	40.2	Argon	175	Air	3	-120	11	1739	23.0	2619	30.6	2.8
11950	2.7	40.2	Argon	175	Air	3	-121	11	1728	22.0	2578	29.7	2.8
11951	2.7	40.2	Argon	175	Air	3	-121	11	1877	22.5	2827	27.7	3.1
<i>Campaign 2</i>													
12112	2.6	40.2	Argon	202	Air	3	-120	12	1766	22.8	2583	30.8	2.8
12113	2.6	40.2	Argon	202	Air	3	-120	12	1761	23.7	2595	31.9	2.8
12114	2.8	40.2	Argon	202	Air	3	-122	12	1766	25.8	2648	34.0	2.9
12115	2.8	40.2	Argon	202	Air	3	-122	12	1755	24.5	2603	32.8	2.8
12116	2.8	40.2	Argon	205	Air	3	<i>Trigger Fault, no Data Recorded</i>						
12117	2.8	40.2	Argon	205	Air	3	-	-	1734	24.9	2570	33.7	2.8
12118	2.8	40.2	Argon	205	Air	3	-122	12	1734	26.3	2600	35.3	2.8
12119	2.8	40.2	Argon	205	Air	3	-121	12	1723	25.2	2560	34.3	2.7
12120	2.8	40.2	Argon	205	Air	3	-121	12	1718	24.6	2528	33.8	2.7
12121	2.8	40.2	Argon	205	Air	3	-121	12	1708	24.7	2527	34.1	2.7
12122	2.8	40.2	Argon	205	Air	3	-122	12	1718	25.4	2556	34.6	2.7
12123	2.8	40.2	Argon	205	Air	3	-122	12	1723	24.5	2546	33.6	2.7

Table D.1: (continued)

Shot -	Res.	Compression Tube		Shock Tube		Facility Motion			Nozzle Supply Conditions				
		p_R MPa	p_{CT} kPa	Driver Gas	p_{ST} kPa	Test Gas	d_D mm	Recoil mm	Over Run mm	V_{ss} km s^{-1}	p_s MPa	T_s K	ρ_s kg m^3
<i>Campaign 3</i>													
12197	2.6	40.2	Argon	155	Air	3	-119	11	1883	23.0	2900	27.5	3.3
12198	2.6	40.2	Argon	155	Air	3	-119	11	1871	22.9	2878	27.5	3.2
12199	2.6	40.2	Argon	155	Air	3	-119	11	1871	23.5	2893	28.2	3.2
12200	2.6	40.2	Argon	155	Air	3	-119	11	1840	21.5	2794	26.7	3.1
12201	2.6	40.2	Argon	155	Air	3	-119	11	1877	22.5	2879	27.1	3.2
12202	2.6	40.2	Argon	155	Air	3	-119	11	1871	22.8	2877	27.5	3.2
12203	2.6	40.2	Argon	155	Air	3	-119	12	1871	23.0	2881	27.7	3.2
12204	2.6	40.2	Argon	155	Air	3	-119	11	1852	22.2	2832	27.2	3.2
12205	1.6	27.4	Argon	100	Air	2	-106	12	1777	13.5	2680	17.5	2.9
12206	1.6	27.4	Argon	100	Air	2	-106	12	1805	13.5	2721	17.2	3.0
12207	1.6	27.4	Argon	100	Air	2	-106	12	1703	13.6	2568	18.4	2.8
12208	1.6	27.4	Argon	100	Air	2	-106	12	1823	13.3	2745	16.9	3.0
12209	1.6	27.4	Argon	100	Air	2	-105	12	1794	13.9	2721	17.7	3.0
12210	1.6	27.4	Argon	100	Air	2	-106	12	1772	13.1	2654	17.1	2.9
12211	1.6	27.4	Argon	100	Air	2	-107	12	1794	13.9	2721	17.7	3.0
12212	1.6	27.4	Argon	100	Air	2	-107	11	1772	12.2	2618	16.2	2.9
12213	1.6	27.4	Argon	100	Air	2	-106	11	1800	13.0	2696	16.8	3.0
12214	1.6	27.4	Argon	100	Air	2	-107	11	1800	13.6	2718	17.3	3.0
12215	2.6	40.2	Argon	155	Air	3	-118	12	1852	22.1	2828	27.1	3.2

Table D.1: (continued)

Res.	Shot	Compression Tube		Shock Tube		Facility Motion			Nozzle Supply Conditions					
		p_R	p_{CT}	Driver	p_{ST}	Test	d_D	Recoil	Over Run	V_{ss}	p_s	T_s	ρ_s	H_s
-	-	MPa	kPa	Gas	kPa	Gas	mm	mm	mm	km s ⁻¹	MPa	K	kg m ⁻³	MJ kg ⁻¹
12216	2.6	40.2	Argon	155	Air	3	-119	11	1852	22.6	2840	27.6	3.2	
12217	2.6	40.2	Argon	155	Air	3	-119	11	1858	22.4	2845	27.2	3.2	
12218	2.6	40.2	Argon	155	Air	3	-119	11	1864	22.3	2852	27.1	3.2	
12219	2.6	40.2	Argon	155	Air	3	-119	11	1864	22.4	2856	27.2	3.2	
12220	2.6	40.2	Argon	155	Air	3	-119	11	1852	22.1	2828	27.1	3.2	
12221	2.6	40.2	Argon	155	Air	3	-118	12	1858	22.3	2842	27.1	3.2	
12222	2.6	40.2	Argon	155	Air	3	-119	12	1829	22.5	2801	27.8	3.1	
12223	2.6	40.2	Argon	155	Air	3	-119	11	1834	21.9	2796	27.2	3.1	
12224	2.6	40.2	Argon	155	Air	3	-118	12	1846	21.3	2800	26.4	3.1	
12225	2.6	40.2	Argon	155	Air	3	-118	12	1846	21.6	2807	26.7	3.1	
12226	2.6	40.2	Argon	155	Air	3	-118	12	1871	21.5	2845	26.2	3.2	
12227	2.6	40.2	Argon	155	Air	3	-118	11	1846	22.4	2826	27.5	3.1	
12228	2.6	40.2	Argon	155	Air	3	-117	12	1829	21.5	2777	26.9	3.1	
12229	2.6	40.2	Argon	155	Air	3	-118	11	1840	21.3	2790	26.5	3.1	
12230	2.6	40.2	Argon	155	Air	3	-118	11	1829	21.6	2780	27.0	3.1	
12231	2.6	40.2	Argon	155	Air	3	-118	12	1840	22.5	2819	27.7	3.1	
12232	2.6	40.2	Argon	155	Air	3	-118	11	1846	20.8	2787	25.9	3.1	
12233	2.6	40.2	Argon	155	Air	3	-118	12	1858	21.9	2832	26.8	3.2	
12234	2.6	40.2	Argon	155	Air	3	-118	12	1852	21.9	2822	26.8	3.1	
12235	2.6	40.2	Argon	155	Air	3	-118	12	1840	21.8	2801	26.9	3.1	

Table D.2: The freestream conditions, test gas properties and composition of all shots.

Shot -	Freestream							Test Gas					
	p_0 Pa	T_0 K	ρ_0 gm^{-3}	M_0 -	u_0 ms^{-1}	q_0 kPa	$Re_{u,0}$ $\times 10^6$	R_0 $\text{Jkg}^{-1}\text{K}^{-1}$	γ_0 -	Y_{N2} -	Y_{O2} -	Y_{NO} -	Y_O -
<i>Campaign 1</i>													
11928 <i>Data System Error, no Data Recorded</i>													
11929	2045	244	29.2	7.58	2376	82.4	4.3	287.0	1.4	0.76	0.23	-	-
11930	2028	221	32.0	7.67	2284	83.5	5.0	287.0	1.4	0.76	0.23	-	-
11931	2035	247	28.7	7.57	2387	81.8	4.2	287.0	1.4	0.76	0.23	-	-
11932	1867	247	26.3	7.57	2387	75.0	3.9	287.0	1.4	0.76	0.23	-	-
11933	2081	258	28.1	7.54	2427	82.8	4.1	287.0	1.4	0.76	0.23	-	-
11934	<i>Xenon Arc Lamp Triggered DAQ, no Data Recorded</i>												
11935	<i>Xenon Arc Lamp Triggered DAQ, no Data Recorded</i>												
11936	1873	256	25.4	7.65	2462	76.8	3.8	288.2	1.4	0.77	0.23	-	-
11937	2094	251	29.0	7.56	2403	83.8	4.3	287.0	1.4	0.76	0.23	-	-
11938	2110	268	27.4	7.50	2464	83.2	3.9	287.0	1.4	0.76	0.23	-	-
11939	1765	252	24.3	7.67	2447	72.7	3.6	288.2	1.4	0.77	0.23	-	-
11940	1715	250	23.8	7.68	2439	70.7	3.6	288.2	1.4	0.77	0.23	-	-
11941	1783	259	23.9	7.64	2472	72.9	3.5	288.2	1.4	0.77	0.23	-	-
11942	2159	263	28.6	7.52	2445	85.5	4.1	287.0	1.4	0.76	0.23	-	-
11943	2122	276	26.8	7.47	2492	83.1	3.8	287.0	1.4	0.76	0.23	-	-
11944	2088	268	27.1	7.50	2464	82.3	3.9	287.0	1.4	0.76	0.23	-	-
11945	2255	283	27.8	7.46	2513	87.8	3.9	287.0	1.4	0.76	0.23	-	-
11946	2224	279	27.8	7.47	2499	86.8	3.9	287.0	1.4	0.76	0.23	-	-

Table D.2: (continued)

Shot	Freestream							Test Gas					
	p_0	T_0	ρ_0	M_0	u_0	q_0	$Re_{u,0}$	R_0	γ_0	Y_{N2}	Y_{O2}	Y_{NO}	Y_O
-	Pa	K	gm^{-3}	-	ms^{-1}	kPa	$10^{-6} m^{-1}$	$Jkg^{-1} K^{-1}$	-	-	-	-	-
11947	2205	274	28.1	7.48	2483	86.5	4.0	287.0	1.4	0.76	0.23	-	-
11948	2130	249	29.8	7.57	2394	85.4	4.4	287.0	1.4	0.76	0.23	-	-
11949	2135	250	29.7	7.56	2399	85.6	4.4	287.0	1.4	0.76	0.23	-	-
11950	2031	244	29.0	7.58	2377	81.8	4.3	287.0	1.4	0.76	0.23	-	-
11951	2149	282	26.6	7.46	2510	83.7	3.7	287.0	1.4	0.76	0.23	-	-
<i>Campaign 2</i>													
12112	2113	245	30.1	7.58	2379	85.0	4.5	287.0	1.4	0.76	0.23	-	-
12113	2200	247	31.1	7.58	2386	88.4	4.6	287.0	1.4	0.76	0.23	-	-
12114	2410	254	33.0	7.55	2414	96.2	4.8	287.0	1.4	0.76	0.23	-	-
12115	2275	248	32.0	7.57	2390	91.3	4.7	287.0	1.4	0.76	0.23	-	-
12117	2298	243	32.9	7.59	2373	92.7	4.9	287.0	1.4	0.76	0.23	-	-
12118	2441	247	34.4	7.57	2388	98.0	5.1	287.0	1.4	0.76	0.23	-	-
12119	2328	242	33.6	7.59	2367	94.0	5.0	287.0	1.4	0.76	0.23	-	-
12121	2271	237	33.4	7.61	2349	92.1	5.0	287.0	1.4	0.76	0.23	-	-
12122	2342	241	33.8	7.59	2365	94.6	5.0	287.0	1.4	0.76	0.23	-	-
12123	2261	240	32.9	7.60	2359	91.4	4.9	287.0	1.4	0.76	0.23	-	-
<i>Campaign 3</i>													
12197	2108	280	26.1	7.53	2530	83.5	3.8	288.3	1.4	0.75	0.22	2.7×10^{-2}	3.2×10^{-4}
12198	2090	277	26.2	7.54	2518	83.0	3.8	288.3	1.4	0.75	0.22	2.6×10^{-2}	3.0×10^{-4}

Table D.2: (continued)

Shot	Freestream							Test Gas					
	p_0 Pa	T_0 K	ρ_0 gm^{-3}	M_0 -	u_0 ms^{-1}	q_0 kPa	$Re_{u,0}$ 10^{-6}m^{-1}	R_0 $\text{Jkg}^{-1} \text{K}^{-1}$	γ_0 -	Y_{N2} -	Y_{O2} -	Y_{NO} -	Y_O -
12199	2152	279	26.7	7.54	2526	85.4	3.9	288.3	1.4	0.75	0.22	2.7×10^{-2}	3.1×10^{-4}
12200	1947	266	25.4	7.57	2478	78.1	3.8	288.3	1.4	0.76	0.22	2.3×10^{-2}	2.4×10^{-4}
12201	2060	277	25.8	7.54	2519	81.8	3.7	288.3	1.4	0.75	0.22	2.6×10^{-2}	3.1×10^{-4}
12202	2087	277	26.1	7.54	2518	82.9	3.8	288.3	1.4	0.76	0.22	2.6×10^{-2}	3.0×10^{-4}
12203	2105	278	26.3	7.54	2520	83.6	3.8	288.3	1.4	0.75	0.22	2.6×10^{-2}	3.0×10^{-4}
12204	2021	271	25.9	7.56	2496	80.7	3.8	288.3	1.4	0.76	0.22	2.4×10^{-2}	2.7×10^{-4}
12205	1233	252	17.0	7.60	2420	49.8	2.6	288.3	1.4	0.76	0.22	1.9×10^{-2}	2.3×10^{-4}
12206	1235	258	16.6	7.58	2441	49.6	2.5	288.3	1.4	0.76	0.22	2.0×10^{-2}	2.7×10^{-4}
12207	1220	237	17.9	7.65	2363	50.0	2.8	288.2	1.4	0.76	0.22	1.5×10^{-2}	1.2×10^{-4}
12208	1229	261	16.3	7.57	2453	49.2	2.4	288.3	1.4	0.76	0.22	2.1×10^{-2}	2.9×10^{-4}
12209	1273	257	17.2	7.58	2441	51.1	2.6	288.3	1.4	0.76	0.22	2.0×10^{-2}	2.6×10^{-4}
12210	1190	249	16.6	7.61	2407	48.1	2.5	288.2	1.4	0.76	0.22	1.8×10^{-2}	2.1×10^{-4}
12211	1273	257	17.2	7.58	2441	51.1	2.6	288.3	1.4	0.76	0.22	2.0×10^{-2}	2.6×10^{-4}
12212	1108	244	15.8	7.62	2390	45.0	2.4	288.2	1.4	0.76	0.22	1.7×10^{-2}	1.9×10^{-4}
12213	1193	254	16.3	7.59	2428	48.0	2.4	288.3	1.4	0.76	0.22	1.9×10^{-2}	2.5×10^{-4}
12214	1245	257	16.8	7.58	2439	50.0	2.5	288.3	1.4	0.76	0.22	2.0×10^{-2}	2.6×10^{-4}
12215	2006	270	25.7	7.56	2494	80.2	3.8	288.3	1.4	0.76	0.22	2.4×10^{-2}	2.7×10^{-4}
12216	2055	272	26.2	7.56	2500	82.0	3.8	288.3	1.4	0.76	0.22	2.4×10^{-2}	2.7×10^{-4}
12217	2037	273	25.9	7.55	2503	81.2	3.8	288.3	1.4	0.76	0.22	2.5×10^{-2}	2.8×10^{-4}
12218	2033	274	25.8	7.55	2507	81.0	3.8	288.3	1.4	0.76	0.22	2.5×10^{-2}	2.9×10^{-4}
12219	2047	274	25.9	7.55	2508	81.5	3.8	288.3	1.4	0.76	0.22	2.5×10^{-2}	2.9×10^{-4}

Table D.2: (continued)

Shot	Freestream							Test Gas					
	p_0 Pa	T_0 K	ρ_0 gm^{-3}	M_0 -	u_0 ms^{-1}	q_0 kPa	$Re_{u,0}$ 10^{-6}m^{-1}	R_0 $\text{Jkg}^{-1} \text{K}^{-1}$	γ_0 -	Y_{N2} -	Y_{O2} -	Y_{NO} -	Y_O -
12220	2008	270	25.8	7.56	2494	80.2	3.8	288.3	1.4	0.76	0.22	2.4×10^{-2}	2.7×10^{-4}
12221	2028	272	25.8	7.55	2501	80.9	3.8	288.3	1.4	0.76	0.22	2.5×10^{-2}	2.8×10^{-4}
12222	2035	266	26.5	7.57	2480	81.6	3.9	288.3	1.4	0.76	0.22	2.3×10^{-2}	2.3×10^{-4}
12223	1987	266	25.9	7.57	2479	79.7	3.8	288.3	1.4	0.76	0.22	2.3×10^{-2}	2.3×10^{-4}
12224	1934	267	25.2	7.57	2481	77.5	3.7	288.3	1.4	0.76	0.22	2.3×10^{-2}	2.5×10^{-4}
12225	1960	267	25.4	7.57	2484	78.5	3.7	288.3	1.4	0.76	0.22	2.3×10^{-2}	2.5×10^{-4}
12226	1964	273	25.0	7.55	2502	78.3	3.7	288.3	1.4	0.76	0.22	2.5×10^{-2}	2.9×10^{-4}
12227	2035	270	26.1	7.56	2494	81.3	3.8	288.3	1.4	0.76	0.22	2.4×10^{-2}	2.6×10^{-4}
12228	1942	263	25.6	7.58	2469	78.1	3.8	288.3	1.4	0.76	0.22	2.2×10^{-2}	2.2×10^{-4}
12229	1929	265	25.3	7.58	2476	77.4	3.7	288.3	1.4	0.76	0.22	2.2×10^{-2}	2.4×10^{-4}
12230	1955	263	25.7	7.58	2470	78.6	3.8	288.3	1.4	0.76	0.22	2.2×10^{-2}	2.2×10^{-4}
12231	2043	269	26.3	7.56	2490	81.7	3.9	288.3	1.4	0.76	0.22	2.4×10^{-2}	2.5×10^{-4}
12232	1886	265	24.8	7.58	2475	75.7	3.7	288.3	1.4	0.76	0.22	2.2×10^{-2}	2.4×10^{-4}
12233	1990	271	25.5	7.56	2497	79.5	3.7	288.3	1.4	0.76	0.22	2.4×10^{-2}	2.7×10^{-4}
12234	1986	270	25.6	7.56	2492	79.4	3.7	288.3	1.4	0.76	0.22	2.4×10^{-2}	2.6×10^{-4}
12235	1974	267	25.7	7.57	2481	79.1	3.8	288.3	1.4	0.76	0.22	2.3×10^{-2}	2.4×10^{-4}